DISSERTATION

submitted to the
Combined Faculty of Natural Sciences and Mathematics
of the University of Heidelberg, Heidelberg, Germany
for the degree of
Doctor of Natural Sciences (Dr. rer. nat.)

presented by
Dipl.-Chem. Anna Keese
born in Hannover, Germany

Oral examination: November 16th, 2012

Investigation of dye-functionalized TiO_2 nanoparticles using vibrational sum-frequency-generation spectroscopy

The dissertation was carried out at the

Department of Applied Physical Chemistry

University of Heidelberg, Heidelberg, Germany

and reviewed by

Prof. Dr. Michael Grunze
Department of Applied Physical Chemistry, University of Heidelberg

Prof. (apl.) Dr. Hans-Robert Volpp
Department of Applied Physical Chemistry, University of Heidelberg

Summary

Investigation of dye-functionalized TiO_2 nanoparticles using vibrational sum-frequency generation spectroscopy

The steadily increasing demand for energy worldwide has resulted in the depletion of the existing fossil energy resources and the pollution of the atmosphere by greenhouse gases such as CO_2, which are responsible for global warming. To curb these problems, research activities aiming at CO_2 conversion into value-added products, e.g. fuels like methanol, using sunlight have intensified over the last few years. In this work, TiO_2 nanoparticles functionalized with perylene-based dyes containing either a carboxylic acid or anhydride group as molecular anchor to the TiO_2 surface were studied as potential photocatalyst for solar light-driven CO_2 reduction. The dye binding geometry is of particular importance since it influences the electron transfer from the dye to TiO_2 and hence the photocurrent output of any given dye/TiO_2 system. Two dyes, ID1157 and ID1152, structurally identical apart from their anchor group, were selected to allow direct comparison. In addition, a simple model substance bearing an anhydride group was investigated to facilitate the interpretation of the lesser known anhydride binding mode. Surprisingly, despite their structural similarity, the observed photocurrent amplitude of the ID1157/TiO_2 system containing a carboxylic acid anchor was much higher than for the ID1152/TiO_2 system containing an anhydride anchor. With the help of ultraviolet/visible (UV/Vis) absorption, infrared (IR), Raman and vibrational sum-frequency generation (VSFG) spectroscopy it was sought to determine whether the photocurrent signals were correlated to the dissimilar anchor groups and their binding modes. From the UV/Vis spectra it was found that the anhydride group opened upon binding. As for the IR and Raman studies it could be concluded that the carboxylic acid anchor of ID1157 and both carboxylate groups of the opened anhydride of ID1152 bound via a bidentate bridging pattern. Furthermore, it was shown from the background-suppressed VSFG spectra of the bound dyes in air and water that these adsorbed in an orderly fashion, ID1157 more so than ID1152, but with both only slightly disturbed in the presence of water. In addition, it was found that all molecules in the ID1157 dye layer were adsorbed on the TiO_2 surface via chemisorption. By contrast, the ID1152 dye layer was composed of chemisorbed as well as physisorbed dyes, the latter being coordinated via a closed anhydride group. Also, ID1157 displayed a higher surface density of adsorbed molecules compared to ID1152. From a preliminary polarization analysis, it was suggested that the dyes with carboxylic acid anchor adopted a tilted binding geometry. In view of the results obtained on the binding geometry of the dyes ID1157 and ID1152 it was possible to identify some criteria important for the generation of a high photocurrent: 1) binding of the dye via chemisorption with 2) a high surface density and possibly through 3) a tilted geometry. These findings have important implications for the understanding of the mechanism of dye functionalization. Finally, methanol and CO_2 adsorption on TiO_2 films was investigated by VSFG spectroscopy. Only molecularly adsorbed methanol was observed which was easily displaced by water or methanol/water mixtures. However, CO_2 adsorption could not be detected in the spectral range which was investigated.

Zusammenfassung

Untersuchung von Farbstoff-funktionalisierten TiO_2 Nanopartikeln mittels Schwingungs-Summenfrequenzgenerations-Spektroskopie

Der weltweit stetig ansteigende Energiebedarf resultiert bereits in der Ausbeutung der existierenden fossilen Energieressourcen und der Verschmutzung der Atmosphäre mit Treibhausgasen wie CO_2, welche für die Erderwärmung verantwortlich gemacht werden. Um diese Probleme zu dämpfen, haben sich über die letzten Jahre die Forschungsaktivitäten mit dem Ziel der CO_2 Umwandlung in wertgesteigerte Produkte, z.B. Brennstoffe wie Methanol, mit Sonnenlicht verstärkt. In dieser Arbeit wurden TiO_2 Nanopartikel funktionalisiert mit Perylen-basierten Farbstoffen, die entweder eine Carbonsäure- oder Anhydridgruppe als molekularen Anker an die TiO_2 Oberfläche enthalten, als potentieller Photokatalyst für die Sonnenlicht getriebene CO_2 Reduktion untersucht. Die Bindungsgeometrie der Farbstoffe ist besonders wichtig, da sie den Elektronentransfer vom Farbstoff zum TiO_2 und damit den Photostrom eines jeden Farbstoff/TiO_2 Systems beeinflusst. Zwei Farbstoffe, ID1157 und ID1152, die strukturell identisch sind, abgesehen von ihrer Ankergruppe, wurden ausgewählt um einen direkten Vergleich zu ermöglichen. Außerdem wurde eine einfache Modellsubstanz mit Anhydridgruppe untersucht um die Interpretation des weniger bekannten Anbindungsmodus des Anhydrids zu erleichtern. Trotz der strukturellen Ähnlichkeit war überraschenderweise die Photostromamplitude des ID1157/TiO_2 Systems mit Carbonsäureanker viel größer als die des ID1152/TiO_2 Systems mit Anhydridanker. Mit Hilfe von Ultraviolet/Visible (UV/Vis)-Absorptions-, Infrarot (IR)-, Raman- und Schwingungs-Summenfrequenzgenerations (VSFG)-Spektroskopie sollte herausgefunden werden, ob das Photostromsignal mit den verschiedenen Ankergruppen und ihren Bindungsmodi korreliert war. Durch die UV/Vis Spektren wurde gefunden, dass sich die Anhydridgruppe bei der Anbindung öffnete. Unter Einbeziehung der IR und Raman Spektren konnte geschlussfolgert werden, dass der Carbonsäureanker von ID1157 und beide Carboxylatgruppen der geöffneten Anhydridgruppe von ID1152 über eine zweizähnige Brücke banden. Zusätzlich konnte durch die Hintergrund-unterdrückten VSFG Spektren der gebundenen Farbstoffe in Luft und Wasser gezeigt werden, dass diese geordnet adsorbierten, ID1157 mehr als ID1152, wobei allerdings beide nur wenig durch die Anwesenheit von Wasser gestört waren. Darüber hinaus wurde gefunden, dass alle Moleküle in der ID1157 Farbstoffschicht durch Chemisorption an die TiO_2 Oberfläche gebunden waren. Im Gegensatz dazu setzte sich die ID1152 Farbstoffschicht aus chemisorbierten und physisorbierten Farbstoffen zusammen, wobei letztere über eine geschlossene Anhydridgruppe koordiniert waren. Auch zeigte ID1157 eine höhere Oberflächendichte an adsorbierten Molekülen im Vergleich zu ID1152. Ausgehend von einer vorläufigen Polarisationsanalyse wurde vorgeschlagen, dass die Farbstoffe mit Carbonsäureanker eine geneigte Bindungsgeometrie einnahmen. Mit Blick auf die Ergebnisse, die bezüglich der Bindungsgeometrie der Farbstoffe ID1157 und ID1152 erhalten wurden, war es möglich einige Kriterien, die für die Erzeugung eines starken Photostroms wichtig sind, zu identifizieren: 1) Bindung des Farbstoffes durch Chemisorption mit 2) einer hohen Oberflächendichte und möglicherweise mit 3) einer geneigten Geometrie. Diese Erkenntnisse sind wichtig für das Verständnis des Mechnismus der Farbstofffunktionalisierung. Abschließend wurde die Methanol und CO_2 Adsorption an TiO_2 Filmen mit VSFG Spektroskopie untersucht. Es wurde nur molekular adsorbiertes Methanol beobachtet, das leicht durch Wasser oder Methanol/Wasser Mischungen verdrängt wurde. CO_2 Adsorption jedoch konnte nicht in der untersuchten spektralen Region detektiert werden.

Table of Contents

List of Figures

List of Tables

List of Abbreviations

AFM	atomic force microscopy
ATR	attenuated total internal reflection
as	asymmetric
BET	Brunauer-Emmett-Teller
bpy	bipyridyl
BSE	backscattered electron
CB	conduction band
CCD	charge-coupled device
cps	counts/s
CT	charge transfer
DFG	difference-frequency generation
DFT	density functional theory
DMF	dimethylformamide
DSSC	dye-sensitized organic solar cell
DR	doubly-resonant
DRIFT	diffuse reflectance infrared fourier transform
fs	femtosecond
FTIR	Fourier-transform infrared
FSR	free spectral range
FTO	fluorine-doped tin oxide
FWHM	full width at half maximum
GC	gas chromatography
HOMO	highest occupied molecular orbital
HREELS	high resolution electron energy loss spectroscopy
ip	in plane
IR	infrared
ITO	tin-doped indium oxide, indium-tin oxide
LEED	low-energy electron diffraction
NA	1,8-naphthalic anhydride
K2NA	1,8-naphthalene dicarboxylic acid dipotassium salt
LUMO	lowest unoccupied molecular orbital
MCT	mercury-cadmium-telluride
MeOH	methanol
MIR-IRAS	multiple-internal-reflection geometry-infrared absorption spectroscopy
NEXAFS	near edge X-ray absorption fine structure
NDFG	non-collinear difference-frequency generator
Nd:YAG	neodymium-doped yttrium aluminum garnet
NR	non-resonant

OEG	oligo(ethylene glycol)
OPA	optical parametric amplifier
OR	optical rectification
OTS	octadecyltrichlorosilane
PE	primary electron
PES	photoelectron spectroscopy
ps	picosecond
PTCDA	3,4,9,10-perylene-tetracarboxylic dianhydride
PTCDI	3,4,9,10-perylene-tetracarboxylic diimide
R	resonant, side-chain group
RF	radio-frequency
RGA	regenerative amplifier
RH	relative humidity
s	symmetric
S/N	signal-to-noise
SE	secondary electron
SEM	scanning electron microscopy
SFG	sum-frequency generation
SHG	second-harmonic generation
STM	scanning tunneling microscopy
TCO	transparent conducting oxide
TEA	triethylamine
TEOA	triethanolamine
THF	tetrahydrofuran
TIR	total internal reflection
TPD	temperature-programmed desorption
UV	ultraviolet
VB	valence band
Vis	visible
VSFG	vibrational sum-frequency generation
XPS	X-ray photoelectron spectroscopy

List of Symbols

α	polarizability
α_0	polarizability at the equilibrium position
a	lattice constant, force constant (Morse potential)
A	absorbance
$A_{\mathrm{R},q}$	amplitude of the q^{th} vibrational mode
β	first-order hyperpolarizability
b	lattice constant
$\chi^{(1)}$	linear susceptibility
$\chi^{(2)}$	second-order nonlinear susceptibility
$\chi^{(2)}_{jkl}$	j, k, l tensor elements of $\chi^{(2)}$
$\chi^{(2)}_{\mathrm{NR}}$	non-resonant contribution to $\chi^{(2)}$
$\chi^{(2)}_{\mathrm{R}}$	resonant contribution to $\chi^{(2)}$
$\chi^{(2)}_{\mathrm{R},q}$	q^{th} resonant contribution
$\chi^{(3)}$	third-order nonlinear susceptibility
c	lattice constant, speed of light, concentration
δ	bending vibration
ΔE_n	maximum transition energy
$\Delta\nu$	frequency difference
$\Delta\nu_{\mathrm{ads}}$	frequency difference of adsorbed species
$\Delta\nu_{\mathrm{salt}}$	frequency difference of salt compound of free species
d	thickness
d_p	penetration depth
dq	nuclear displacement
D_e	Morse potential well minimum
ε_0	vacuum electric permittivity
$\varepsilon, \varepsilon(\nu)$	molar extinction coefficient at frequency ν
E_0	amplitude of incident electric field
E_1	energy state of HOMO
E_2	energy state of LUMO
$\mathbf{E}$	electric field
$\mathbf{E}_{\mathrm{IR}}$	incident electric field of IR beam
$\mathbf{E}_{\mathrm{Vis}}$	incident electric field of Vis beam
E_{Fermi}	Fermi level (energy)
E_υ	energy levels of harmonic potential
ϕ_{NR}	phase factor of NR contribution
$\phi_{\mathrm{R},q}$	phase factor of q^{th} resonant contribution
F	restoring force
F_{eff}	effective finesse

γ	second-order hyperpolarizability
Γ_q	line width of the q^{th} vibrational mode
h	Planck constant
$\hbar$	reduced Planck constant
h^+	hole
$I(\nu)$	intensity of transmitted light at frequency ν
I_0	intensity of incident light
$I_0(\nu)$	intensity of incident light at frequency ν
I_{IR}	intensity of incident IR beam
I_{SFG}	intensity of emitted SFG beam
I_{Vis}	intensity of incident Vis beam
k	force or spring constant
k_{IR}	momentum of IR beam
k_{SFG}	momentum of SFG beam
k_{Vis}	momentum of Vis beam
λ	wavelength
λ_{max}	wavelength of electronic absorption maximum
λ_{SFG}	wavelength of SFG beam
L	2,2'-bipyridyl-4,4'-dicarboxylate
L	length
μ	dipole moment, reduced mass
$\boldsymbol{\mu}$	induced electric dipole moment
$\boldsymbol{\mu}_0$	static electric dipole moment
m_e	electron mass
ν	frequency, stretching vibration
n	non-bonding, refractive index
n_f	integral quantum number of final state f
n_i	integral quantum number of initial state i
N	number of π-electrons, number density
N_s	number surface density
O_{2c}	twofold coordinated bridging oxygen atoms
O_{3c}	threefold coordinated bridging oxygen atoms
π	multiple bond
π^*	anti-bonding
$\mathbf{P}$	bulk polarization field
$\mathbf{P_0}$	static bulk polarization field
$\mathbf{P}^{(1)}$	first-order polarization field
$\mathbf{P}^{(2)}$	second-order polarization field
$\mathbf{P}^{(3)}$	third-order polarization field
$\mathbf{P}^{(2)}_{\mathrm{NR}}$	non-resonant polarization field
$\mathbf{P}^{(2)}_{\mathrm{R}}$	resonant polarization field
θ	incident angle
θ_{IR}	incident angle of IR beam
θ_{SFG}	emitted angle of SFG beam
θ_{Vis}	incident angle of visible beam
q	vibrational coordinate
q_0	vibrational amplitude around equilibrium position
r	displacement
r_e	equilibrium bond length

σ	single bond
σ^*	anti-bonding
S	ground state
S^*	excited state
S^+	oxidized state
S_0	ground singlet state
S_1	first excited singlet state
t	time
T	transmittance
Ti_{5c}	fivefold coordinated titanium atoms
Ti_{6c}	sixfold coordinated titanium atoms
υ	vibrational quantum number
V	potential energy
V_{acc}	accelerating voltage
ω	frequency
ω_0	incident frequency
ω_{IR}	IR frequency
ω_R	Raman frequency
ω_q	center frequency of the q^{th} vibrational mode
ω_{SFG}	SFG frequency
ω_{Vis}	visible frequency
Z	atomic number

Chapter 1

Introduction

1.1 Motivation

Since the beginning of the industrial era, human activity has had an ever-increasing demand for energy. To date 15 TW are consumed worldwide per year. Due to progressing industrialization and urbanization on all continents the energy consumption will even increase to 27 TW in 2050 and may reach 43 TW by 2100 [1, 2]. Currently, fossil fuels constitute our main energetic source. However, these resources are limited and might be depleted in 40 to 100 years already [3]. Moreover, the combustion of fossil fuels inevitably leads to pollution of the atmosphere with greenhouse gases like carbon dioxide (CO_2, main contributor), nitrous oxide (N_2O) and methane (CH_4) [4, 5]. It is thought that these gases are responsible for the global temperature increase since they reflect infrared (IR) emission back to the Earth's surface. Global warming seems to be intimately linked to the observed climate changes which are responsible, for example, for the increased rates in glacial melting and desertification. In order to tackle both future energy demands and high CO_2 emissions, alternative carbon-free energy resources are needed. Sunlight immediately comes an attractive candidate since it is the most abundant and powerful renewable energy source by providing worldwide ~100 000 TW per year [6]. The greatest challenge with solar energy is its capture, conversion and storage for later use. Natural photosynthesis shows impressively how sunlight can selectively drive the oxidation of water to oxygen (O_2) and reducing equivalents and the reduction of CO_2 to carbohydrates. Taking Nature as an example, it has been in recent years a human endeavor to be able to design artificial photosynthetic devices that allow solar energy conversion into electricity or fuels, often termed solar fuels. Electricity can already be produced by inorganic or organic solar cells as will be explained below. As far as solar fuels are concerned hydrogen can be considered as one when obtained by sunlight-driven water splitting:

$$2\,H_2O \longrightarrow O_2 + 4\,H^+ + 4\,e^- \qquad E^0 = 0.81\,V \tag{1.1}$$

$$2\,H^+ + 2\,e^- \longrightarrow H_2 \qquad E^0 = -0.42\,V \tag{1.2}$$

Potentials E^0 are referenced against normal hydrogen electrode (NHE) at pH 7.

It has the highest energy density of fuels by weight and its only combustion product is water. However, apart from these advantages, hydrogen transport and storage are complicated due to its gaseous state and explosive properties. Liquid fuels are much more desirable in terms of handling issues. An alternative solar fuel in this context is methanol

(CH_3OH), a CO_2 reduction product. Effectively converting CO_2 into fuels would both reduce CO_2 emissions and provide an alterative energy resource. Yet, this is not an easy task because CO_2 is a thermodynamically very stable compound by being fully oxidized. Moreover, the CO_2 reduction is not selective but can yield several products [7]:

$$\mathrm{CO_2 + e^- \longrightarrow CO_2^{\bullet -}} \qquad E^0 = -1.90\,\mathrm{V} \tag{1.3}$$
$$\mathrm{CO_2 + 2\,H^+ + 2\,e^- \longrightarrow HCOOH} \qquad E^0 = -0.61\,\mathrm{V} \tag{1.4}$$
$$\mathrm{CO_2 + 2\,H^+ + 2\,e^- \longrightarrow CO + H_2O} \qquad E^0 = -0.53\,\mathrm{V} \tag{1.5}$$
$$\mathrm{CO_2 + 4\,H^+ + 4\,e^- \longrightarrow HCHO + H_2O} \qquad E^0 = -0.48\,\mathrm{V} \tag{1.6}$$
$$\mathrm{CO_2 + 6\,H^+ + 6\,e^- \longrightarrow CH_3OH + H_2O} \qquad E^0 = -0.38\,\mathrm{V} \tag{1.7}$$
$$\mathrm{CO_2 + 8\,H^+ + 8\,e^- \longrightarrow CH_4 + 2\,H_2O} \qquad E^0 = -0.24\,\mathrm{V} \tag{1.8}$$

Potentials E^0 are referenced against normal hydrogen electrode (NHE) at pH 7.

Thus, the CO_2 reduction reaction requires a highly efficient and selective photocatalyst. In the case of methanol production, the CO_2 reduction reaction is a 6-electrons process (Eq. 1.7). Since in photochemical reactions one photon can only induce the transfer of one electron, the applied photocatalyst has to favor the conversion of a one-electron transfer step to a multi-electron reduction of CO_2 i.e. by the intermediary of electron-sink entities. Furthermore, the photocatalyst should consist of inexpensive and sustainable materials in order to make solar fuels a marketable renewable energy alternative.

1.2 Current photocatalytic CO_2 conversion systems

In the style of natural photosynthesis many reported artificial photocatalysts are composed of a visible (Vis) light harvesting unit mimicking the chlorophyll chromophore in plants and a catalyst center representing the manganese and magnesium ion centers of the photosynthetic water splitting and CO_2 reduction enzymes, respectively. Light absorption can be achieved by metal complexes, organic compounds such as dyes, or by semiconductors. These are coupled to other metal complexes, metal particles or enzymes for CO_2 reduction. Based on their combination, the types of photocatalysts can be classified into homogenous, heterogeneous and mixed hybrid systems. A comprehensive overview and literature compilation of the different types of photocatalysts has been given previously in several reviews [8–10], the main aspects of which are summarized below:

– **Homogenous systems**
  Homogeneous systems are usually based on transition metal complexes. In single-component systems Re(I) bipyridyl (bpy) carbonyl complexes function both as light harvesting unit and as catalytic center. The main reduction product is carbon monoxide (CO) in the presence of a sacrificial electron donor, mostly triethanolamine (TEOA) or triethylamine (TEA). The latter are added to recover the ground state of the photosensitizer. Fe- and Co-porphyrins can also perform both the sensitizing and catalyzing steps. With these as well CO_2 is mainly reduced to CO. In multi-component systems usually one metal complex is chosen as the photosensitizer and another metal complex as the catalyst. Mixed in solution with a sacrificial donor CO, formic acid (HCOOH)

and even methane (CH_4) are possible CO_2 reduction products and are selectively obtained. Tris(2,2'-bipyridyl)Ru(II) complexes mostly form the sensitizer but also Re(I) bipyridyl carbonyl complexes or organic molecules can be applied. As catalyst, Ni, Co and also Re complexes with nitrogen-coordinated ligands are employed. Similar complexes are also combined in supramolecular assemblies where one sophisticated ligand coordinates both metal centers thus bringing them in spatially defined distances to each other. All these systems exhibit long-lived excited states thus allowing the promoted electron to undergo chemical reactions right at the point of formation or after inter- or intramolecular charge transfer at the catalytic site. Drawbacks of using transition metal complexes however, are their high costs, toxicity and their low ability to yield more than two-electron reduction products.

– **Heterogeneous systems**
Heterogeneous systems are commonly based on inorganic semiconductors. In these, light is absorbed by exciting an electron from the valence band (VB) of the semiconductor to the conduction band (CB). Among other processes the excited electron can be transferred to adsorbed acceptor molecules such as CO_2. The positive charge in the conduction band, often called hole (h^+), can be filled by electrons from molecules such as water or sacrificial donors, namely TEOA, TEA, dimethylformamide (DMF) and isopropanol. With water as reductant the product yield is fairly low due to poor CO_2 solubility, competition with H_2 formation and the weak electron donor strength of water. For a successful photocatalysis, the potential of the CB must be more negative than the redox potential of the product (i.e. of CH_3OH/H_2CO_3) when methanol is to be obtained from CO_2 and H_2O, and the potential of the VB must be more positive than the oxidation potential of the donor molecule. Another important issue are organic contaminants on the semiconductor surfaces which can function both as reductant and as carbon source [11]. Hence, all contamination has to be thoroughly removed prior to photocatalysis in order to insure that solely CO_2 reduction is taking place. Various semiconductors have so far been tested, namely TiO_2, ZnO, ZrO_2, CdS, Fe_2O_3, WO_3, GaP and SiC. Among these, TiO_2 is the most intensively used because of its low cost, abundance, non-toxicity, durability under reaction conditions and large bandgap. The latter provides VB and CB potentials which are sufficiently positive and negative for H_2O oxidation and CO_2 reduction, respectively. However, in order to excite the bandgap, Vis light is not sufficient but ultraviolet (UV) light is instead needed. Semiconductors are especially attractive because they can be doped or loaded with metal particles which function as traps for the excited electrons. Thus, these so-called co-catalysts enable multi-electron reduction reactions so that CH_3OH and CH_4 can be obtained. For instance, CH_3OH could be selectively produced applying TiO_2 doped with 3.0 wt% of CuO under UV irradiation [12]. Also, Pd-deposited TiO_2 gave CH_4 in good yields [13]. With bare TiO_2 little to no products were generated. Besides metal doping several other approaches have been undertaken to modify TiO_2. In order to narrow the bandgap so that Vis light can be used to trigger the reduction reaction, several strategies have been carried out including TiO_2 particle size modification, elemental doping, combination with a narrow bandgap semiconductor, and dye-functionalization. As such, modified photocatalysts are called hybrid catalysts.

– **Mixed hybrid systems**
Successful CO_2 reduction to CH_3OH and/or CH_4 using Vis light was reported for Pt-loaded TiO_2 combined with CdSe quantum dots [14] as well as for dye-functionalized

metal-deposited TiO_2 particles. The light harvesting dyes in the latter case were Ru bipyridyl complexes [15, 16]. An interesting three-component photocatalyst producing CO selectively is composed of TiO_2 nanoparticles functionalized with a Ru dye as light collector and a natural enzyme with an active CO_2 reduction site [17, 18]. Dye-functionalization of TiO_2 is a promising way to render TiO_2-based photocatalysts excitable with solar light. This is clearly demonstrated by the already commercialized dye-sensitized organic solar cell (DSSC) [19], the working principle of which will be explained below. Basically, this cell converts solar energy in electricity using dye-functionalized TiO_2 nanoparticles. Despite the success of the DSSC the CO_2 reduction applying dye-functionalized TiO_2 as photocatalyst has so far been studied only by two groups [15, 16]. The efficiency and selectivity achieved are not yet convincing and consequently more research is needed in this field of CO_2 reduction. To this end, further studies with the aim to improve the catalyst's composition have to be performed and the *in situ* analytics of the reaction have to be intensified in order to optimize reaction parameters towards high efficiency and selectivity.

1.3 Solar2Fuel project: Novel method of CO_2 reduction

As stated in the previous paragraph further research on photocatalytic CO_2 conversion is required. Having this in mind, the project called *Solar2Fuel* (S2F) was initiated by BASF SE (Ludwigshafen, Germany) in 2009. This project is one of the various projects forming the Leading-Edge Cluster *Forum Organic Electronics* located in the Rhine-Neckar region and is supported by the German Federal Ministry of Education and Research (BMBF). The aim of the S2F project is to convert CO_2 from industrial flue gas streams into value-added products like fuels, e.g. methanol which could power combustion engines or fuel cells, in aqueous media by the use of sunlight. The photocatalyst chosen for this task is composed of dye-functionalized TiO_2 nanoparticles impregnated with different metal particles (Fig. 1.1). The dyes under investigation are purely organic perylene derivatives. These dyes are advantageous compared to transition metal complexes because of their low costs and low toxicity. They possess either a carboxylic acid group or an anhydride group to anchor to TiO_2. While the carboxylic group is frequently used as anchoring moiety for dye attachment, the anhydride group is not.

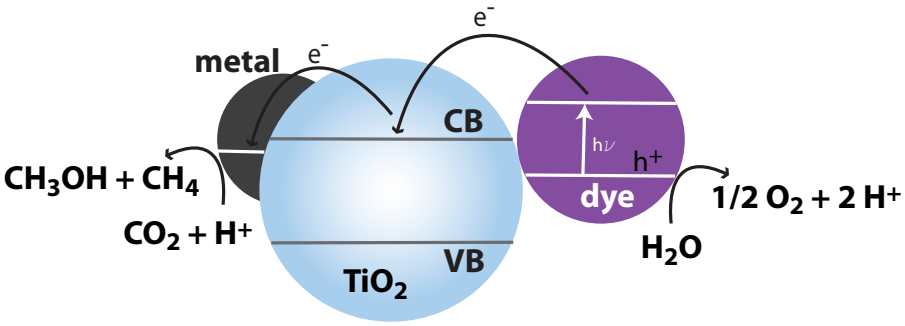

Fig. 1.1: Schematic representation of the CO_2 reduction reaction with water as the reductant and dye-functionalized TiO_2 nanoparticles impregnated with metal particles as photocatalyst.

The S2F project stems from a collaboration between five partners namely, BASF SE – Division of Dyes for Electronics, Energie Baden-Württemberg (EnBW) AG in collaboration

with Forschungszentrum Jülich, and several research groups from the Karlsruhe Institute of Technology (KIT) (Bockhorn group), the University of Heidelberg (Bürgi group and working team Grunze with Koelsch and Zharnikov groups), and the Ludwig Maximilian University of Munich (LMU) (Schmidt-Mende group). The responsibility of BASF within the project is to develop novel photoactive materials with strong absorption in the Vis wavelength region and to analyze them together with the Schmidt-Mende group at LMU in regards to conversion rate and selectivity in a test reactor. EnBW determines the emission and energy balances as well as the economic perspectives of the CO_2 reduction process, thereby considering all necessary steps from the capture of the exhaust gas stream to the separation of methanol from the reaction mixture. The Bockhorn group at KIT focuses on both experimental and theoretical studies of the layout of a potential photoreactor. Finally, completing the analysis of the photocatalytic CO_2 reduction, the Bürgi, Koelsch and Zharnikov groups at the University of Heidelberg concentrate on the mechanistic investigation of the reaction. Both *in situ* and *in vacuo* studies of the photocatalyst are performed. Dye/TiO_2 interactions with and without CO_2/H_2O present and with and without irradiation are studied with linear and nonlinear vibrational spectroscopies as well as with X-ray photoelectron spectroscopy (XPS) and temperature-programmed desorption (TPD). The reduction products are analyzed by gas chromatography (GC). On one hand, these techniques provide information on dye binding properties and stabilities and, on the other hand, on the CO_2 reduction mechanism. Knowing the fate of the materials under reaction conditions is essential in order to optimize the reaction parameters and thus the CO_2 reduction efficiency and selectivity. Especially important is the dye adsorption pattern since it influences the charge transfer from the dye to TiO_2 and therefore also the CO_2 reduction efficiency. For this reason, the focus of this thesis lies on elucidating the dye/TiO_2 interactions. For these investigations, vibrational sum-frequency generation (VSFG) spectroscopy in combination with IR and Raman spectroscopy is employed.

1.4 Objectives and Hypothesis

The main objective of this thesis is the determination of the specific binding modes of the two different dye anchoring moieties, namely the carboxylic acid and the anhydride group, at the TiO_2 surface. Special focus is put on the investigation of the anhydride group since this anchoring unit is not frequently employed and therefore its binding pattern is much less known. Moreover, the present work aims at analyzing the orientational order of the dye molecules on the TiO_2 surface both in air and in water. With the acquired knowledge it is hoped to explain the photocurrent outputs of different dye/TiO_2 systems which only differ in the anchoring moiety so that parameters defining an efficient photocatalyst for CO_2 reduction can be determined. Furthermore, a side objective of this thesis is to study methanol and CO_2 adsorption on TiO_2 in order to elucidate important (intermediary) steps of the CO_2 reduction reaction.

In the case of the carboxylic acid anchoring group it is hypothesized that it transforms upon binding to TiO_2 into a carboxylate group which coordinates in a bidentate fashion (see Section 2.2.1). In contrast, for the anhydride group it is expected that it opens up upon binding and coordinates with both newly formed groups in a bidentate pattern. This will have an influence on the photocurrent which is assumed to depend on the anchor group and the packaging of the dye molecules on the TiO_2 surface. As for methanol molecular and dissociative adsorption is anticipated and for CO_2 carbonate formation seems most likely.

In order to prove these hypotheses, two perylene dyes exhibiting the same structural body but different anchor groups were chosen for direct comparison. While the binding mode was studied with ultraviolet/visible (UV/Vis), IR, and Raman spectroscopy, the orientational order was investigated with VSFG spectroscopy. Moreover, because of its greater surface sensitivity, the latter method was applied to distinguish between bulk and surface related binding modes thus enabling further insights into the dye binding patterns. The findings were verified by studies on structurally similar dyes and also on a simple model dye in the case of the dyes with anhydride group. The methanol and CO_2 adsorption experiments were carried out *in situ* from the liquid phase and analyzed with VSFG spectroscopy. In order to perform the VSFG spectroscopic studies on the rather complex samples it was necessary to develop a sample preparation method (e.g. TiO_2 nanoparticulate films coated on CaF_2 prisms) as well as to implement a special VSFG measuring mode (time-delay technique).

1.5 Outline of the thesis

Chapter 2 reviews the theoretical background and the current state of research essential for the discussion of the experimental results. In the first part, the working principle of dye-functionalization in semiconductor photocatalysis is explained and the photocatalytic properties of TiO_2 are presented. In addition, sensitizing dyes are introduced and the charge transfer dependence on binding properties is shown. In a second part linear spectroscopic studies on carboxylic acid and anhydride groups containing molecules are summarized and lastly, VSFG spectroscopic studies of TiO_2 surfaces are discussed.

Chapter 3 introduces the materials utilized for the experiments and explains shortly the methods employed, both theoretically and in terms of the measurement parameters used.

Chapter 4 discusses the results obtained on the dye-functionalized TiO_2 nanoparticles with UV/Vis, IR, Raman, and VSFG spectroscopy and relates them to photocurrent results. Prior to this, images of the TiO_2 surface obtained by scanning electron microscopy (SEM) and atomic force microscopy (AFM) are shown. The remainder of the chapter is then divided into linear and nonlinear optical spectroscopic results. Each of these sections successively analyzes data on the dyes with carboxylic acid and anhydride anchor groups. Afterwards, the results on the two different anchoring units are compared and related to photocurrent signals observed for the respective dye/TiO_2 systems. Finally, the VSFG spectroscopic studies on methanol and CO_2 adsorption are presented.

Chapter 5 formulates the conclusions that can be drawn from the results obtained in Chapter 4 and gives an outlook of future prospective works.

Chapter 2

Theoretical background and current state of research

In the following chapter the basics of dye-functionalization in semiconductor photocatalysis are presented. Special focus is put on the properties of the materials involved and on the possible binding configurations of the dye molecules on the semiconductor surface depending on their anchor group. It will be shown how the binding influences the charge transfer from the dye to the semiconductor and how optical spectroscopy can assist to deduce the different binding modes.

2.1 Dye-functionalization of semiconductor nanoparticles

2.1.1 Dye-sensitized organic solar cells

Dye-functionalized TiO_2 nanoparticles are already successfully employed in DSSCs. As mentioned above these cells convert solar irradiation into electricity. Since the first functional prototype was developed by Michael Grätzel [19] it is also termed Grätzel cell. The layout of a DSSC consists of two glass electrodes coated with a transparent conducting oxide (TCO) layer. The working electrode is covered with a mesoporous layer of the dye-functionalized TiO_2 nanoparticles and the counter electrode is covered with Pt. Other large bandgap semiconductors than TiO_2 such as SnO_2 and ZnO were tested but found less efficient. The advantage of the mesoporous layer is its high surface area providing sufficient adsorption sites for the dyes. The space between the two electrodes is filled with an electrolyte solvent, often acetonitrile, containing a redox mediator, usually a mixture of iodide/triiodide (I^-/I_3^-). The TCO is generally made of tin-doped indium oxide (In:SnO_2, ITO) or fluorine-doped tin oxide (F:SnO_2, FTO) in order to achieve a low sheet resistance and a high solar light transmittance [20, 21].

When sunlight hits the dye-functionalized TiO_2 nanoparticles it promotes an electron from the ground state (S) of the dye to an excited state (S^*) (Fig. 2.1). This electron can then be injected into the CB of the semiconductor by electronic coupling between TiO_2 and the dye transforming the dye into its oxidized state (S^+). From there it migrates to the TCO layer and continues to travel through an external load to the Pt counter electrode. In order to close the electronic circuit the dye must be regenerated. This is achieved by the redox mediator. It transfers an electron to the ground state of the dye being oxidized during this process. The circuit is fully completed when the Pt-coated electrode donates an electron to reduce the oxidized redox mediator. The redox potentials for the chosen cell components must be adjusted such that this electron flow is enabled [20, 21].

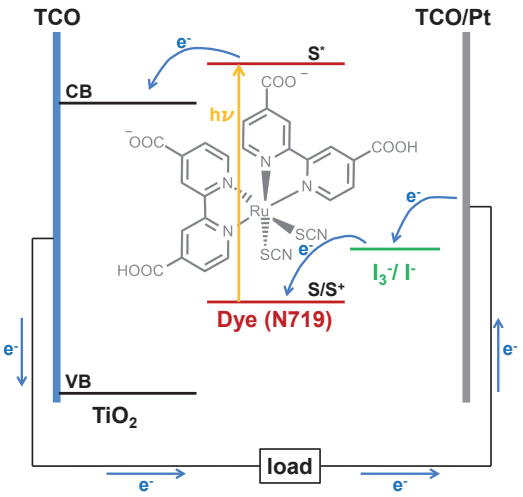

Fig. 2.1: Working principle of a DSSC with energy level scheme of TiO_2, the dye (here N719 which will be introduced later on) and the redox mediator I^-/I_3^-.

A similar working principle is assumed for the CO_2 reduction reaction using dye-functionalized TiO_2 nanoparticles. The major difference however is that the promoted electrons are consumed for chemical bond formation (see Fig. 1.1). Here, upon irradiation with solar light the dye is excited and an electron is transferred to the CB of TiO_2. Deposited metal particles can function as electron trap thus collecting the electrons from the CB of the semiconductor. As such they adopt the role of a co-catalyst and act as the CO_2 reduction site [22]. In the ideal case the dye is recovered by electrons generated by water oxidation. Both water and CO_2 are consumed and have to be refilled in order to allow continuous reactions.

The best solar-to-electrical energy conversion efficiencies are obtained for cells using Ru(II) polypyridyl complexes. The highest conversion efficiency achieved so far amounts to ∼11 % employing the diprotonated cis-di(thiocyanato)-bis(2,2′-bipyridyl-4,4′-dicarboxylate)-Ru(II) complex $(Ru(II)(LH)_2(NCS)_2^{2-}$, where L = 2,2′-bipyridyl-4,4′-dicarboxylate; N719) as the sensitizing dye (see Fig. 2.1) [23, 24]. This value is promising but still lower than for conventional Si-based inorganic solar cells which reach up to 25 % efficiency [24]. Thus, it is important to further improve the key components of the DSSC individually and collectively. For the optimization process, a detailed understanding of the elementary steps including electron excitation, charge injection, dye recovery, etc., and in addition how these are influenced by the cell design is essential. This is where optical spectroscopic techniques come into play. Time-resolved femtosecond spectroscopy can follow the charge transfer processes [25–27] and vibrational spectroscopy can study the dye stability, configuration, and binding *in situ* and non-destructively [28–31]. The analysis of the properties of the dye-functionalized TiO_2 nanoparticles employed in DSSCs is much further advanced than when used in the CO_2 reduction reaction. Therefore, in the present study of the dye binding properties, the former analysis is taken as a starting point as well as for comparison.

2.1.2 Properties of TiO_2

As mentioned above TiO_2 is the most commonly used semiconductor in DSSCs as well as in heterogeneous CO_2 reduction because of its many advantages. Besides exhibiting suitable VB and CB potentials for water oxidation and CO_2 reduction, it is photocatalytically stable under reaction conditions, non-toxic, and inexpensive [32–34]. Its photocatalytic properties are not only exploited in solar cells and CO_2 reduction but also in self-cleaning coatings and in air and waste water treatments [35]. Moreover, due to its non-toxicity and high reflective index it is applied as white pigment in ceramics, paints and cosmetic products. As surface layer on Ti bone implants it has also been found to increase the biocompatibility of the latter. Finally, it also finds applications as gas sensor since its conductivity changes upon molecular adsorption [35].

Unmodified or undoped TiO_2 itself is photocatalytically active because the electron promotion from the VB to the CB due to light irradiation generates electron-hole pairs in the bulk structure i.e. excess negative and positive charges come to reside in the CB and VB, respectively. There exist several pathways for the deactivation of the electron-hole pairs. The unwanted one is charge recombination without catalytic activity. The desired one is charge separation and its migration to the semiconductor surface where oxidation or reduction of adsorbed species can occur. Usually the surface is covered with adsorbed oxygen and water molecules. Their reduction creates oxygen and hydroxyl radicals which attack adsorbed organic molecules and decompose them. This mechanism explains the self-cleaning properties of TiO_2 [22, 36].

The photocatalytically important crystal phases of TiO_2 are rutile and anatase. In each crystalline structure the Ti^{4+} atoms are encased by six O^{2-} atoms forming an octahedron. The structures differ by the distortion and assembly of the single octahedra. In rutile these octahedra are connected via their corners and edges and the unit cell dimensions are $a = b = 4.584\,\text{Å}$ and $c = 2.953\,\text{Å}$ (Fig. 2.2 A). The crystal structure belongs to the point group D_{4h}^{14} and the space group $P4_2/mnm$. As for anatase the octahedra are linked via edges and planes forming a unit cell with $a = b = 3.782\,\text{Å}$ and $c = 10.24\,\text{Å}$ (Fig. 2.2 B). The point group is D_{4h}^{19} and the space group is $I4_1/amd$. Both the space groups of rutile and anatase exhibit centrosymmetry [35]. The dissimilar lattice structures of rutile and anatase lead to slightly different bandgap energies (3.0 eV and 3.2 eV for rutile and anatase, respectively [37]). Hence, an electron can only be excited from the VB to the CB applying UV light ($\lambda \gtrsim 3\,\text{eV}$). Rutile is the thermodynamically more stable polymorph which is why the pure bulk phase of anatase transforms into rutile at temperatures above 600 °C. However, small TiO_2 particles, i.e. nanoparticles, mainly exist in the anatase phase. This is due to the fact that the latter exhibits a lower surface energy compared to the rutile phase [38]. Furthermore, anatase shows better photocatalytic performance as a result of a higher surface-adsorbed hydroxyl radical concentration and a slower charge recombination after excitation [37].

In addition, each of the TiO_2 crystal phases has a face which is most thermodynamically stable. In rutile crystals and in anatase nanoparticles, the (110) and (101) faces, respectively, exhibit highest stability and, consequently, are predominantly exposed. These surfaces expose twofold coordinated bridging oxygen atoms (O_{2c}) and fivefold coordinated Ti atoms (Ti_{5c}), in addition to three-bonded oxygen atoms (O_{3c}) and sixfold coordinated Ti atoms (Ti_{6c}). The latter two are the typical bulk species. Therefore, the undercoordinated Ti_{5c} atoms form reactive chemisorption sites, e.g. for anchor groups of dye

molecules. Moreover, surface defect sites, i.e. oxygen vacancies, release underlying Ti_{5c} atoms which form reactive sites as well [35, 39]. Side views of both planes are displayed in Fig. 2.2 A and B.

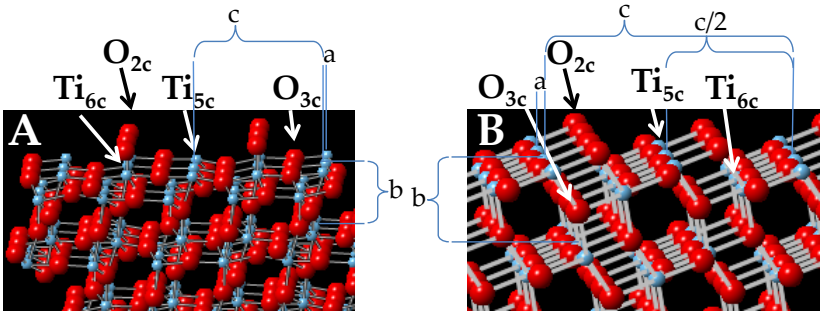

Fig. 2.2: Ball-and-stick models of the (A) rutile(110) and (B) anatase(101) crystal faces (side view). The red and blue balls represent oxygen and Ti atoms, respectively.

For the study of the dye adsorption, it is important to know that under ambient conditions the TiO_2 surface is hydroxylated. Molecularly adsorbed water partly dissociates to form two types of hydroxyls: 1) terminal hydroxyls which are adsorbed to Ti_{5c} sites and 2) bridging hydroxyls which result from protonation of O_{2c} atoms [40, 41]. It is known that the terminal hydroxyls are preferred adsorption sites for carboxylic acid anchor groups [42].

2.1.3 Sensitizing dyes

The performance of a DSSC depends strongly on the properties of the sensitizing dye and consequently the CO_2 reduction efficiency will depend on it as well. In order to be efficient, a photosensitizer must satisfy several criteria: 1) it must possess an anchor group (e.g. carboxylic acid, phosphonic acid or anhydride group) which binds it covalently via the hydroxyl groups on the semiconductor surface, 2) it must exhibit broad absorption overlap with the solar spectrum including the near-IR region with high molar extinction coefficient ($\varepsilon > 10\,000\,\mathrm{L\,mol^{-1}\,cm^{-1}}$) for strong solar light harvesting, 3) it must have a long-lived excited state which is localized near the anchor group and which lies energetically above the CB of TiO_2, 4) it must have a ground state which is localized on the periphery of the dye in order to prevent charge recombination between TiO_2 and the excited dye and which lies below the energy level of the redox mediator or water, 5) it must be stable under working conditions and, finally, 6) it must not aggregate on the semiconductor surface so that radiationless decay of the excited state is avoided [42–45].

The aforementioned Ru bipyridyl transition metal complexes fulfill most of these requirements. However, they exhibit relatively low molar extinction coefficients ($\varepsilon \leq 20\,000\,\mathrm{L\,mol^{-1}\,cm^{-1}}$) so that $\sim$10 μm-thick TiO_2 films in DSSCs and high TiO_2 particles suspension concentrations in CO_2 reduction are needed in order to achieve efficient light harvesting, thereby increasing the material consumption. Furthermore, Ru complexes are expensive due to the costs of raw Ru material and labor-intensive because of the numerous sophisticated purifications steps required [45].

For these reasons, several organic dyes such as merocyanine, coumarin, indoline, tetrahydroquinoline, cyanine, carbazole, porphyrins and rylene dyes, have been tested in solar

cell applications [46]. Advantageously, organic dyes are rather inexpensive, less toxic, possess high molar extinction coefficients and their light absorption and energy level properties can be tuned via molecular design. However, efficiencies and stabilities of organic dye-based DSSCs still need to be improved [44, 47].

Perylene dyes are particularly interesting as sensitizers in DSSCs because of their strong absorption in the Vis regime with a high molar extinction coefficient (in some cases $\varepsilon \leq 100\,000\,\mathrm{L\,mol^{-1}\,cm^{-1}}$), chemical and photochemical stability, and highly emissive excited state which allows ultrafast (fs timescale) electron injection from the dye into TiO_2 [48, 49]. The stability and chromaticity of the perylene dyes is clearly demonstrated by their commercial use as pigments in automotive paints, as colorants of synthetic fibers and engineering resins [50]. The structures of the two most important and well-characterized pigments whose derivatives form the class of perylene dyes used in solar cells are shown in Fig. 2.3, namely 3,4,9,10-perylene-tetracarboxylic dianhydride (PTCDA) and 3,4,9,10-perylene-tetracarboxylic diimide (PTCDI). Furthermore, these dyes display organic semiconductor characteristics which make them suitable for application in optoelectronic devices [51].

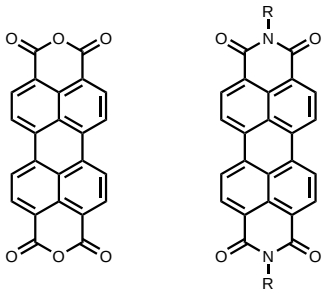

Fig. 2.3: Molecular structure of PTCDA and a PTCDI derivative. R designates a side-chain group, often an H atom or an alkyl chain.

The first successful DSSC employing perylene-based dyes was presented in 1997 by Ferrere *et al.* [52, 53]. They sensitized a colloidal SnO_2 film with perylene derivatives anchoring via two carboxylic acid groups and reached efficiencies of 0.89 %. One year before, Burfeindt *et al.* investigated the interfacial charge injection dynamics at a perylene-modified TiO_2 electrode via femtosecond pump-probe spectroscopy [54]. Perylene derivatives are suitable candidates for such fundamental experiments because of their highly emissive excited states allowing the detection of spectra with good signal-to-noise (S/N) ratios. After these proof-of-principle experiments, many other perylene derivatives with both carboxylic acid and anhydride groups as anchoring units were synthesized by modifying the PTCDA and PTCDI pigments and tested in solar cells but efficiencies remained low (for a recent review, see [50]). A reason for the latter were the poor electron-donating abilities of the used perylene dyes thus achieving only low electron transfer from the excited state of the dye to the CB of the semiconductor. Solar cell efficiencies however could be greatly improved by adding electron donor groups to the dye structures thus creating dyes with intramolecular push-pull properties. As donor groups, alkyl or aryl amine substituents proved effective [55–60]. Adopting this strategy, the most promising perylene sensitizer obtained to date yields 6.8 % efficiency [57]. It is a direct derivative of PTCDA: one anhydride group is kept as the binding moiety, whereas the other one is replaced by a bulky diphenylamine donor group at the 9-position, thus preventing dye

aggregation on the TiO_2 surface. Furthermore, it bears two thiophenol groups at the 1- and 6-positions.

The perylene dyes investigated in this thesis show very similar molecular designs (Fig. 3.1). The latter as well as the other donor-acceptor perylene dyes exhibit ground states localized on the donor moiety with energies below the ones of the typical redox mediator I^-/I_3^- and excited states localized on the anchoring moiety with energies higher than the CB of TiO_2. Thus, efficient dye regeneration and charge injection, respectively, is possible. In general, a strong donor group directly connected to the acceptor part shifts both ground state and excited state energy levels showing the potential of molecular design in tuning the photochemical dye properties [50].

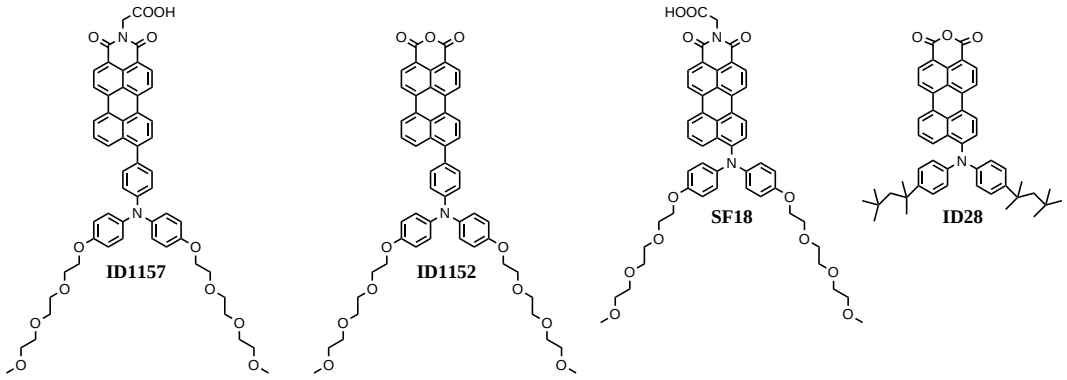

Fig. 2.4: Chemical structures of perylene dyes investigated in this work.

2.1.4 Link between dye binding and charge injection

As stated above high charge injection efficiencies improve the overall performance of a DSSC and presumably the CO_2 reduction efficiencies as well. Charge injection depends on the energy level matching of the CB of TiO_2 and the excited state of the adsorbed dye molecule as well as on the electronic coupling strength between semiconductor and dye. Both processes are determined by the anchor group which connects the dye to the TiO_2 surface. This is due to the fact that the anchor group in most cases influences the dye's excited state energy and that it mediates the electron transfer from the dye to the semiconductor. Moreover, the anchoring strength plays a role in the stability of the device [27, 43, 61–63]. Most frequently dyes are attached to metal oxide surfaces by phosphonic acids, carboxylic acids and derivatives of the latter, e.g. esters, acid chlorides, acetic anhydrides, carboxylate salts or amides. They all form bonds by reacting with surface hydroxyl groups [20, 61]. The most frequently applied and successful functional groups are based on carboxylic acids because these have proven to achieve strong electronic coupling by tight binding which in turn leads to fast electron injection rates [42, 64, 65].

In search of alternative anchor groups which might even perform better than the carboxylic acid group, Ambrosio *et al.* calculated electron injection times from perylene bound to rutile(110) and anatase(101) surfaces by various possible anchor groups. The excited state energy level was kept at a constant value above the CB energy of TiO_2. They found that phosphonic acid, dihydroxyl (like in catechol), hydroxamic acid and imide groups exhibited faster electron injection times than the carboxylic acid group [63]. This indicates that dyes with different anchor groups should be more explored as photosensitizers in order to improve electron injection efficiencies and overall device performance.

However, electron injection is not only influenced by the nature of the anchor group but also by the orientation and molecular packing of the dye on the surface induced by the anchor group. Despite the relevance of the dye configuration for interfacial processes like through-space charge tunneling, dipole moment alignment of the dye, interfacial local electric field, and undesired recombination reactions, experimental studies remain scarce [66]. However, it is known that dye multilayer formation and dye aggregation influence the charge injection efficiencies negatively. In the case of multilayers the outer dye layers just absorb light without contributing to photosensitization and attenuate the light needlessly which should excite the anchored dye molecules [67]. As for dye aggregation such as dimer formation, radiationless deactivation pathways of the dye's excited state are enhanced and charge injection is reduced [45].

Only few examples exist where dye orientation on the semiconductor surface was studied in the context of charge transfer dynamics. For instance, Imahori *et al.* could show that Zn-porphyrin sensitizer molecules coupled via a spacer and a carboxylic acid anchor to a TiO_2 electrode adopted a tilted geometry on the surface which greatly influenced charge injection. In comparison to more upright bound Zn-porphyrins the charge injection time of the tilted ones was much faster. As a consequence, they concluded that through-space charge tunneling from the core of the chromophore to the semiconductor surface occurred rather than charge transfer through the anchor group. Furthermore, they argued that gaining knowledge about the binding geometry of the dye on the surface should allow to correlate it to electron injection rates thus providing a ground for the design of photosensitizers with predictable characteristics [68, 69]. Similarly, Gundlach *et al.* investigated the electronic coupling strength, tilt angle and electron injection dynamics of perylene dyes attached through different rigid spacers and anchor groups (carboxylic and phosphonic acid) to both single crystal rutile(110) and colloidal anatase surfaces. They found faster electron injection through the carboxylic acid group because of stronger electronic coupling and fast through-space electron transfer components at the anatase particle surface in the case of a tilted dye geometry induced by a long rigid spacer. They explained these fast injection rates by the rough particulate surface incorporating many cavities which brought the dye in closer proximity to other TiO_2 particles than the one onto which it was bound, thus creating shorter routes for through-space charge tunneling [70–72]. Another interesting experiment by Griffith *et al.* determined the orientation of several porphyrin dyes on a planar amorphous TiO_2 surface with high accuracy by X-ray reflectometry. They showed that dye structure and dye surface layer depended on each other. However, they did not measure electron injection rates [66]. Furthermore, Lim *et al.* could show that strongly adsorbed and non-aggregated N719 dye molecules improved photoinduced electron generation [73]. In their work, they developed a low-temperature stearic acid-assisted anchoring method which enabled the dye molecules to bind with two carboxylic acid groups. In order to improve solar cell and CO_2 reduction efficiencies a better understanding of dye binding geometry and packaging on the semiconductor surface is needed. To this end, the work of this thesis was carried out.

2.2 Linear vibrational spectroscopic studies of dye attachment

2.2.1 Carboxylic acid group binding to TiO_2

Generally, the anchor groups can adopt different binding modes on the TiO_2 surface. Thus, not only the nature of the anchor group but also its coordination influences the electron injection efficiency from the dye to the semiconductor. Consequently, in a first step, the determination of the binding mode is essential for the understanding of the dye sensitization phenomenon and, in a second step, for the optimization of the overall device efficiency and the design of new photosensitizers [61]. Both IR and Raman spectroscopy are specially suited techniques in order to study the dye/TiO_2 interaction since they simultaneously provide structural information on the dye, the anchor group and the TiO_2 surface. Experiments can be performed *in situ* to follow the dynamics of the binding process [31, 74] and *ex situ* to study the adsorbed state/configuration of the dye after sensitization [28–30]. However, other methods such as photoelectron spectroscopy (PES) [75–77] and near edge X-ray absorption fine structure (NEXAFS) spectroscopy [78] provide information on the dye/TiO_2 interface as well. Most IR and Raman studies found in the literature investigate the binding of the Ru complex N719 and its variants, e.g. the fully protonated species (Ru(II)$(LH_2)_2(NCS)_2$, N3) or complexes where the thiocyanato groups are replaced by another bpy ligand. The bpy ligands may be dicarboxylated or not giving Ru(II)$(LH_2)(bpy)_2^{2+}$ (Fig. 2.5). Only very few studies can be found on purely organic dyes [79–81]. All these dyes possess a carboxylic acid or carboxylate group as anchoring moiety.

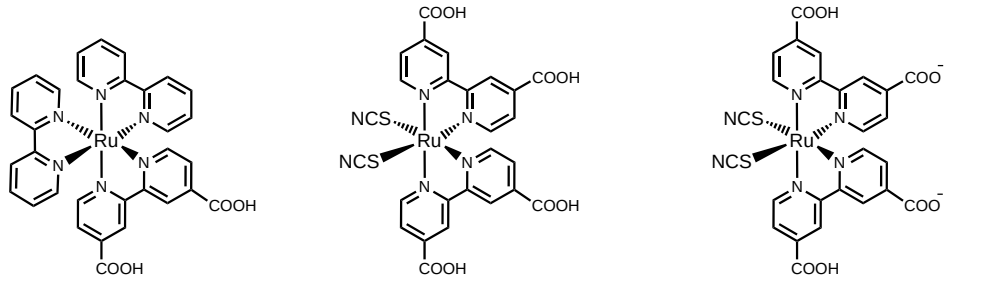

$Ru(II)(LH_2)(byp)_2^{2+}$ **$Ru(II)(LH_2)_2(NCS)_2$ (N3)** **$Ru(II)(LH)_2(NCS)_2^{2-}$ (N719)**

Fig. 2.5: Structures of Ru complexes. Ru(II)$(LH_2)(bpy)_2^{2+}$, N3 and N719.

Upon interaction with the TiO_2 surface the carboxylic acid group either stays protonated or reacts in a dissociative way with the surface hydroxyl groups to form a surface-bound carboxylate group. The possible binding modes of a carboxylic acid or carboxylate group with Ti atoms are depicted in Fig. 2.6. They can bind via chemisorption in a monodentate fashion to form an ester-like linkage or they can bind with each of their two oxygen atoms either to one Ti atom (bidentate chelating) or to two of them (bidentate bridging). Moreover, they can interact with the TiO_2 surface via physisorption through hydrogen bonding either with a surface-bound hydroxyl group and/or a lattice oxygen atom [30].

The chemisorptive binding modes can be distinguished by vibrational frequency analysis of the C−O stretching frequencies according to an empirical rule established by Deacon and Phillips [82]. They evaluated the vibrational spectra of a series of acetate salts with known crystallographic structure and found a correlation between the frequency difference of the asymmetric (as) and symmetric (s) CO_2^- stretching modes ($\Delta\nu = \nu_{as}(CO_2^-)$ -

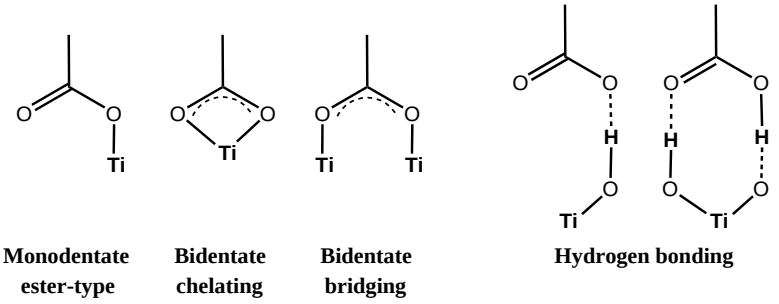

Fig. 2.6: Possible binding modes of carboxylic acid and carboxylate groups.

$\nu_s(CO_2^-)$) of the free carboxylate group (e.g. the sodium salt of the compound, $\Delta\nu_{salt}$) and the one of the adsorbed species ($\Delta\nu_{ads}$) [82]. If $\Delta\nu_{ads} > \Delta\nu_{salt}$, then monodentate binding is most likely. On the contrary, if $\Delta\nu_{ads} < \Delta\nu_{salt}$, then one has chelating or bridging coordination. In most cases chelating coordination is observed for $\Delta\nu_{ads} \ll \Delta\nu_{salt}$ and bridging coordination for $\Delta\nu_{ads} \leq \Delta\nu_{salt}$ [28]. This classification is based on the fact that with different binding modes the bond order of the C−O bond changes [82]. Monodentate coordination of the two oxygen atoms in a carboxylate group removes their equivalence and the C−O bond order is strongly affected, which increases $\nu_{as}(CO_2^-)$, decreases $\nu_s(CO_2^-)$ and, in turn, increases $\Delta\nu_{ads}$ compared to the $\Delta\nu_{salt}$ value of the free carboxylate groups. Chelating or bridging coordination should not alter the bond order too much and hence, $\Delta\nu_{ads}$ is found to be similar to $\Delta\nu_{salt}$ values. Typical wavenumber values for the $\nu_{as}(CO_2^-)$ and $\nu_s(CO_2^-)$ stretching vibrations, respectively, lie between 1750–1550 cm^{-1} and 1450–1350 cm^{-1} [82].

In the present thesis the binding mode of the perylene dyes with carboxylic acid as well as anhydride group anchors will be investigated by applying the above-mentioned rule and by comparing the obtained data to the studies available in the literature on the carboxylic acid anchors of the Ru metal complexes and organic dyes. In the early studies of the Ru metal complexes the determination of the binding mode is at variance showing the difficulty to identify the actual binding mode. Different modes of coordination were concluded because the quality of the spectra was not high enough [83], band assignments were partly wrong [64] and reference spectra of e.g. the salt of the compound or simpler model substances were not taken. This only changed in 1998 with the study by Finnie *et al.* who systematically investigated the salt compounds of the N3 dye and compared the resulting spectra with the ones of benzoic acid and benzoate salt [28].

Umapathy *et al.* were the first in 1990 to perform *in situ* Raman studies on the interaction of $Ru(II)(L)_3^{4-}$ and $Ru(II)(L)_2(H_2O)_2^{2-}$ complexes with colloidal TiO_2. They found that the first complex adsorbed through a solvation layer to the semiconductor and that the second complex coordinated directly via the water ligands and not via the carboxylate groups of the bipyridyl ligand. The coordination mode was not determined [84]. Further Raman experiments were carried out by Meyer *et al.* on TiO_2 powder samples functionalized with $Ru(II)(LH_2)(bpy)_2^{2+}$. They suggested ester-type binding based on the lack of a $\nu_s(CO_2^-)$ stretching band in their Raman spectrum [85]. In contrast to that, Vinodgopal *et al.* who investigated the same complex bound also to TiO_2 powder using diffuse reflectance infrared fourier transform (DRIFT) spectroscopy, assumed a carboxylate link but could not distinguish between chelating or bridging coordination due to a band of bound water overlapping the $\nu_{as}(CO_2^-)$ stretching band [83]. Later on, Duffy *et al.* con-

cluded from their *in situ* attenuated total internal reflection (ATR)-FTIR spectra of the very same dye bound to a TiO_2 nanoparticulate film a bidentate bridging coordination [86].

Several groups afterwards focused on the elucidation of the binding mode of the N3 dye. One of them were Murakoshi and coworkers who applied FTIR spectroscopy in reflectance geometry to dye-coated nanoparticulate TiO_2 films. After spectral band assignment they identified both ester-like linkage and bidentate chelating coordination of the carboxylic acid groups [64]. Going along with that, Falaras *et al.* found ester-type binding when they investigated TiO_2 nanoparticle powder samples using FTIR spectroscopy in transmission geometry [87]. By contrast, Finnie *et al.* who performed a detailed spectral comparison between the dye powder samples, their salt counterparts and the species adsorbed to TiO_2 nanocrystalline films with FTIR spectroscopy in reflection geometry, proposed instead bidentate chelating or bridging coordination of two out of the four carboxylic acid anchor groups and hydrogen bonding as well as non-bonding of the remaining acid groups [28]. The same binding mode was found by Nazeeruddin *et al.* who characterized it even further. They employed ATR-FTIR spectroscopy to similar samples and determined the coordination type as bidentate bridging. According to their data, they concluded that two out of the four carboxylic acid anchor groups were involved in the link to the TiO_2 surface and went even further by saying that these two groups belonged to two different bipyridyl ligands [88]. Their findings were also supported by simulations [39].

The most recent studies are concerned with the investigation of the N719 dye, it being the most efficient sensitizer to date. Leon *et al.* investigated dye-coated nanocrystalline TiO_2 films with Raman and ATR-FTIR spectroscopy. They concluded from their spectral analysis that the carboxylic acid and carboxylate groups, respectively, bound in a bidentate chelating or bridging coordination. They also found spectral contributions from free acid groups which they partly assigned to non-adsorbed dyes or unbound acid groups [29]. Hirose and coworkers studied the dye binding process under varying experimental conditions with multiple-internal-reflection geometry-infrared absorption spectroscopy (MIR-IRAS) but did not comment on the binding mode. They showed that the dye binding process occurred via surface hydroxyl group consumption [89]. Furthermore, they observed that heating the dye solution during the adsorption process increased the amount of chemisorbed dyes [90]. Lee *et al.* were also interested in the role of surface bound water molecules and hydroxyl groups. They applied ATR-FTIR and Raman spectroscopy to different dye-sensitized nanostructured TiO_2 films. Their analysis of the binding mode led them to the conclusion that the dye N719 bound via two neighboring carboxylic acid/carboxylate groups to the TiO_2 surface. One group coordinated in a bidentate bridging fashion and the other one via hydrogen bonding either with surface hydroxyl groups in the case of a carboxylate group or with bridging oxygen atoms in the case of a carboxylic acid group [30]. The latest binding mode study was carried out by Suto *et al.* who investigated the binding dynamics on nanoporous TiO_2 films using Raman and FTIR spectroscopy in transmission geometry. They observed bidentate chelating or bridging coordination [31].

As mentioned before only very little organic sensitizers were analyzed with respect to their binding mode on TiO_2. Hara *et al.* investigated coumarin and dimethylaniline dyes with cyanocarboxylic acid anchor adsorbed to TiO_2 nanoparticulate films employ-

ing both ATR-FTIR spectroscopy and simulations of the IR spectrum of the dye salt. By comparing the experimental and theoretical spectra they suggested bidentate carboxylate formation [79, 80]. Srinivas *et al.* studied anthracene-based dyes with cyanoacrylic or malonic acid anchor. The dyes were bound to TiO_2 nanoparticulate films and analyzed with ATR-FTIR spectroscopy in combination with density functional theory (DFT) calculations. The binding mode of the formed carboxylate groups was determined as bidentate bridging. In the case of the malonic acid anchor only one out of the two carboxylic acid groups was observed to bind [81]. A summary of the literature reviewed can be found in Tab. 2.1 including the characteristic bands the binding mode assignment was based on.

2.2.2 Anhydride group binding to TiO_2

The binding process of the anhydride group is assumed to involve the attack of a carbonyl carbon by a surface-bound hydroxyl group, thereby opening the anhydride group (Fig. 2.7). Thus, a carboxylate group is formed that is directly bound to the TiO_2 surface, e.g. in a bidentate bridging fashion, and a carboxylic acid group [91, 92]. The latter one can stay isolated, interact via hydrogen bonding or bind in one of the chemisorptive modes illustrated in Fig. 2.6.

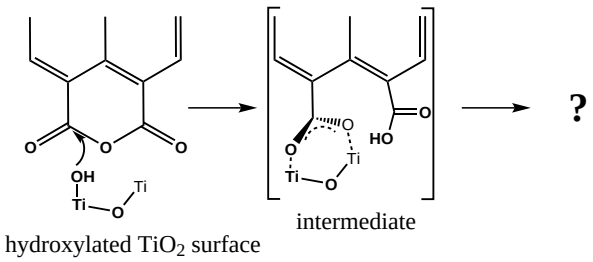

Fig. 2.7: First step of the anhydride opening mechanism.

Since the anhydride group is not as often incorporated in sensitizer molecules as the carboxylic acid group its anchoring mechanism is not as frequently studied. Hence, investigations on complex molecules do not exist, however small model molecules like acetic anhydride and maleic anhydride have been studied with various techniques. For instance, Do *et al.* applied FTIR spectroscopy to analyze the binding mode of maleic anhydride from the gas phase onto TiO_2 powder used as catalyst support. They concluded from their spectra that the anhydride opened up upon interaction with surface hydroxyls and bound with two carboxylate groups in a monodentate coordination [93]. Wilson *et al.* studied the adsorption of maleic anhydride on the rutile(001) single crystal surface by TPD and computational calculations. They suggested that the anhydride groups bound dissociatively by involving one surface oxygen and one Ti atom, thus forming a monodentate coordination for both carboxylates, bound to the same Ti atom though [94]. Johansson *et al.* looked at the binding mechanism of maleic anhydride from the gas phase onto the anatase(101), (100) and (001) surfaces using XPS. After spectral analysis, they proposed that maleic anhydride bound dissociatively in a bidentate fashion on the (101) and (100) surfaces. Their binding model for the predominantly exposed (101) surface predicts bidentate bridging coordination for both carboxylates involving one surface oxygen atom [95]. Furthermore, Ashima *et al.* studied the adsorption of acetic anhydride on the rutile(110) surface with XPS, low-energy electron diffraction (LEED) and high resolution electron energy loss spectroscopy (HREELS). They observed dissociative adsorp-

Tab. 2.1: List of literature studies of Ru complexes' and organic dyes' binding modes by linear vibrational spectroscopy.

Dye	Anchor groups	Surface	Method	Characteristic bands [cm^{-1}]			Binding mode	Reference
				ν(C=O)	$\nu_{as}(CO_2^-)$	$\nu_s(CO_2^-)$		
(1) $Ru(II)(L)_3^{4-}$ (2) $Ru(II)(L)_2(H_2O)_2^{2-}$	-COO^-	TiO_2 colloids	Raman	—	—	—	(1) adsorption through solvation layer (2) direct physisorption via H_2O ligands	[84]
$Ru(II)(LH_2)(bpy)_2^{2+}$	-COOH	TiO_2 powder	Raman	1690	1544	—	monodentate	[85]
$Ru(II)(LH_2)(bpy)_2^{2+}$	-COOH	TiO_2 powder	DRIFT	—	1650 (broad)	1380	carboxylate link, either chelating or bridging	[83]
$Ru(II)(LH_2)(bpy)_2^{2+}$	-COOH	TiO_2 film	ATR-FTIR	—	1599	1379	bidentate bridging	[86]
N3	-COOH	TiO_2 nanoparticulate film	FTIR	1728	1610	—	both monodentate and bidentate chelating	[64]
N3	-COOH	TiO_2 nanoparticulate powder	FTIR	1738	—	—	monodentate	[87]
N3	-COOH	TiO_2 nanocrystalline film	FTIR	1770, 1740	1610	1380	bidentate chelating or bridging of two carboxylates and free acid	[28]
N3	-COOH	TiO_2 nanocrystalline film	ATR-FTIR	1722	1593	1383	bidentate bridging of two carboxylates and free acid	[88]
N719	-COOH/-COO^-	TiO_2 nanocrystalline film	ATR-FTIR, Raman	1715	1602	1375	bidentate chelating or bridging and free acid	[29]
N719	-COOH/-COO^-	anatase surfaces	MIR-IRAS	1713	1607	1375	—	[89, 90]
N719	-COOH/-COO^-	TiO_2 nanostructured film	ATR-FTIR, Raman	1713	1607	1377	bidentate bridging of one carboxylate and hydrogen bonding	[30]
N719	-COOH/-COO^-	TiO_2 nanoporous film	FTIR	—	1605	1381	bidentate chelating or bridging	[31]
coumarin, dimethylaniline dyes	-COOH	TiO_2 nanoparticulate film	ATR-FTIR	—	~1580	—	bidentate carboxylate	[79, 80]
anthracene based dyes	-COOH	TiO_2 nanoparticulate film	ATR-FTIR	1730	1586, 1587	1382, 1395	bidentate bridging	[81]

Legend: L = 2,2′-bipyridyl-4,4′-dicarboxylate and bpy = bipyridyl.

tion of the anhydride group and binding of two carboxylates in a bidentate coordination by involving one surface oxygen atom [96].

2.3 Nonlinear spectroscopic studies of TiO_2 surfaces

VSFG spectroscopy is a surface/interface-specific method and as such particularly suited to examine the interfacial dye/TiO_2 binding. As a vibrational method it has the same advantages as IR and Raman spectroscopy, meaning it provides structural information both on the surface-adsorbed species and the substrate while at the same time being non-destructive and functionable under ambient conditions. Moreover, polarization-dependent measurements allow the determination of the molecular orientation of the adsorbate on the surface.

VSFG spectroscopic studies of TiO_2 surfaces are not very numerous despite the frequent use of these surfaces in photocatalytic applications. This is especially true for nanoparticulate films were studies are scarce. Important results on nanoparticulate films were mainly obtained by Wang and coworkers. They studied the species adsorbed to an anatase film and detected a contaminating hydrocarbon layer that could be removed under UV irradiation. Furthermore, they could show that the UV irradiation increased the amount of surface-adsorbed hydroxyl groups [97]. In addition, they examined the adsorption of methanol and found both molecularly and dissociatively adsorbed molecules [98]. Performing a competitive adsorption study of acetic acid, methanol and water they detected preferential adsorption of acetic acid [99, 100]. Asong *et al.* investigated the influence of Fe-doping of the TiO_2 film on the methanol adsorption. They could show that Fe-doping quenched dissociative adsorption [101]. The Fe-free nanoparticulate anatase films were also investigated with respect to their interaction with ionic liquids (including binding geometry) by Aliaga *et al.*. [102].

Furthermore, thin TiO_x films vapor-deposited on Pt(111) surfaces were studied by Chen *et al.* with formate as probe molecule. They concluded from their spectra that the majority of formate molecules adsorbed in a bidentate fashion and the reminder in a monodentate coordination. Their studies also allowed them to distinguish between three different kinds of surface active sites in the TiO_2 film [103]. Paszti *et al.* examined the adsorption of different amino acids on amorphous TiO_2 films. They observed that aspartic acid and glutamic acid both possessing a side chain with carboxylic acid group formed ordered layers on TiO_2, whereas amino acids without an extra carboxylic acid did not interact strongly with TiO_2. Moreover, a detailed investigation of aspartic acid showed that one of its two carboxylic acid groups adsorbed in a monodentate fashion and the other one via hydrogen coordination [104].

Rutile(110) and (001) single crystal surfaces were investigated by Ishibashi *et al.* and Anfuso *et al.*, respectively. The first group studied retinoic acid adsorption and could prepare ordered layers bound through a carboxylate group in a bidentate bridging coordination [105]. The second group examined the adsorption geometry of the $Re(CO)_3Cl(LH_2)$ complex. In combination with DFT calculations they could show that the complex bound in an upright orientation with either both carboxylic acid groups coordinated in a monodentate fashion or only one adsorbed with a monodentate binding pattern and the other one with a bidentate bridge [106]. Finally, thin TiO_2 films on SiO_2 substrates were studied in contact with water. Uosaki *et al.* investigated the interfacial water structure under the

influence of UV light illumination and found an increased ordering of the water layer which they ascribed to an increase in hydroxyl groups on the TiO_2 surface [107].

The above-described studies are all somewhat relevant for the adsorption studies of the perylene dyes on TiO_2 performed in the work of this thesis. In particular, the ones deducing the binding geometry of the molecules possessing carboxylic acid groups. Moreover, the investigations on methanol adsorption are important since methanol is the desired product of the CO_2 reduction reaction to be performed with the dye-functionalized TiO_2 nanoparticles.

However, the TiO_2 interface has not only been studied by VSFG spectroscopy but also by surface second-harmonic generation (SHG) spectroscopy, a related surface-selective, nonlinear spectroscopic method whose response at double the frequency than the exciting frequency originates from the resonant enhancement of electronic transitions from surface atoms or interfacial molecular species. In this resonant mode, the intensity of the SHG signal depends on the number density and the second-order hyperpolarizability averaged over all molecular orientations of these species. For instance, Liu *et al.* could show, in a study relevant for the present work, that an interfacial charge-transfer complex is formed upon adsorption of catechol bearing two hydroxyl anchor groups onto colloidal anatase particles in aqueous solution [108]. Moreover, this technique allows to determine surface defects on the rutile(110) surfaces [109–111], symmetry characteristics of single crystal faces [112, 113] as well as surface electronic states [114].

Chapter 3

Materials, Methods, and Instruments

In this chapter the experiments performed in this thesis are described and a short theoretical background on each instrumental method applied is given. The substrate as well as the sample preparations are considered in detail. Special focus is put on VSFG spectroscopy and the special measuring mode implemented.

3.1 Dyes and TiO_2 particles

The perylene dyes ID1157, ID1152, SF18 and ID28 studied in this work were provided as powder samples by BASF SE (Ludwigshafen, Germany). Their chemical structures are shown in Fig. 3.1. To date, only the synthetic route of ID28 has been published [56]. Additionally, the structurally simpler model dye 1,8-naphthalic anhydride (NA) was purchased from Sigma-Aldrich (Germany) and used as received. NA was chemically cleaved to obtain the 1,8-naphthalene dicarboxylic acid dipotassium salt (K2NA) (see Section 3.4). The structures of the model substances are included in Fig. 3.1. The TiO_2 nanoparticle powder used was also provided by BASF SE and corresponds to the AEROXIDE® TiO_2 P25 particles from Evonik Industries AG (Germany). This powder is composed of anatase and rutile particles in the ratio 80:20. The Brunauer-Emmett-Teller (BET) surface of the 23.5 nm-sized particles amounts to 55 m^2/g.

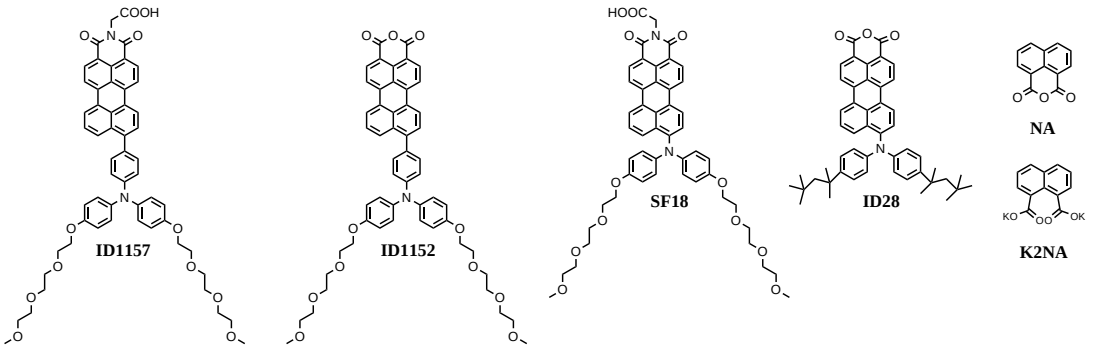

Fig. 3.1: Chemical structures of investigated dyes.

In all experiments water of MilliQ grade ($\geq$ 18.2 MΩ·cm at 25 °C; Synergy UV, Millipore, Germany) was used and found to be slightly acidic (pH 5–6) owing to dissolved atmospheric CO_2. The CO_2 adsorption studies were performed using CO_2 ($\geq$ 99.9 vol.%; basi Schöberl GmbH & Co. KG, Germany) dissolved in water. Dissolution was achieved by passing the gas through a glass frit. Most of the solvents (acetone ($(CH_3)_2CO$), di-

chloromethane (CH_2Cl_2), ethanol (C_2H_5OH) and tetrahydrofuran (THF)) used for cleaning and dye solutions preparation were of the highest grade (CHROMASOLV® HPLC grade) and purchased from Sigma-Aldrich (Germany), with the exception of isopropanol ($(CH_3)_2CHOH$) which was from Carl Roth (Germany). Methanol (CH_3OH) used for adsorption studies was also of the highest grade and purchased from Sigma-Aldrich. The deuterated compounds, i.e. deuterated methanol (CD_3OD, 99.8 atom%D) and deuterium oxide (D_2O, standard, 99.98 $\pm$ 0.01 atom%D) were bought from Carl Roth and Sigma-Aldrich, respectively.

3.2 Substrates

For most measurements done on TiO_2 films, CaF_2 was chosen as substrate because of its high transparency in the Vis and IR ranges ($\geq$ 75–95 % for 1 mm thickness over 0.4–10.0 μm). CaF_2 plates (10 mm $\times$ 10 mm $\times$ 1 mm; two-sided, optically polished (60/40); MaTecK, Germany) were used for UV/Vis absorption spectroscopic studies of the bound dyes, while CaF_2 hemicylindrical prisms (RCX-13-20-10CF, A = 13 mm $\times$ 20 mm, r = 10 mm; optically polished (10/20); Laser Components, Germany) were used for AFM, SEM and VSFG spectroscopy.

For VSFG measurements, half of the basal face of each prism was coated with a 100 nm-thick Au layer on top of a 10 nm-thick Ti adhesion layer by radio-frequency (RF) magnetron sputtering in the laboratory of M. Bruns (Institute for Applied Materials – Material Process Technology (IAM-WPT, KIT-Campus North, Eggenstein-Leopoldshafen, Germany) in order to facilitate the sample alignment in the VSFG setup. Sputtering was made on an Au target (3.00" diameter $\times$ 0.125" thickness (7.62 cm $\times$ 0.32 cm), 99.99 %; EJT-AUXX403A2, Kurt J. Lesker Materials Group, Germany) in an Ar atmosphere. A special holder was designed (D. Verreault, Department of Applied Physical Chemistry (APC), University of Heidelberg, Heidelberg) and fabricated (K. Schmitt and coworkers, machine shop of APC, University of Heidelberg) specifically for the sputtering of the CaF_2 prisms.

Only for CO_2 adsorption studies by VSFG spectroscopy was the basal face of one prism sputter-coated with a 30 nm-thick layer of SiO_2 covering the Au film and the free CaF_2 surface. The SiO_2 layer is needed in order to improve the adhesion of the TiO_2 film in acidic aqueous media. An SiO_2 target (3.00" $\times$ 0.125", 99.995 %; EJT-SIO2453A2, Kurt J. Lesker Materials Group) was used. A gas mixture of Ar/O_2 (80:20 v/v%) was chosen as pre-sputtering and sputtering atmospheres in order to compensate for the oxygen loss from the SiO_2 target.

Some VSFG experiments were also performed on TiO_2 films deposited on Au substrates. These substrates were fabricated in the laboratory of M. Bruns again using RF magnetron sputtering. Si wafers (Si-Mat Silicon Materials, Germany) were covered with a 10 nm-thick Cr adhesion layer, followed by an Au layer to produce a 100 nm-thick polycrystalline (predominantly with (111) orientation) Au film. The wafers were cut into small pieces ($\sim$10 mm $\times$ 10 mm) for sample preparation.

3.3 Preparation of substrates

Prior to TiO_2 film preparation, the Au-free parts of the CaF_2-based substrates were cleaned for 20 min in acetone and subsequently for 20 min in isopropanol in an ultrasonic bath (Elmasonic® S10 H, Elma, Germany). Afterwards these were blown dry under a nitrogen (N_2) flow and put in a UV/ozone cleaner (42-220, Jelight, USA) for 1 hr. In the case of used TiO_2-covered CaF_2 substrates, the TiO_2 film was gently removed with optical lens cleaning tissue before putting them into the solvents. As for the Au surfaces, they were cleaned for 2.5 hrs by UV/ozonolysis only.

3.4 Chemical cleavage of anhydride anchor group of NA

The dipotassium salt K2NA for the dye binding studies was obtained by chemical cleavage of the anhydride group of NA. The reaction could be carried out with the help of D. Jacubcyk at the Institute of Functional Interfaces (IFG, KIT-Campus North, Eggenstein-Leopoldshafen, Germany) based on a reaction protocol adapted from Ref. [115]. Briefly, NA powder (200 mg) was suspended in 50 mL water in a 250 mL two-neck round bottom flask. Under stirring 130 μL of a 85 wt% potassium hydroxide (KOH) aqueous solution was added and the mixture was heated up to 60–70 °C for 4 hrs. The reaction scheme of this cleavage is shown in Fig. 3.2. After cooling to room temperature the water was removed and the residue was dissolved in methanol for recrystallization. Upon placing this solution on dry ice the product precipitated and could be obtained by filtration. The completeness of the cleavage was confirmed by ^{13}C-NMR analysis. In the NMR spectrum of the product no peak attributed to anhydride carbons was observed but instead a peak associated with the carboxylate carbons was detected. All other peaks present in the spectrum could be assigned to the naphthalene unit, confirming that a pure product was obtained.

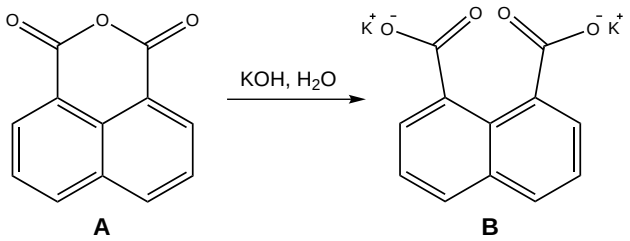

Fig. 3.2: Reaction scheme of chemical cleavage of (A) NA to (B) K2NA.

3.5 Preparation of dye solutions and bulk samples

The dye solutions for *ex situ* dye adsorption onto TiO_2 were prepared by dissolving the dyes containing a perylene ring system (ID1157, ID1152, SF18 and ID28) in dichloromethane, NA in THF and K2NA in ethanol at a concentration of 0.5 mM (for comparison see [116]). Dilutions of 1:50 of the 0.5 mM dye solutions were made to obtain transparent solutions, necessary for the study of free dyes with UV/Vis absorption spectroscopy.

Prior to further processing, the TiO_2 nanoparticle powder (P25) was cleaned by UV/ozonolysis for 2 hrs in order to remove remaining organic impurities from the production

process as well as adsorbed hydrocarbons. For IR and Raman spectroscopy measurements of the adsorbed dyes, the cleaned TiO_2 powder (∼30 mg) was suspended in 4 mL of the concentrated dye solutions (ID1157, ID1152, SF18, ID28, NA and K2NA) in Eppendorf vials by ultrasonication for at least 5 min. The immersion step was carried out overnight. To remove any unbound dye from the particles, the samples were centrifuged and washed five times with pure solvent. Finally, the samples were let to dry in air. As a reference sample pure TiO_2 powder was suspended in dichloromethane. Spectra of the free dyes were taken from the powder samples as received.

3.6 TiO_2 film preparation

For the TiO_2 film preparation, the TiO_2 nanoparticle powder was suspended in ethanol using an ultrasonic homogenizer (45 %, 90 min, pulsed mode; SONOPULS® HD 3200, Bandelin electronic & Co. KG, Germany). The suspension was spin-coated (G3P-8 Spincoat, Cookson Electronics Equipment, USA; Fig. 3.3 A) onto the various cleaned substrates. For the CaF_2 hemicylindrical prisms a special holder was designed and custom-built in the machine shop of the APC (University of Heidelberg; Fig. 3.3 B). The film thickness and quality depends on the suspension concentration, the spin speed, and also on the number of spin-coating steps. After many trial and error tests, transparent and homogeneous TiO_2 films on CaF_2 substrates were obtained for a suspension concentration of 8 g/L, spin speeds of 2000 rpm for 30 s followed by 3000 rpm for 3 s, and subsequent spin-coating steps ($6 \times 60\,\mu$L) of the prepared suspension (Fig. 3.3 C). On Au substrates, fewer steps ($4 \times 30\,\mu$L) were needed. These fresh films were put face down on a hot plate at ∼300 °C for 2 hrs in order to stabilize the film. After cooling in air for 15 min, the films were rinsed with water because it was found that this step improved the film stability, cleaned by UV/ozonolysis for 1 hr and then, after another cooling period of 15 min, incubated in the dye solutions (concentrations were identical compared to the preparation of the dye-coated particles) overnight ($\geq$ 20 hrs). Finally, the films were thoroughly rinsed with copious amounts of solvent and dried under a nitrogen stream.

3.7 Characterization of TiO_2 film

3.7.1 Atomic force microscopy

In order to determine their thickness and roughness the TiO_2 films were analyzed by AFM in dynamic contact mode. This technique is based on measuring the forces (van der Waals, ionic repulsion forces, etc.) between the sample surface and a very sharp probe tip which is attached to a cantilever (spring constant of about 0.1–1.0 N/m) and scanned over the sample surface. The movement of the tip is realized by a piezoelectric element. The change of the force on the cantilever with surface topography results in a deflection of the cantilever. This deflection is optically detected by reflecting a focused laser beam onto the surface of the cantilever. A photodiode divided into four quadrants (A, B, C, and D) then detects the position of the reflected beam. If the laser beam is displaced vertically between the bottom (C-D) and top (A-B) quadrants, a bending force is exerted on the cantilever which is due to topography; in contrast, if the beam is displaced horizontally between the left (A-C) and right (B-D) quadrants, then a torsion force is present due to friction of the cantilever with the surface. These deflections can be used to generate either a depth profile that shows the vertical deviations along the surface or, by scanning

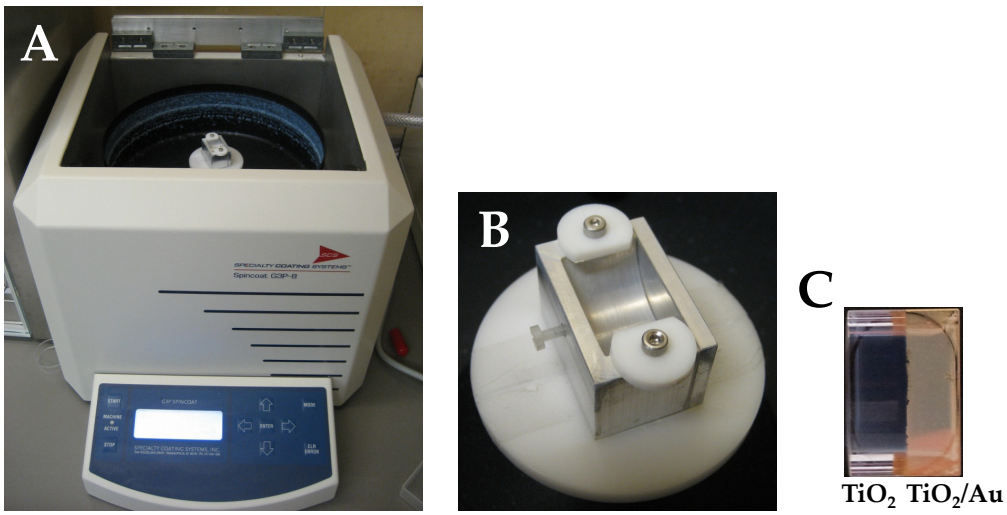

Fig. 3.3: Spin-coating system and spin-coated film. (A) Commercial spin-coater, (B) custom-built spin-coater holder for hemicylindrical CaF_2 prims and (C) spin-coated TiO_2 film on CaF_2 prism (basal face view with TiO_2 film and TiO_2 film on Au on the left and right halves, respectively.).

the sample laterally, a topographic image of the surface. Spatial resolutions range from the pm to the atomic scale. The microscope is usually operated in constant force mode meaning that the force between the tip and the surface is kept constant by adjusting the height of the cantilever while scanning over the surface. If the tip was scanned over the surface at constant height, it could hit the surface leading to damages. The advantage of AFM is that it is possible to analyze both conductive and non-conductive materials under vacuum, in air and in liquid.

The operation modes of AFM can be divided into static and dynamic modes. While in static mode the cantilever is just moved over the sample surface, in dynamic mode the cantilever is oscillated close to its resonance frequency and then moved over the surface. In the former mode surface information is obtained directly from the deflection of the cantilever, while in the latter it originates from changes in the oscillation frequency due to tip/surface interactions. An attractive (repulsive) force destabilizes (stabilizes) the spring and the resonance frequency is decreased (increased). With the resonance curve fixed, profiles of constant gradient can be measured and hence the topography is imaged. In static mode the tip of the cantilever is usually brought in mechanical contact with the surface, whereas in dynamic mode non-contact and tapping (intermittent contact) mode are distinguished. In tapping mode the damage done to the surface and the tip is reduced compared to full contact [117–119].

An AFM (Dimension 3100, Digital Instruments, USA) mounted on an electrical damping unit (Halcyonics, Accurion, Germany) was operated with the help of L. Pöttinger (APC, University of Heidelberg). Representative TiO_2 films on CaF_2 prisms were investigated. In order to measure the film thickness half of the film was wiped away and the resulting edge was imaged in tapping mode and analyzed with respect to its height profile using the AFM analysis software (Nanoscope 6.11, Digital Instruments, Veeco Metrology Group, USA).

3.7.2 Scanning electron microscopy

SEM was applied to study the homogeneity and porosity of TiO_2 film surfaces. An SEM micrograph is obtained by scanning a focused electron beam over an electrically conductive sample in vacuum. The interactions of these so-called primary electrons (PEs) with the sample result in the generation of emitted electrons and photons that can be collected by appropriate detectors to give information on the composition and topography of the sample surface. When the PEs hit the sample they lose energy by different pathways in a teardrop-shape interaction volume within the specimen. As a consequence secondary electrons (SEs), backscattered electrons (BSEs) and X-ray irradiation are produced. SEs and BSEs are the result of PEs scattered by the atoms in the sample. The scattering process is called inelastic when a PE collides with an atomic electron and an energy transfer occurs. If the transferred energy is greater than the work function of the electron this electron can leave the material. Emitted electrons with less than 50 eV are referred to as SEs. BSEs are the result of elastic scattering, meaning a PE bounces against the nucleus of an atom in the sample without loss of energy. The energy of BSEs is typically greater than 50 eV. The probability of elastic scattering increases with higher value of the atomic number (Z) of the material, thus leading to elemental contrast in the image. Characteristic X-ray irradiation is generated when a PE removes an inner shell electron from the sample and the atom decays to its ground state by emitting irradiation.

SEs originating within a few nanometers from the sample surface are mainly used to image the topography of the specimen because of their low energy. This low energy makes their collection easily achievable by a positively biased collector grid which is placed on one side of the sample. Behind the grid the electrons are accelerated towards a scintillator, also positively biased, and the generated photons are then detected by a photomultiplier (Everhart-Thornley detector). Modern SEMs also have a so-called InLens-detector, located at a small distance above the sample. Hence, very bright images can be recorded even at high resolutions due to effective SE capture. The more energetic BSEs originating from several nanometers deep are usually collected by a semiconductor detector installed above the sample because they leave the sample on straight trajectories [118, 120].

The micrographs of TiO_2 films on CaF_2 substrates were recorded with an SEM (Zeiss Supra 55, Carl Zeiss NTS, Germany) equipped with a highly energetic ($\sim$0.5–50 keV) Schottky field emission electron gun (V_{acc} = 0.1–30 kV) and an Everhart-Thornley and an InLens SE detector. The magnification was chosen between 5 000 and 10 000×, the accelerating voltage was set to 15.0 kV, and the working distance was in the range of 2.3–2.5 mm. The resolution for this SEM instrument is 1.7 nm at 1 kV. The measurements were performed in collaboration with U. Geckle (IAM-WPT, KIT-Campus North).

3.7.3 Photocurrent

The photocurrent of the dye/TiO_2 system was measured by an Au electrode coated with a dye-functionalized TiO_2 film and a Pt counter electrode, both immersed in a 1 M KCl solution. When the film is irradiated with Vis light (75 W Xe light source (Oriel Instruments) with 435 nm cut-off filter) the electrons excited in the dye are transferred via the TiO_2 film to the Au electrode and can thus be detected as current. The higher the photocurrent the better the electronic coupling between the dye and TiO_2 and thus the charge injection from the excited dye into the CB of TiO_2 [61]. The photocurrent measurements were performed by F. Staier (APC, University of Heidelberg).

3.8 Spectroscopic characterization of dye binding at TiO_2 films

3.8.1 Ultraviolet–visible absorption spectroscopy

Optical spectroscopy in general investigates light-matter interactions, meaning the absorption or scattering of electromagnetic radiation by molecules. In the case of UV/Vis absorption spectroscopy radiation from the UV to the Vis range (λ = 200–800 nm) is applied to the sample. This photon energy is sufficient to excite transitions between energy states of valence electrons in the molecule [121]. Thus, the technique was applied here in order to observe changes in the electronic structure of the dye molecules upon binding to TiO_2.

In a molecule atomic orbitals combine to molecular orbitals, which can be of single bond (σ), multiple bond (π), non-bonding (n) or anti-bonding (σ^*, π^*) character. σ electrons are energetically the lowest lying ones and thus not excitable by conventional UV light ($\lambda > 200$ nm). Consequently, only molecules with π or n electrons can be excited. Moreover, the transition dipole moment must change. Typical electronic transitions are $n - \pi^*$ and $\pi - \pi^*$ transitions. In the case of aromatic systems with donor and acceptor groups so-called intramolecular charge transfer (CT) transitions from the donor to the acceptor group can be triggered within one molecule. In contrast, intermolecular CT transitions take place between two different molecules, e.g. a ligand and a metal or metal oxide center.

The highest occupied molecular orbital (HOMO) and the lowest unoccupied molecular orbital (LUMO) are termed the frontier orbitals of a molecule, independent of their orbital character. The HOMO usually corresponds to the ground singlet state (S_0) of the molecule and the LUMO to the first excited singlet state (S_1). The light ($h\nu$) impinging on the sample must, according to Bohr's frequency condition, match or be greater than the energy gap between the HOMO and the LUMO in order to promote an electron i.e.

$$h\nu \geq E_2 - E_1, \tag{3.1}$$

where ν is the frequency, h is the Planck's constant, and E_1 and E_2 are the energy states of the HOMO and LUMO, respectively.

Also, an electron can be promoted from a lower lying occupied molecular orbital (HOMO-1) to the LUMO or even a higher unoccupied molecular orbital (LUMO+1), if the photon energy matches this gap, resulting in more than one possible electronic transition for a compound. The color of a substance is dependent on the gap energy. For example, a dye absorbing yellow light ($\lambda \approx 600$ nm) appears blue and vice versa.

If the π-electrons are part of a conjugated system, i.e. highly delocalized, the energies of the orbitals lie closer together and the energy required for a transition is less. In this case the maximum transition energy ΔE_n can be obtained from the quantum mechanical one-dimensional particle-in-a-box model:

$$\Delta E_n = h\nu = h\frac{c}{\lambda} = \frac{\left(n_f^2 - n_i^2\right) h^2}{8 m_e L^2} = \frac{\left(n_f^2 - n_i^2\right) h^2}{8 m_e (N+1)^2}, \tag{3.2}$$

where c denotes the speed of light, λ the wavelength of the exciting photon, and n_f and n_i are the integral (non-zero) quantum number of the LUMO and the HOMO, respectively. The length L of the conjugated chain is approximated as the spacing between the

walls of the box. m_e is the mass of the excited electron and N represents the number of π-electrons [122, 123].

In the case of inorganic compounds such as semiconductors (e.g. TiO_2), the HOMO corresponds to the valence band and the LUMO corresponds to the conduction band. A semiconductor usually exhibits minimal optical absorption for photons with energies smaller than the bandgap and high absorption for photons with energies greater than the bandgap. As a result, there is a sharp increase in absorption at energies close to the bandgap resulting in an absorption edge in the spectrum.

Typically, an UV/Vis absorption spectrum exhibits a few broad absorption bands instead of sharp lines as would be expected from the discrete energy levels. This broadness is the result of vibrational transitions that are superimposed on the electronic transitions. As a consequence to the electron displacement upon excitation, the nuclei in the molecule start vibrating. The absorption process can be quantified by the Beer-Lambert law:

$$A = \log_{10} T^{-1} = \log_{10} \frac{I_0(\nu)}{I(\nu)} = \varepsilon(\nu) \cdot c \cdot d, \tag{3.3}$$

where A and T are the absorbance and transmittance of the material, $I_0(\nu)$ is the intensity of monochromatic light entering the sample and $I(\nu)$ is the transmitted light intensity both at frequency ν, $\varepsilon(\nu)$ is the molar extinction coefficient, characteristic of the material, c the concentration of the light-absorbing substance, and d the thickness of the material. This law is a limiting law for dilute solutions, meaning that the extinction coefficient is only independent of the concentration at a given wavelength for diluted solutions [124].

The transmittance of the dye solutions and the dye-coated TiO_2 films on CaF_2 plates in the UV to Vis spectral range was measured using a commercial UV/Vis high-resolution spectrophotometer (HR2000+, Ocean Optics, Germany). Input and output UV/Vis light beams are provided by a balanced deuterium tungsten-halogen light source (DH-2000-BAL, Ocean Optics) and transmitted through two steel-jacketed optical fibers (QP400-2-SR-BX, Ocean Optics; 400 μm core diameter) optimized for transmission in the spectral range 200–1100 nm. The transmitted light beam is dispersed into its various wavelengths by a monochromator and send to a CCD detector. All spectra were recorded and processed using the SpectraSuite software (Ocean Optics). The absorption spectra were taken as the negative logarithmic ratio of background-corrected signals. For the dye solutions a quartz cuvette (101-QS, Hellma Analytics, Germany) with d = 10 mm was used. As reference the pure solvent was recorded. As for the dye-coated TiO_2 films, a bare TiO_2 film on a CaF_2 plate was measured as reference. For comparability the spectra were Min/Max normalized.

3.8.2 Fourier-transform infrared absorption spectroscopy

In contrast to UV/Vis absorption spectroscopy, FTIR spectroscopy applies light in the IR spectral range (λ = 1–100 μm) to the sample. Instead of electronic transitions, transitions between vibrational energy states are triggered. Many vibrational modes involve the displacement of just a few atoms while the rest of the molecule stays stationary. The frequencies of these vibrations are characteristic for the type of bond and the group of atoms involved and are very weakly affected by the nature of the other atoms in the molecule. Certain spectral features are thus indicative of a specific chemical group in a

molecule. Other vibrational motions vary from molecule to molecule and cause spectral features known as *fingerprint* bands [125]. Hence, because of its chemical selectivity, FTIR spectroscopy was employed to deduce which functional groups participate in the binding process of the dye molecules to the TiO_2. In addition, it enables to elucidate the coordination mechanism of the functional groups.

Vibrations involving the displacement of nuclei in a molecule only occur if they induce a change in dipole moment (permanent or induced) μ:

$$\left(\frac{\partial \mu}{\partial q}\right)_0 \neq 0, \tag{3.4}$$

where q denotes the vibrational coordinate.

For example, in a diatomic molecule, small movements of the atoms from their equilibrium position follow a nearly harmonic displacement. The restoring force $F(r)$ of the bond, which compares to a spring, obeys Hooke's law:

$$F(r) = -k\,(r - r_e)\,, \tag{3.5}$$

with the potential energy $V(r)$ described by:

$$V(r) = \frac{1}{2} k\,(r - r_e)^2\,, \tag{3.6}$$

where k is the force constant of the bond, indicating the bond stiffness, and r the displacement from r_e, the equilibrium position of the molecule.

The allowed energy levels or vibrational states E_υ of the harmonic potential are given by:

$$E_\upsilon = \left(\upsilon + \frac{1}{2}\right)\hbar\omega \quad \text{with} \quad \upsilon = 0, 1, 2, \ldots \quad \text{and} \quad \omega = \left(\frac{k}{\mu}\right)^{\frac{1}{2}}, \tag{3.7}$$

where υ is the vibrational quantum number, ω is the frequency, $\hbar$ the reduced Planck constant, and μ the reduced mass of the molecule [122].

The picture of a harmonic potential, albeit simple, is only partly realistic since it does not allow for a possible dissociation of the molecule. In addition, it predicts a finite energy if the two atoms find themselves in the same place (i.e. an intercept of the potential curve with the energy axis exists). In contrast, an anharmonic potential is found to account better for the higher energy vibrational states of a molecule. An example of an anharmonic potential is given by the Morse potential:

$$V(r) = D_e\{1 - e^{-a(r-r_e)}\}^2 \quad \text{with} \quad a = \sqrt{\frac{k}{2D_e}}, \tag{3.8}$$

where D_e denotes the minimum of the potential well and a the force constant of the bond. The dissociation energy for the diatomic molecule can be calculated by subtracting the zero point energy $V(0)$ from D_e.

The IR spectra of the dye powder samples and the dyes bound to TiO_2 were recorded using an ATR unit built into an FTIR spectrometer (Tensor 27, Bruker Optics, Germany).

ATR-IR spectroscopy has for advantage that it requires little to no sample preparation so that even opaque samples (like the dyes) can be measured easily. The sample is placed in contact with an internal reflection element, e.g. a diamond or Ge crystal, and the IR light is directed into the crystal at an incident angle so that it undergoes total internal reflection (TIR) at the crystal/sample interface before it leaves the sample towards the detector. This TIR condition gives rise to a traveling surface wave called *evanescent wave* whose electric field decays along the normal to the interface. The penetration depth d_p of the evanescent field is given by:

$$d_p = \frac{\lambda}{2\pi n_1 \sqrt{\sin^2\theta - (n_2/n_1)^2}}, \tag{3.9}$$

where θ is the angle of incidence and n_1, n_2 are the refractive indices of the ATR crystal and the sample, respectively. Since the penetration depth is dependent on the wavelength an ATR-IR spectrum will have different band intensities compared to an IR transmission spectrum [125].

As the reference in the ATR-IR experiments the spectrum of the bare ATR crystal was recorded. The IR light source used was a Globar (resistively-heated Si carbide rod) and the signal coming from the sample via a Michelson interferometer was captured by a liquid nitrogen-cooled mercury-cadmium-telluride (MCT) detector. The spectral information from the interferogram was obtained after FT analysis. The IR spectra were recorded with 32 sample scans at a resolution of $4\,cm^{-1}$ and processed with the OPUS software (Bruker Optics). As data preprocessing steps the spectra of both the free and bound dyes were corrected for atmospheric contributions from water vapor and CO_2 when necessary and the spectra of the bound dyes were divided by a spectrum of a pure TiO_2 sample in order to remove spectral features originating from TiO_2 and bound water. Finally, all spectra were vector-normalized for better comparison. Thus, the absolute intensity of the spectra presented is only due to normalization and not to the amount of dye.

3.8.3 Fourier-transform Raman spectroscopy

Raman spectroscopy is concerned with the scattering of light from a molecule and is another type of vibrational spectroscopy like IR spectroscopy [126]. For this reason, it was also applied to investigate the binding of the dyes to TiO_2. In contrast to UV/Vis and IR spectroscopy, the incident light does not need to correspond to the difference between two energy levels in a molecule to scatter from the latter. In fact, applied monochromatic light distorts (polarizes) the electron cloud around the nuclei in the sample molecule to form a short-lived virtual state. Two scattering types are known: (i) elastic (Rayleigh) and (ii) inelastic (Raman) scattering. The first one occurs when only electron cloud distortion is involved. In this case the frequency of the scattered light does not change and it is the dominant process. In the second case nuclear motions are induced and the scattered photon has either lost or gained energy corresponding to one vibrational transition. Energy loss is known as Stokes scattering and energy gain is known as anti-Stokes scattering. However, the latter process is less intense. Overall, Raman scattering is an inherently weak process as only one out of 10^6–10^8 scattered photons undergoes Raman scattering. To compensate for this drawback, intense lasers are used to increase the amount of inelastically scattered photons. Moreover, the cross section of a molecule, describing the likelihood of a scattering event to take place, determines the Raman intensity. Finally, incident light in the UV to Vis wavelength range is usually chosen over light in the IR range

since the Raman scattering process is dependent on the fourth power of the frequency of the incident light:

$$I_{Stokes} \propto I_0 \left(\omega_0 - \omega_R\right)^4 |\alpha|^2 , \tag{3.10}$$

where I_0 represents the intensity of the incident light, ω_0 the incident frequency, ω_R the Raman frequency, and α the polarizability, a property characteristic of the material which depends on the molecular structure and the type of bonds.

Classical theory explains Raman scattering by the resultant dipole moment $\boldsymbol{\mu}$ induced by the incident time-harmonic electric field $\mathbf{E}(t)$:

$$\boldsymbol{\mu} = \boldsymbol{\alpha} \cdot \mathbf{E}(t), \tag{3.11}$$

or, equivalently,

$$\mu = \alpha E_0 \cos \omega_0 t, \tag{3.12}$$

where E_0 is the amplitude or strength of the incident electric field.

For a vibrating molecule the nuclear displacement dq from the equilibrium position can be written as:

$$dq = q_0 \cos \omega_R t, \tag{3.13}$$

where q_0 is the vibrational amplitude. For small enough amplitudes of vibration around the equilibrium position q_0, α can be approximated as a linear function of q:

$$\alpha = \alpha(q) \approx \alpha_0 + \left(\frac{\partial \alpha}{\partial q}\right)_0 dq, \tag{3.14}$$

where $\alpha_0 = \alpha(q_0)$ is the polarizability at the equilibrium position, and $\left(\frac{\partial \alpha}{\partial q}\right)_0$ is the rate of change of α with respect to the change in q, evaluated at the equilibrium position.

After combining Eqs. 3.12, 3.13 and 3.14, one has that

$$\mu = \left\{\alpha_0 + \left(\frac{\partial \alpha}{\partial q}\right)_0 q_0 \cos \omega_R t\right\} E_0 \cos \omega_0 t. \tag{3.15}$$

Finally, Eq. 3.15 can be rearranged to give

$$\mu = \alpha_0 E_0 \cos \omega_0 t + \frac{q_0 E_0}{2}\left[\left(\frac{\partial \alpha}{\partial q}\right)_0 \cos\left(\omega_0 - \omega_R\right) t + \left(\frac{\partial \alpha}{\partial q}\right)_0 \cos\left(\omega_0 + \omega_R\right) t\right]. \tag{3.16}$$

The first term represents an oscillating dipole that emits light without change in frequency ω_0 (Rayleigh scattering), whereas the second and third terms correspond to the Raman scattering of frequency $(\omega_0 - \omega_R)$ (anti-Stokes) and $(\omega_0 + \omega_R)$ (Stokes). If $\left(\frac{\partial \alpha}{\partial q}\right)_0 \neq 0$ (compare with Eq. 3.4), the vibration is considered as Raman-active. In other words, vibrations which come along with a change in the polarizability of the molecule, are excitable. As a rule of thumb this is the case for symmetric vibrations and nonpolar molecular fragments [127].

Fluorescence is a major problem in Raman spectroscopy, especially if light in the Vis wavelength region is used because it will also excite electronic transitions. Once electronic transitions are stimulated, one possible decay pathway is fluorescence which is a

much stronger process than Raman scattering. As a result, the fluorescence signal generally overshadows the Raman signal. The influence of fluorescence can be minimized by using lasers with wavelengths in the near-IR such that electronic excitation cannot occur. One of the frequently used wavelengths is the 1064-nm line of the neodymium-doped yttrium aluminum garnet (Nd:YAG) laser. It can be made intense enough to make up for the drastic Raman signal loss which results due to the fourth power dependence on the incident photon frequency when going from Vis to IR radiation (see Eq. 3.10). Not only the Raman signal decrease but also the low sensitivity of the detectors needed in the IR region is a problem. A solution to the latter is the use of a Michelson interferometer with FT analysis. In general, the Rayleigh-scattered light is filtered out by a so-called notch filter [125]. Since the dyes studied exhibit a strong electronic transition in the Vis the FT-Raman technique was applied to circumvent fluorescence.

In this work, the Raman spectra of the dye powder samples and the dye-functionalized TiO_2 particles were recorded on a FT-Raman spectrometer (Vertex 80, Bruker Optics) equipped with a Nd:YAG laser and a liquid nitrogen-cooled Ge detector. The Raman spectra were recorded with 100 sample scans at a resolution of $4\,cm^{-1}$ and the data was analyzed using the OPUS software (Bruker Optics). The spectra were also vector-normalized for comparison.

3.9 Characterization of dye, methanol and CO_2 binding by VSFG spectroscopy

VSFG spectroscopy is a surface-specific nonlinear vibrational technique with sub-monolayer sensitivity. In a typical VSFG experiment, two intense laser beams, one at fixed Vis frequency and one at a tunable IR frequency are temporally and spatially overlapped at the surface between two bulk media. Because of the inherent lack of inversion symmetry at interfaces, another beam is generated at the sum of the two incident frequencies through a second-order nonlinear process called sum-frequency generation (SFG). This non-centrosymmetric condition is a selection rule and confers to VSFG its surface specificity. The VSFG signal is resonantly enhanced when the tunable IR frequency matches a vibrational mode of interfacial and adsorbed molecular species. As a consequence the vibrational spectrum of these species can be obtained by scanning through a defined range of IR frequencies. The underlaying physical principle of this technique will be discussed below.

Shortly after the development of the first ruby laser in 1960 [128], the phenomenon of frequency conversion or frequency generation was demonstrated by Franken *et al.* in 1961 who generated a second-harmonic signal (conversion of light at frequency ω to light at frequency 2ω) from the bulk of a quartz crystal [129]. This was rapidly followed by the discovery of similar processes in other materials as well as other nonlinear processes [130, 131]. Later on, the theoretical basis of such nonlinear phenomena was laid down by Bloembergen *et al.* [132, 133]. Much later, in 1987, Shen *et al.* [134–136] and Harris *et al.* [137] independently reported the first applications of VSFG as a surface vibrational spectroscopy.

3.9.1 SFG Theory

As already stated in the previous section the electric field $\mathbf{E}$ of a light beam interacting with the bulk or a surface of a given medium polarizes the material and creates induced molecular electric dipoles $\boldsymbol{\mu}$. In the case of a weak electric field the induced dipole is proportional to the strength of the field:

$$\boldsymbol{\mu} = \boldsymbol{\mu}_0 + \alpha \mathbf{E}, \tag{3.17}$$

where $\boldsymbol{\mu}_0$ is the static electric dipole [138]. In a condensed phase, the sum of the dipole moments gives rise to a dipole moment per unit volume or bulk polarization $\mathbf{P}$:

$$\mathbf{P} = \mathbf{P}_0 + \varepsilon_0 \chi^{(1)} \mathbf{E}, \tag{3.18}$$

where ε_0 is the vacuum permittivity and $\chi^{(1)} = N\langle\alpha\rangle$ is the first-order or linear susceptibility and N is the number density. Only few materials have a static polarization, thus the term $\mathbf{P}_0$ is not carried on in the following equations.

The electric fields of intense pulsed lasers might become comparable in strength to the fields felt by the electrons in a molecule and as a consequence the response of the electrons to the electric field is no longer linear. Higher order terms must be included in the description of the induced dipole moment:

$$\boldsymbol{\mu} = \alpha \cdot \mathbf{E} + \beta : \mathbf{E}^2 + \gamma \vdots \mathbf{E}^3 + \dots. \tag{3.19}$$

β and γ are known as the first- and second-order hyperpolarizabilities. Accordingly, the bulk polarization is written as:

$$\begin{aligned} \mathbf{P} &= \varepsilon_0 (\chi^{(1)} \cdot \mathbf{E} + \chi^{(2)} : \mathbf{E}^2 + \chi^{(3)} \vdots \mathbf{E}^3 + \dots) \\ &= \mathbf{P}^{(1)} + \mathbf{P}^{(2)} + \mathbf{P}^{(3)} + \dots, \end{aligned} \tag{3.20}$$

where $\chi^{(2)} = N\langle\beta\rangle$ and $\chi^{(3)} = N\langle\gamma\rangle$ are the second- and third-order nonlinear susceptibilities, respectively [139, 140].

As a result of the higher-order terms in Eq. 3.20 the refractive index and absorption coefficient become dependent on the intensity of the light. Moreover, the frequency of the light can change. This is demonstrated here in nonlinear optical processes such as SHG and SFG, whose dominant polarization term is of second-order:

$$\mathbf{P}^{(2)} = \varepsilon_0 \chi^{(2)} : \mathbf{E}^2, \tag{3.21}$$

where the second-order nonlinear susceptibility $\chi^{(2)}$ is a third-rank tensor describing the relationship between the applied electric field and the resulting polarization field. The combined electric field of two intense laser beams overlapping at an interface can be expressed as the sum of the two corresponding electric fields oscillating at different frequencies ω_1 and ω_2:

$$\mathbf{E} = \mathbf{E}_1 \cos \omega_1 t + \mathbf{E}_2 \cos \omega_2 t. \tag{3.22}$$

Inserting Eq. 3.22 into Eq. 3.21 gives:

$$\begin{aligned} \mathbf{P}^{(2)} = \varepsilon_0 \chi^{(2)} : (&\mathbf{E}_1^2 + \mathbf{E}_2^2 + \mathbf{E}_1^2 \cos 2\omega_1 t + \mathbf{E}_2^2 \cos 2\omega_2 t \\ &+ 2\mathbf{E}_1 \mathbf{E}_2 \cos(\omega_1 - \omega_2) t + 2\mathbf{E}_1 \mathbf{E}_2 \cos(\omega_1 + \omega_2) t) \end{aligned} \tag{3.23}$$

with the different frequency components of the second-order polarization $\mathbf{P}^{(2)}$ given by

$$\begin{array}{lll} \mathbf{P}^{(2)}(0) & = \varepsilon_0\chi^{(2)} : (\mathbf{E}_1^2 + \mathbf{E}_2^2) & (\mathrm{OR}), \\ \mathbf{P}^{(2)}(2\omega_1) & = \varepsilon_0\chi^{(2)} : (\mathbf{E}_1^2 \cos 2\omega_1 t) & (\mathrm{SHG}), \\ \mathbf{P}^{(2)}(2\omega_2) & = \varepsilon_0\chi^{(2)} : (\mathbf{E}_2^2 \cos 2\omega_2 t) & (\mathrm{SHG}), \\ \mathbf{P}^{(2)}(\omega_1 - \omega_2) & = \varepsilon_0\chi^{(2)} : (2\mathbf{E}_1\mathbf{E}_2 \cos{(\omega_1 - \omega_2)t}) & (\mathrm{DFG}), \\ \mathbf{P}^{(2)}(\omega_1 + \omega_2) & = \varepsilon_0\chi^{(2)} : (2\mathbf{E}_1\mathbf{E}_2 \cos{(\omega_1 + \omega_2)t}) & (\mathrm{SFG}). \end{array} \tag{3.24}$$

The underlying physical processes of the different frequency components are optical rectification (OR) (with no frequency dependence), second-harmonic generation (SHG), difference-frequency generation (DFG), and sum-frequency generation (SFG).

In the case of VSFG spectroscopy with incident IR and Vis electric fields the SFG polarization field can then be written as (ignoring the time-dependence):

$$\mathbf{P}^{(2)} \propto \chi^{(2)} : \mathbf{E}_{\mathrm{IR}}\mathbf{E}_{\mathrm{Vis}}. \tag{3.25}$$

In order to achieve selectively an SFG process at an interface, the two incident light beams must be coincident spatially and temporally. A coherent SFG signal is subsequently generated at a definite angle θ_{SFG} relative to the surface normal, which can be calculated using the conservation of momentum (k) of all three beams parallel to the interface:

$$k_{\mathrm{SFG},\parallel} = k_{\mathrm{IR},\parallel} + k_{\mathrm{Vis},\parallel} \tag{3.26}$$

or, equivalently,

$$n(\omega_{\mathrm{SFG}})\omega_{\mathrm{SFG}} \sin\theta_{\mathrm{SFG}} = n(\omega_{\mathrm{IR}})\omega_{\mathrm{IR}} \sin\theta_{\mathrm{IR}} + n(\omega_{\mathrm{Vis}})\omega_{\mathrm{Vis}} \sin\theta_{\mathrm{Vis}}, \tag{3.27}$$

where n is the refractive index of the medium for each beam of frequency $\omega_{\mathrm{SFG}}, \omega_{\mathrm{IR}}$ or ω_{Vis} and $\theta_{\mathrm{SFG}}, \theta_{\mathrm{IR}}$ and θ_{Vis} are the angles relative to the surface normal for each beam. SFG beams are generated in both the reflected and transmitted directions and the more accessible and/or most intense of these two beams is usually detected.

3.9.1.1 Second-order susceptibility $\chi^{(2)}$

The second-order nonlinear susceptibility $\chi^{(2)}$ is characteristic of the material and a third-rank tensor that can be expressed as a sum of 3^3 = 27 different elements:

$$\chi^{(2)} \propto \sum_{j,k,l} \chi^{(2)}_{jkl}, \tag{3.28}$$

where the indices j, k, l can take any of the axes (x, y, z) of the surface rectangular coordinate system.

The intrinsic symmetry of $\chi^{(2)}_{jkl}$ leads to the surface specificity of the SFG process. In a centrosymmetric environment $\chi^{(2)}_{jkl}$ must be invariant under the inversion operation and thus

$$\chi^{(2)}_{jkl} = \chi^{(2)}_{-j-k-l} \tag{3.29}$$

must apply. In addition, $\chi^{(2)}_{jkl}$ is a polar tensor i.e. a tensor which changes sign under the inversion operation:

$$\chi^{(2)}_{jkl} = -\chi^{(2)}_{-j-k-l}. \tag{3.30}$$

In order to satisfy both conditions (Eqs. 3.29 and 3.30) $\chi^{(2)}_{jkl}$ must be equal to zero. Hence, the SFG process is forbidden in centrosymmetric media. Since the inversion symmetry is broken at an interface between two centrosymmetric media (and in the bulk of some non-centrosymmetric crystals), an SFG signal can be generated. At the interface molecules can adopt a net polar orientation and thus $\chi^{(2)}_{jkl}$ is non-zero and SFG can occur. Consequently, the magnitude of $\chi^{(2)}_{jkl}$ is very sensitive to the degree of orientational order. Figure 3.4 gives a schematic representation of the air/dye-TiO_2 interface investigated in the present work.

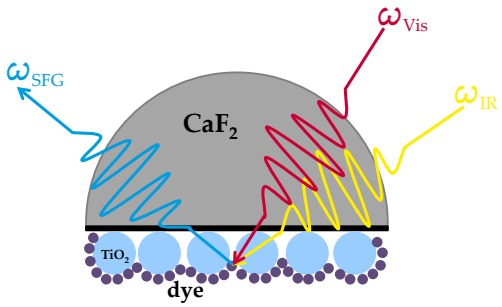

Fig. 3.4: Schematic representation of air/dye-TiO_2 interface leading to a non-zero $\chi^{(2)}$.

The number of non-zero components of $\chi^{(2)}_{jkl}$ are constrained by symmetry considerations. At a surface with C_∞ symmetry around the z-axis, which corresponds to the surface normal in the chosen cartesian coordinate system, only seven non-zero $\chi^{(2)}_{jkl}$ components may contribute to a generated SFG signal:

$$\chi^{(2)}_{zxx}(\equiv \chi^{(2)}_{zyy}) \quad \chi^{(2)}_{xzx}(\equiv \chi^{(2)}_{yzy}) \quad \chi^{(2)}_{xxz}(\equiv \chi^{(2)}_{yyz}) \quad \chi^{(2)}_{zzz}.$$

By appropriately choosing the polarization combination of the incident beams it is possible to selectively probe certain components of $\chi^{(2)}_{jkl}$. This is due to the fact that s-polarized light has its electric field component solely along the y-axis whereas p-polarized light possesses components along the x- and z-axis. In Tab. 3.1 it is summarized which polarization combination probes which $\chi^{(2)}_{jkl}$ elements [138].

Tab. 3.1: $\chi^{(2)}_{jkl}$ elements probed by specific incident polarization combinations. The polarization states of each beam are listed in the order of increasing wavelength (SFG, Vis, IR).

Polarization combination	**Probed elements of** $\chi^{(2)}_{jkl}$
pss	$\chi^{(2)}_{zyy}$
sps	$\chi^{(2)}_{yzy}$
ssp	$\chi^{(2)}_{yyz}$
ppp	$\chi^{(2)}_{zzz}, \chi^{(2)}_{zxx}, \chi^{(2)}_{xzx}, \chi^{(2)}_{xxz}$

3.9.1.2 VSFG spectrum

The recorded VSFG beam intensity $I_{\mathrm{SFG}}(\omega_{\mathrm{IR}})$ is proportional to the intensity of the two incident beams (I_{IR} and I_{Vis}), scaled with the second-order susceptibility and is given by:

$$I_{\mathrm{SFG}}(\omega_{\mathrm{IR}}) \propto \left|\mathbf{P}^{(2)}\right|^2 \propto \left|\chi^{(2)}(\omega_{\mathrm{IR}}) : \mathbf{E}_{\mathrm{IR}}\mathbf{E}_{\mathrm{Vis}}\right|^2 = \left|\chi^{(2)}(\omega_{\mathrm{IR}})\right|^2 I_{\mathrm{IR}} I_{\mathrm{Vis}}. \tag{3.31}$$

For the spectral analysis it is important to know that $\mathbf{P}^{(2)}$ and $\chi^{(2)}$ stem from non-resonant (NR) as well as resonant (R) contributions thus giving:

$$I_{\mathrm{SFG}}(\omega_{\mathrm{IR}}) \propto \left|\mathbf{P}^{(2)}_{\mathrm{NR}} + \mathbf{P}^{(2)}_{\mathrm{R}}\right|^2 \propto \left|\chi^{(2)}_{\mathrm{NR}} + \chi^{(2)}_{\mathrm{R}}(\omega_{\mathrm{IR}})\right|^2 I_{\mathrm{IR}} I_{\mathrm{Vis}}, \tag{3.32}$$

where $\mathbf{P}^{(2)}_{\mathrm{NR}}$, $\chi^{(2)}_{\mathrm{NR}}$ and $\mathbf{P}^{(2)}_{\mathrm{R}}$, $\chi^{(2)}_{\mathrm{R}}$ are the non-resonant and (frequency-dependent) resonant parts of the polarization field and second-order nonlinear susceptibility originating from interfacial adsorbed molecular species and from the bulk of the substrate, respectively. In the case of dielectrics such as CaF_2 or SiO_2, $\chi^{(2)}_{\mathrm{NR}} \approx 0$ but for conducting materials such as noble metals the NR contributions are significant. These contributions are the result of electronic transitions within the band structure of the conducting material [141]. Furthermore, in an VSFG experiment using a broadband SFG laser system, I_{Vis} is considered constant over the spectral region of interest and I_{IR} can be modeled using a Gaussian function due to the near-Gaussian-shaped profile of the broadband IR beam, which is applied in the present work.

Both $\chi^{(2)}_{\mathrm{NR}}$ and $\chi^{(2)}_{\mathrm{R}}$ are complex parameters and can be put in polar form with an amplitude and a phase. Moreover, $\chi^{(2)}_{\mathrm{R}}$ represents the sum over the single resonant vibrational modes, each of which can be modeled by a Lorentzian-like line shape:

$$\begin{aligned}\chi^{(2)}_{\mathrm{NR}} + \chi^{(2)}_{\mathrm{R}}(\omega_{\mathrm{IR}}) &= \left|\chi^{(2)}_{\mathrm{NR}}\right| e^{i\phi_{\mathrm{NR}}} + N_s \sum_q \left|\chi^{(2)}_{\mathrm{R},q}(\omega_{\mathrm{IR}})\right| e^{i\phi_{\mathrm{R},q}(\omega_{\mathrm{IR}})} \\ &= \left|\chi^{(2)}_{\mathrm{NR}}\right| e^{i\phi_{\mathrm{NR}}} + N_s \sum_q \left|\frac{A_{\mathrm{R},q}}{(\omega_{\mathrm{IR}} - \omega_q) + i\Gamma_q}\right| e^{i\phi_{\mathrm{R},q}(\omega_{\mathrm{IR}})},\end{aligned} \tag{3.33}$$

where $A_{\mathrm{R},q}$, ω_q and Γ_q represent the amplitude, center frequency, and half-width half-maximum line width, respectively, of the Lorentzian line shape of the q^{th} vibrational mode. N_s is the number surface density of molecular species. ϕ_{NR} and $\phi_{\mathrm{R},q}$ are the phase factors associated with the non-resonant and resonant contributions. From Eq. 3.33 it is seen that the SFG intensity is enhanced when $\omega_{\mathrm{IR}} \to \omega_q$.

The energy level diagram of the SFG process is depicted in Fig. 3.5. The diagram shows that the IR pulse excites a molecular vibration, which is up-converted by the Vis pulse to a virtual state. The latter decays by the emission of an SFG photon through an anti-Stokes Raman process. This demonstrates that only vibrational modes which are both IR- and Raman-active can be probed with SFG.

Because of the complex nature of both the resonant and NR terms, they interfere with each other when the intensity is computed. This can be seen more clearly if Eq. 3.33 is

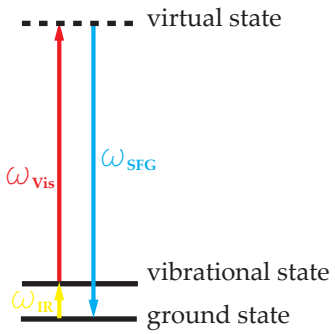

Fig. 3.5: Energy level diagram of the SFG process. A molecular vibration is excited by the IR pulse, up-converted by the Vis pulse and an SFG pulse is generated through an anti-Stokes Raman process.

inserted into Eq. 3.32 (considering only one resonant vibrational mode):

$$\begin{aligned} I_{\mathrm{SFG}}(\omega_{\mathrm{IR}}) &\propto \left| \left|\chi^{(2)}_{\mathrm{NR}}\right| e^{i\phi_{\mathrm{NR}}} + \left|\chi^{(2)}_{\mathrm{R}}(\omega_{\mathrm{IR}})\right| e^{i\phi_{\mathrm{R}}(\omega_{\mathrm{IR}})} \right|^2 I_{\mathrm{IR}} I_{\mathrm{Vis}} \\ &\propto \left| \left|\chi^{(2)}_{\mathrm{NR}}\right| e^{i\phi_{\mathrm{NR}}} + \left|\chi^{(2)}_{\mathrm{R}}(\omega_{\mathrm{IR}})\right| e^{i\phi_{\mathrm{R}}(\omega_{\mathrm{IR}})} \right| \cdot \left| \left|\chi^{(2)}_{\mathrm{NR}}\right| e^{-i\phi_{\mathrm{NR}}} + \left|\chi^{(2)}_{\mathrm{R}}(\omega_{\mathrm{IR}})\right| e^{-i\phi_{\mathrm{R}}(\omega_{\mathrm{IR}})} \right| I_{\mathrm{IR}} I_{\mathrm{Vis}} \\ &\propto \left[\left|\chi^{(2)}_{\mathrm{NR}}\right|^2 + \left|\chi^{(2)}_{\mathrm{R}}(\omega_{\mathrm{IR}})\right|^2 + 2 \left|\chi^{(2)}_{\mathrm{NR}}\right| \left|\chi^{(2)}_{\mathrm{R}}\right| \cos(\phi_{\mathrm{NR}} - \phi_{\mathrm{R}}(\omega_{\mathrm{IR}})) \right] I_{\mathrm{IR}} I_{\mathrm{Vis}}, \end{aligned} \tag{3.34}$$

Clearly, Eq. 3.34 exhibits a cross-term which is responsible for the interference of resonant and NR contributions [138, 142]. In some cases the NR signal can be very strong and thus overwhelms the resonant signal. Therefore it is desirable to be able to suppress the non-resonant background from the resonant signal. A recently developed background suppression technique applied in this work will be introduced in the next section in combination with the SFG spectrometer setup used because both are related.

3.9.2 Instrumentation

As mentioned in the previous section, the generation of nonlinear signals from molecules adsorbed at interfaces requires high intensity laser light sources. Therefore, picosecond (ps) and femtosecond (fs) laser setups are most often used in SFG spectroscopy [143]. Ps-based SFG systems usually have a large scanning range ($\sim$1000 cm^{-1}) but a spectral acquisition time on the order of tens of minutes. In this system, the frequency of the narrowband ps IR pulse is tuned within a certain frequency range and the VSFG signal is recorded by integrating the intensity at each frequency. In contrast, fs-based SFG systems produce a broadband fs IR pulse allowing the detection of a narrower spectral window of $\sim$100–200 cm^{-1} however with a temporal resolution usually on the order of seconds. Thus, dynamic processes on time scales from seconds to minutes can be followed in real-time and over a broad spectral range.

The fs-based IR-Vis SFG spectroscopy setup used in the present work is based on a broad-bandwidth scheme [144] in which broadband, fs IR and narrowband, ps Vis (or NIR) pulsed laser beams are mixed at the interface of interest. All optical components and lasers are mounted on optical tables (RS 2000TM, Newport-Spectra Physics, Germany) and are protected by a clean room hood (Opta, Germany) maintaining a constant temperature and humidity (typically, RH $\leq$ 40 % and T = 22 $\pm$ 1 °C). The setup is shown in Fig. 3.6 [145].

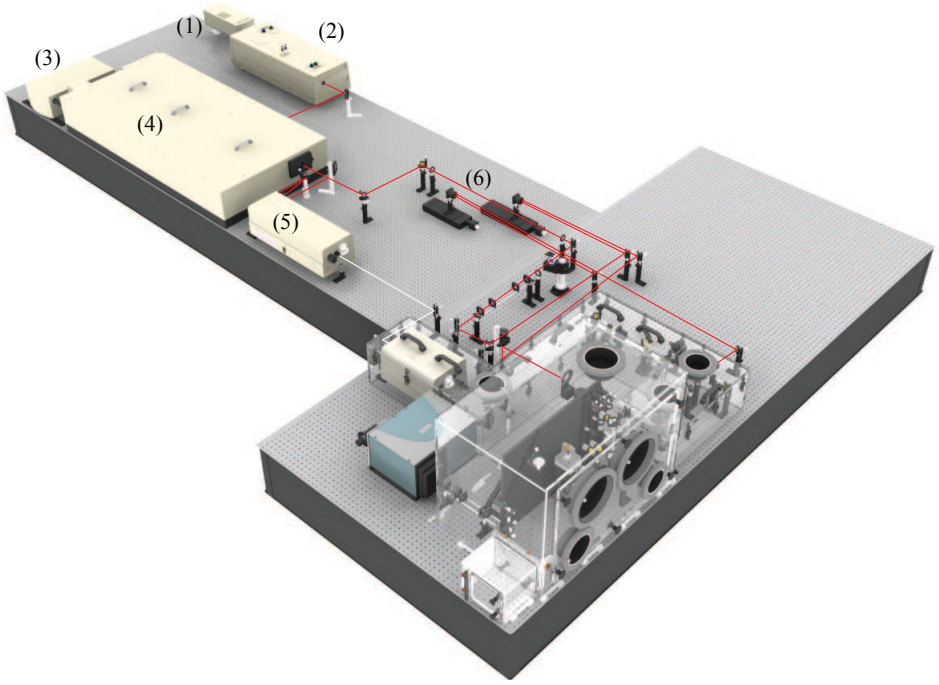

Fig. 3.6: General optical layout of the SFG spectrometer setup. Several components such as (1) the pump laser of the seed laser, (2) the seed laser, (3) the pump laser of the amplifier, (4) the regenerative amplifier, (5) the optical parametric amplifier, and (6) the delay stages are shown. The Vis (*red line*) as well as signal/idler (*white line*) beams are also represented. For clarity, the beams have been drawn until they reach the purging chamber (Source: D. Verreault).

It consists of a fs regenerative amplifier (RGA) (Spitfire Pro 35F XP, Spectra-Physics, Germany; sub-35 fs, 1 kHz) seeded by a mode-locked Ti:sapphire oscillator (Tsunami 3941-MS, Spectra-Physics; sub-30 fs, 80 MHz) with a tunable wavelength centered at 800 nm. The regenerative amplifier and seed laser are pumped by frequency-doubled Q-switched Nd:YLF (Empower 30, Spectra-Physics; 30 W, 1 kHz, 527 nm) and Nd:YVO_4 (Millenia Pro 5s, Spectra-Physics; 5 W, 532 nm) solid-state lasers, respectively. The RGA generates 90-fs duration pulses centered at 800 nm with a repetition rate of 1 kHz and an average power of 4 W. The amplified output beam is then split up and the larger fraction (∼80 %) is used to pump an automated optical parametric amplifier (OPA) (TOPAS-C, Light Conversion) coupled to a non-collinear difference-frequency generator (NDFG) (Light Conversion, Lithuania). This generates broadband (FWHM∼100–200 cm^{-1}) IR pulses which can be tuned from 2.6 to 12 μm. The signal and idler beams are spatially separated and spectrally filtered by a Ge plate (Crystec, Germany; OD = 3" (7.62 cm), $d = 5$ mm). The remaining fraction of the output beam (∼20 %) is fed into an air-spaced Fabry-Perot etalon (SLS Optics, UK; spacing $d = 12.5\,\mu$m, free spectral range FSR = 398.29 cm^{-1}, effective finesse F_{eff} = 57.48 at 790 nm) which gives narrowband (FWHM∼1 nm), time-asymmetric ps Vis pulses. After being focused in a telescope the beam is directed onto a motorized delay line, which is basically made of hollow retroreflectors, allowing for the exact adjustment of the temporal overlap of IR and Vis beam. The generated SF signal can be maximized by optimizing the temporal overlap with the help of the delay line. The maximal obtainable output energies for the IR and Vis beams were ∼20 μJ/pulse and ∼25 μJ/pulse, respectively. However, in order to prevent heat-induced damages of the sample or the

used CaF_2 prism, the IR and Vis energies were reduced to 3.5 μJ/pulse each by the use of pinholes and kept at this value over the spectral range investigated.

The sample stage is mounted to a vertically aligned breadboard restricting the beam paths to the same plane. The stage itself consists of a rolling block with manual micrometer screws coupled to a goniometer (GO90, Owis, Germany; $\pm 15°$ rotation). Thus, it can be moved in the x, y and z directions and the incident angles can be changed without changing the mirror positions. The incident Vis beam is focused onto the sample through a BK7 lens at an incident angle of 54° (relative to the surface normal) while the IR beam is focused by a curved mirror and incident on the sample at an angle of 64°. The goniometer is set to its maximum position in the positive direction increasing the incident angles of Vis and IR beam to 81° and 71°, respectively. Thus, TIR condition at the CaF_2/H_2O interface is achieved. The two beams were overlap and focused at the sample surface within a spot of ~200 μm in diameter (Fig. 3.7).

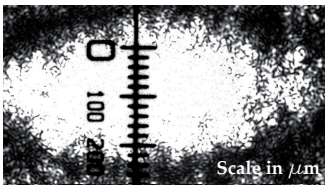

Fig. 3.7: Beam profile of the Vis beam at the sample stage. The Vis beam is incident on a small piece of paper and the image was acquired using a microscope mounted directly above the sample stage.

The generated SF signal is directed by several mirrors through a telescope to be collimated and any Vis light reflected from the sample is filtered out. After being dispersed by an imaging spectrograph (Shamrock SR-301i-B, Andor Technology) equipped with both a photomultiplier (R9110, Hamamatsu, Germany) and a water-cooled, back-illuminated high-resolution CCD camera (iDus DU420A-BR-DD, Andor Technology) the SFG beam is recorded by the latter. SFG spectra with reasonable S/N ratio on gold are typically obtained on a time scale of milliseconds to seconds. For alignment purposes, spectra can be recorded within one or two pulses, allowing real-time intensity optimization and frequency adjustment. The polarization combination (*ppp* and *ssp*) for the SFG, Vis, and IR beams is adjusted by rotation of the Vis beam through the use of half-wave plates and/or a periscope.

The NDFG stage, the whole IR beam path as well as the previously described sample stage are incorporated in a custom-built purging chamber to remove ambient water vapor and hence prevent IR beam absorption. The atmosphere in the chamber is constantly dried by two FTIR purging gas generators (75-45-12 VDC, Parker-Balston, Germany). The use of the chamber enables measurements in lower wavenumber spectral regions (e.g. in the Amide I region centered around 1650 cm^{-1}) which would be otherwise not accessible due to IR beam attenuation by water vapor absorption.

3.9.2.1 NR background suppression

As mentioned in Section 3.9.1.2 it is desirable to suppress NR contributions interfering with the resonant SFG signal. In 2007 Lagutchev *et al.* developed a NR background suppression technique using a broadband SFG spectrometer equipped with an air-spaced

Fabry-Perot etalon [146, 147]. The use of an etalon enables to produce time-asymmetric ps Vis pulses. Then by time-delaying this Vis pulse with respect to the fs IR pulse the NR background can be suppressed. In contrast, the same procedure applied with a time-symmetric picosecond pulse does not achieve a high level of discrimination between NR background and resonant contributions [146].

In order to understand this, it is useful to consider the time-dependence of the SFG polarizations $\mathbf{P}^{(2)}_{\mathrm{NR}}(t)$ and $\mathbf{P}^{(2)}_{\mathrm{R}}(t)$. As previously described $\mathbf{P}^{(2)}_{\mathrm{NR}}(t)$ is due to electronic transitions and $\mathbf{P}^{(2)}_{\mathrm{R}}(t)$ is the result of vibrational transitions. Figure 3.8 illustrates the temporal development of $\mathbf{P}^{(2)}_{\mathrm{NR}}(t)$, $\mathbf{P}^{(2)}_{\mathrm{R}}(t)$ and the ps Vis pulse in the case of zero time delay between the Vis and the IR pulse and in the case where the Vis pulse is time-delayed past the $\mathbf{P}^{(2)}_{\mathrm{NR}}(t)$.

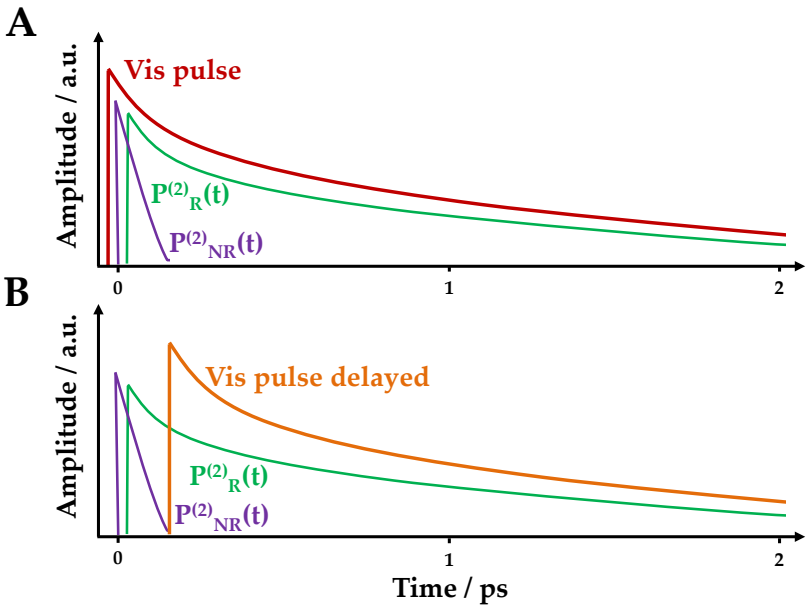

Fig. 3.8: NR background suppression by time-delaying the time-asymmetric ps Vis pulse taking advantage of the differing time-dependencies of the SFG polarizations $\mathbf{P}^{(2)}_{\mathrm{NR}}(t)$ and $\mathbf{P}^{(2)}_{\mathrm{R}}(t)$. (A) The Vis pulse interacts with $\mathbf{P}^{(2)}_{\mathrm{NR}}(t)$ and $\mathbf{P}^{(2)}_{\mathrm{R}}(t)$ creating a NR and a resonant response. (B) The Vis pulse is time-delayed past $\mathbf{P}^{(2)}_{\mathrm{NR}}(t)$ generating only a resonant signal.

Once the IR pulse has decayed it cannot up-convert the electronic transitions causing the NR contribution ($\mathbf{P}^{(2)}_{\mathrm{NR}}(t)$) anymore [141]. However, the longer-lived vibrations ($\mathbf{P}^{(2)}_{\mathrm{R}}(t)$) can still be up-converted by the ps Vis pulse when the IR pulse has already decayed. The involved SFG processes are depicted in Fig. 3.9. For example, the NR contributions from a metallic substrate are due to electronic interband transitions excited by the Vis pulse. In the case of Au, transitions between d- and s-bands are involved. The electronic transitions are up-converted by the IR pulse to the Fermi level (E_{Fermi}) of the metal and then the SFG beam is generated [141]. Simultaneously, the vibrational transitions of adsorbed molecular species causing the resonant contributions are first excited by the IR pulse, then up-converted by the Vis pulse thus finally leading to an SFG output. Since the interaction time of the fs IR pulse with the electronic transitions is much shorter than the decay time of the longer-lived vibrations, shifting the temporal overlap of IR and Vis pulse allows to

record background-suppressed VSFG spectra. Fortunately, the delaying process weakens the resonant contributions only slightly and purely resonant SFG spectra can be obtained by time delay-shifting the Vis pulse.

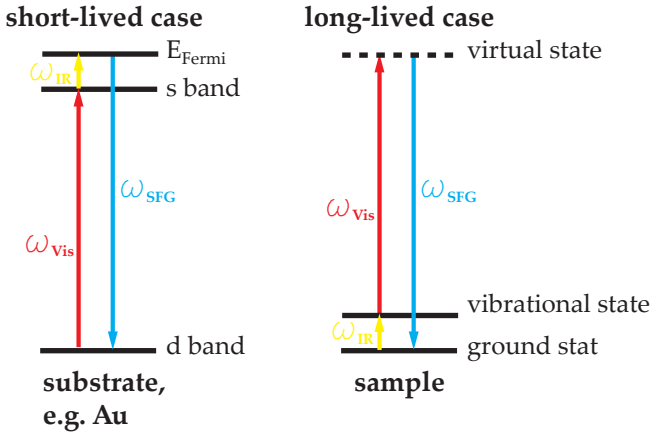

Fig. 3.9: Origin of NR contributions. The NR contributions of a metallic substrate (e.g. noble metals like Au) due to electronic interband transitions (for Au, between d- and s-bands) are excited by the Vis pulse and up-converted by the IR pulse. In contrast, the resonant contributions are due to vibrational transitions excited by the IR pulse and up-converted by the Vis pulse. The NR contributions are shorter-lived than the resonant ones.

3.9.2.2 Photocatalytic flow cell

The measuring cell for the VSFG studies of the dyes, methanol and CO_2 bound to TiO_2, hereafter called photocatalytic flow cell, was designed by D. Verreault (APC, University of Heidelberg) and fabricated in the machine shop of APC (University of Heidelberg). It allows *in situ* VSFG measurements in TIR geometry of light-induced processes in air and solution. In order to achieve this, the sample cell is made of three parts (Fig. 3.10). The bottom part consists of a reservoir which can be filled with a temperature-controlled medium from a thermostated bath by an inlet and outlet provided by commercial quick disconnect couplings (Cole-Parmer, USA) to adjust the sample temperature. The reservoir is designed such that a gold mirror at a 45° angle can be placed in the center of the cell. The mirror reflects light provided through an optical fiber to the sample surface. A round quartz window in the intermediary plate lets UV and Vis light pass. Moreover, the intermediary plate houses inlet and outlet for the solutions to be studied in contact with the sample surface. The solutions are transported by a peristaltic pump (REGLO *Digital* MS-4/8, Ismatec, Germany) through Tygon tubings (MHSL 2001, Ismatec). As a reminder the sample surface is the base plane of a CaF_2 prism. This prism is fixed in a cavity centered on the top plate by a prism adapter which can be fastened via a threaded rod and a round nut which are stabilized by an overhead bridge. The solution reservoir is formed between the intermediary and top plates through an O-ring sealing. This reservoir has a capacity of $\sim$300 μL. The quartz window and the prism are also sealed by O-rings to make the cell leakproof. All parts are made of acetal resin, with the exception of the thermostated reservoir and the overhead bridge which are made of stainless steel.

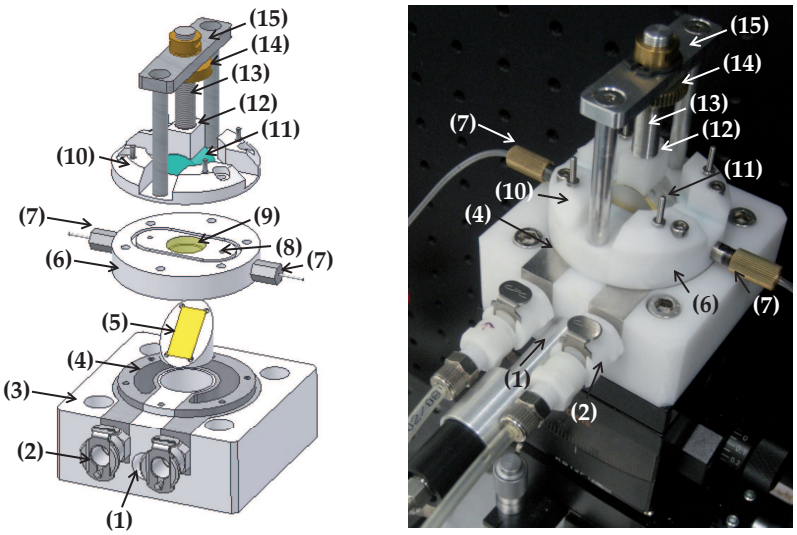

Fig. 3.10: Photocatalytic flow cell. (1) Fiber port, (2) quick disconnect couplings, (3) bottom plate, (4) thermostated reservoir, (5) gold mirror, (6) intermediary plate, (7) solution inlet/outlet, (8) solution reservoir, (9) quartz window, (10) top plate, (11) CaF_2 prism, (12) prism adapter, (13) threaded rod, (14) round nut, (15) overhead bridge.

3.9.3 Measurements

The dye spectra were recorded in the spectral regions from 3100–2800 cm^{-1} and 1900–1200 cm^{-1}. Each spectral range was subsequently scanned in 100 cm^{-1} steps. For each spectral window the sample was newly aligned by maximizing the VSFG signal originating from the Au stripe in real-time. This was achieved by optimizing spatial and temporal overlap of IR and Vis beam. After alignment the sampling spot was moved on the TiO_2 film assuming unchanged spatial and temporal overlap of IR and Vis beams and a background spectrum with only the Vis beam reaching the sample was recorded. Usually in real-time no signal was observed from the TiO_2 film. Thus, integrations times of 2 (accumulations) $\times$ 20 s or 2 $\times$ 30 s were chosen for ID1152, ID28, NA, K2NA and 2 $\times$ 5 s for ID1157, SF18. In the case of the methanol and CO_2 adsorption studies, spectra were recorded at 2 $\times$ 30 s. Background-corrected spectra were recorded using the spectrograph software (Andor SOLIS v. 4.12, Andor Technology). In order to suppress the NR background in the VSFG spectra the time delay was subsequently shifted after each spectrum acquisition by 33 fs (corresponding to 10 μm change in Vis beam path length) until all resonant features had disappeared. Doing so, sets of time-delay shifted spectra with different center frequencies were obtained. For each spectral window, the optimal NR background-suppressed spectrum of each set was selected and was used to compose a complete VSFG spectrum covering the whole spectral range of interest.

After data acquisition all spectra were processed in the graphing and data analysis software OriginPro (v. 8.6, OriginLab, USA) using customized routines. The spectra were freed from most of the cosmic spikes by a percentile filter (5 points and percentile 50), then they were smoothed applying a Savitzky-Golay filter (10 data points) and finally normalized by the integration time to give the SFG intensity in counts/s (cps). Unremoved cosmic spikes were manually masked with the Origin masking tool.

Chapter 4

Results

In this chapter the investigations of the interaction of purely organic perylene dyes possessing different anchor groups with TiO_2 nanoparticles as powder or deposited as thin film on a substrate are presented. Both linear and nonlinear optical methods are used in order to deduce the binding mode of the anchoring moiety of the dye molecules on TiO_2 as well as to learn about the organization of the dyes at the TiO_2 film surface. Prior to this, a qualitative analysis of the pure TiO_2 films by SEM and AFM is presented. Then, UV/Vis absorption, IR and Raman spectroscopic data obtained from bulk samples in air and VSFG spectroscopic results of dye-coated TiO_2 films in different environments and on different substrates are discussed. The experimental findings are correlated with the photocatalyst's efficiency which can be accessed by measuring the photocurrent of the dye/TiO_2 system. Finally, VSFG spectroscopy studies of methanol and CO_2 adsorption on TiO_2 are presented.

4.1 TiO_2 film properties

4.1.1 Surface morphology

The surface morphology can be well visualized with SEM. Figure 4.1 shows the SEM micrographs of a TiO_2 film spin-coated on a CaF_2 prism at 10 000× and at 100 000× magnification. Similar films were employed in all experiments. It can be seen that the spherical-like TiO_2 nanoparticles cover the substrate surface completely giving a highly porous film. The resulting large surface area offers many docking sites for dye molecules so that these molecules can anchor numerously and harvest immense amounts of light. Moreover, a high surface area is advantageous because it provides enough adsorption sites also for CO_2 molecules which can only be reduced during the photocatalytic cycle if adsorbed. The majority of the TiO_2 particles can be identified as single particles and their average diameter proves to be around 25 nm in good agreement with the specifications given by Evonik Industries AG. The film is rather homogeneous with some peaks in height (visible as bright spots in Fig. 4.1 B).

4.1.2 Film thickness

The film thickness is estimated from AFM and SEM images (Fig. 4.2). With the help of AFM, a height profile of an edge between the substrate where the TiO_2 film is wiped off and the TiO_2 film itself is measured in the center of the substrate (Fig. 4.2 A). The differ-

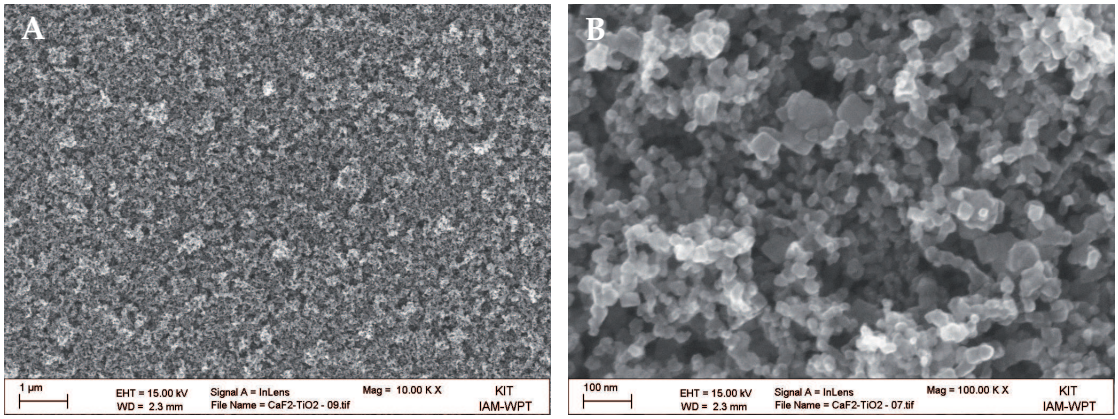

Fig. 4.1: SEM micrographs of a TiO_2 film spin-coated on a CaF_2 prism. (A) 10 000× magnification, (B) 100 000× magnification (in collaboration with U. Geckle (IAM-WPT, KIT-Campus North)).

ence in height amounts to 439 nm for the presented sample. This value falls in the average film thickness range of 300–500 nm measured for various other samples. The AFM image itself could not be obtained in very high quality since the AFM tip tends to scratch some particles off during the scan over the film resulting in a loss of resolution. Furthermore, the SEM image of the side of a TiO_2-coated CaF_2 prism is shown (Fig. 4.2 B). The dark grey and compact region of the image represents the CaF_2 prism, while the white and porous layer on top corresponds to the TiO_2 film. The film measured 1700 nm. This value is about four times higher than the one obtained by AFM because the film is measured directly at the rim of the prism and not in the center as for AFM. The thicker film at the edge is a result of TiO_2 suspension accumulation during the spin-coating process due to the prism holder rim being slightly higher than the prism. Consequently, the value of 1700 nm confirms the film thickness measured with AFM since it is reasonable to assume that the film is much thicker at the rim than in the center of the substrate.

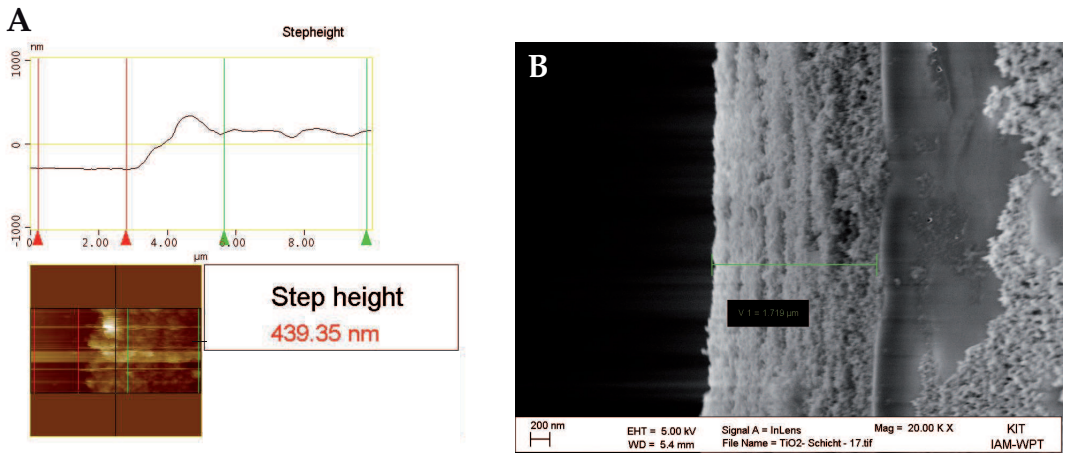

Fig. 4.2: TiO_2 film thickness determination by AFM and SEM. (A) AFM height profile of an edge between substrate and TiO_2 film (in collaboration with L. Pöttinger (APC, University of Heidelberg)). (B) SEM image of one side of a TiO_2-coated CaF_2 prism (in collaboration with U. Geckle (IAM-WPT, KIT)).

4.2 Dye-TiO_2 interaction

4.2.1 Dye selection

The main focus of the dye investigation will lie on the comparison of the spectra of the two perylene dyes ID1157 and ID1152 (Fig. 4.3) since they differ only in their anchoring moiety but are otherwise structurally completely identical. This fact allows to relate differences detected in any kind of spectra directly to the anchor group. The binding moiety of ID1157 is called a glycine anchor with the carboxylic acid functionality playing the active anchoring part. By contrast, ID1152 anchors via its anhydride group. The dye SF18 differs from the dye ID1157 by one phenyl spacer between the perylene system and the diphenylamine group. The respective spectra of these two dyes can thus be compared directly in order to confirm results obtained for the dye ID1157. The dye ID28 was chosen in order to complement the results found on the dye ID1152. Both dyes contain an anhydride group but differ in their side chains; ID1152 possesses oligo(ethylene glycol) (OEG) chains, while ID28 has 1,1,3,3-tetramethylbutyl side chains. The comparison of the spectra of these two dyes should hence help to study the influence of different side chains on the binding of the dye molecules. An advantage of the dye ID28 is that it is well documented in literature [56, 116]. The model substance NA is chosen in order to have a structurally simpler molecule containing the anhydride anchor. Beneficially, the spectral band assignment of this molecule is known. Therefore it is hoped that a spectral comparison between NA and dyes ID1152 and ID28 will assist the interpretation of the spectra of the latter two so that the binding mode of the anhydride group can be elucidated. To this end, the cleaved analogue K2NA is also investigated.

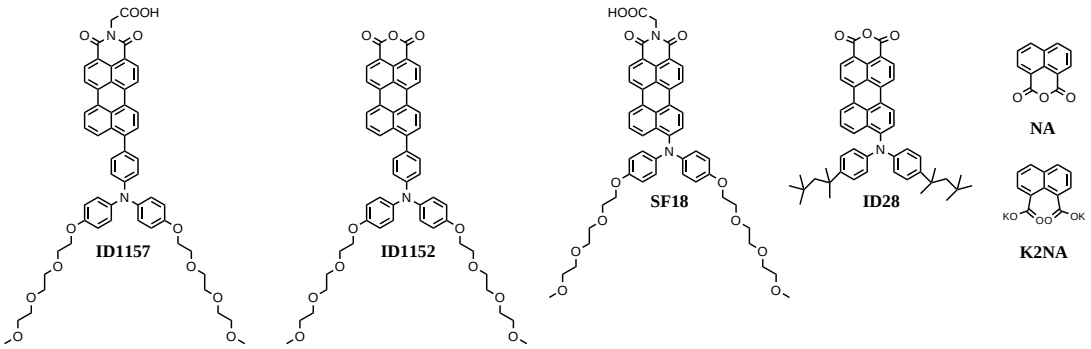

Fig. 4.3: Chemical structures of investigated dyes and model substances.

4.2.2 Photocurrent behavior of the systems ID1157/TiO_2 and ID1152/TiO_2

As stated above the dyes ID1157 and ID1152 structurally differ only in their anchoring group, with ID1157 possessing a carboxylic acid and ID1152 an anhydride group as anchoring unit. Surprisingly, this difference in anchoring group leads to very different photocurrent outputs for these two dyes. Figure 4.4 shows the time evolution of the photocurrent for ID1157 and ID1152 over three light-on/-off cycles. For the first light-on phase the photocurrent peak intensity is maximal. During the first light-off phase the dyes cannot regenerate fully so that the peak intensity for the second light-on phase amounts only to about half the value as compared to the first light-on phase. This process repeats itself for subsequent light-on/-off cycles. Since the experimental setup does not include a redox mediator, e.g. I^-/I_3^-, which gets oxidized during the irradiation cycle and fills the holes

in the dye molecules, the photocurrent decreases with time. It can be seen that the first peak intensity amounts to 7 μA for ID1157 and only to 0.5 μA for ID1152 indicating that ID1157 injects electrons more efficiently than ID1152.

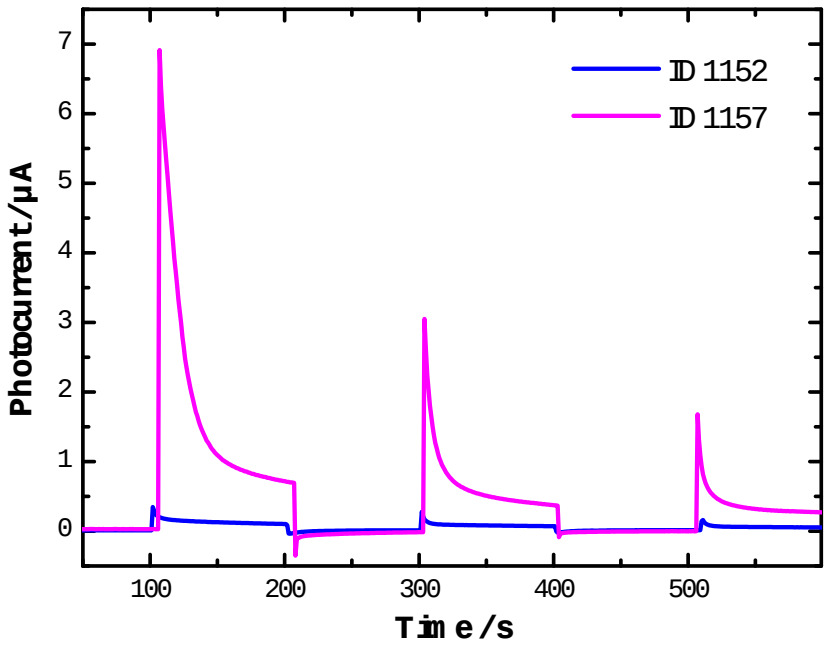

Fig. 4.4: Photocurrents of dyes ID1157 and ID1152 bound to TiO_2 films on gold (in collaboration with F. Staier (APC, University of Heidelberg)).

This poses the question whether it is possible to define a structure-function relationship between the catalyst's efficiency (photocurrent) and the type of dye binding (anchor group).

4.2.3 UV/Vis transmittance of dye-loaded TiO_2 films

Figure 4.5 depicts the UV/Vis absorption spectra of the dyes ID1152, ID28, ID1157 and SF18 free in solution and bound to TiO_2. Upon binding of ID1152 and ID28, a blue shift of the absorption maximum from 548 nm to 488 nm and 613 nm to 497 nm, respectively, is observed. This change of absorption maximum can also be followed by eye. While the dye ID28 free in solution appears blue, it changes color towards purple upon binding to TiO_2. These shifts indicate changes in the dye structures related to the binding process which most probably involves the opening of the anhydride group. A confirmation of this mechanism comes from the fact that the same blue-shift is observed in the spectra of the disodium salts of the dyes when the anhydride group is chemically cleaved with sodium carbonate [56]. With the opening of the anhydride group the effective conjugation length of the molecule shortens and thus the absorption maximum is blue-shifted (see Section 3.8.1). In contrast, no shift is observed upon binding of the dyes ID1157 and SF18 pointing to very little to no change in the bound dye structure compared to the free dye structure. The main absorption bands correspond to electronic transitions from the HOMO to the LUMO. Since the HOMO is mainly located on the diphenylamine donor and the LUMO mainly on the perylene acceptor core, excitation of this transition leads to an intramolecular CT from the donor to the acceptor enabling directed electron injection from these dyes into TiO_2 [56, 116, 148].

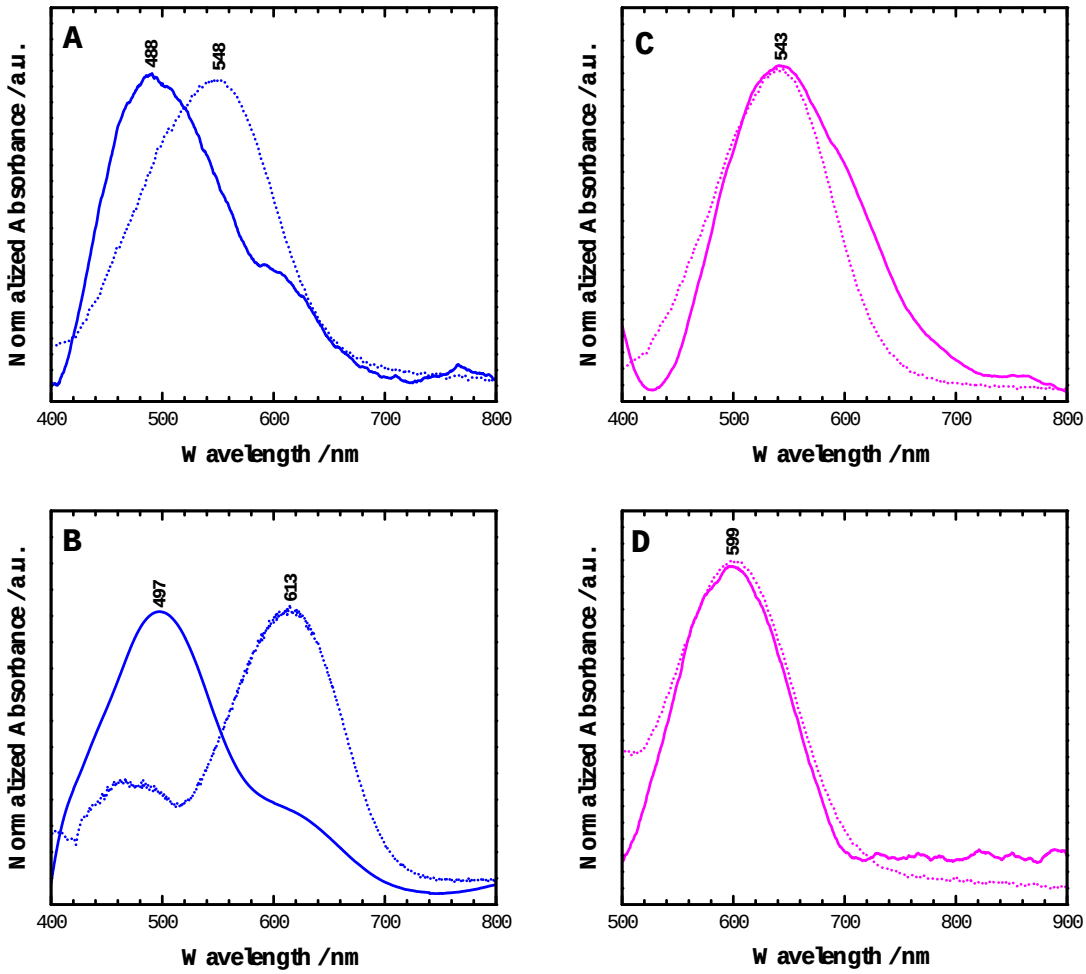

Fig. 4.5: UV/Vis spectra of dyes (A) ID1152, (B) ID28 (*blue*), (C) ID1157 and (D) SF18 (*magenta*) free in solution (*dotted curves*) and bound (*solid curves*) to TiO_2.

4.2.4 Dye binding in bulk samples

4.2.4.1 Assignment of IR bands in spectra of free dyes

In addition to UV/Vis absorption spectroscopy the dye/TiO_2 interaction is examined by IR and Raman spectroscopy in order to study the dyes' anchoring to TiO_2. A thorough interpretation of the spectra of the pure dyes is essential before analyzing the spectra of the bound dyes in order to understand the changes between the spectra of the free and the bound dye. In Fig. 4.6 the IR spectra of the four selected dyes ID1157, SF18, ID1152 and ID28 are compared. Since the Raman spectra are not composed of more bands than the IR spectra an assignment of the bands will only be carried out for the latter. The dye structures are rather complex and such are their spectra. Fortunately, the precursors of the dyes, PTCDA and PTCDI derivatives, have already been studied with vibrational spectroscopies and a band assignment of the obtained spectra with the help of simulations has been achieved [149–161]. The band assignment of the present dye spectra, which has to be regarded as tentative, is carried out on the basis of the data available on the precursor dyes in literature.

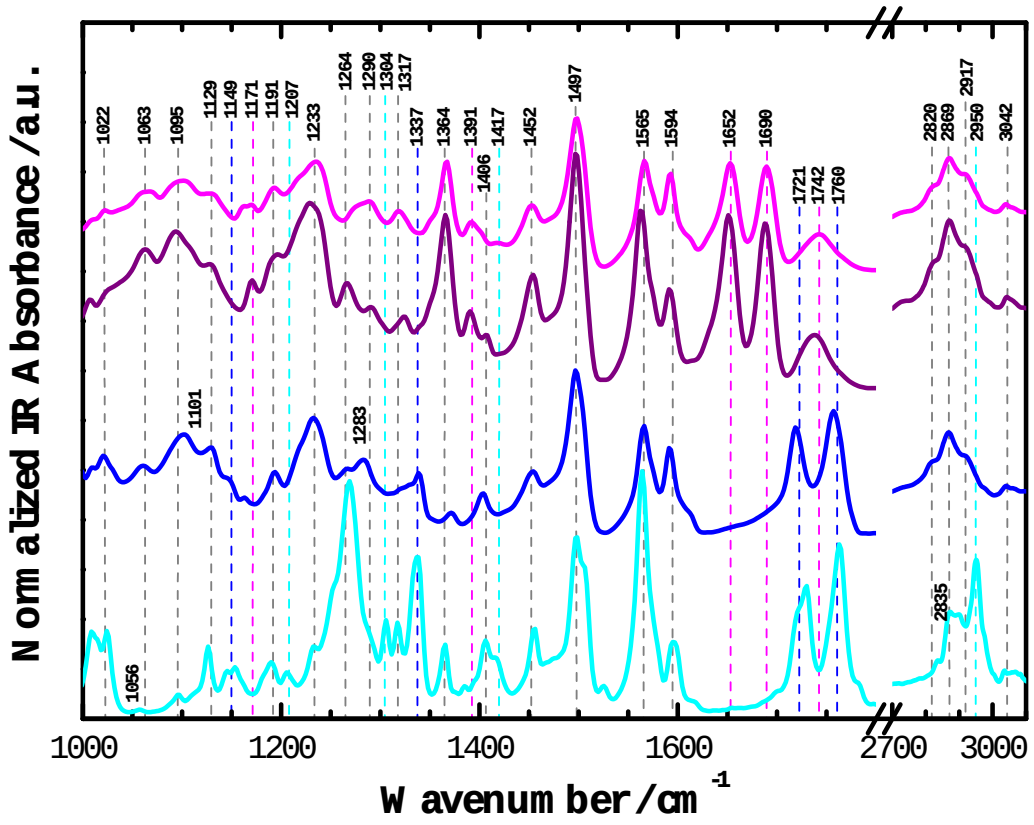

Fig. 4.6: Comparison of IR powder spectra of ID1157 (*magenta*), SF18 (*purple*), ID1152 (*blue*) and ID28 (*cyan*).

Of importance are the bands representing the anchor groups. They can be assigned with good certainty since they occur at characteristic spectral positions and are not present in the spectra of the other class of dyes. For dyes ID1157 and SF18 the ν(C=O) stretching vibrations of the carboxylic acid groups are found as broad bands at 1742 cm^{-1} and 1738 cm^{-1}, respectively. Further characteristic bands originate from the ν_s(C=O) and ν_{as}(C=O) stretching vibrations of the imide functionality at 1690 and 1652 cm^{-1} for both dyes. The ν(C−N) stretching vibrations are assigned among others to the bands at 1406 and 1364 cm^{-1} also for both dyes. In contrast, the anhydride anchoring moiety of the dyes ID1152 and ID28 is represented by pairs of ν_s(C=O) and ν_{as}(C=O) stretching vibrations at 1757 and 1718 cm^{-1} and 1762 and 1727 cm^{-1}, respectively. The assignment of the ν_s(C=O) stretching mode to a higher frequency than the ν_{as}(C=O) stretching vibration is confirmed by ab initio calculations [149]. The ν_{as}(C−O−C) stretching vibrations are found at 1022 cm^{-1} for both dyes. The ν_s(C−O−C) stretching vibrations are expected below 1000 cm^{-1}.

Bands originating from ν(C=C−C) stretching vibrations of the perylene system are found at 1592, 1565, 1497, 1452, 1406, 1391, 1364, 1337 and 1317 cm^{-1}. δ_{ip}(C=C−C−H) in plane (ip) bending vibrations of the perylene core are assigned to bands at 1290, 1191, 1171, 1149, 1129, 1095 and 1063 cm^{-1}. Although the CH stretching region of the dye spectra is not considered further in the context of the present work its assignment and that of the CH bending vibrations are given here for the sake of completeness. The ν_s(C=C−H) stretching vibrations of the aromatic rings are clearly seen at 3042 cm^{-1} for all dyes. Fur-

thermore, it can be distinguished between the $\nu(CH_3)$ and $\nu(CH_2)$ stretching vibrations of the OEG and alkyl chains. Both the $\nu_{as}(CH_3)$ and $\nu_{as}(O{-}CH_3)$ stretching vibrations are represented by the bands at 2950 for ID28 and 2953 cm^{-1} for ID1157, SF18 and ID1152, respectively. The corresponding $\nu_s(CH_3)$ and $\nu_s(O{-}CH_3)$ vibrations are found at 2872 cm^{-1} for all dyes. The deformation vibrations $\delta_{as}(CH_3)$, $\delta_{as}(O{-}CH_3)$, $\delta_s(CH_2)$ and $\delta_s(O{-}CH_2)$ lie at 1452 cm^{-1}. The $\delta_s(O{-}CH_3)$ bending vibrations are found at 1406 cm^{-1}. However, the assignment of the $\delta_s(CH_3)$ bending vibration is more complicated because of the branched structure of the alkyl chain of the dye ID28. The $\delta_s(CH_3)$ bending vibration of the trimethyl group is found as a doublet at 1406 and 1417 cm^{-1} and the $\delta_s(CH_3)$ bending vibration of the *gem*-dimethyl group as another doublet at 1304 and 1317 cm^{-1}. Last but not least the $\nu_{as}(O{-}CH_2)$, $\nu_{as}(CH_2)$, $\nu_s(CH_2)$ and $\nu_s(O{-}CH_2)$ stretching vibrations are assigned to the bands at 2917, 2900, 2835 and 2820 cm^{-1}, respectively. The $\nu(C{-}O)$ stretching vibrations within the OEG chains appear at 1233 and 1095 cm^{-1}. $\delta_{ip}(C{-}H)$ vibrations are assigned to bands at 1264 and 1207 cm^{-1}. The complete band assignment is summarized in Tab. 4.1.

4.2.4.2 Binding of the carboxylic acid group of ID1157 and SF18

The preceding band assignment of free dyes should help towards an interpretation of the spectra of the bound dyes. As already discussed in Section 2.2.1 (Fig. 2.6) the carboxy group can coordinate in different ways to the TiO_2 surface. With the aid of the IR and Raman spectra of the free and bound dyes and their comparison it is sought to assign the $\nu_{as}(CO_2^-)$ and $\nu_s(CO_2^-)$ stretching modes of the bound anchoring groups and thus determine their binding mechanism. One may notice that the IR spectra of the bound dyes look a bit distorted in the spectral region around 1640 cm^{-1}. This is because the absorption peak of water bound on TiO_2 is found at 1640 cm^{-1} [162] and the spectra are corrected for this peak by dividing them by a spectrum of pure TiO_2 after the measurement. In the case where the intensity of the water band is not the same in both spectra because adsorbed dye molecules displaced water molecules from the surface, the intensity of bands in close proximity to the water band will be influenced when the spectrum is corrected against the TiO_2 spectrum (see Section 3.8.2).

Figure 4.7 shows the IR and Raman spectra of powder samples of all dyes in their free and adsorbed states. In particular, the plots Fig. 4.7 A and B display the spectra of dyes ID1157 and SF18, respectively. The most obvious spectral difference observed between the IR spectra of the free and the adsorbed dyes can be found with the band located around 1740 cm^{-1} assigned to the $\nu(C{=}O)$ stretching vibration. This band completely disappears in the spectra of the bound dyes indicating a loss of the carbonyl functionality of the acid group and thus binding of the dyes via this group. Since no new band appears in the region between 1750–1720 cm^{-1} characteristic for ester carbonyl vibrations [151], a monodentate binding coordination of the carboxy group can already be ruled out. Consequently, it must be possible to find two bands in the spectra of the bound dyes corresponding to the $\nu_{as}(CO_2^-)$ and $\nu_s(CO_2^-)$ stretching modes of the formed carboxylate. In fact, two new bands can be identified in the IR spectra of the bound dyes at 1404 and 1422 cm^{-1} for both dyes. These two bands fall in the spectral region where $\nu_s(CO_2^-)$ stretching vibrations are expected [28–30] and are therefore both possible candidates. With the help of the Raman data it should be feasible to tell which of the two bands actually represents the $\nu_s(CO_2^-)$ vibration. Since this vibration is strongly Raman-active due to its symmetry it should appear as a new or stronger band in the Raman spectra of the bound dyes. Unfortunately, neither of the two bands can be found

Tab. 4.1: Tentative IR band assignment for dyes ID1157, SF18, ID1152 and ID28.

Band assignment	**Wavenumber** [cm^{-1}]			
	ID1157	SF18	ID1152	ID28
ν_s(C=C−H)[a, b, c, d]	3042	3042	3042	3042
ν_{as}(CH_3), ν_{as}(O−CH_3)[a, b, c, d]	2953	2953	2953	2950
ν_{as}(O−CH_2)[b, c, d]	2917	2917	2917	—
ν_{as}(CH_2)[c, d]	—	—	—	2900
ν_s(CH_3), ν_s(O−CH_3)[b, c, d]	2872	2872	2872	2872
ν_s(CH_2)[b, c, d]	—	—	—	2835
ν_s(O−CH_2)[c, d]	2820	2820	2820	—
ν_s(C=O)[a, e, f] anhydride	—	—	1757	1762
ν(C=O)[c, d] acid	1742	1738	—	—
ν_{as}(C=O)[a, e, f] anhydride	—	—	1718	1727
ν_s(C=O)[a, b, e, g, h, i] imide	1690	1690	—	—
ν_{as}(C=O)[a, b, e] imide	1652	1652	—	—
ν(C=C−C)[a, b, e, f, g, h, i, j] perylene	1592	1592	1592	1592
ν(C=C−C)[a, b, g, h, i, j, k] perylene	1565	1565	1565	1565
ν(C=C−C)[a, b, f] perylene	1497	1497	1497	1497
ν(C=C−C)[e, g, h, i, j] perylene and δ_{as}(CH_3), δ_{as}(O−CH_3), δ_s(CH_2), δ_s(O−CH_2)[a, b, e]	1452	1452	1452	1452
δ_s(CH_3)[d] trimethyl	—	—	—	1417
ν(C=C−C)[a, e, f, i] perylene and δ_s(CH_3)[d] trimethyl, δ_s(O−CH_3)[e] and ν(C−N)[e]	(1406)	1406	1402	1406
ν(C=C−C)[a, h, i] perylene	1391	1391	—	—
ν(C=C−C)[e, g, h, j] perylene and ν(C−N)[a, e, i]	1364	1364	1372	1364
ν(C=C−C)[b, h] perylene	—	—	1337	1337
ν(C=C−C)[g] perylene and δ_s(CH_3)[c, d] *gem*-dimethyl	1317	1324	(1317)	1317
δ_s(CH_3)[c, d] *gem*-dimethyl	—	—	—	1304
δ_{ip}(C=C−C−H)[e, f, h, k]	1290	1290	1283	—
δ_{ip}(C−H)[a, i]	—	1264	(1264)	1264
ν(C−O) ? OEG and δ_{ip}(C−H)[a, b, i]	1233	1233	1233	(1233)
δ_{ip}(C−H)[d] ?	—	—	—	1207
δ_{ip}(C=C−C−H)[a]	1191	1191	1191	1191
δ_{ip}(C=C−C−H)[a, i]	1171	1171	—	—
δ_{ip}(C=C−C−H)[f]	—	—	1149	1149
δ_{ip}(C=C−C−H)[a, f, i]	1129	1129	1129	1129
δ_{ip}(C=C−C−H)[g, h, i] and ν(C−O−C)[l] OEG	1095	1095	1101	(1095)
δ_{ip}(C=C−C−H)[h, i, j]	1063	1063	1063	(1056)
ν_{as}(C−O−C)[e, f] anhydride	(1022)	(1022)	1022	1022

Legend: ν, stretching; δ, bending; s, symmetric; as, asymmetric; ip, in plane; values in parenthesis indicate very weak bands.
Literature assignment: [a], Ref. [149], [b], Ref. [150], [c], Ref. [151], [d], Ref. [152], [e], Ref. [153], [f], Ref. [154], [g], Ref. [155], [h], Ref. [156], [i], Ref. [157], [j], Ref. [158], [k], Ref. [159], [l], Ref. [160].

as such. But it might also be that a new band is hidden under the already present band at 1404 cm^{-1}. In this case the contribution of this new band to the Raman spectra of the bound dyes is just too subtle to be distinguished. In contrast, Voelker could detect a new Raman band at 1404 cm^{-1} in the spectrum of the bound dye called ID176 [148] featuring a glycine anchor and an aromatic body like the dye ID28 [163]. This discrepancy might be due to the different excitation wavelengths used in both experiments, namely 1064 nm

vs 473 nm. Nevertheless, with this Raman spectrum it is now possible to assign the band at 1404 cm^{-1} to the $\nu_s(CO_2^-)$ stretching vibration.

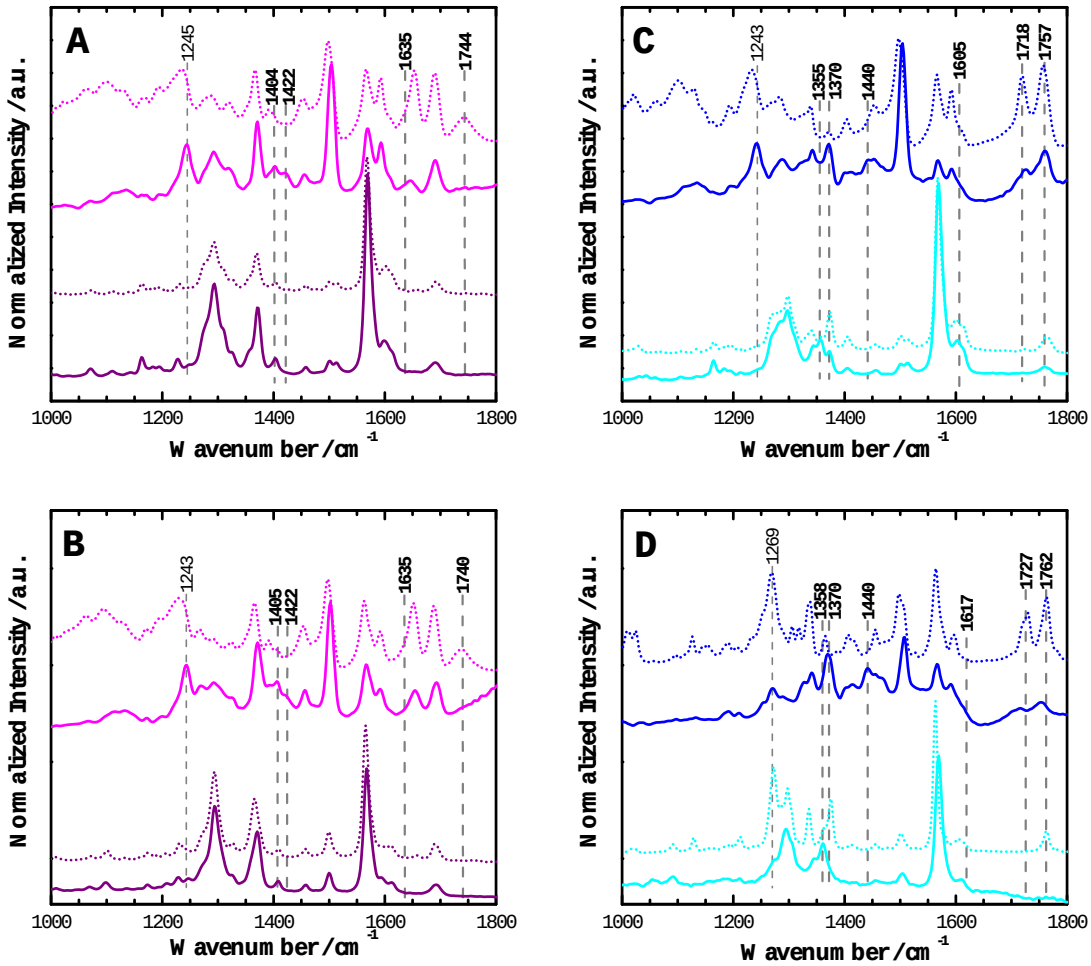

Fig. 4.7: IR and Raman spectra of dyes (A) ID1157, (B) SF18 (*magenta/ purple*) (the rise of the baseline in the IR spectrum of the bound dye towards higher wavenumbers is a result of data pre-processing (see Section 3.8.2)), (C) ID1152 and (D) ID28 (*blue/ cyan*), free (*dotted curves*) and bound (*solid curves*) to TiO_2. The IR and Raman spectra are given by the pairs of upper and lower curves, respectively.

The assignment of the $\nu_{as}(CO_2^-)$ stretching vibration is even more difficult. There should be a new or intensified band in the characteristic region of this vibration between 1610–1550 cm^{-1} [151]. But no such band can be identified. Nonetheless, Voelker managed to detect a small band variation in the IR spectrum of the bound dye ID176 at 1635 cm^{-1} [163] which was assigned to the $\nu_{as}(CO_2^-)$ stretching vibration. On the basis of Voelker's result it is assumed that the bound dyes ID1157 and SF18 also exhibit a $\nu_{as}(CO_2^-)$ stretching vibration which leads to a band at 1635 cm^{-1}. A possible reason for the different results are most certainly the different detection methods used. The present spectra were recorded from powder samples in ATR-FTIR reflection mode, whereas the spectrum of the bound dye ID176 was taken in normal FT-IR transmission mode through a TiO_2 film coated on a transparent Si wafer. In addition, the measurement was performed under vacuum so that the influence of atmospheric water bands which occur in the region from

1800–1400 cm^{-1} could be excluded [125]. Since the spectra of ID1157 and SF18 were recorded under ambient conditions and afterwards corrected for atmospheric bands it is likely that the weak new band at 1635 cm^{-1} got deleted. The decrease of the band at 1652 cm^{-1} in the IR spectrum of bound ID1157 is also ascribed to this data processing step since the absorption peak of bound water on TiO_2 is found at 1640 cm^{-1} [162]. Thus, the intensity of bands in close proximity to this water band can be influenced when the spectrum is corrected against the TiO_2 spectrum (see Section 3.8.2).

The two binding possibilities for the carboxylate, considering that the ester-type binding is excluded, are the bidentate chelating or bidentate bridging coordination. It is yet not easy to differentiate between the two coordinations. A common approach is to calculate the wavenumber difference $\Delta\nu$ of the $\nu_{as}(CO_2^-)$ and $\nu_s(CO_2^-)$ bands for the free (e.g. the sodium salt of the compound) carboxylate and the adsorbed one and to compare the two (see Section 2.2.1). The salts of the dyes ID1157 and SF18 are not available and therefore it is not possible to compare the calculated $\Delta\nu_{ads}$ = 231 cm^{-1} to the $\Delta\nu$ value of the free acid. From calculations however it is known that the bidentate bridging coordination is the more stable binding type of the two [164, 165]. Hence, it can be assumed that the dyes with the carboxy anchor most likely bind via a bidentate bridging coordination of the formed carboxylate, a conclusion also reached by Voelker for the dye ID176 [163]. The binding of the carboxylic acid group is accompanied by other structural changes occurring in the dye molecule upon binding. This is indicated by band shifts (e.g. around 1245 cm^{-1}) in the spectra of the bound dyes and also by relative intensity changes. Some groups arrange differently in the bound dye than in the free dye so that they come to reside in different chemical environments.

4.2.4.3 Binding of the anhydride group of ID1152 and ID28

The binding of an anhydride group as anchoring moiety as part of a complex molecule is not as commonly studied as the binding of the carboxylic acid group. This is due to the fact that most dye molecules employed in DSSCs are anchored with a carboxylic acid. Nevertheless, the anhydride group interaction with TiO_2 surfaces was analyzed for small molecules [93–96]. The attachment of dyes with anhydride anchor involves the opening of the anhydride group by a surface bound hydroxyl group, which then leads to the formation of carboxylate and carboxylic acid groups [91, 92]. Similar to dyes with a single carboxylic acid anchoring group, the binding of the formed carboxylate and acid groups can be analyzed spectroscopically. However, a difficulty in the analysis of this type of anchoring comes from the fact that it has to be found out whether one or both of the newly formed groups bind and if so whether they bind in the same way.

The opening of the anhydride group in the molecules of the dyes ID1152 and ID28 is already proven by UV/Vis spectroscopy (see Section 4.2.3). The binding mode itself is investigated by IR and Raman spectroscopy just as it was for the dyes ID1157 and SF18. The respective IR and Raman spectra of the free and bound dyes ID1152 and ID28 are overlayed in Fig. 4.7 C and D. It is seen that the intensity of the band pairs at 1757 and 1718 cm^{-1}, and at 1762 and 1727 cm^{-1} associated with the anhydride group decreases in the IR spectra of the bound dyes. This is in contrast to the band of the carboxylic acid group which completely disappears upon binding of the dye. This fact indicates that there are also unopened dye molecules adsorbed to TiO_2 in addition to the opened ones. The question arises whether they are in contact with the surface or simply attached through multilayer formation. At this point it has to be mentioned that Voelker

did not observe remaining intensity of the anhydride group bands in the IR spectra of bound ID28 [163]. This fact indicates that in her samples the anhydride groups of all adsorbed dye molecules were open. Most probably, the same dye molecules behave differently in different laboratories because they were bound to dissimilar TiO_2 substrates. Whereas in the present study the dye was bound to TiO_2 (P25) nanoparticles, the dye in Voelker's study was bound to a standard anatase nanoparticulate paste for the fabrication of DSSCs, Dyesol-18-NRT. Dyesol most probably possesses more hydroxyl groups on its surface than TiO_2 (P25), and thus provides more units for the opening of the anhydride groups. Further discussion on that will follow in the VSFG section.

In the same manner as for the dyes with the carboxylic acid group, the $\nu_{as}(CO_2^-)$ and $\nu_s(CO_2^-)$ stretching modes of the the adsorbed carboxylates of the molecules with the opened anhydride group have to be identified in the spectra of the bound dyes. The formation of carboxylates is very probable because no new band appears in the region between 1750–1720 cm^{-1} characteristic for ester carbonyl vibrations [151] and therefore a monodentate coordination can be ruled out for the opened anhydride groups as well. The IR spectra exhibit for both dyes a new band at 1440 cm^{-1} and a band with significant stronger intensity at 1370 cm^{-1}. Again it has to be ascertained which of these two bands stands for the $\nu_s(CO_2^-)$ vibration. In this case a look at the Raman spectra is helpful. The Raman spectra of both dyes bound clearly show a new band at 1355 cm^{-1}. This demonstrates that neither the band at 1440 cm^{-1} nor the one at 1370 cm^{-1} is associated with the $\nu_s(CO_2^-)$ vibration. The intensity of the latter band increases because of an underlying new band, the band at 1355 cm^{-1}. Consequently, this band is assigned to the $\nu_s(CO_2^-)$ stretching vibration.

The assignment of the $\nu_{as}(CO_2^-)$ stretching vibration is equally difficult as for the carboxylic acid group. The only possible assignment seems to be the high energy tail of the band at 1592 cm^{-1}. This results in a $\nu_{as}(CO_2^-)$ stretching vibration band at 1605 cm^{-1} for the dye ID1152 and at 1617 cm^{-1} for the dye ID28, similar to the position observed by Voelker with the dye ID28 [163]. [1] Since only one pair of $\nu_{as}(CO_2^-)$ and $\nu_s(CO_2^-)$ stretching vibrations is found for both dyes, it is assumed that both the carboxylate and the carboxylic acid group of the opened anhydride group bind in the same way.

For ID1152 and ID28, the calculated wavenumber difference amounts to $\Delta\nu_{ads} = 250\ cm^{-1}$ and $\Delta\nu_{ads} = 262\ cm^{-1}$, respectively. Also here the salts of the dyes ID1152 and ID28 are not available and it can only be assumed that both the carboxylate and the carboxylic acid group of the opened anhydride group bind via a bidentate bridging coordination. Consistently to the dyes ID1157 and SF18 the binding of ID1152 and ID28 goes along with further structural changes as indicated by band shifts and intensity changes in the IR spectra of the bound dyes.

4.2.4.4 *In situ* adsorption studies of ID1157 and ID1152

In order to remove all doubts and to demonstrate that the residual anhydride group intensity in the ATR-IR spectra of bound ID1152 and ID28 is not an experimental artifact but rather due to the substrate, Fig. 4.8 shows the IR spectra of the *in situ* adsorbed dyes ID1152 and ID1157 to a thin film of TiO_2 (P25) nanoparticles on a Ge substrate. After *in*

1. It is interesting to note that the $\nu_{as}(CO_2^-)$ stretching vibrations appear at different positions for the single carboxylic acid group and the groups of the opened anhydride group. Possibly different dye arrangemets at the TiO_2 surface are preferred.

situ adsorption the films were rinsed *in situ* for 30 min with solvent. These as-prepared samples exhibit the same residual anhydride group bands as the powder samples. The band representing the carboxylic acid group of the dye ID1157 disappears as it does for the powder samples. In conclusion, differently prepared and measured samples on the same substrate give the same spectra. The spectra were kindly provided by L. Pöttinger (APC, University of Heidelberg).

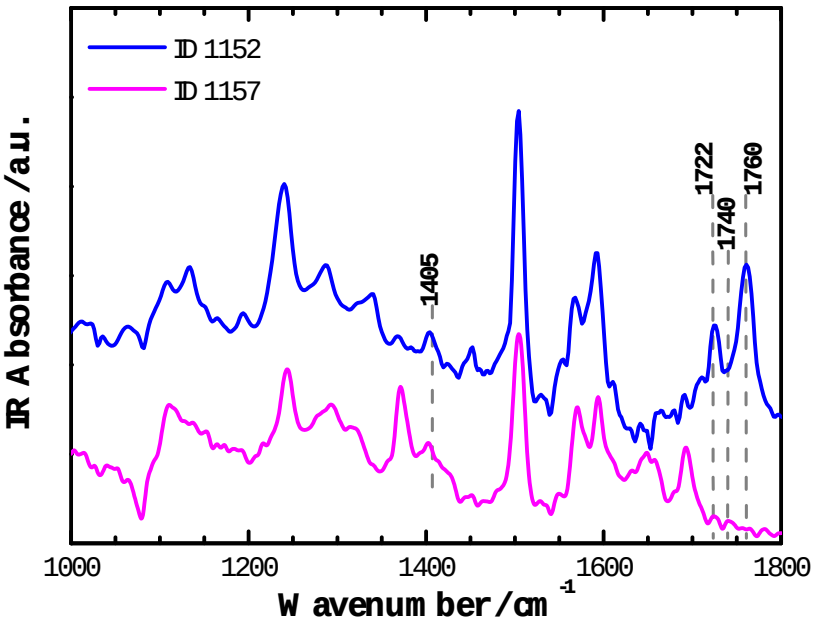

Fig. 4.8: Comparison of ATR-IR spectra of bound ID1157 (*magenta*) and ID1152 (*blue*).

4.2.4.5 Binding of model dye NA

With the aid of the model dye NA it is sought to shed more light on the binding type of the anhydride group as part of an aromatic molecule. The idea is to investigate a structurally simpler molecule of which the vibrational spectra are well-known so that the bands of the $\nu_{as}(CO_2^-)$ and $\nu_s(CO_2^-)$ stretching vibrations in the spectra of bound NA can be identified and assigned with high certainty. In turn it should be possible to check the assignment for the dyes ID1152 and ID28 and if necessary to correct it. Another advantage of the NA molecule is that it is commercially available in good quantities. This fact allows for the chemical cleavage of some part of it into the potassium salt (K2NA). The salt is needed for a comparison of the spectra of free and bound NA so that it can finally be determined whether the formed carboxylates bind via bidentate chelating or bridging coordination. A model substance was exclusively chosen only for the anhydride anchoring group because the binding of the latter is far less studied and understood than the binding of the carboxylic acid group. In addition, the results of the binding study of NA should be transferrable to the binding of the carboxylic acid group because after opening of the anhydride group a carboxylic acid group and a carboxylate are formed.

The IR spectra of both NA and K2NA free and bound are displayed in Fig. 4.9. The spectrum of free NA possesses a rather complicated band pattern due to the vibrations of the aromatic naphthalene ring. This pattern changes drastically upon binding of 1) NA to TiO_2, 2) cleaving of the anhydride group, and 3) binding of K2NA, albeit in the same

way for all three processes. The strong similarity of the spectra of free and bound K2NA with the spectrum of bound NA demonstrates first that the anhydride group opens upon binding and second that the structural configuration of bound K2NA and thus bound NA is comparable to the configuration of free K2NA.

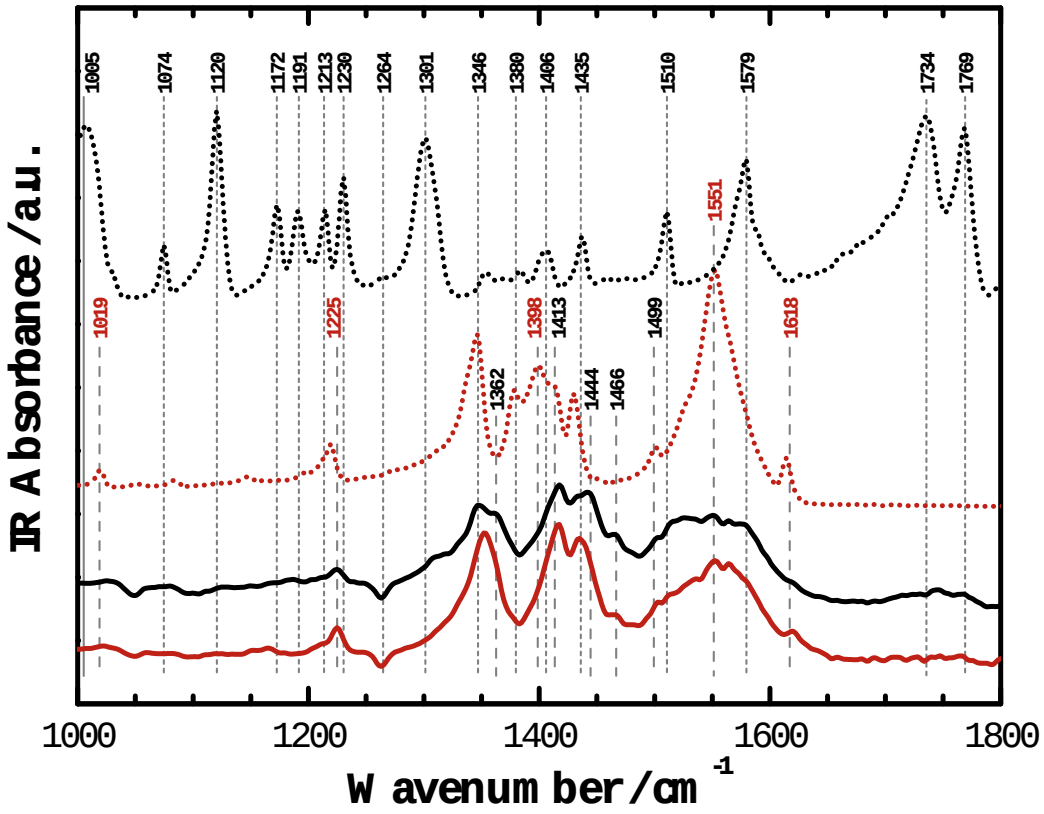

Fig. 4.9: Comparison of IR spectra of NA (*black*) and K2NA (*red*), free (*dotted curves*) and bound (*solid curves*) to TiO_2.

The band assignment of NA and the dicarboxylic acid of NA can be found in the literature [149, 166–168]. With the help of this data the assignment of the bands in the spectra at hand is achieved (Tab. 4.2). Especially the comparison of the spectra of K2NA and the corresponding dicarboxylic acid (literature data, Ref. [166]) leads to a valid assignment of the bands associated with the $\nu_{as}(CO_2^-)$ and $\nu_s(CO_2^-)$ stretching vibrations in the spectrum of the bound NA molecule. The characteristic anhydride group bands of the ν_s(C=O) and ν_{as}(C=O) stretching vibrations in the spectrum of NA are found at 1769 and 1734 cm^{-1}, respectively. Upon binding of NA the intensity of these bands decreases to a very small contribution. This is consistent with the behavior of the dye molecules ID1152 and ID28. The spectra of free and bound K2NA do not show any anhydride group contribution demonstrating the successful chemical cleavage of this functional group. The pair of ν_{as}(C−O−C) and ν_s(C−O−C) stretching vibrations is found at 1172 and 1120 cm^{-1}. The other bands in the region between 1630–1000 cm^{-1} are assigned to ν(C=C−C), δ(C=C−C), ω(C=C−C−H), and δ_{ip}(C=C−C−H) vibrations of the naphthalene ring system. Almost the same aromatic ring vibrations are found in the spectra of free and bound K2NA and bound NA although with different relative intensities and band widths. In addition, two intense and broad bands appear in the spectra of these compounds at 1551 and around 1350 cm^{-1}. These two bands are not observed as such

in the spectrum of free NA and are thus good candidates for the $\nu_{as}(CO_2^-)$ and $\nu_s(CO_2^-)$ stretching vibrations of the newly formed carboxylates. Especially, since all other bands in the spectra can be associated with ring vibration modes. The band at 1551 cm^{-1} is assigned to the $\nu_{as}(CO_2^-)$ stretch because it is a new band that is not found in the spectrum of NA and is also not listed as a band in the spectrum of the dicarboxylic acid [166].

Tab. 4.2: IR band assignment for NA, NA@TiO_2, K2NA and K2NA@TiO_2 according to Ref. [166] and references therein.

Band assignment	**Wavenumber** [cm^{-1}]			
	NA	NA@TiO_2	K2NA	K2NA@TiO_2
ν_s(C=C−H)	3070	—	3063	3063
ν_s(C=O) anhydride	1769	1769	—	—
ν_{as}(C=O) anhydride	1734	1744	—	—
ν(C=C−C)	(1628)	(1623)	1618	1618
ν(C=C−C)	1579	1579	—	(1579)
$\nu_{as}(CO_2^-)$	—	**1551**	**1551**	**1551**
ν(C=C−C)	1510	1499	1499	1499
ν(C=C−C)	—	1466	—	1466
δ(C=C−C)	1435	1435/1444	1429	1435
ω(C=C−C−H)	1406	1416	1413	1413
???	—	—	1398	—
δ_{ip}(C=C−C−H)	1383	—	1380	—
ν(C=C−C)	—	1362	—	—
ν(C=C−C), **$\nu_s(CO_2^-)$**	1354	**1346**	**1346**	**1351**
ω(C=C−C−H)	1301	—	—	1308
δ_{ip}(C=C−C−H)	1264	—	1270	—
δ_{ip}(C=C−C−H)	1230	1225	—	1225
δ_{ip}(C=C−C−H)	1213	—	1218	—
ω(C=C−C−H)	1191	—	1199	—
ν(C−O) anhydride	1172	—	—	—
ν(C−O) carboxylate	—	—	1146	—
ν(C−O) anhydride	1120	—	—	—
ν(C−O) carboxylate	—	—	1082	—
δ(C=C−C)	1074	—	—	—
δ(C=C−C)	1005	—	1019	—

Legend: ν, stretching; δ, bending; ω, wagging; s, symmetric; as, asymmetric; ip, in plane.

Concerning the band around 1350 cm^{-1} it is seen that there is already a band at this position in the spectrum of NA but with very low intensity. The strong increase of this band in the spectra of K2NA, bound K2NA and bound NA indicates the contribution of a new vibration to this band like it was observed for the dyes ID1152 and ID28. All doubts about the assignment of this band to the $\nu_s(CO_2^-)$ stretching vibration are removed by analyzing the Raman spectra of free and bound NA and K2NA. In Fig. 4.10 A the IR and Raman spectra of free and bound NA are compared and in Fig. 4.10 B the respective spectra of K2NA are shown. The strong bands at 1768, 1744 cm^{-1} and 1579 cm^{-1} in the Raman spectrum of NA are due to the anhydride group vibrations and a ν(C=C−C) ring vibration, respectively. The Raman spectrum of bound NA could only be obtained in low quality and the signal intensity is very weak. Nevertheless, the absence of the bands representing the vibrations of the anhydride group is not due to the low quality

of the spectrum but indicates the opening of the anhydride group. The band observed at 1579 cm^{-1} is observable because it is already strong in the spectrum of free NA. The same argumentation however cannot hold true for the other band observed at 1351 cm^{-1} since the intensity of this band is low in the spectrum of free NA. The only explanation for the existence of this band is the appearance of a new vibration in the bound NA molecule, namely the $\nu_s(CO_2^-)$ stretching vibrations of the carboxylates. The same picture is found for the Raman spectra of free and bound K2NA (Fig. 4.10 B). A very strong band in the spectrum of free K2NA is observed at 1354 cm^{-1} which is also present in the spectrum of bound K2NA. Since there is no such similarly intense band found in the spectrum of free NA it becomes certain that the band around 1350 cm^{-1} is due to the $\nu_s(CO_2^-)$ stretching vibration both in the Raman and the IR spectra.

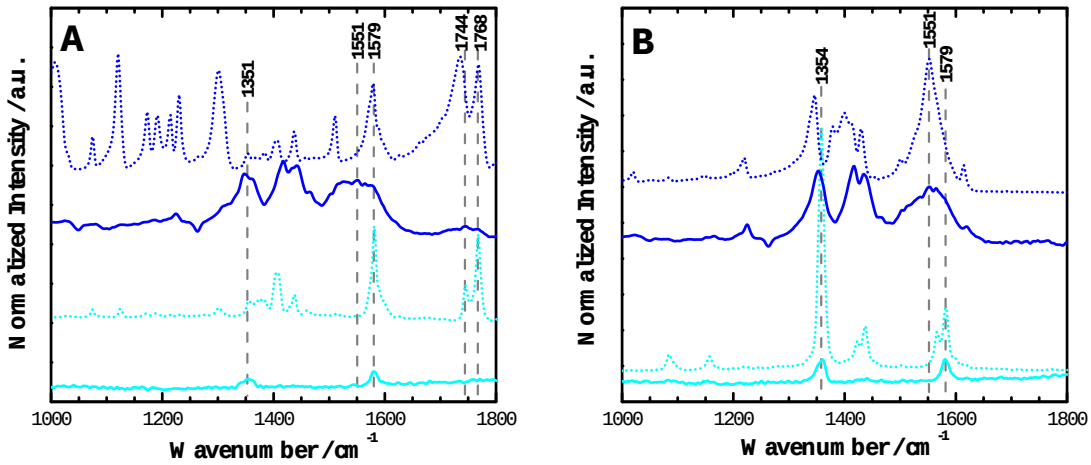

Fig. 4.10: IR and Raman spectra of (A) NA and (B) K2NA (*blue/ cyan*), free (*dotted curves*) and bound (*solid curves*) to TiO_2. The IR and Raman spectra are given by the pairs of upper and lower curves, respectively.

This finding confirms the assignment of the band at 1355 cm^{-1} in the spectra of the bound dyes ID1152 and ID28 to the $\nu_s(CO_2^-)$ stretching vibration. In contrast, the assignment of the band at 1605 cm^{-1} and 1617 cm^{-1}, respectively, to the $\nu_{as}(CO_2^-)$ stretching vibration cannot be confirmed. Since the assignment was without proof and only conducted because the presence of a $\nu_s(CO_2^-)$ stretching vibration calls for the presence of a $\nu_{as}(CO_2^-)$ stretching vibration, the assignment itself should be thought over. It can also be that there is a band at around 1551 cm^{-1} in the IR spectra of the bound dyes ID1152 and ID28 which is simply hidden by the strong ν(C=C−C) vibrations of the perylene ring. Further investigations on the binding of NA will follow in the VSFG section. An open question still remains as to whether the formed carboxylates bind in a bidentate chelating or bridging coordination. In order to answer this question, the calculated IR wavenumber difference $\Delta\nu_{ads}$ = 205 cm^{-1} of NA is compared to that calculated for free K2NA, i.e., $\Delta\nu_{salt}$ = 205 cm^{-1}. Because $\Delta\nu_{ads} = \Delta\nu_{salt}$ bridging coordination is most likely.

4.2.5 Dye binding at the TiO_2 surface

With IR and Raman spectroscopy it was already possible to deduce detailed information on the coordination type of both the carboxylic acid and anhydride anchors. However, these techniques cannot differentiate between contributions from the dye/TiO_2 interface

and contributions from the bulk of the sample. In order to obtain further knowledge on the binding mechanism, especially at the interface, as well as to get an idea about the orientation of the dye molecules on the TiO_2 nanoparticles VSFG spectroscopy is employed. This technique is intrinsically surface selective and allows for the detection of buried interfaces *in situ* [169] as well as the determination of molecular organization, conformation and orientation [170]. The following section describes in detail how the VSFG spectra are obtained from the dye-coated TiO_2 films and what can be learned about the dye binding at the interface.

4.2.5.1 VSFG survey spectrum using the example of ID1157 bound to TiO_2

One advantage of broadband VSFG spectroscopy is the recordability of spectra in a short time (s to ms). However, the spectral width (200–150 cm^{-1}) is not broad enough to encompass the entire dye spectrum from 3100–1200 cm^{-1}. This is only achieved by scanning over the whole spectral range in 100 cm^{-1} steps and combining all spectra into one single spectrum (see Section 3.9.3). Figure 4.11 shows VSFG spectra of the dye ID1157 bound to TiO_2 in air for a selection of three different center frequencies, namely at 1380, 1480, and 1680 cm^{-1}. The dye ID1157 is chosen here as a representative of the other dyes because it gives clear VSFG spectra with strong signal intensity. The spectra are taken with increasing time delay between the Vis pulse and the IR pulse giving a set of Vis beam time delay-shifted spectra per center frequency. The procedure of delay-shifting was implemented because a strong NR contribution to the VSFG spectra is observed, which distorts peak positions and complicates the determination of the number of peaks present [142, 170–174]. The identifiable part of the NR contribution is labeled with a black arrow in the sets of delay-shifted spectra. Upon delay-shifting the suppression of the NR background can be followed as a red-shifting band for wavenumbers below 1900 cm^{-1} and as a blue-shifting band in the CH stretch region. The NR background is completely suppressed when a straight baseline with the resonant peak contributions is obtained. The delay-shifting is continued in the ideal case until a flat line is obtained to ensure that the peaks are due to vibrations from the sample with a certain lifetime and not to permanent external light sources or stray light from the sample.

A *real* vibrational peak is characterized by a longer lifetime than that of the NR contribution (from the time delay-shifted spectra it is observed that the NR background vanishes on average in about one third to half of the time compared to a vibration) and a more or less fixed position. Peaks are bound to shift slightly around their spectral position like the peaks e.g. at 1290 or 1490 cm^{-1} in the different sets of delay-shifted spectra because of the chirp of the Vis laser pulse. This chirp is caused in the amplifier and means that the Vis pulse exhibits a changing instantaneous frequency. As a consequence, at different time delays slightly different Vis pulse frequencies overlap with the constant IR pulse frequency. For this reason the position of the peaks in the spectra changes slightly during a time delay-shifting series [171, 175]. The peak around 1692 cm^{-1} seems to shift from a slightly lower spectral position to its final position at 1692 cm^{-1}. This effect is attributed to a phase-relation change between the resonant and NR contributions during the delay-shifting process.

The observed amplitude or intensity of a peak is dependent on the center frequency of the probing IR pulse and the sample itself. The center frequency of the IR pulse plays a role in the observed peak intensity because of its Gaussian-like profile. At the low intensity flank of the IR profile less molecular groups are excited to vibrate than at the maximum

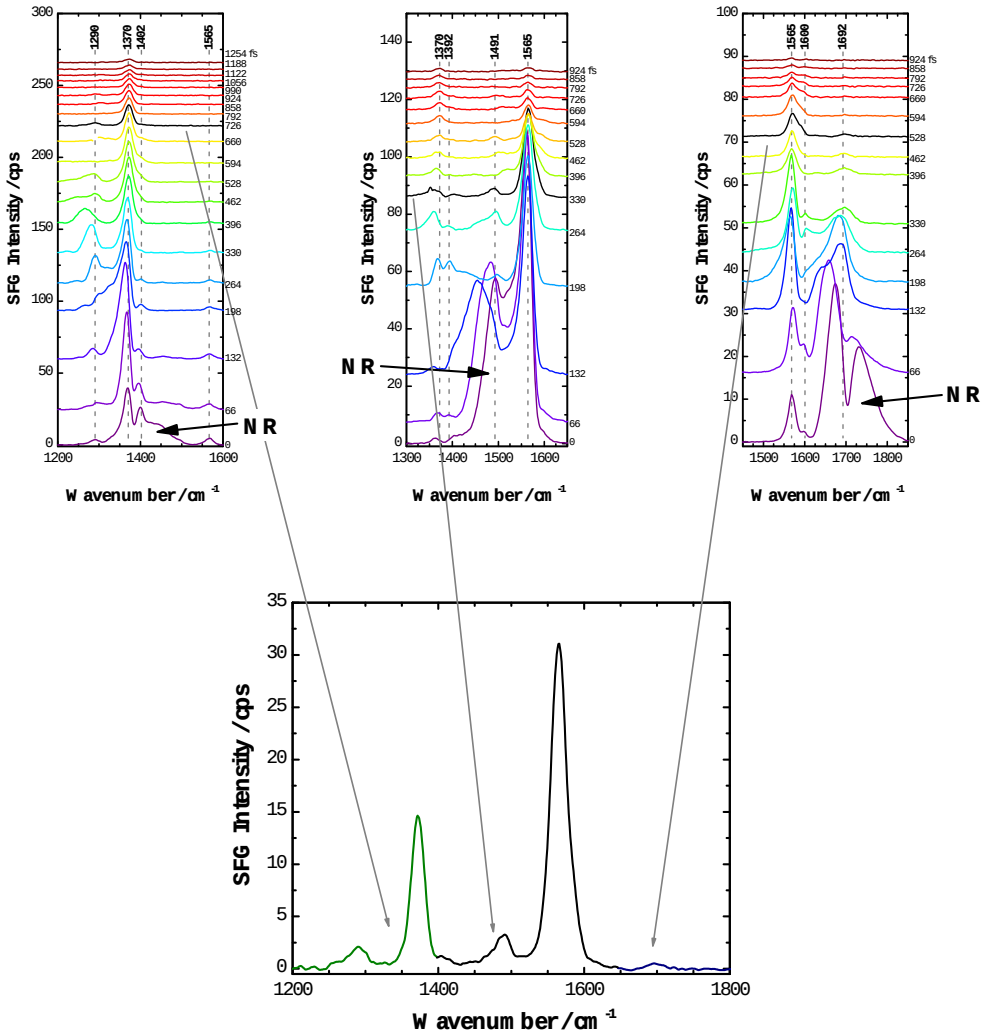

Fig. 4.11: Creation of resonant VSFG survey spectrum using the example of ID1157. Top panel: Sets of Vis beam time delay-shifted spectra of ID1157 bound to TiO_2 centered at 1380 cm^{-1}, 1480 cm^{-1}, and 1680 cm^{-1}. Bottom panel: Resultant resonant VSFG survey spectrum.

intensity of the same profile. This fact explains why the observed peak intensity of the very same vibration appears different for different center frequencies. Finally, the peak intensity of a vibration correlates with the overall signal intensity of a sample. An example is here the perylene ring vibration at 1565 cm^{-1} in the dye molecules ID1157 and ID1152. It seems to have a lower peak intensity in the spectra of dye ID1152 as will be seen in the next section. This might be due to, among other factors, the amount of dye adsorbed. Another criterion for the identification of a real peak is that it must appear for different center frequencies at more or less the same spectral position. That is why the center frequency is changed in 100 cm^{-1} steps although the pulse width is broader. Therefore, one part of the currently probed spectral region always overlaps with the previous one. Any change in the center frequency has an influence on the spectra with NR contribution since the background is frequency-dependent [172]. This fact has to be considered when comparing spectra of different samples at zero time delay taken at slightly different center frequencies. The spectra will look somewhat different.

The question arises about the origin of the NR contribution. For a long time the substrate was considered to be the only source of the NR background, but recently it was shown that the NR contribution changes also with frequency, aging of the sample and a different solvent environment [142]. In the present case it seems reasonable to assign the NR background to contributions from the TiO_2 film as well as the adsorbed dye itself. The freshly cleaned TiO_2 film shows little VSFG signal as can be seen in Fig. 4.12. The signal increases slightly with increasing frequency. It can be noted that contaminations due to hydrocarbons adsorbed from the environment cannot be avoided. They are already detected on the freshly cleaned film as can be seen by bands in the CH stretch region. The NR signal of TiO_2 films is assumed to originate from surface defect sites which destroy the centrosymmetry of the TiO_2 crystals as it was observed for a MgO(001) surface [176]. However, the biggest part of the NR contribution is ascribed to the dye because a NR background is still observed when the dye is measured in dichloromethane against the pure CaF_2 substrate without TiO_2 present (spectra not shown). A possible reason for the strong NR contribution from the dye could be the electronic resonance condition under which the VSFG spectra are taken. For instance, at $\omega_{IR} = 1680\,cm^{-1}$, $\lambda_{SFG} \approx 705\,nm$ which falls at the onset of the electronic absorption band of the bound dye (see Fig. 4.5 C). This condition enhances the sensitivity for the dye detection [105, 177] but also leads to a large NR contribution from the dye [178].

In the case where ω_{IR} is near a surface vibrational transition and ω_{SFG} or ω_{Vis} is near a surface electronic transition, one then speaks of doubly-resonant SFG (DR-SFG) [179]. However, DR enhancement occurs only when the probed vibrational and electronic transitions are coupled. This allows for more selective and sensitive spectroscopic information and better assignment of the vibrational modes [180]. In the present case the excited electronic transition in the adsorbed dye molecule involves the diphenylamine group and the perylene core. The strong peaks observed in the VSFG spectra of the bound dyes must thus be due to vibrations accompanying this transition, i.e. vibrations related to the aromatic system of the dye. This finding is confirmed by resonant Raman studies on PTCDA and PTCDI derivatives that predominantly exhibit peaks related to the perylene core [155, 158, 161]. On one hand this enhancement of the perylene vibrations is advantageous because it allows for a sensitive detection of the dye molecules but on the other hand it means that vibrations of the anchoring groups outside the aromatic ring are most probably not enhanced and thus only little information on the binding coordination can be expected from VSFG. However, VSFG can still provide valuable information on the molecular organization of the dye molecules at the TiO_2 surface. Especially, since it is known that the dominant band at $1565\,cm^{-1}$ is associated with a symmetrical ν_{ip}(C=C) vibration of the two parallel naphthalene fragments of the perylene core [159], it should be possible to determine the orientation of the dipole moment of this vibration and, in turn, of the entire molecule, with respect to the surface normal by polarization-dependent measurements of this particular mode.

Electronic resonance enhancement of vibrational features accompanying an electronic transition within DR-SFG experiments has already been demonstrated for various systems; for the first time for a spin-coated film of the dye Rhodamine 6G on a silica substrate [177]. Following that a series of other molecules were studied on different substrates exploiting the enhancement effect of DR-SFG [181–187]. Particularly important for the work in this thesis is the study of a retinoate monolayer prepared on rutile(110) [105]. The electronic resonance condition was chosen in order to sensitively detect the

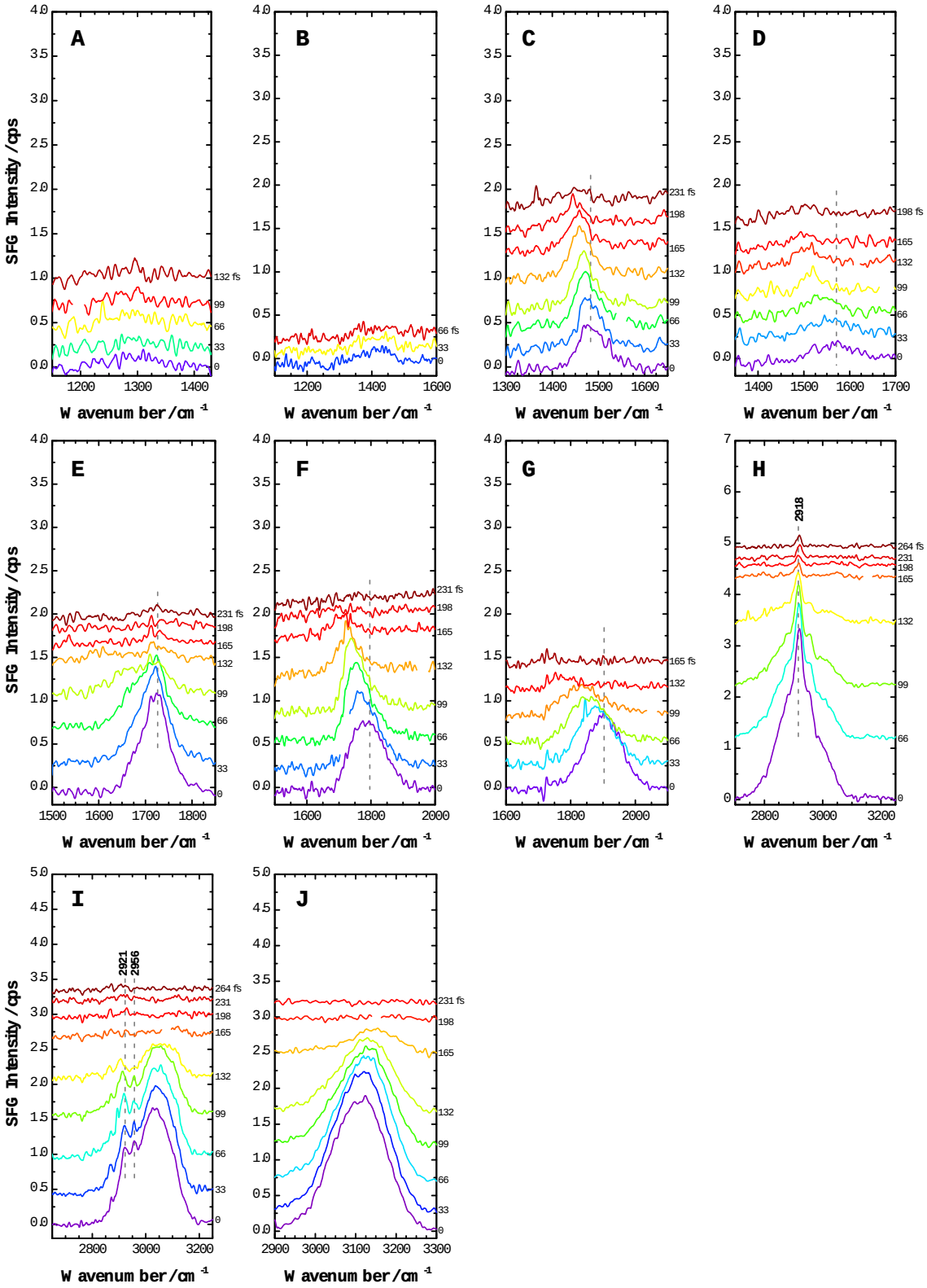

Fig. 4.12: Sets of time delay-shifted spectra of a pure TiO_2 film spin-coated on a CaF_2 prism at various spectral positions. Set (A) is centered at 1290 cm^{-1}, (B) at 1380 cm^{-1}, (C) at 1480 cm^{-1}, (D) at 1560 cm^{-1}, (E) at 1680 cm^{-1}, (F) at 1760 cm^{-1}, (G) at 1880 cm^{-1}, (H) at 2890 cm^{-1}, (I) at 2990 cm^{-1} and (J) at 3080 cm^{-1} .

molecule on the surface and to determine the order of the retionate monolayer. Further details on the theory of the DR-SFG phenomenon can be found in Refs. [179, 180].

The preceding arguments explain the sensitivity for the perylene dye and thus the high S/N ratio in the obtained VSFG spectra but so far not the origin of the NR background. Actually, the NR contribution is also tributary to the DR condition. For instance, Wu *et al.* observed an interfering continuous NR background when measuring the dye Rhodamine 6G adsorbed at the air/water interface with DR-SFG [178]. In this case, the NR contribution could not be related to the interfacial water molecules but had to originate from the dye molecules themselves. Since optical interference can only occur when two or more coherent processes are involved, they concluded that the NR background was of coherent nature. The origin of this coherent event could be unraveled by a closer look at the DR-SFG process as illustrated in Fig. 4.13.

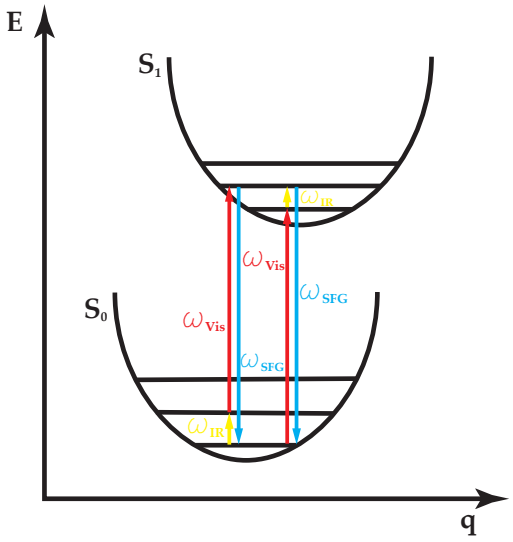

Fig. 4.13: Schematic energy level diagram of the DR-SFG process.

In general there are two ways in which the IR and the Vis pulse can interact doubly resonant with the sample: 1) in an IR-Vis DR-SFG process, meaning an excited vibrational transition followed by an electronic transition and, oppositely, 2) in a Vis-IR DR-SFG process, meaning an electronic absorption followed by a vibrational absorption. The latter process is usually neglected because the electronic relaxation times are generally much shorter than the vibrational ones [177]. However, if the decay dynamics of the excited state S_1 are ultrafast, it indicates that the S_1 state undergoes very fast non-radiative decay, thereby causing a continuous vibronic band structure. In this particular case the Vis-IR DR-SFG process can lead to a continuous SFG spectrum. Similar to that of a nobel metal substrate. In the case of Rhodamine 6G the decay time of the S_1 state was found to be less than 30 fs supporting the contribution of a continuous Vis-IR process to the VSFG spectrum. In the case of the perylene dye a decay time of the S_1 state is not directly available but it can be assumed that it is very similar to the one of the PTCDA molecule. The decay time of the latter could be determined by femtosecond spectroscopy with a duration of 250–360 fs, which is still ultrafast [188]. Keeping this in mind, the Vis-IR DR-SFG process is a very likely origin of the NR background also in the VSFG spectra of the perylene dye bound to TiO_2. This assumption is confirmed by the fact that the NR

contribution increases with IR frequency, thus causing λ_{SFG} to fall closer in the electronic absorption maximum of the dye (e.g. for $\omega_{IR} = 2890\,cm^{-1}$, $\lambda_{SFG} = 650\,nm$). It seems that the dye spectra are only the second example of a NR background observed due to the DR condition.

The advantage of the delay-shifting procedure is clearly seen in the set of spectra centered at $1680\,cm^{-1}$ (Fig. 4.11). The spectrum at zero delay looks as if there are four peaks at 1568, 1593, 1674 and $1729\,cm^{-1}$. Upon delay-shifting however it is observed that the peaks at 1674 and $1729\,cm^{-1}$ are not real peaks but actually the result of the NR background interfering with a resonant contribution at $1692\,cm^{-1}$ leading to a dip in the spectrum. Hence, without the use of the delay-shifting, the VSFG spectrum would have been misleading and its interpretation fundamentally wrong.

Still, the best proof for real peaks remains to compare the VSFG spectra with its IR and Raman counterparts since the VSFG spectra should represent bands that are simultaneously IR- and Raman-active. In order to do so, a survey spectrum is created from chosen time delay-shifted spectra without NR contribution by combining them over the entire spectral range (see Fig. 4.11, bottom panel). The selected individual spectra are marked in *black* within the sets of delay-shifted spectra. It is not necessary to pick a resonant spectrum from every delay set since some peaks are redundant. For the survey spectra it is important that they contain all peaks observed during the delay-shifting process. The CH stretch region is not depicted in the survey spectra since this region is not relevant for the analysis of the dye binding type and also because contributions from contaminations, e.g. adsorbed hydrocarbons, cannot be excluded. The relative intensities in the survey spectrum cannot be compared since the spectral parts are taken from different sets and at different time delays. Nevertheless, intensity trends of entire spectra can be compared when delay-shifted spectra with the same time delay and the same center frequency are compared over the same spectral range. Absolute intensities are not obtained because the spectra are not corrected against a reference sample for laser intensity fluctuations and intensity losses due to manual alignment issues. However, trends as already stated above can be compared since input beam powers were always kept at the same values and observed to be very stable. Besides, for the study of the dye binding mechanism the intensity plays only a minor role compared to the existence and position of a peak. All resonant survey spectra in the course of the thesis are obtained as described and the selected time delay-shifted spectra are highlighted in *black*. The complete assembly of sets of delay-shifted spectra of the bound dye ID1157 is depicted in Fig. 4.14. One may notice that some of the spectra in the delay sets discussed later on might show a disconnection which is due to the manual removal of spikes as a result of cosmic radiation hitting the detector during measurement.

4.2.5.2 Discussion of VSFG spectra of ID1157 bound to TiO_2

An overlay of the IR and Raman spectra of bound ID1157 with the VSFG spectra at zero time delay of the Vis beam over the spectral window from 1200–$1900\,cm^{-1}$ is shown in Fig. 4.15 A. It can be easily seen that each peak is detected at least twice in the course of the tuning of the IR pulse center frequency. This is the control which guarantees that the peaks are real. More importantly, the peaks can be found both in the IR and the Raman spectra which demonstrates that they originate from the bound dye. An overlay of the VSFG spectra with temporal delay of the Vis pulse, namely the resonant spectrum (same as in Fig. 4.11, bottom panel), with the IR and Raman spectra is presented in Fig. 4.15 B.

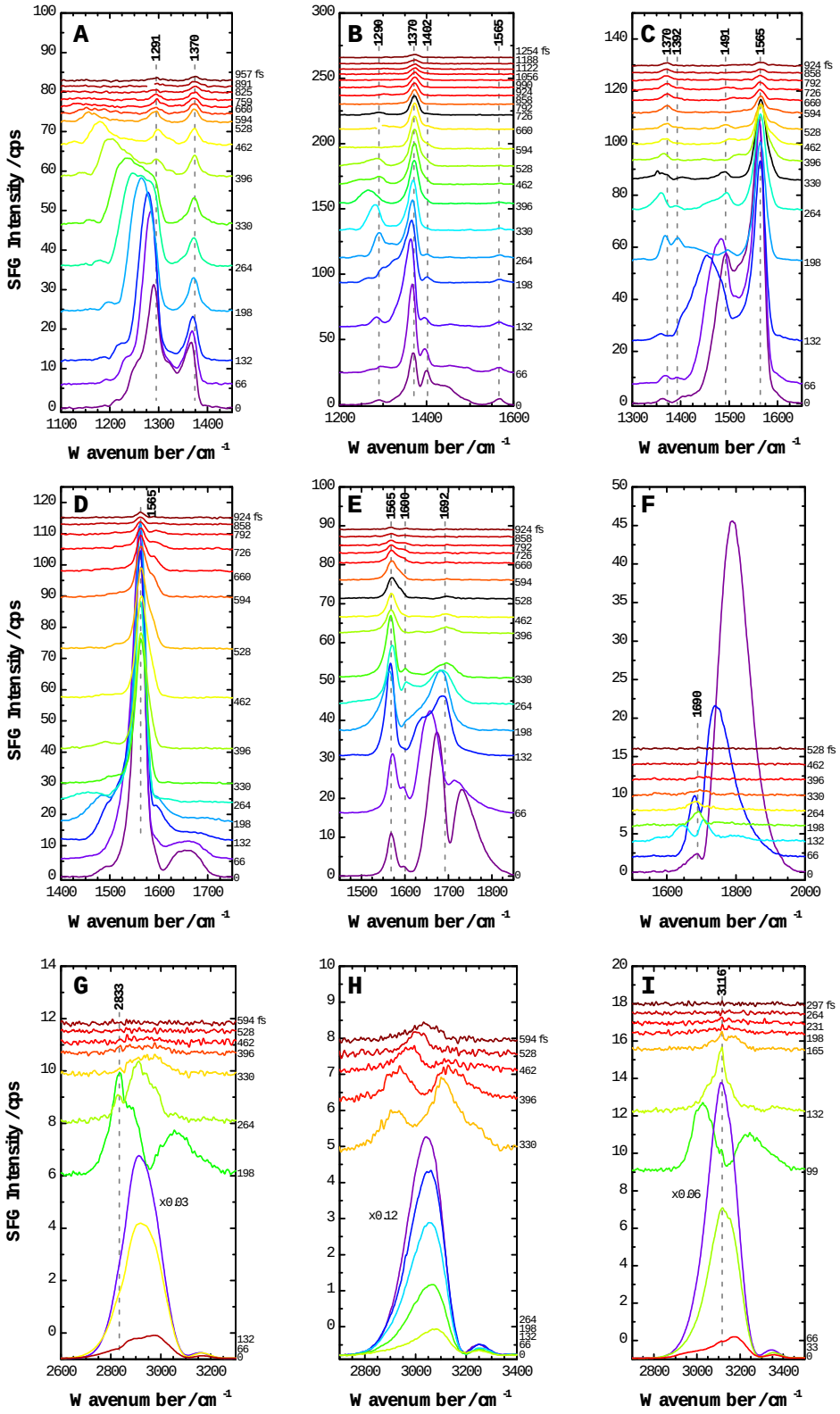

Fig. 4.14: Sets of time delay-shifted spectra of ID1157 bound to a TiO_2 film spin-coated on a CaF_2 prism at various spectral positions. Set (A) is centered at 1290 cm^{-1}, (B) at 1380 cm^{-1}, (C) at 1480 cm^{-1}, (D) at 1560 cm^{-1}, (E) at 1680 cm^{-1}, (F) at 1780 cm^{-1}, (G) at 2890 cm^{-1}, (H) at 2980 cm^{-1} and (I) at 3080 cm^{-1}.

It is observed that the detected bands again represent bands both IR- and Raman-active but this time only the ones with strong intensity. Bands which are present in the IR and Raman spectrum but with low intensity are not clearly seen in the resonant VSFG spectrum. This is due to the fact that for the resonant spectrum only delay-shifted spectra without NR contribution are chosen and thus weak bands are not present in these spectra anymore. With this it becomes clear that the sets of delay-shifted spectra are the most precise source when it has to be decided whether a peak is existent or not.

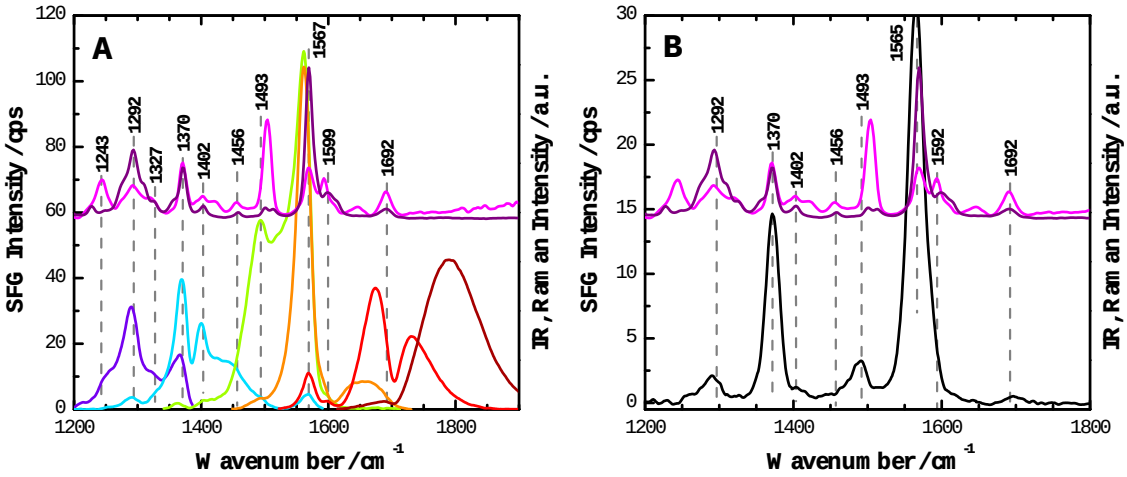

Fig. 4.15: (A) Overlay of VSFG spectra without temporal delay of the Vis beam (*rainbow colors*) and (B) with temporal delay (*black*) of bound ID1157 at different spectral positions in comparison with IR (*magenta*) and Raman (*purple*) spectra of bound ID1157.

Strong peaks are found at 1292, 1370, 1402, 1493, 1565 and 1692 cm^{-1}. They are all, apart from the latter, due to perylene ring vibrations as expected because of the DR-SFG condition (compare Tab. 4.1). The latter peak at 1692 cm^{-1} is due to the ν_s(C=O) stretch of the imide group [189]. The strong bands from the perylene system and in general the fact that an VSFG spectrum of the bound dye is detectable, implies that the dye molecules adsorb in an ordered arrangement. This is ascribed to the fact that the VSFG signal intensity shows an order dependence [190]. At first glance, the observation of order on the rough and highly porous nanoparticulate TiO_2 film without defined interface between the dye layer and the TiO_2 film seems surprising. Especially, knowing that the VSFG signal is obtained from a relatively large sampling spot ($\sim$200 μm in hight) and thus averaged over multiple dye-coated TiO_2 nanoparticles randomly oriented in the film. However, a resultant net order in the dye layer might be measurable because the anatase nanoparticles mostly expose their (101) faces [39, 191]. This in turn leads to a rough TiO_2 film but with preferred orientation. Moreover, an atomically rough surface can still be optically flat enough [101].

The adsorption behavior of small organic molecules with carboxylic acid anchor onto the (101) anatase surface was previously studied by scanning tunneling microscopy (STM) and DFT calculations [164, 192]. According to these works, the molecules bind side by side in a bidentate bridging coordination to the rows of fivefold coordinated Ti atoms (Ti_{5c}) [192]. Under complete surface coverage the molecules pack densely achieving additional order among themselves on the TiO_2 surface. In the case of the dye molecules a full surface coverage is expected because of the long immersion times and thus also a close

packing of the molecules. During the adsorption process the perylene cores most probably orient parallel since this configuration enables adsorption of the most molecules. This preferential alignment of the dye molecules on the (101) surfaces including the alignment of the perylene cores leads to an ordered dye/TiO_2 interface detectable with VSFG spectroscopy. An interaction of the perylene rings due to π-π stacking is unlikely because the distance of the rows of Ti_{5c} atoms is about 5.11 Å (see distance c/2 in Fig. 2.2) [39], i.e. larger than the observed spacing of 3–4 Å observed in π-π stacks of PTCDI derivative films without substrate interaction [193, 194]. Negligible π-π interaction of aromatic adsorbates was also observed within STM studies [195, 196]. Another important fact is that there is no new band found in the spectral region from 1750–1700 cm^{-1} indicative of a surface-bound ester [151]. With VSFG spectroscopy it is thus possible to obtain further information on the dye arrangement on the TiO_2 surface as well as to confirm the results obtained with IR and Raman spectroscopy from the bulk.

4.2.5.2.1 Comparison of VSFG spectra of ID1157 and SF18 both bound to TiO_2 Since there are no similar studies on dye-coated TiO_2 nanoparticles with VSFG spectroscopy to compare the obtained results with, an experimental proof is thus desirable. For this reason the dye SF18 bearing the carboxylic anchor as well but not the spacer between the perylene unit and the diphenylamine group is investigated under conditions similar to the ones used for ID1157. The sets of time delay-shifted spectra are depicted in Fig. 4.16. By comparing the sets of delay-shifted spectra of bound ID1157 (Fig. 4.14) and SF18 (Fig. 4.16) it is seen that overall the signal intensity of bound SF18 at zero delay is stronger. Fluctuations in input beam powers can be excluded as possible cause since they were the same for both measurements. However, a possible reason can be the sample itself. Sample preparation was always carried out in the same way but slight variations in the TiO_2 film quality were always observed. Consequently, the NR contribution to the spectra will be different [142]. Another reason might be the different electronic structure of both molecules. While ID1157 exhibits an absorption maximum at $\lambda_{max} = 543$ nm, SF18 has one at $\lambda_{max} = 599$ nm. Therefore, the electronic resonance condition which enhances the signal of the dye is already reached for SF18 at lower center frequencies. The spectral shapes of the delay-shifted spectra at comparable center frequencies however are very similar for both dyes. For instance, the sets of delay-shifted spectra at 1680 cm^{-1} (Fig. 4.14 E and Fig. 4.16 E) show the same spectral behavior. In contrast, the sets of delay-shifted spectra centered at 1480 cm^{-1} (ID1157) and 1450 cm^{-1} (SF18) show the influence of a slightly different center frequency. Both detected spectral windows display the same bands but with different relative intensities. Whereas for the center frequency of 1480 cm^{-1} the band at 1565 cm^{-1} is stronger, the band at 1370 cm^{-1} is stronger at a center frequency of 1450 cm^{-1}.

An overlay of the VSFG spectra of bound SF18 at zero delay (of the Vis beam at different spectral positions) with the IR and Raman spectra of SF18 bound to TiO_2 is depicted in Fig. 4.17 A. The spectra with temporal delay are compared to the IR and Raman spectra in Fig. 4.17 B. In order to better analyze the peak positions in the VSFG spectra of SF18 with the ones of ID1157, a direct comparison of the resonant spectra of ID1157 and SF18 is shown in Fig. 4.17 C. The latter shows that the resonant spectra can be nicely overlaid. In the spectrum of SF18 the same peaks are observed as in the spectrum of ID1157. Accordingly, it can be concluded that both dyes bind and align in the same way on the TiO_2 surface. This in turn confirms the VSFG spectra obtained from ID1157 and the results drawn from them. Even the resonant intensities of the peaks at 1370 cm^{-1} can be com-

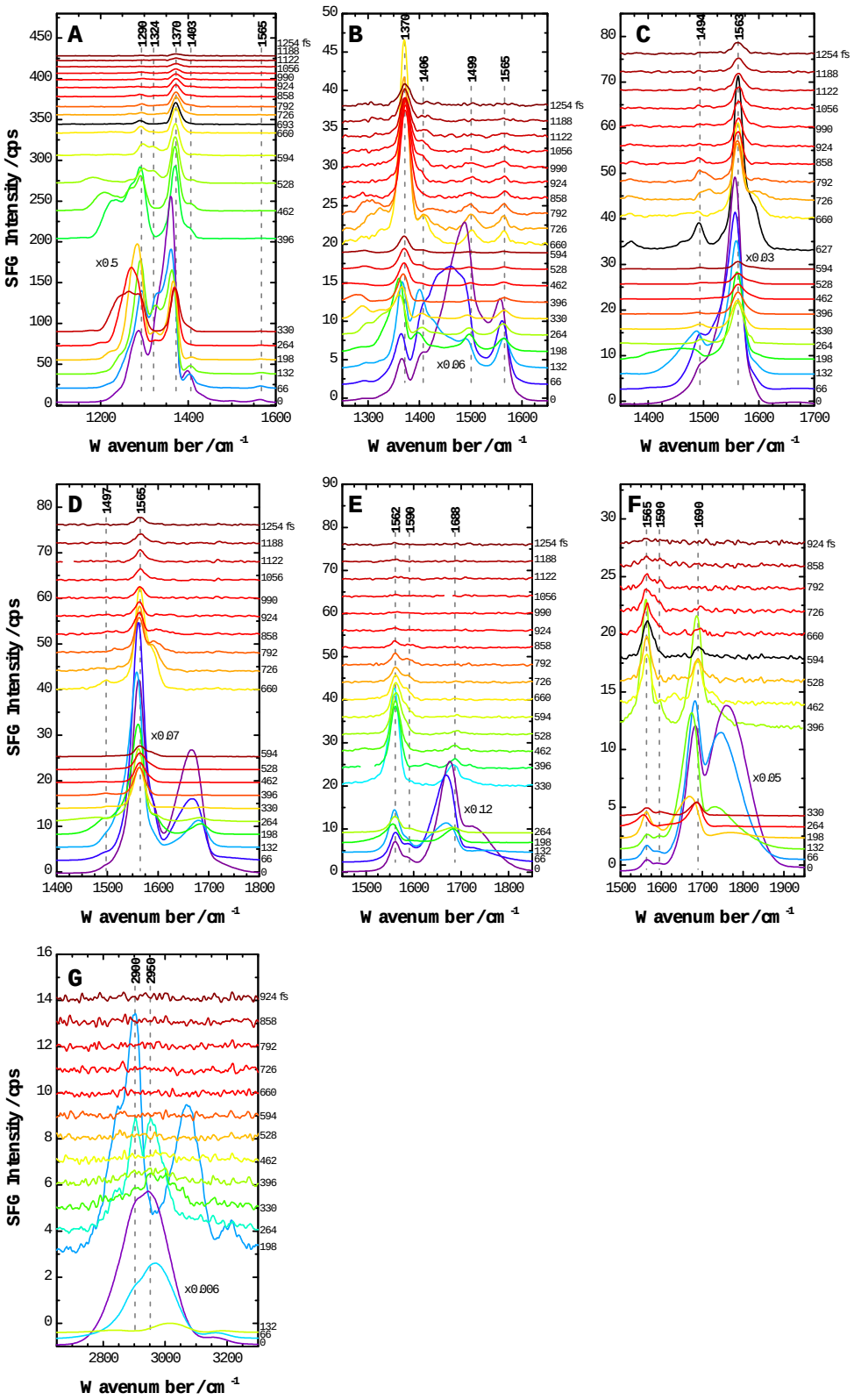

Fig. 4.16: Sets of time delay-shifted spectra of SF18 bound to a TiO_2 film spin-coated on a CaF_2 prism at various spectral positions. Set (A) is centered at 1340 cm^{-1}, (B) at 1450 cm^{-1}, (C) at 1550 cm^{-1}, (D) at 1610 cm^{-1}, (E) at 1680 cm^{-1}, (F) at 1720 cm^{-1} and (G) at 2890 cm^{-1}.

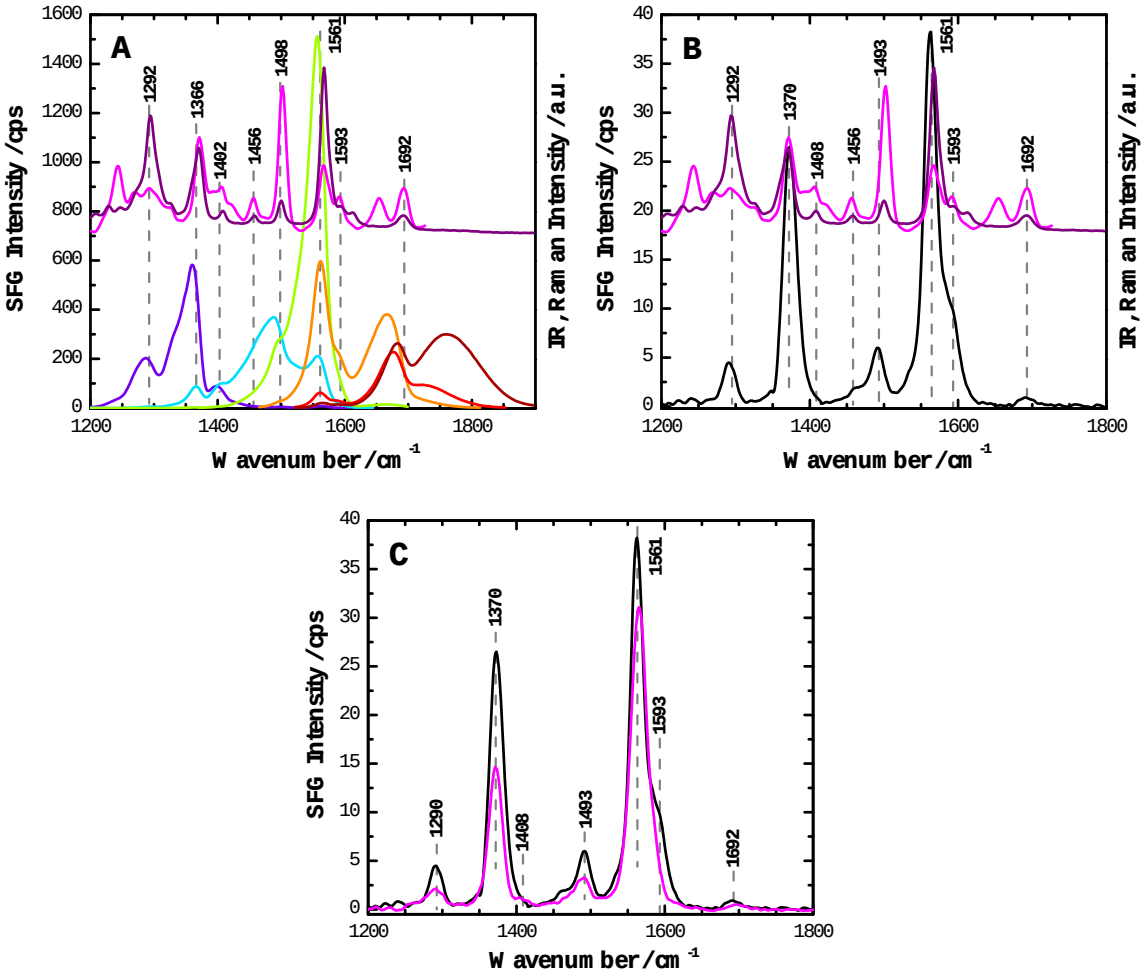

Fig. 4.17: (A) Overlay of VSFG spectra without temporal delay of the Vis beam (*rainbow colors*) and (B) with temporal delay (*black*) of bound SF18 at different spectral positions in comparison with IR (*magenta*) and Raman (*purple*) spectra of bound SF18. (C) Comparison of delay-shifted spectra of ID1157 (*magenta*) and SF18 (*black*).

pared because the corresponding spectra are taken at very similar delay times, namely 726 fs for ID1157 and 660 fs for SF18 (see spectra marked in *black* at center frequencies around 1380 cm^{-1}). Since the intensity decreases with time delay and the one of ID1157 is slightly longer the intensity difference of the peak at 1370 cm^{-1} is negligible. Therefore, the intensity differences found for the spectra at zero time delay can be solely attributed to NR contributions.

4.2.5.2.2 Comparison of VSFG spectra of SF18 bound to TiO_2 obtained in *ppp* and *ssp* polarizations By applying VSFG spectroscopy with different input beam polarization configurations, information on the relative orientation of a certain functional group with respect to the surface normal can be obtained [197]. In this work two polarization combinations, namely *ppp* and *ssp* (where the configuration refers to the polarization states of the input and output beams in the order of increasing wavelength, i.e. SFG, Vis and IR), are used. These two polarization configurations are sufficient to probe components of the vibrational transition dipole moment that lie perpendicular and parallel to the sam-

ple surface. The *ppp*/*ssp* intensity ratio obtained by the two polarization combinations for a single mode can be used as an indicator of orientation [138, 198, 199]. As previously mentioned, the mode at 1565 cm^{-1} (dipole moment along molecular axis) should be analyzed in order to obtain orientational information on the perylene unit of the dye molecules.

The sample of bound SF18 is chosen for a polarization-dependent measurement because of the high signal intensity of its VSFG spectra both in *ppp* and *ssp* polarization combinations. In the *ppp* polarization combination, the sample alignment is usually performed via a signal obtained from an Au stripe vapor-deposited on the basal face of the CaF_2 prism. With the *ssp* combination, the Au stripe does not provide enough signal output for alignment purposes due to decreased reflectivity [198] and the low laser powers that have to be used in order not to damage the CaF_2 substrate. Fortunately, as a result of the strong signal intensity of the spectra of SF18, the VSFG signal from the TiO_2 film can be used directly to align the sample.

The sets of delay-shifted spectra recorded in *ssp* polarization combination are summarized in Fig. 4.18. Comparing the intensities of the spectra at zero time delay with the ones of the same sample obtained in *ppp* polarization (Fig. 4.16) it can be seen that they are slightly weaker, even more so for the spectrum centered at 1550 cm^{-1}. In contrast, the observed spectral shapes are similar at comparable center frequencies. For the two sets of delay-shifted spectra at a center frequency around 1350 cm^{-1}, it appears that the spectra without temporal delay strongly differ in shape. However, the spectrum of SF18 recorded in *ssp* polarization at a time delay of 132 fs is very alike to the spectrum of SF18 without temporal delay measured in *ppp* polarization. This fact can be related to the subjectively chosen time of zero delay. At zero time delay the signal intensity on the Au reference should be maximal. But falling on the maximum is not always straightforward because the intensities are very similar for subsequent time delays. Consequently, the spectral shape difference of the discussed spectra might be a result of the choice of the initial time of zero delay. The latter might also be different because in *ssp* polarization the sample was not aligned on Au but on the TiO_2 film.

The spectra without temporal delay at various center frequencies are compared for both polarization combinations in Fig. 4.19 A. Similarly, the resonant spectra are overlayed with each other in Fig. 4.19 B. The same peaks are found for both polarization combinations. In the present case spectra from the same center frequency with identical time delay are selected to present the peaks at 1372 and 1565 cm^{-1}. As a consequence their intensities can be directly compared. The *ppp*/*ssp* intensity ratio for the two polarization combinations of the mode at 1565 cm^{-1} representing the symmetrical ν_{ip}(C=C) stretching vibration of the two parallel naphthalene fragments of the perylene core is 1.2. This value is not definite because the spectra were not recorded under the same alignment conditions but it is a hint that the dye molecules orient neither completely upright nor flat on the surface but with a certain tilt relative to the surface normal. In order to acquire absolute numbers substantial calculations like detailed in Ref. [198] are needed. For other dye/TiO_2 systems with aromatic dyes as large as the present dyes and also coupled via a carboxylic acid group tilt angles of about 50° with respect to the surface normal have been reported [66, 68, 69, 71]. It can be expected that the perylene dyes adopt a similar tilt angle due to the similarity of the dyes under investigation.

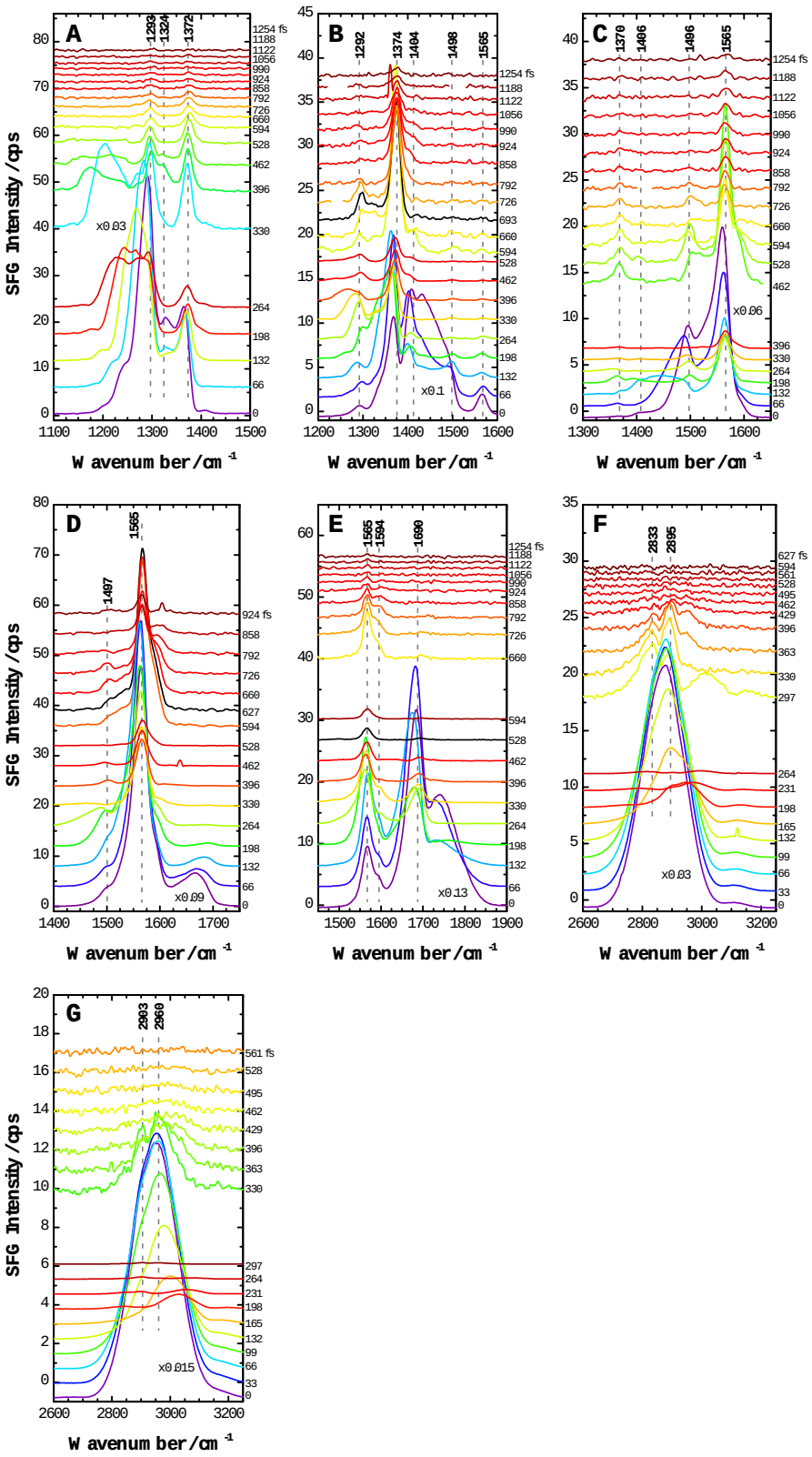

Fig. 4.18: Sets of time delay-shifted spectra of SF18 bound to a TiO_2 film spin-coated on a CaF_2 prism at various spectral positions in *ssp* polarization. Set (A) is centered at 1250 cm^{-1}, (B) at 1350 cm^{-1}, (C) at 1450 cm^{-1}, (D) at 1550 cm^{-1}, (E) at 1650 cm^{-1}, (F) at 2860 cm^{-1} and (G) at 2900 cm^{-1}.

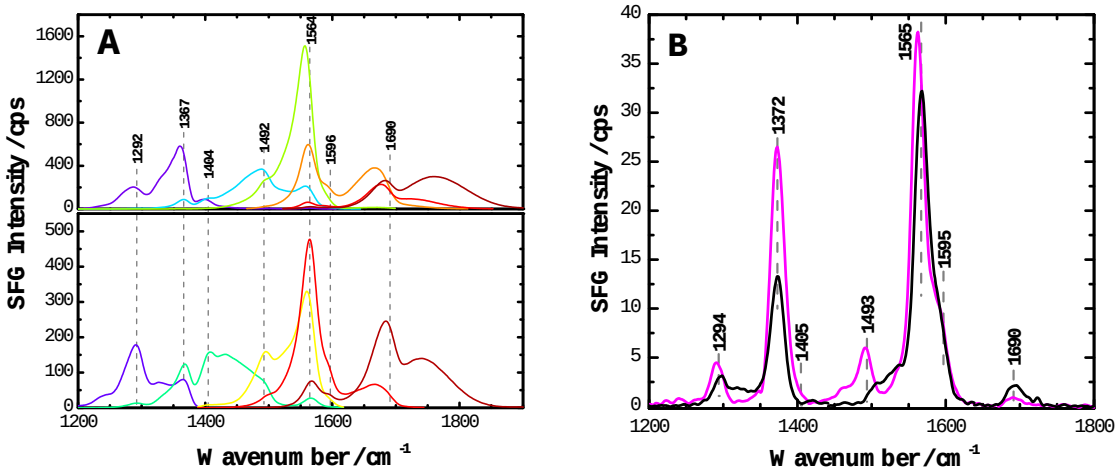

Fig. 4.19: (A) Comparison of VSFG spectra without temporal delay of the Vis beam of bound SF18 recorded in *ppp* (top row) and in *ssp* polarization (bottom row) and (B) overlay of the corresponding VSFG spectra with temporal delay in *ppp* (*magenta*) and in *ssp* (*black*) polarization.

Even though the preceding analysis seems reasonable one should keep in mind that the TiO_2 film does not possess a defined surface. Therefore the measured ratio of 1.2 could also mean that the dyes themselves bind e.g. in an upright fashion and the observed tilt is only due to the random orientation of the nanoparticle surfaces (Fig. 4.20). Most probably the VSFG response contains a combination of both cases. The intensity of the band at 1372 cm^{-1}, also assigned to a ν(C=C−C) stretching vibration of the perylene ring, does not exhibit the same intensity ratio as the band at 1565 cm^{-1}. Instead, it is much lower for the spectrum taken in *ssp* combination. However, since the orientation of the perylene is sufficiently determined by the vibration representing the band at 1565 cm^{-1} this is ascribed to the dissimilar conditions of the measurement. These polarization-dependent measurements show that there is no additional peak information obtained by changing the polarization combination. Hence, the preceding and the following spectra are recorded in *ppp* polarization combination, also because they yield higher signal intensities.

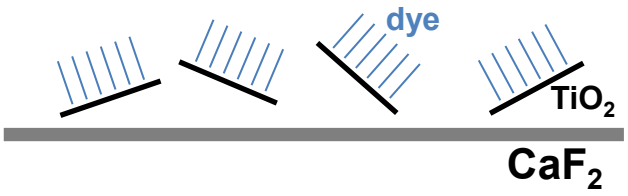

Fig. 4.20: Possible arrangement of the dye molecules on the TiO_2 nanoparticles within the TiO_2 film.

4.2.5.2.3 Water influence on ID1157 dye layer bound to TiO_2 thin film Since it is favored to perform the CO_2 reduction reaction in water the influence of the latter on the dye's organization, namely binding mode and alignment, on the TiO_2 surface is investigated. In order to do so a thin water film is added underneath the TiO_2 film via the solution inlet of the measuring cell. The obtained time delay-shifted spectra are depicted in Fig. 4.21. Only the sets of relevant spectral regions were measured.

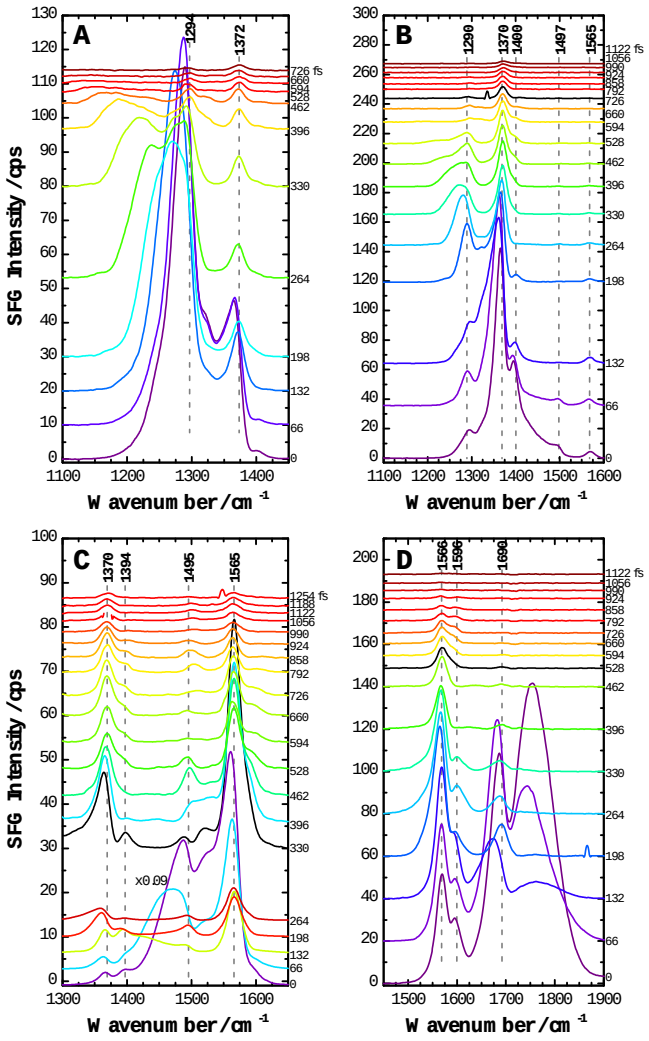

Fig. 4.21: Sets of time delay-shifted spectra of ID1157 bound to a TiO_2 film spin-coated on a CaF_2 prism in contact with water at various spectral positions. Set (A) is centered at 1270 cm^{-1}, (B) at 1360 cm^{-1}, (C) at 1450 cm^{-1} and (D) at 1700 cm^{-1}.

It is found that the spectral shape for similar center frequencies is the same for spectra measured in air (Fig. 4.14) and in water. However, the signal intensity of the spectra at early time delays measured in water is different. For all center frequencies it is much stronger than the corresponding intensities of the spectra measured in air. One must keep in mind that a quantitative intensity comparison is not possible because the spectra are not corrected against a reference, only the input beams' laser powers were always set to the same values. In addition, it must be considered that the reflectivities at the air/dye-TiO_2 interface are different than at the water/dye-TiO_2 interface. This reflectivity difference might also contribute to the signal increase. An intensity increase upon

addition of water was repeatedly observed for different samples. Therefore, it is not due to this specific sample and/or the specific measurement conditions under which the spectra were taken, that being laser power and sample alignment. In the case where only the spectra at zero time delay would have been measured in air and water, it could be concluded that the addition of water drastically increases the order of the adsorbed dye layer. This result though would contradict findings which demonstrate that the order of self-assembled monolayers of OEG-terminated alkanethiols in air is disturbed when water is added to the sample due to the repulsive interaction of the water molecules with the OEG units [200]. In the present case the ID1157 dye molecules contain OEG side chains which should also interact with the water molecules and, in turn, hinder the perylene systems from packing densely.

This inconsistency can be cleared up by comparing the resonant spectra recorded in air and in water as will be seen in the following discussion. In Fig. 4.22 A the spectra at zero time delay for consecutive center frequencies taken in air and in water are compared. The intensity increase upon addition of water is clearly seen. The overlay of the corresponding survey spectra of the time delay-shifted spectra is shown in Fig. 4.22 B. For both conditions, the survey spectra are composed of three time delay-shifted spectra taken at center frequencies around 1380 cm^{-1}, 1480 cm^{-1} and 1680 cm^{-1}. Moreover, for each center frequency identical time delays are selected. Consequently, differences in the spectra can only be due to the dye-coated TiO_2 film itself and addition of water. It is observed that the peak positions do not change under the influence of water but that a new peak appears at 1520 cm^{-1}. Since there is no equivalent peak in the IR or Raman spectra of the bound dye ID1157 and since this peak is not fixed in position upon time delay-shifting, it is not classified as a real peak. Thus, it must be related to the NR contribution. The survey spectrum of ID1157 in air, in contrast, is free of NR contributions. As a result the peak at 1520 cm^{-1} is assigned to an interference effect between a changed NR contribution due to the presence of water. This demonstrates also that the time delay at which all NR background is suppressed depends strongly on the sample. The purely resonant spectrum of bound ID1157 in contact with water is obtained 198 fs later than the one in air. Solvent-dependent changes in the NR contribution were also found by Curtis *et al.* who studied octadecyltrichlorosilane (OTS) films in methanol and water [173].

In Fig. 4.22 B it is observed that the intensity of the peak at 1565 cm^{-1} is stronger in the spectrum taken in water. But this is only the case because this spectrum still contains NR background. If the purely resonant spectrum of the sample in water (at 528 fs time delay of the Vis pulse) is compared to the one taken in air, it is found that the peak intensity decreases by half its initial value (spectrum in *grey* in Fig. 4.22 B). Going along with that the intensity of the band at 1370 cm^{-1} is also lower in the spectrum recorded in water. From the set of time delay-shifted spectra taken at a center frequency of 1380 cm^{-1} it is seen that this spectrum is already the purely resonant spectrum (flat baseline with solely resonant peaks). All this indicates that some degree of order is lost in the dye film upon addition of water and agrees with the findings obtained with OEG films. Despite reduced ordering, the dye is still chemically bound to the TiO_2 film when the latter is in contact with water because there are no other bands found than the ones detected in the spectrum taken in air. In conclusion, an aqueous environment has little effect on the dye layer bound to TiO_2, such that the film should keep its properties under CO_2 reduction conditions.

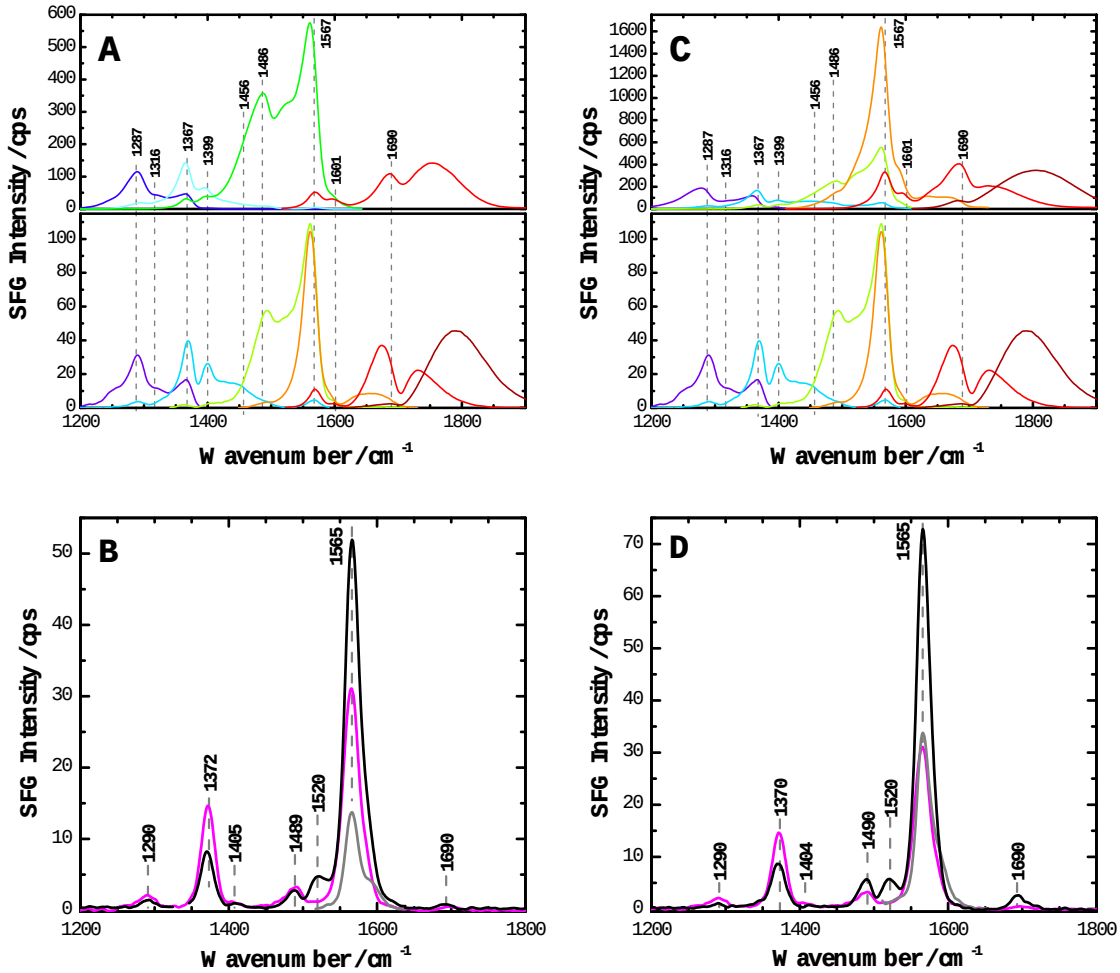

Fig. 4.22: (A) Comparison of VSFG spectra without temporal delay of the Vis beam of bound ID1157 in air (bottom row) and in water (top row) and (B) overlay of the corresponding VSFG spectra with temporal delay, in air (*magenta*) and in water (*black*). Resonant spectrum at 528 fs time delay at a center frequency of 1450 cm^{-1} (*grey*). (C) Comparison of VSFG spectra without temporal delay of the Vis beam of bound ID1157 on CaF_2 prism (bottom row) and on Au wafer (top row) and (D) overlay of the corresponding VSFG spectra with temporal delay, on CaF_2 prism (*magenta*) and on Au wafer (*black*). Resonant spectrum at 528 fs time delay at a center frequency of 1480 cm^{-1} (*grey*).

4.2.5.2.4 Substrate influence on VSFG spectra of ID1157 bound to TiO_2 thin film Using the CaF_2 prism as substrate the VSFG spectra of the dye-functionalized TiO_2 films are obtained under TIR conditions after transmission of the light through the substrate. It is assumed that the VSFG signal is generated at the free interface, namely the air/dye-TiO_2 or water/dye-TiO_2 interface, because the signal originating from the dye is strong. However, it cannot be totally excluded that the CaF_2/TiO_2 interface, the so-called buried interface, is probed since dye molecules diffusing into the porous TiO_2 film can also be present at this interface. By changing to a different substrate such as an Au film on an Si wafer it should be possible to deduce which of the two interfaces is actually probed. Since the different materials have differing nonlinear reflectivities, the VSFG response from the buried interface should vary with the substrate and consequently, in case a signal is gen-

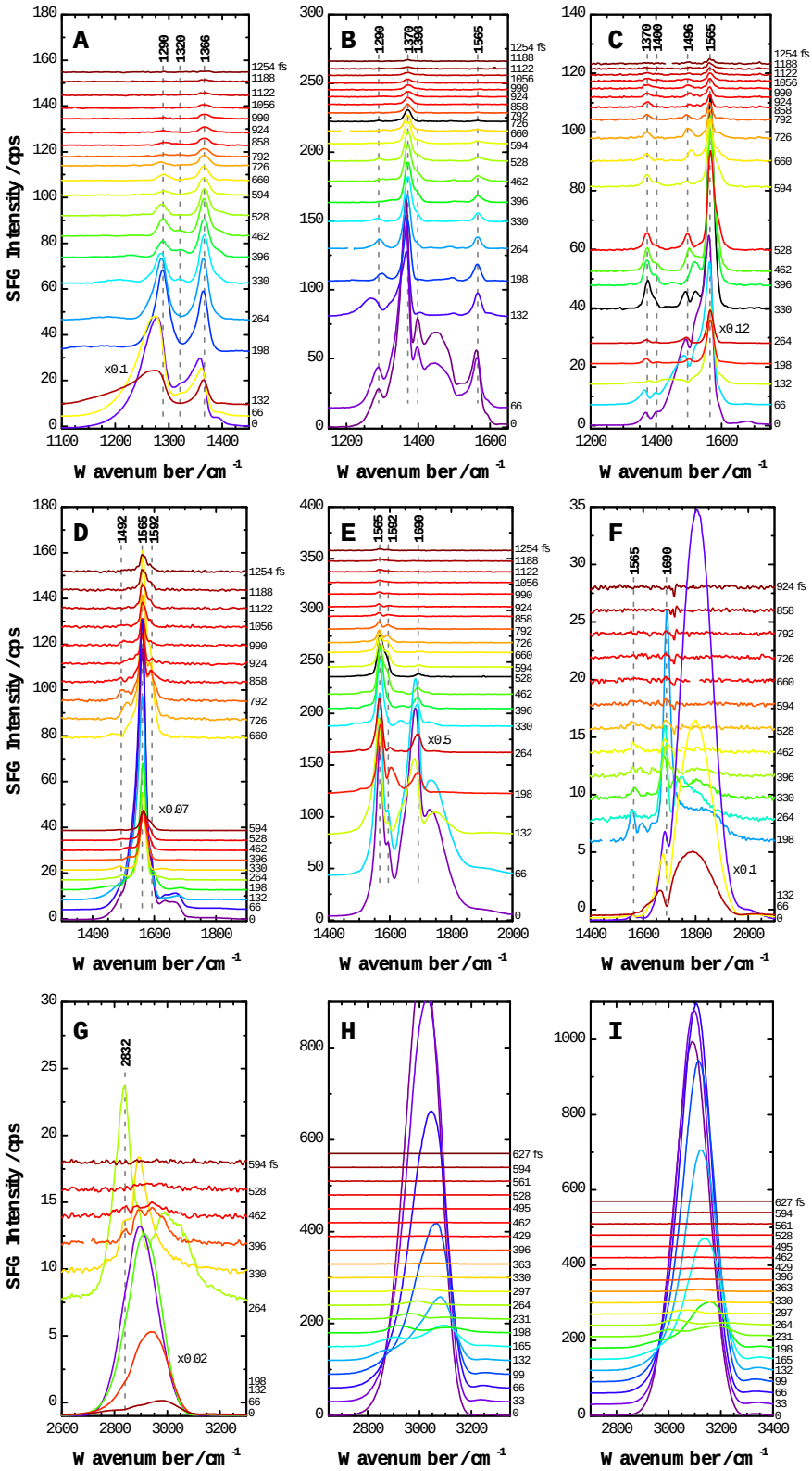

Fig. 4.23: Sets of time delay-shifted spectra of ID1157 bound to a TiO_2 film spin-coated on an Au wafer at various spectral positions. Set (A) is centered at 1280 cm^{-1}, (B) at 1380 cm^{-1}, (C) at 1480 cm^{-1}, (D) at 1580 cm^{-1}, (E) at 1680 cm^{-1}, (F) at 1780 cm^{-1}, (G) at 2890 cm^{-1}, (H) at 2980 cm^{-1} and (I) at 3080 cm^{-1}.

erated at both the free and buried interface, these signals should interfere and effect the measured spectra [142, 201]. If the VSFG signal does not change with the substrate it is very likely that the free interface is the one being probed.

The sets of time delay-shifted spectra recorded from a ID1157 dye-coated TiO_2 film on an Au wafer are presented in Fig. 4.23 (previous page). It can be seen that the signal intensity is much stronger than the one of the spectra taken from a similar film but on a CaF_2 substrate (Fig. 4.14). This intensity increase is most probably attributed to the fact that the Au wafer is a reflective substrate and intensity losses due to transmission do not play a role. Moreover, the Au layer exhibits its own NR background due to $d \rightarrow s$ interband transitions in the metal [141, 198]. As the TiO_2 film is transparent, this background can add on to the one coming from the dye. The shape of the spectra taken on the Au and CaF_2 substrates is very similar, for both the spectra without temporal delay and the resonant spectra (Fig. 4.22 C and D). As mentioned previously, this fact indicates that the free interface of the samples is probed. The time delay-shifted spectra for the assembled resonant spectrum are selected in the same way as for the spectrum of the sample in contact with water. Consequently, the same considerations regarding the intensity comparison of the spectra hold. Also upon change of substrate the peak positions do not change but cause the appearance of a new band at 1520 cm^{-1}. Just as for the spectra recorded from the sample in water this peak disappears in the purely resonant spectrum of the dye-functionalized TiO_2 film on the Au substrate at a time delay of 528 fs (Fig. 4.23 C). The intensity of the peak at 1565 cm^{-1} in the purely resonant spectrum (spectrum in *grey* in Fig. 4.22 D) is identical to the one in the spectrum taken from the sample on the CaF_2 substrate. This indicates that the dye layer ordering is the same in both samples and once more that the substrate has no influence on the TiO_2 film.

4.2.5.3 Summary of the binding properties of dyes with carboxylic acid group

With the help of UV/Vis absorption, IR, Raman and VSFG spectroscopy it can be concluded that the dye ID1157 binds its carboxylic acid anchor in a bidentate coordination to the TiO_2 surface. This finding is confirmed by the same studies on the bound dye SF18. Moreover, it is suggested that the dye molecules form an ordered layer adopting a tilted geometry on the TiO_2 surface. This order is slightly disturbed by the presence of water but not completely destroyed. In addition, the binding mode is not changed upon water contact. VSFG-specific results show that the free interface of the TiO_2 film is probed and that measurements with other polarization combinations than *ppp* do not provide further peak information on the sample. Based on these findings, a tentative and simplistic binding model of ID1157 dye molecules on a TiO_2 film is proposed and depicted in Fig. 4.24.

4.2.5.4 Discussion of VSFG spectra of ID1152 bound to TiO_2

In contrast to the dye ID1157 it is not as straightforward to obtain a VSFG spectrum of the bound dye ID1152. For instance, the samples of freshly bound ID1152 exhibit rather poor signal intensity. Only the strong band at 1565 cm^{-1} can be detected but with very little intensity. However, it is possible to increase the signal intensity drastically by bringing the dye-coated TiO_2 film in contact with water. As previously mentioned, the measuring cell is built such that a thin water film can be pumped underneath the sample while continuously measuring the same spot. The corresponding VSFG spectra at zero time delay are shown in Fig. 4.25.

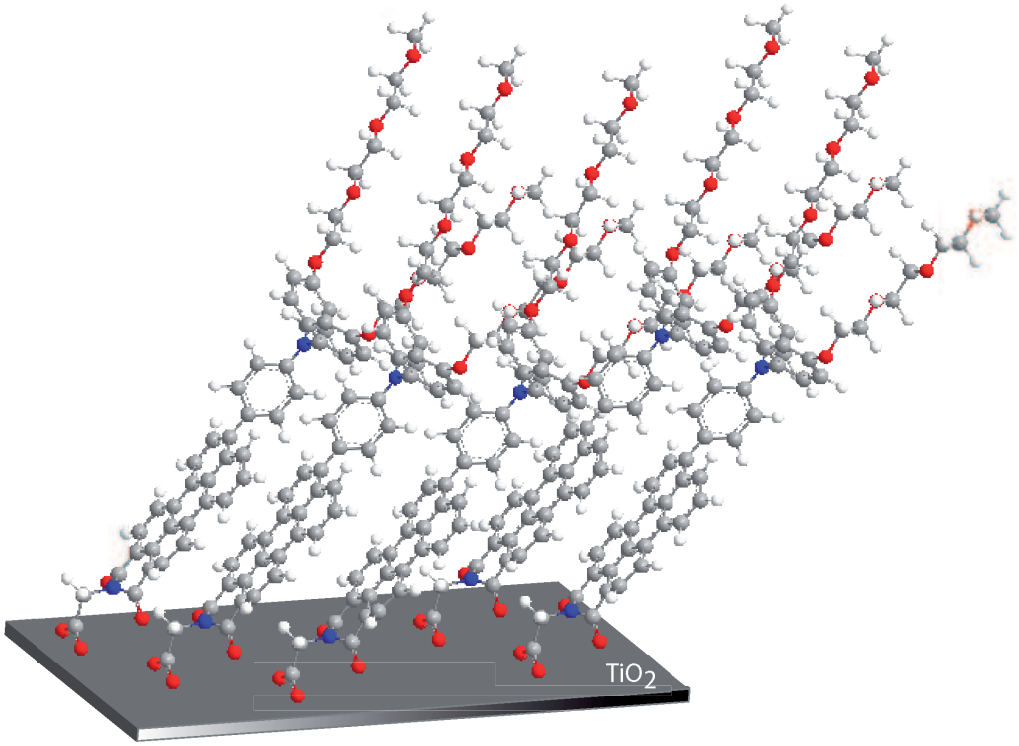

Fig. 4.24: Binding model of ID1157 to TiO_2.

A sixtyfold intensity increase is seen for the first addition of water. Although the signal decreases again when the film has dried (most probably due to changes in reflectivities and NR background contribution), it does not revert back to its initial intensity. The intensity increase of the spectra without temporal delay also parallels an intensity increase of the resonant spectra (not shown). These facts demonstrate that the first addition of water triggers ordering in the dye layer bound via the opened anhydride group. It is assumed that the presence of water enables at least one of the two bound carboxylates to detach and rebind at a different surface site. As a consequence the bound dye molecules can rearrange in a way that enables more efficient packing and creation of a low energy state. Moreover, this observation allows the speculation that reimmersing the dried film in dye solution should lead to additional dye binding and in turn to more efficient light harvesting properties. Bazzan *et al.* could already show for the dye N719 that the reimmersing procedure increases the amount of dye adsorbed and as a result also the overall DSSC efficiency [202]. A second addition of water again enhances the signal, although to a slightly higher value than for the first addition. As seen for the dye ID1157 this intensity increase is due to an enhancement of the NR contribution to the spectrum measured from the sample in contact with water. The water influence on the bound dye ID1152 will be discussed in more detail later on. For now it is important to remember that the bound dye ID1152 only exhibits a distinct VSFG spectrum after contact with water. Hence, the following spectra in air are taken from a dried film.

The sets of time delay-shifted spectra of bound ID1152 are shown in Fig. 4.26. The presence of a NR contribution is observed also for the dye ID1152 and eliminated by gradually delaying the Vis pulse with respect to the IR pulse. However, the NR contribution

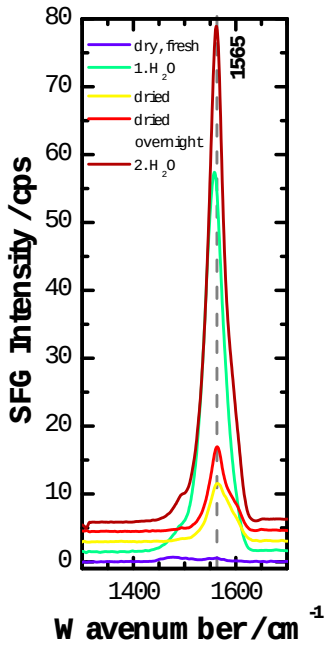

Fig. 4.25: Water influence on the signal intensity of VSFG spectra of ID1152 without temporal delay of the Vis beam.

for the dye ID1152 is not as pronounced as for the dye ID1157 presumably because λ_{SFG} coincides less with the absorption maximum of ID1152 than with the one of ID1157. As a consequence the VSFG signal of ID1152 is less enhanced than the one of ID1157. The resonant spectra which are taken to compose the survey spectrum (Fig. 4.27 B) are marked in *black*. Two spectra are taken from the delay set centered at 1380 cm^{-1}. The top one is chosen to represent the band at 1286 cm^{-1} because the delay set centered at 1300 cm^{-1} does not give a meaningful resonant spectrum. Accordingly, the bottom one is used to represent the peak at 1342 cm^{-1}, the part of the NR contribution is cut off.

The resonant survey spectrum as well as the spectra at zero time delay are compared to the IR and Raman spectra of bound ID1152 in Fig. 4.27 A and B, respectively. The spectra at zero delay suggest already that all simultaneously IR- and Raman-active bands are present in the VSFG spectra. This is more clearly seen in the resonant survey spectrum where peaks are found at 1286, 1342, 1451, 1493, 1563, 1606 and 1740 cm^{-1}. Similar to the VSFG spectra of bound ID1157 the bands are all, except for the latter, associated with ring vibrations of the perylene core indicating also here an ordered arrangement of the aromatic rings. The bands at 1451 and 1606 cm^{-1} are not as clearly recognizable as in the spectrum of bound ID1157 and a band at 1342 cm^{-1} is observed in place of the one at 1370 cm^{-1}. A possible reason for this could be the unequal anchors of the otherwise structurally completely identical molecules which connect with different angles to the perylene cores.

The anhydride group is linked in a planar configuration to the perylene body whereas the carboxylic acid group is linked via a methylene group to the imide functionality which extends into the perylene system. This methylene group could be the origin for a dissimilar tilt of the two dye molecules on the TiO_2 surface leading to a different detection of vibrations of the perylene system (compare Figs. 4.24 and 4.37). In addition, whereas the anhydride group is open in the bound dye ID1152, the imide group is closed in the bound dye ID1157. As a result the perylene core vibrations should be per se slightly different.

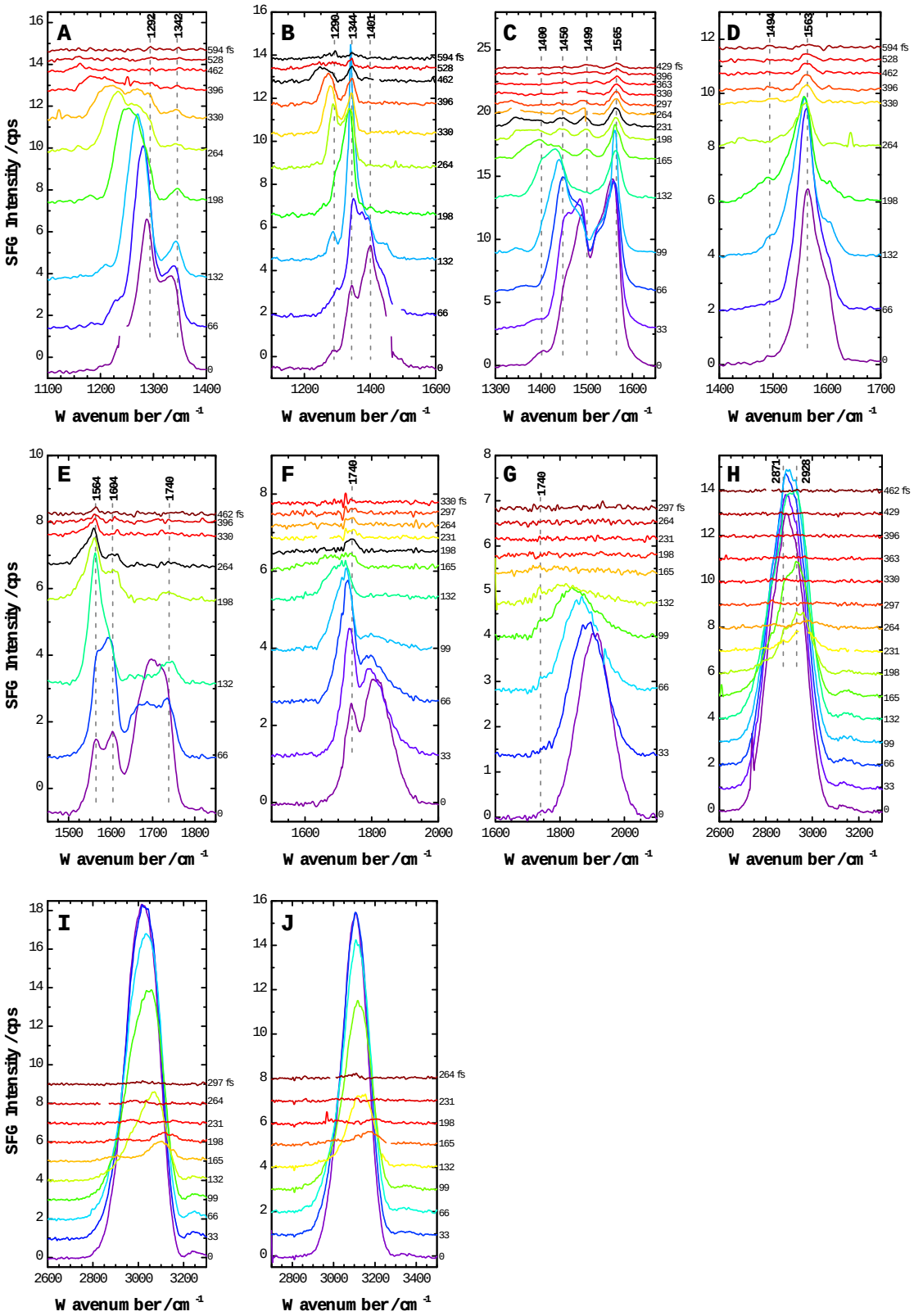

Fig. 4.26: Sets of time delay-shifted spectra of ID1152 bound to a TiO_2 film spin-coated on a CaF_2 prism at various spectral positions. Set (A) is centered at 1300 cm^{-1}, (B) at 1380 cm^{-1}, (C) at 1480 cm^{-1}, (D) at 1560 cm^{-1}, (E) at 1680 cm^{-1}, (F) at 1780 cm^{-1}, (G) at 1880 cm^{-1}, (H) at 2890 cm^{-1}, (I) at 2980 cm^{-1} and (J) at 3080 cm^{-1}.

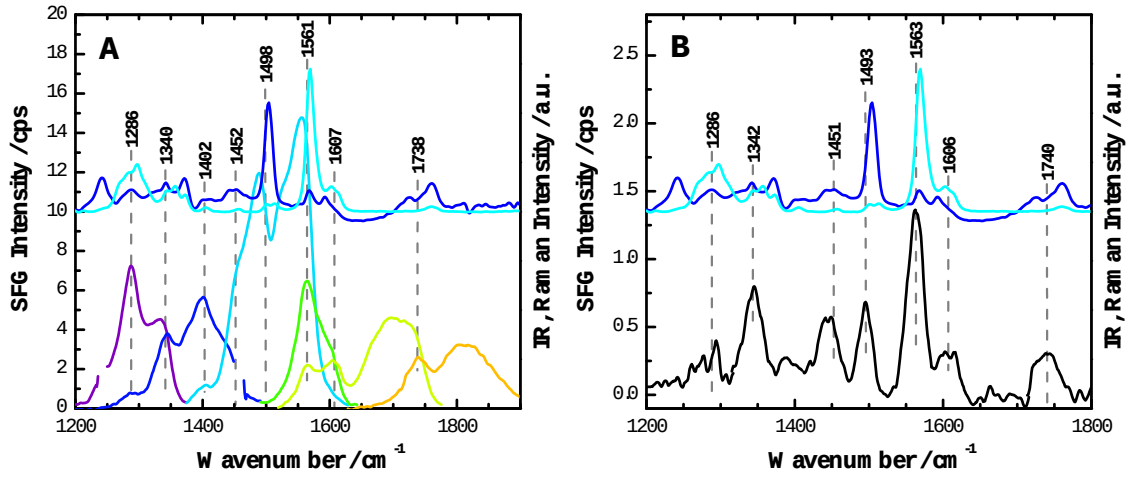

Fig. 4.27: (A) Overlay of VSFG spectra without temporal delay of the Vis beam (*rainbow colors*) and (B) with temporal delay (*black*) of bound ID1152 at different spectral positions in comparison with IR (*blue*) and Raman (*cyan*) spectra of bound ID1152.

Relevant to the analysis of the binding type of the anhydride group is the band at 1740 cm^{-1}. This band does not exactly overlap with corresponding IR and Raman bands. This means that the associated vibration is due to a surface-specific behavior of the dye molecules which cannot be resolved with IR and Raman spectroscopy. It is possible that this band is a shifted anhydride group band or a new band. In order to clarify the origin of this band it is useful to recall the binding mechanism of the anhydride group (Fig. 4.28). An hydroxyl group from the TiO_2 surface attacks the anhydride group and opens it. A carboxylate bound in a bidentate coordination and a free acid group are formed. The acid group can stay free or react further, if there are enough TiO_2 docking sites, to form a bidentate coordination. The vibration of the carbonyl stretch in a free acid group would occur around 1740 cm^{-1} [29, 30]. A further hint that the band at 1740 cm^{-1} is due to a carbonyl stretch in a free acid group comes from the IR spectra of the free dyes ID1157 and SF18 which exhibit their band associated to the carbonyl stretch of the acid group at 1740 cm^{-1} (Fig. 4.7 A and B).

Another possibility would be that some dye molecules bind in a bidentate fashion and additional dye molecules incorporate into the ordered dye layer through π-π stacking but only bind by physisorption via a closed anhydride group. Through physisorption the anhydride group ends up in a different molecular environment resulting in a shift of the band corresponding to the anhydride carbonyl stretches. Here π-π stacking might be a possible interaction between the perylene cores of the dye molecules because the binding position of the dyes with closed anhydride group is not restricted by docking sites. This possibility will be discussed further in the context of the VSFG spectra of bound NA and K2NA. The adsorption of dyes with closed anhydride group would explain the remaining IR intensity of the anhydride group bands in the spectrum of the bound dye ID1152 (Fig. 4.7 C). Although this intensity could also come from multilayer formation due to dye-dye interactions other than incorporation in the ordered layer. If that was the case VSFG spectroscopy gives us the possibility to look through this multilayer and detect the band arising from a free acid group which is obscured by the anhydride group

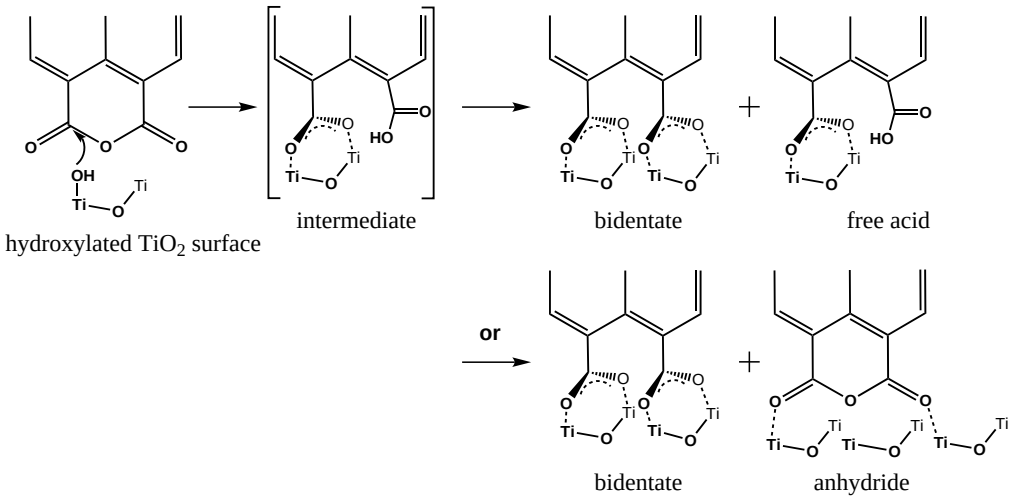

Fig. 4.28: Possible binding mechanism of the anhydride group to TiO_2.

bands in the IR spectrum. With this technique it is possible to distinguish between dye behavior in the bulk of the sample and at the surface of a thin TiO_2 film.

4.2.5.4.1 Comparison of VSFG spectra of ID1152 and ID28 both bound to TiO_2 Just as the results of the binding mode of bound ID1157 should be confirmed by studies of the dye SF18, those obtained from the bound dye ID1152 are supposed to be confirmed by investigations on the dye ID28. The measured time delay-shifted spectra of bound ID28 are presented in Fig. 4.29. The comparison of the spectra of ID1152 (Fig. 4.26) with the ones of ID28 shows that the intensity of the spectra of ID28 is slightly stronger. The reason might be, as for the comparison of the spectra of the dyes ID1157 and SF18, a slightly different sample quality. The spectral shapes of the delay-shifted spectra at comparable center frequencies (1280, 1460, and 1560 cm^{-1}) are very similar and different at differing center frequencies (1370, 1620, 1720, and 1820 cm^{-1}). Especially the sets at 1370 cm^{-1} differ strongly in shape as well as peakwise. A detailed peak comparison is shown in Fig. 4.30. Peak positions appear to be slightly different in the resonant VSFG spectra of bound ID1152 and ID28. The most striking difference is the presence of a peak at 1344 cm^{-1} in the spectrum of ID1152 which is not present in the spectrum of ID28 (the latter shows a band instead at 1371 cm^{-1}). Similar to the comparison of the peaks in the spectra of ID1152 and ID1157 it is assumed here that the different side chains cause different perylene vibrations to dominate. Furthermore, the peaks around 1450 and 1500 cm^{-1} are slightly shifted. This peak-shift is ascribed to the chirp of the Vis pulse as previously mentioned. This is relevant here because the resonant spectra representing these peaks are chosen at different time delays in order to account for all peaks detected in the series of delay-shifted spectra.

As of now, no explanation can be given as to why the peak at 1606 cm^{-1} is not present in the spectrum of bound ID28. Besides, it is important to note that the band at 1740 cm^{-1} in the spectrum of ID1152 appears slightly shifted to 1750 cm^{-1} in the spectrum of ID28. Consequently, the band at 1750 cm^{-1} overlaps exactly with the anhydride group band in the IR spectrum of bound ID28. This finding supports the assumption that dye molecules with a closed anhydride group incorporate into the layer of bound dye molecules at the TiO_2 surface and rules out the option of a free acid group. Overall however the VSFG

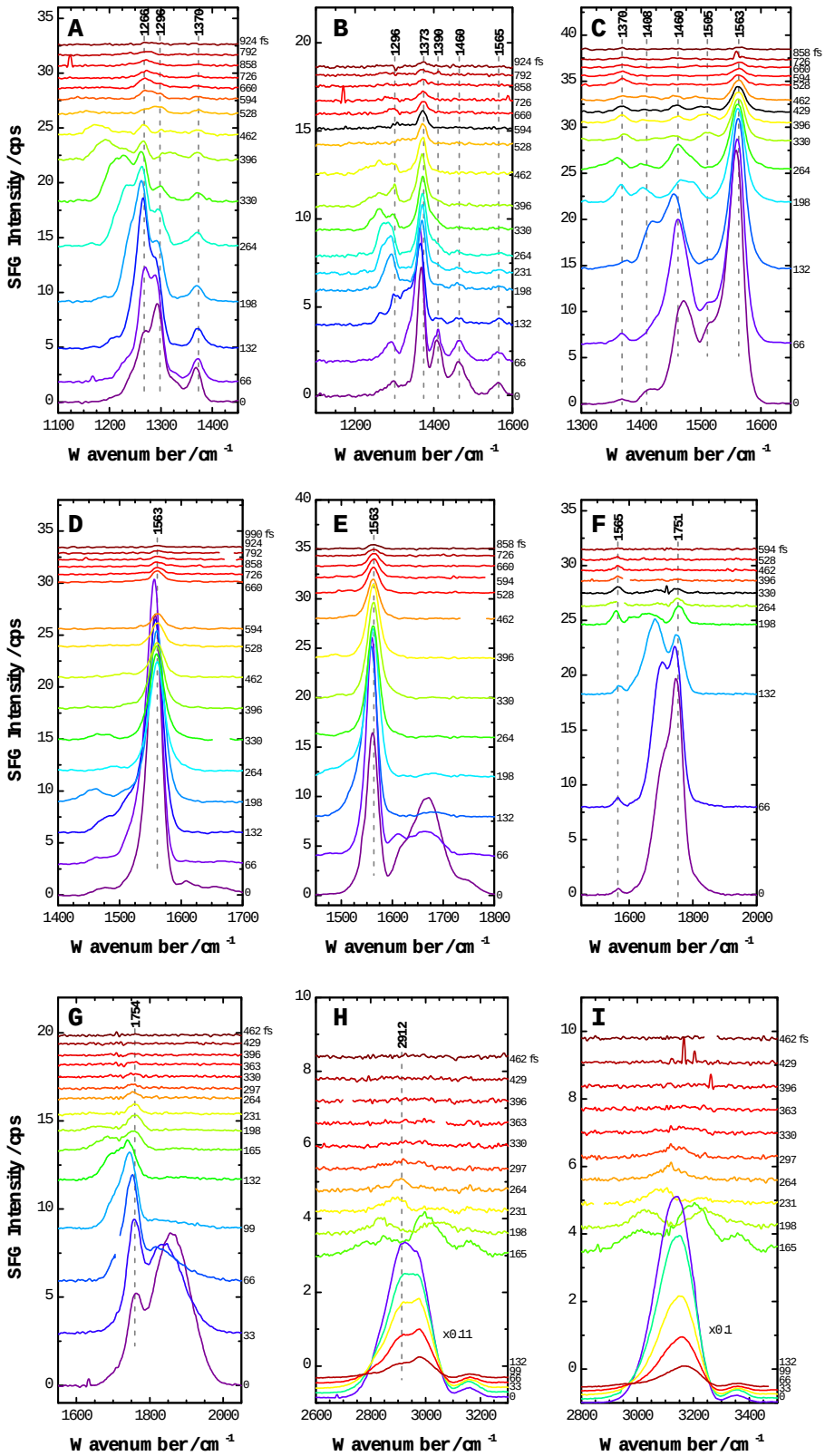

Fig. 4.29: Sets of time delay-shifted spectra of ID28 bound to a TiO_2 film spin-coated on a CaF_2 prism at various spectral positions. Set (A) is centered at 1280 cm^{-1}, (B) at 1370 cm^{-1}, (C) at 1460 cm^{-1}, (D) at 1560 cm^{-1}, (E) at 1620 cm^{-1}, (F) at 1720 cm^{-1}, (G) at 1820 cm^{-1}, (H) at 2890 cm^{-1} and (I) at 3100 cm^{-1}.

study of ID28 confirms the outcome of the investigations of ID1152, meaning that both dyes form an ordered layer on the TiO_2 surface and show a band in the region of the anhydride group.

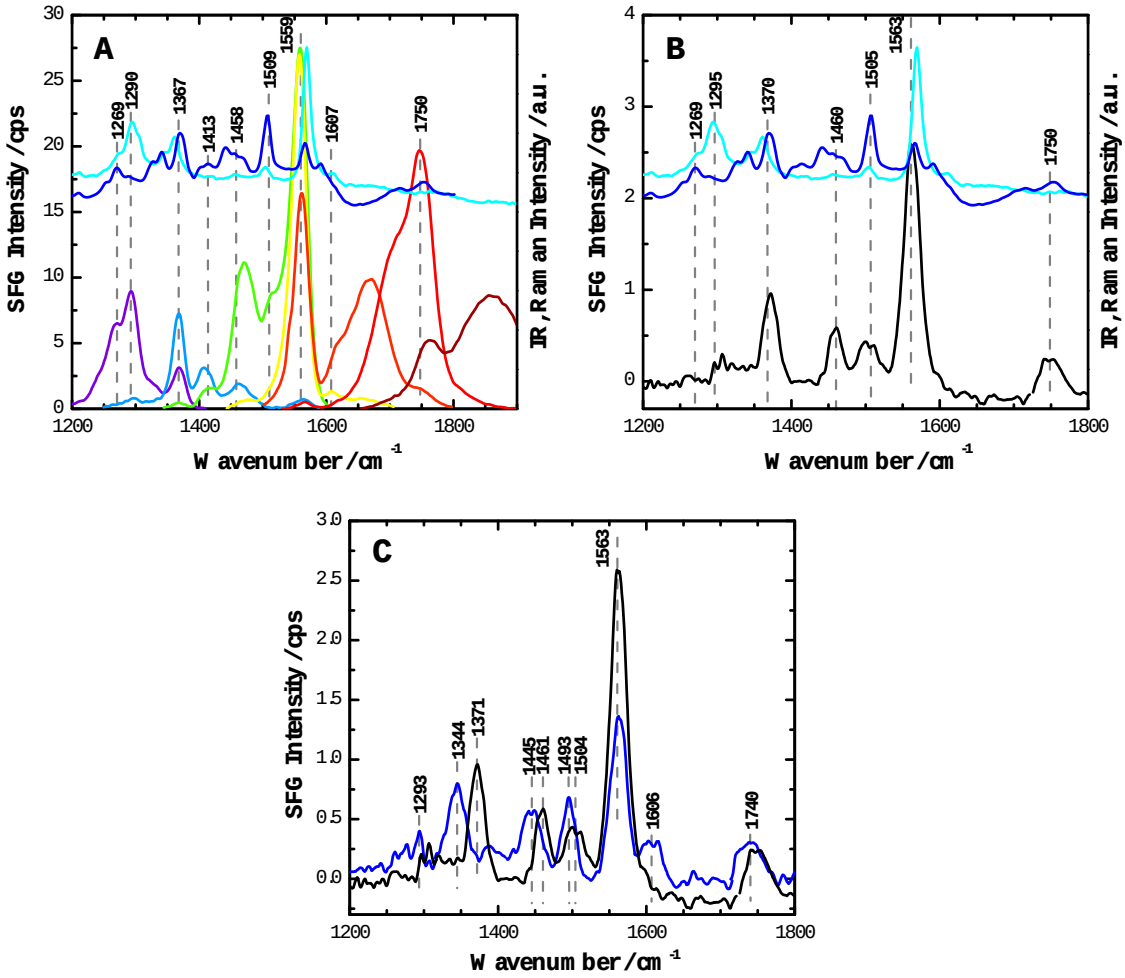

Fig. 4.30: (A) Overlay of VSFG spectra without temporal delay of the Vis beam (*rainbow colors*) and (B) with temporal delay (*black*) of bound ID28 at different spectral positions in comparison with IR (*blue*) and Raman (*cyan*) spectra of bound ID28. (C) Comparison of delay-shifted spectra of ID1152 (*blue*) and ID28 (*black*).

4.2.5.4.2 Water influence on ID1152 dye layer bound to TiO_2 thin film Similar to ID1157, the influence of water on the ID1152 layer is studied. The sets of time delay-shifted spectra that are obtained from the ID1152 dye layer in contact with water are presented in Fig. 4.31. As with the dye ID1157 the intensity of the spectra of ID1152 taken in air at zero time delay (Fig. 4.26) increases upon addition of water. This intensity enhancement is not due to a further ordering of the previously dried dye layer (see Section 4.2.5.4) induced by water but to an increase of NR background as will be seen in the following discussion.

The overall spectral shape of the spectra taken in air and in water is the same due to the choice of identical center frequencies. The spectra without temporal delay and the

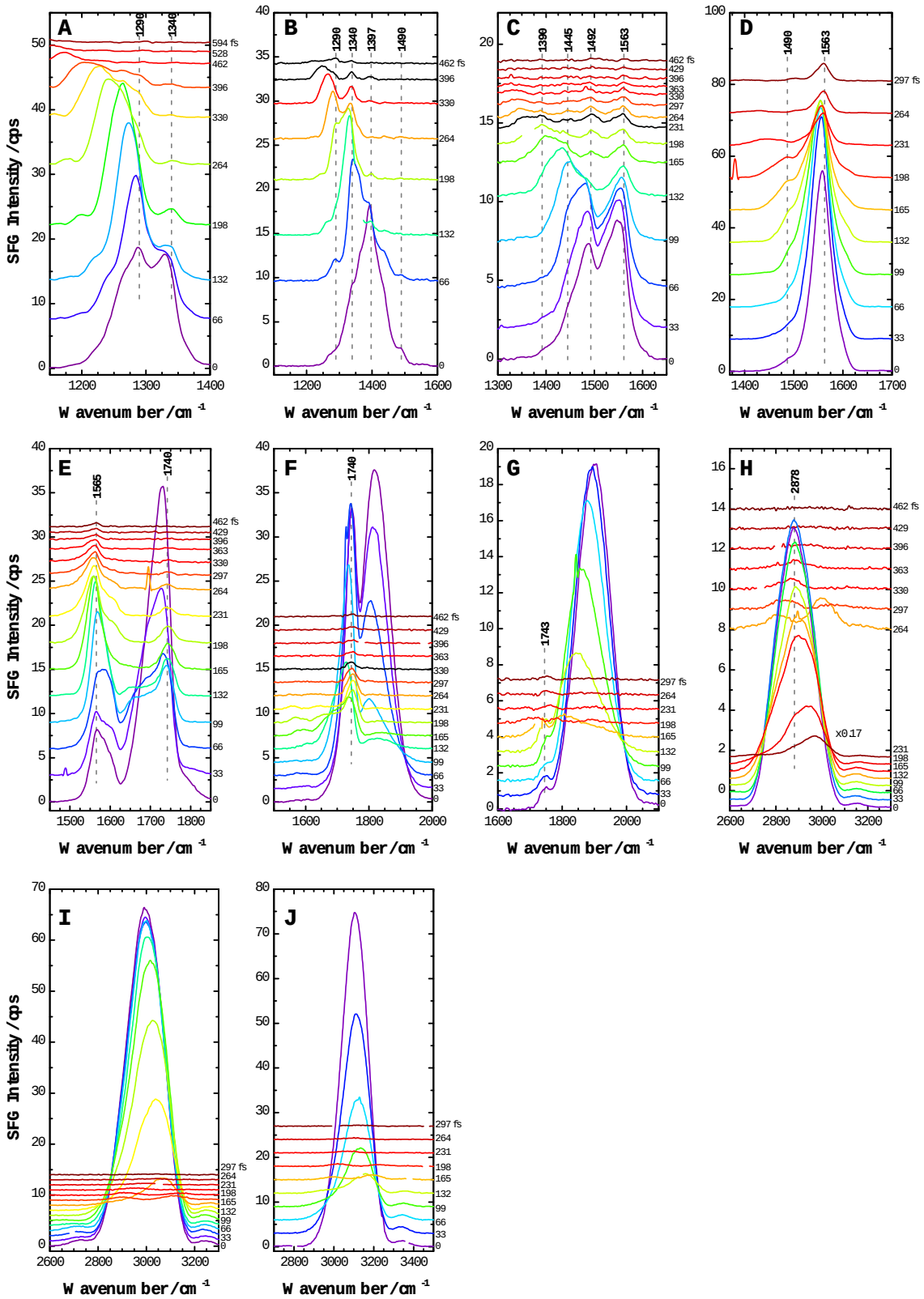

Fig. 4.31: Sets of time delay-shifted spectra of ID1152 bound to a TiO_2 film spin-coated on a CaF_2 prism in contact with water at various spectral positions. Set (A) is centered at 1300 cm^{-1}, (B) at 1380 cm^{-1}, (C) at 1480 cm^{-1}, (D) at 1560 cm^{-1}, (E) at 1680 cm^{-1}, (F) at 1780 cm^{-1}, (G) at 1880 cm^{-1}, (H) at 2890 cm^{-1}, (I) at 2980 cm^{-1} and (J) at 3080 cm^{-1}.

resonant spectra recorded of the ID1152 dye layer under both conditions are compared in Fig. 4.32 A and B, respectively. The intensity increase upon addition of water as well as the high similarity of the spectral shapes is clearly seen and the peak position is also the same. It is important to note that the resonant spectra of ID1152 measured in air and in water are composed of time delay-shifted spectra taken from sets obtained at identical center frequencies but slightly different time delays. This was necessary in order to preserve peak information. However, the peak at 1565 cm^{-1} is for both conditions represented by a time delay-shifted spectrum obtained at a center frequency of 1480 cm^{-1} and a time delay of 231 fs. These spectra still contain a weak NR background but both to the same degree (Fig. 4.26 C and Fig. 4.31 C) so that the intensity of the peak at 1565 cm^{-1} can be compared. Just as in the spectra of ID1157, the peak intensity decreases by a little bit more than half the value upon addition of water. This demonstrates that also for the dye with the anhydride group the order of the dried dye layer bound to TiO_2 induced by a first addition of water is reduced under the influence of subsequently added water. Furthermore, the band at 1740 cm^{-1} is present in both spectra indicating that the coordination of the dye molecules does not change in an aqueous environment.

4.2.5.4.3 Substrate influence on VSFG spectra of ID1152 bound to TiO_2 thin film To complete the picture the influence of the substrate on the VSFG spectra of bound ID1152 is studied as well. It is sought to confirm that VSFG probes the free interface of the sample. The sets of time delay-shifted spectra that are obtained from a ID1152 layer adsorbed to a TiO_2 film on an Au wafer are depicted in Fig. 4.33. The intensity of the spectra at early time delays is significantly higher for the film on Au than on CaF_2 (Fig. 4.26) showing the strong NR contribution originating from the Au substrate itself. However, this large intensity difference for the spectra at early time delays vanishes in the course of the delay-shifting process so that at later time delays the intensities of spectra taken on different substrates become similar again and thus comparable. The present sets of time delay-shifted spectra hence show once more the power of the delay-shifting technique which allows for the suppression of NR contributions to the VSFG spectrum. Not only the intensities become similar but also the spectral shapes. One exception though is found for the sets of time delay-shifted spectra recorded at a center frequency of 1380 cm^{-1}. The spectra measured of the sample on the Au wafer exhibit more and sharper peaks. This it not seen in the corresponding spectra of the dye ID1157 (Fig. 4.23 B). A possible reason might be the less pronounced electronic enhancement of the perylene peaks for the dye ID1152. As a result no dominating peaks are observed, only peaks with similar intensity. Moreover, the spectra of ID1152 only appear to show more peaks since the same peaks are also found in the spectrum of ID1157 upon closer inspection. The peak at 1370 cm^{-1} is just too strong so that small side peaks seem to disappear. Not only the set of time delay-shifted spectra of bound ID1152 on Au at a center frequency of 1380 cm^{-1} shows some peculiarities but also the one centered at 1780 cm^{-1}. This last set seems to contain an unidentified peak at 1717 cm^{-1}. However, this peak was found to be an artifact as it could be traced back to the background spectrum taken before the measurement. The presence of this peak in the VSFG spectrum indicates that the external background changed during the course of the measurement. Knowing this, the interpretation of resonant peaks can still be carried out.

Just as with the other samples the spectra without temporal delay and the resonant spectra of bound ID1152 on Au are compared to the corresponding spectra of bound ID1152 on the CaF_2 substrate in Fig. 4.32 C and D, respectively. The peak positions are equiva-

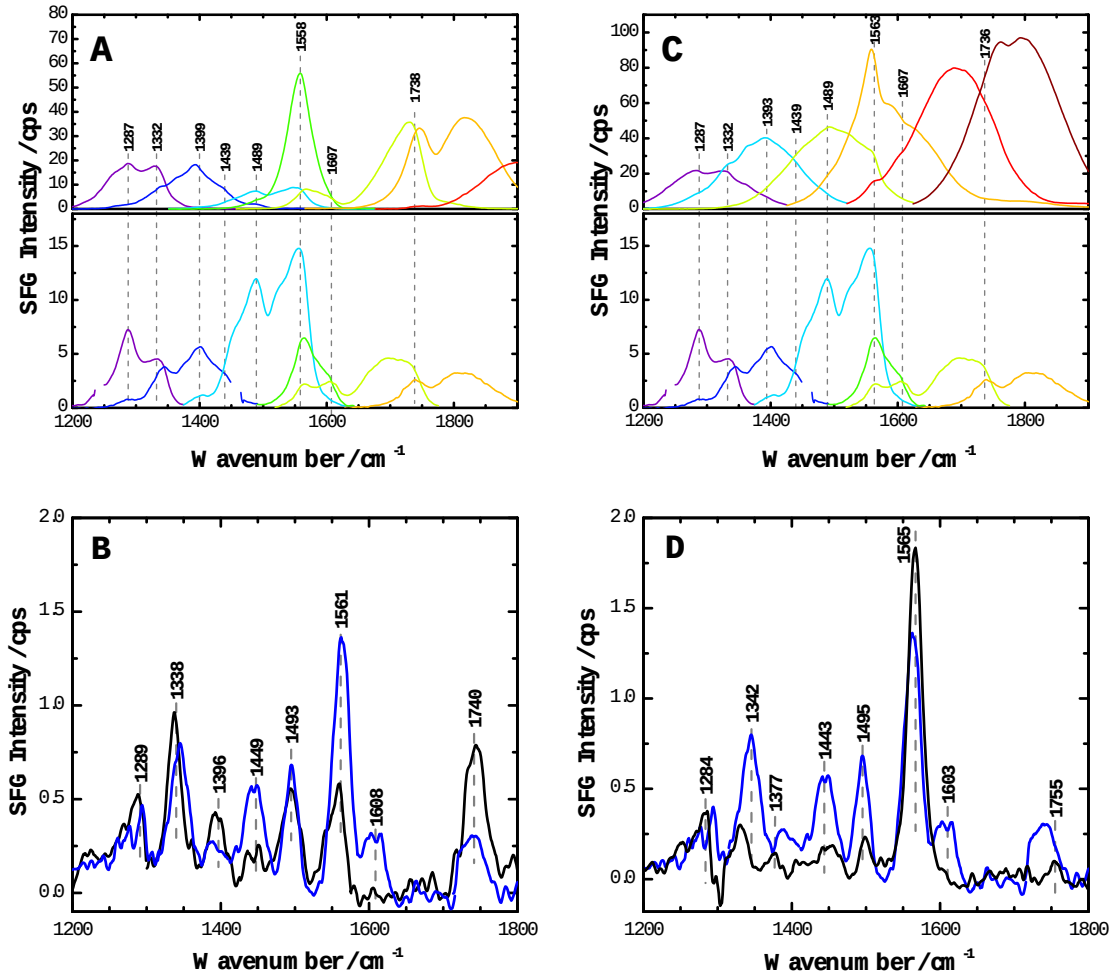

Fig. 4.32: (A) Comparison of VSFG spectra without temporal delay of the Vis beam of bound ID1152 in air (bottom row) and in water (top row) and (B) overlay of the corresponding VSFG spectra with temporal delay, in air (*blue*) and in water (*black*). (C) Comparison of VSFG spectra without temporal delay of the Vis beam of bound ID1152 on CaF_2 prism (bottom row) and on Au wafer (top row) and (D) overlay of the corresponding VSFG spectra with temporal delay, on CaF_2 prism (*blue*) and on Au wafer (*black*).

lent but the intensities cannot be compared because the delay-shifted spectra could not be chosen from sets at similar center frequencies and with identical time delays without losing peak information. With the chosen parameters the intensity of the resonant spectra differs slightly. This observation should not lead however to the conclusion that different interfaces are probed on the different substrates because high quality spectra which could be readily compared for the dye ID1157 are hardly obtained from the dyes with the anhydride group due to the low signal output of these samples. Thus, data reproducibility is more complicated. Since the same film preparation and the same experimental conditions were used as for ID1157, also the same interface as for ID1157 should be probed. Nevertheless, the band at 1755 cm^{-1} in the spectrum of bound ID1152 on Au supports, just as with the spectra of bound ID28, the idea that some dye molecules with a closed anhydride group are involved in the dye coordination on the TiO_2 surface.

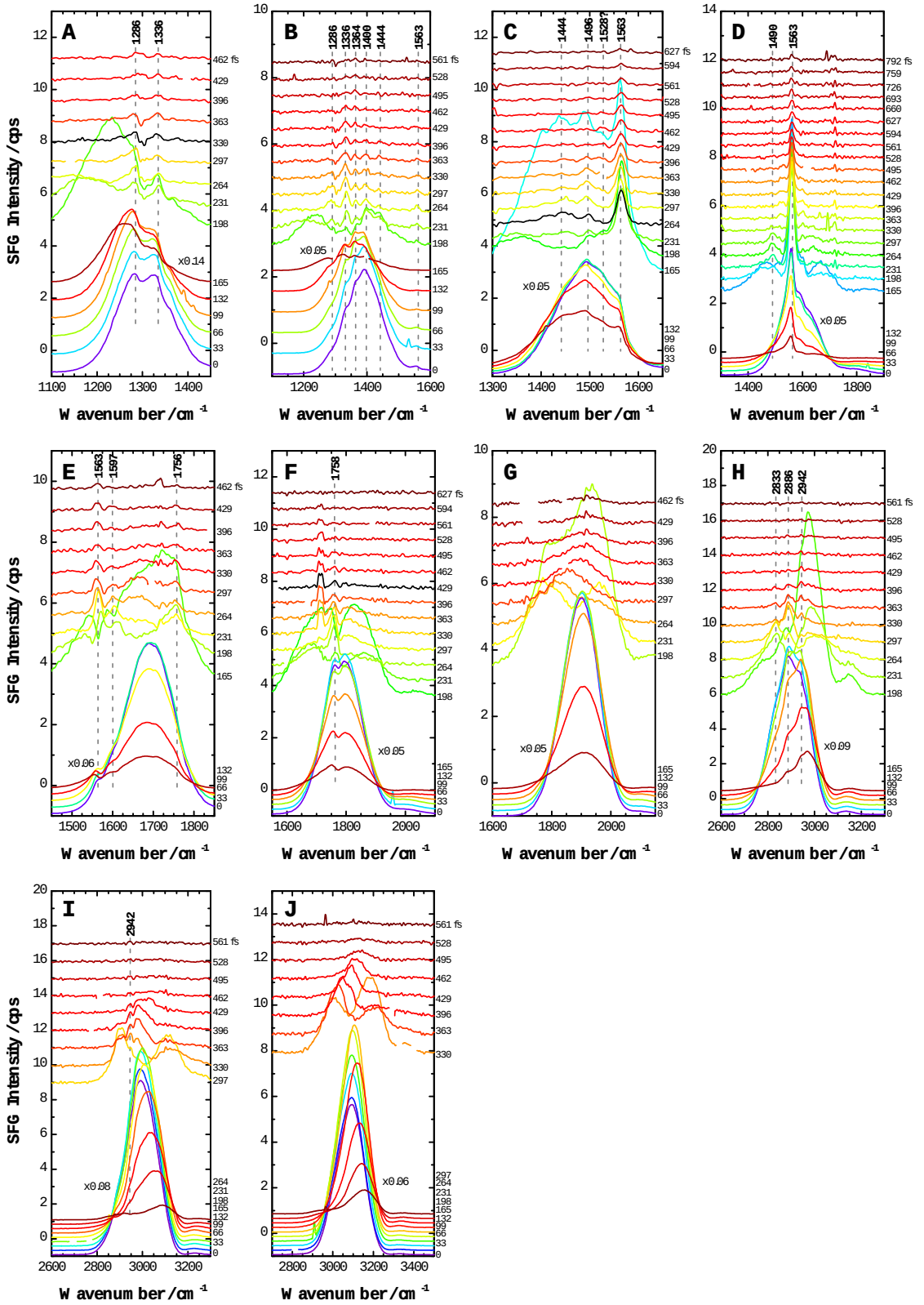

Fig. 4.33: Sets of time delay-shifted spectra of ID1152 bound to a TiO_2 film spin-coated on an Au wafer at various spectral positions. Set (A) is centered at 1280 cm^{-1}, (B) at 1380 cm^{-1}, (C) at 1480 cm^{-1}, (D) at 1580 cm^{-1}, (E) at 1680 cm^{-1}, (F) at 1780 cm^{-1}, (G) at 1880 cm^{-1}, (H) at 2880 cm^{-1}, (I) at 2980 cm^{-1} and (J) at 3080 cm^{-1}.

4.2.5.5 Surface specific binding of anhydride group of NA

With the help of the surface specific binding study of NA and K2NA it is sought to clarify which of the two theories regarding the origin of the band at 1740 cm^{-1} in the spectra of bound ID1152 and ID28 is more likely. Is the band a result of free acid groups due to binding of only the carboxylate after opening of the anhydride group or a result of molecules with closed anhydride group present at the TiO_2 surface? The obvious advantage of the model substance NA lies in its simpler structure compared to the dye structures as well as the known band assignment. The binding mode of NA as well as of K2NA was defined as a bidentate bridging coordination for both of the newly formed groups of the opened anhydride (Section 4.2.4.5). The origin of the residual anhydride group intensity in the IR spectra of bound NA was not tackled. In comparison to the dye VSFG spectra, those of the model substances are much more difficult to obtain. The spectra without temporal delay of the Vis beam (Fig. 4.34 and Fig. 4.35) exhibit a much lower VSFG signal so that great care is necessary in order to distinguish the resonant signal from noise or external background peaks which become more dominant if the overall signal from the sample is low. In order to validate the results the measurements were repeatedly performed and the spectra were found to be reproducible. In addition, the obtained spectra were compared to the external background spectra to avoid having background-related peaks interpreted as resonant peaks.

However, the intensities of the resonant spectra of the dyes (ID1152 and ID28) and the model substances are almost the same. The intensity difference at the beginning of the time delay series must thus be due to NR contributions. The only NR source apart from TiO_2 are the dyes themselves. The question arises why the spectra of the dyes exhibit a strong NR background whereas the ones of NA and K2NA do not. The answer is the electronic resonance condition under which the spectra are recorded. An electronic resonance condition is not fulfilled for NA as it possesses its electronic absorption maxima below 360 nm and is hence not excitable by Vis light [203]. This must also be the reason why NA and K2NA are not as readily detected as the dyes because their signal is not resonantly enhanced. Hence, the NR contribution in the VSFG spectra of bound NA and K2NA must be due to the TiO_2 film. This finding is understood by comparing the sets of delay-shifted spectra of pure TiO_2 with the ones of NA and K2NA (compare Fig. 4.12 to Fig. 4.34 and Fig. 4.35). Their intensities and spectral shapes are almost identical apart from the peaks in the spectra of NA and K2NA. These measurements on- and off-resonance nicely confirm the assumption that the origin of the NR contribution in the dye spectra is a result of an electronic resonance enhancement.

Overall the intensity of the delay-shifted spectra of K2NA is slightly higher than the one of the spectra of NA. This result suggests that the ordering of the NA molecules is less pronounced than the one of the K2NA molecules. Moreover, this could mean that less NA molecules are bound. This observation agrees well with the finding that K2NA gives already reasonable VSFG signal after overnight immersion of the TiO_2 film whereas NA only gives a signal after at least two days of immersion. The reason most probably lies in the required opening of the anhydride and the related fact that its binding takes more time than the binding of the two carboxylates of K2NA. In addition, the binding might occur less frequently.

The detected peaks for both samples are presented in a summarizing way in Fig. 4.36 which shows the spectra at zero time delay and the resonant survey spectra overlaid

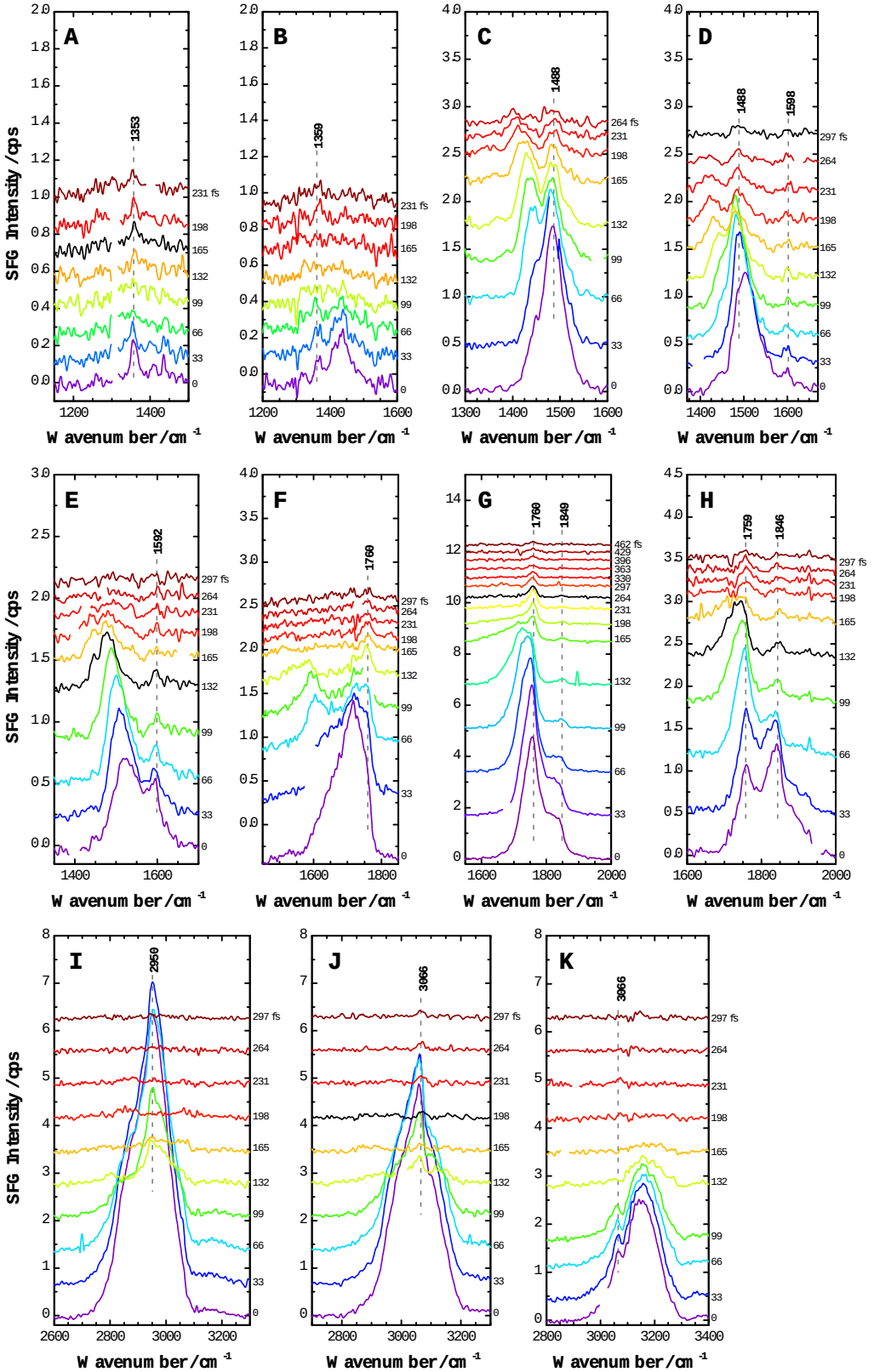

Fig. 4.34: Sets of time delay-shifted spectra of NA bound to a TiO_2 film spin-coated on a CaF_2 prism at various spectral positions. Set (A) is centered at 1320 cm^{-1}, (B) at 1370 cm^{-1}, (C) at 1450 cm^{-1}, (D) at 1500 cm^{-1}, (E) at 1540 cm^{-1}, (F) at 1630 cm^{-1}, (G) at 1750 cm^{-1}, (H) at 1800 cm^{-1}, (I) at 2890 cm^{-1}, (J) at 3000 cm^{-1} and (K) at 3100 cm^{-1}.

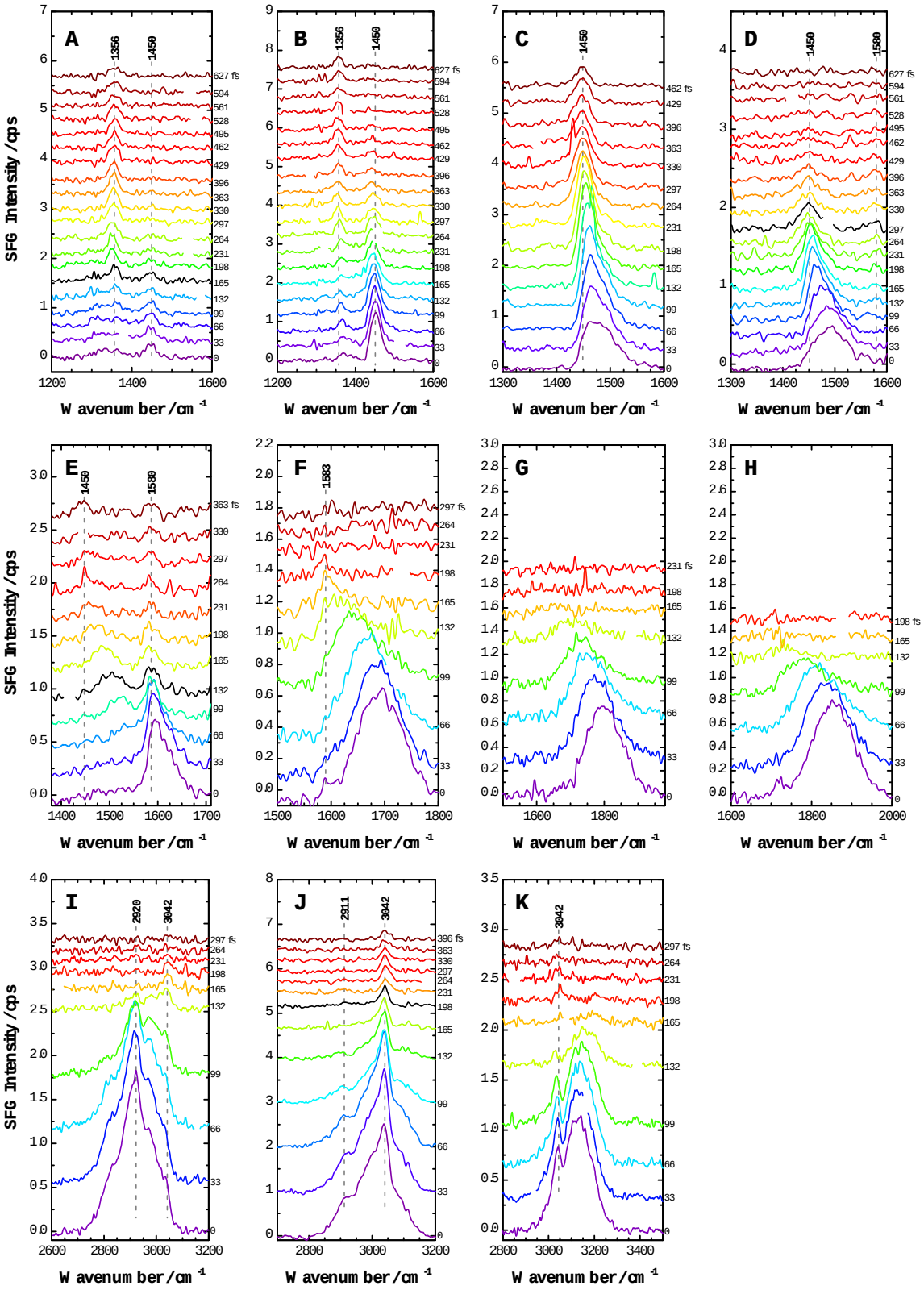

Fig. 4.35: Sets of time delay-shifted spectra of K2NA bound to a TiO_2 film spin-coated on a CaF_2 prism at various spectral positions. Set (A) is centered at 1330 cm^{-1}, (B) at 1390 cm^{-1}, (C) at 1460 cm^{-1}, (D) at 1500 cm^{-1}, (E) at 1580 cm^{-1}, (F) at 1680 cm^{-1}, (G) at 1780 cm^{-1}, (H) at 1830 cm^{-1}, (I) at 2890 cm^{-1}, (J) at 2980 cm^{-1} and (K) at 3100 cm^{-1}.

with the IR and Raman spectra of the free and bound molecules in order to allow exact assignment of the observed peaks in the VSFG spectra. The spectra at zero time delay do not clearly show the resonant peaks which are obvious in the sets of delay-shifted spectra because of the overwhelming NR background. During the delay-shifting process though resonant peaks became clearly observable. For comparison, the resonant spectra were build up using delay-shifted spectra taken at identical center frequencies and time delays. The most obvious difference between the two resonant spectra is seen in the spectral region around 1800 cm^{-1}. While bound NA exhibits two bands at 1760 and 1841 cm^{-1} in this region, K2NA exhibits no bands. The band at 1760 cm^{-1} is assigned to a shifted anhydride group band and not to a free acid group because the shift amounts only to 9 cm^{-1} compared to the free anhydride group band. This goes along with the finding for the dye ID28. The VSFG spectrum of this dye shows a band that overlaps with a corresponding anhydride group band in the IR spectrum of bound ID28 (Fig. 4.30 B). Since the anchor moiety is the same for the dye ID1152, it is concluded that the band at 1740 cm^{-1} in the VSFG spectrum of bound ID1152 (Fig. 4.27 B) is also due to a closed anhydride group vibration. Moreover, the absence of a band in the VSFG spectrum of bound K2NA indicates that the band in the spectrum must originate from a group that is distinct from those of the NA molecule, thus leaving the anhydride group as only possibility.

The VSFG spectra of the bound anhydride group molecules thus demonstrate that the molecules form an ordered layer of dye molecules on the TiO_2 surface. Some molecules bind with an opened anhydride group and others just incorporate into the ordered layer with a closed anhydride group. The molecules with the closed anhydride group cannot just lie on top of the bound dye molecules because in this case the symmetrical carbonyl stretch of the anhydride group could not be detected with VSFG spectroscopy. This conclusion is based on symmetry arguments. Free molecules lying flat on the bound molecules would arrange with the anhydride groups pointing in every direction rather than lining up like pearls on a chain. A random, i.e. isotropic orientation of the related dipole moment, which most presumably lies along the long axis of the molecules for the symmetric stretch [204], leads to a cancelation of its contribution to the VSFG signal.

It can also be excluded that the dye molecules all adsorb with a closed anhydride group firstly because the UV/Vis absorption spectra show that the anhydride group opens up and secondly because there is a band observed at 1357 cm^{-1} in the VSFG spectrum of bound NA and K2NA. This band is associated with the $\nu_s(CO_2^-)$ of a carboxylate group as shown in Section 4.2.4.5. The same assignment was made on a similar band observed in a VSFG spectrum of a retinoate monolayer prepared on rutile(110) [105]. This band would not be detected, if all anhydride groups were closed. Not surprisingly, the band is stronger in the spectrum of bound K2NA since these molecules contains two carboxylate groups already in the free state.

The other bands in the spectra of bound NA and K2NA are observed at 1485, 1593, 3066 cm^{-1} and 1452, 1580, 3055 cm^{-1}, respectively. These bands are all associated with the aromatic naphthalene system. While the bands around 1580 cm^{-1} and 3060 cm^{-1} directly overlap with corresponding IR and Raman bands, this is not observed for the bands around 1460 cm^{-1}. One reason might be that bound NA and K2NA orient slightly differently on the surface due to the adsorbed molecules with closed anhydride group in the case of NA. Besides, it is not seldom that surface-specific spectra exhibit slightly different band positions compared to the normal IR and Raman spectra but still represent

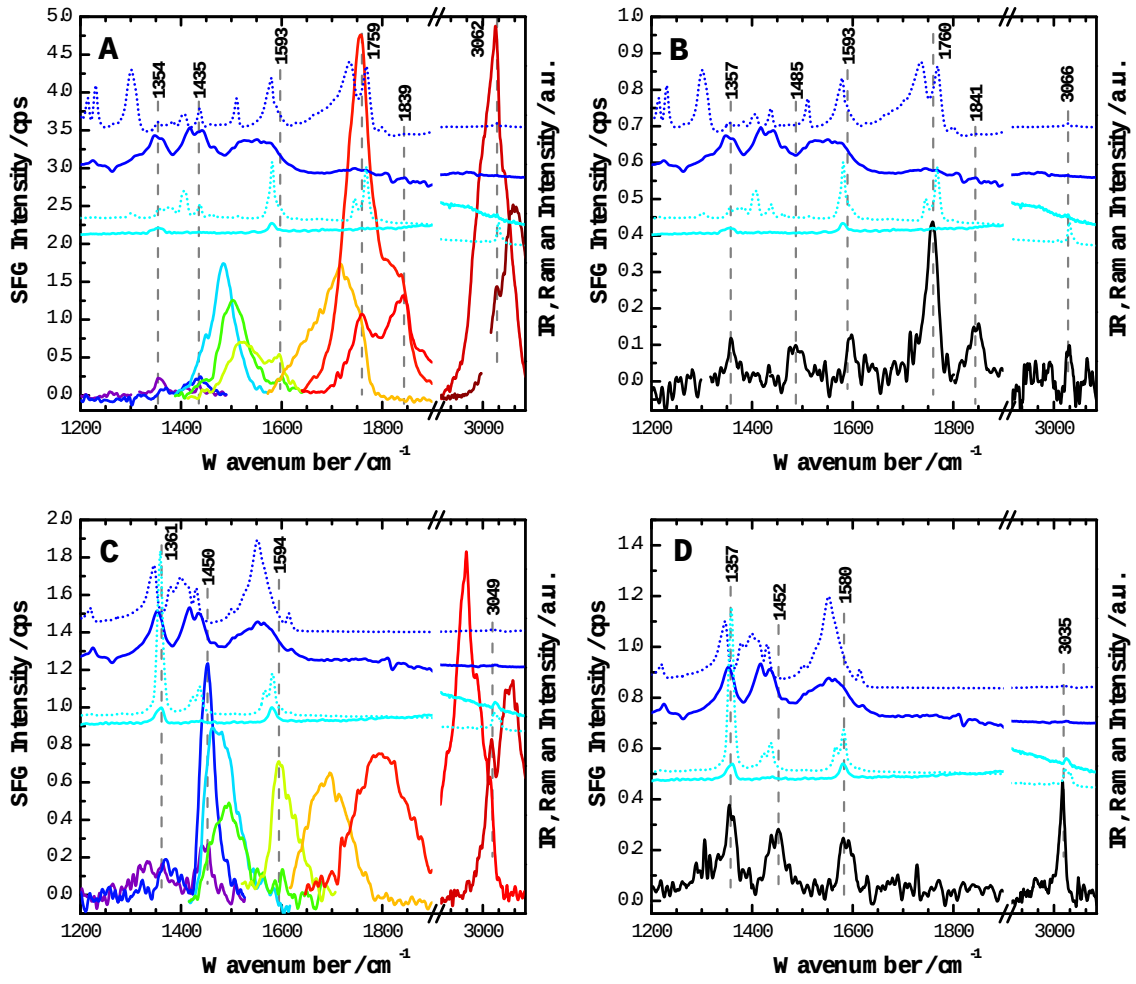

Fig. 4.36: (A) Overlay of VSFG spectra without temporal delay of the Vis beam (*rainbow colors*) and (B) with temporal delay (*black*) of bound NA at different spectral positions in comparison with IR (*blue*) and Raman (*cyan*) spectra of NA, free (*dotted curves*) and bound (*solid curves*) to TiO_2. (C) Overlay of VSFG spectra without temporal delay of the Vis beam (*rainbow colors*) and (D) with temporal delay (*black*) of bound K2NA at different spectral positions in comparison with IR (*blue*) and Raman (*cyan*) spectra of K2NA, free (*dotted curves*) and bound (*solid curves*) to TiO_2.

the same vibrations [142, 173, 205, 206]. Finally, the band at 1841 cm^{-1} in the spectrum of bound NA is due to an overtone or combination of ω(C=C−C−H) vibrations [166].

4.2.5.6 Summary of the binding properties of dyes with anhydride group

UV/Vis absorption, IR and Raman spectroscopic studies on the anhydride group containing molecule ID1152 show that most of the anhydride groups open up upon binding to TiO_2 and that the newly formed carboxylic and carboxylate groups bind in a bidentate bridging coordination to the TiO_2. With further VSFG spectroscopic studies examining also ID28 and NA it is found that the bound dye molecules form an ordered layer on the TiO_2 surface, just as for ID1157, and that additional molecules with closed anhydride group incorporate into this layer. Especially the investigations on the model substance

NA and its cleaved analogue K2NA help in the assignment of new bands in the spectra of the bound molecules and allow to reinforce interpretations of the dye spectra. Water presence slightly disturbs the dye layer ordering but does not destroy its integrity. A simplistic binding model of the dye layer formed by ID1152 on TiO_2 is presented in Fig. 4.37.

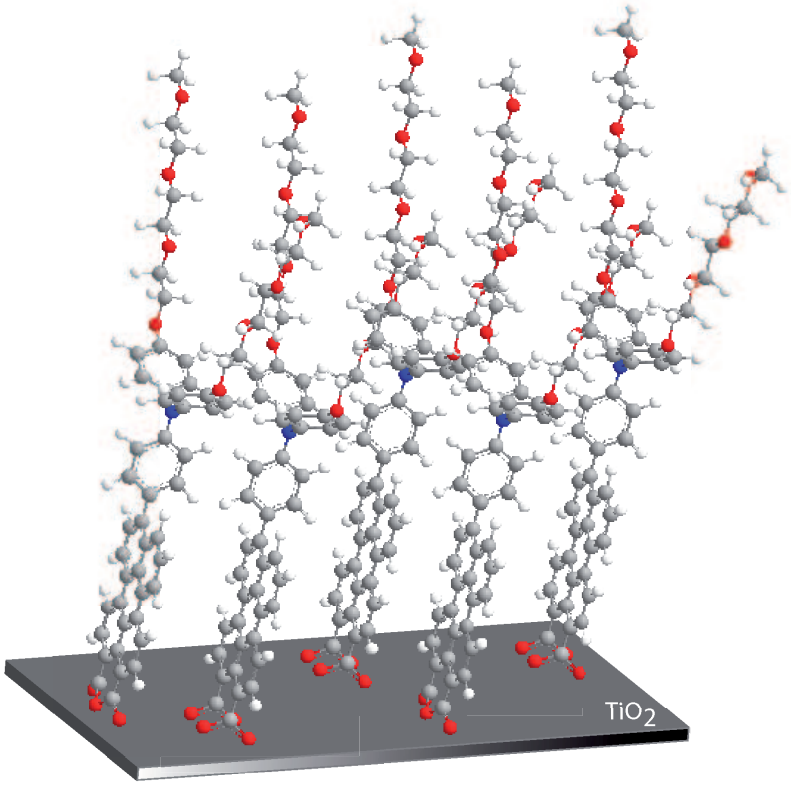

Fig. 4.37: Binding model of ID1152 to TiO_2.

4.2.5.7 Comparison of VSFG spectra of ID1157 and ID1152 bound to TiO_2

After defining the binding mode of the dyes ID1157 and ID1152, a direct comparison of their resonant VSFG spectra can be used to deduce further differences between the two spectra beyond the binding pattern. The respective spectra are compared in Fig. 4.38. It is found that the intensity of ID1157 is about one order of magnitude stronger than the one of ID1152. This is valid for the spectra at zero time delay as well as for the resonant survey spectra. It is to be mentioned that the delay-shifted spectra for both dyes are taken from different spectral regions and at different delay times in order to account for all peaks found during the measurements of the delay series and to combine spectra with all NR background removed. Nevertheless, the intensity trends can be evaluated because the selected delay-shifted spectra of the dye ID1157 are for every spectral region taken at later delay times than the ones of ID1152. And despite the fact that in general the intensity decreases with delay time, the signal intensity of the spectra of ID1157 still remained stronger than that of ID1152.

There are two possible explanations for this difference: 1) a higher surface density and 2) a higher degree of order in the dye layer of ID1157 compared to ID1152. A higher surface

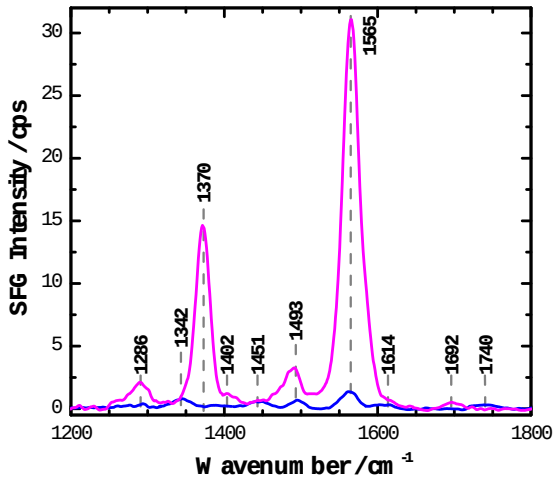

Fig. 4.38: Comparison of the VSFG spectra of ID1157 (*magenta*) and ID1152 (*blue*) bound to TiO_2.

density can be rationalized with the hydroxyl consumption during the adsorption of the two different anchoring moieties. Fig. 4.39 shows that for the adsorption of the carboxylic acid into a bidentate coordination only one hydroxyl group is needed, whereas for the adsorption of an anhydride group two hydroxyl groups are consumed. As a consequence, double the amount of ID1157 can bind compared to ID1152 with the same amount of hydroxyl groups present [74, 163]. A higher ordering of ID1157 can be a result of the higher flexibility of the glycine anchor due to the methylene group around which the bound dye can rotate and align with already bound dyes. This is also necessary for a dense packing of the dye molecules. In the case of the anhydride group, the orientation of the dye on the surface is fixed once bound.

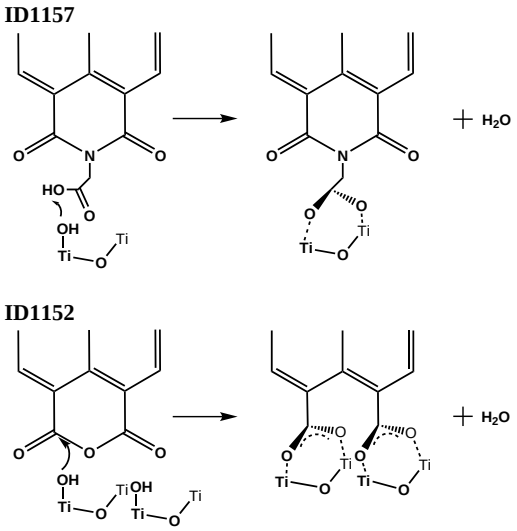

Fig. 4.39: Scheme of hydroxyl consumption for both anchoring moieties.

The amount of dyes that adsorbed to a defined quantity of TiO_2 nanoparticles with from BET measurements known surface area was determined by UV/Vis absorption spectroscopy. The transmittance of a dye solution of known concentration before dye adsorption and the transmittance of the supernatant after dye adsorption was measured. The difference in transmittance was used to calculate the amount of dye molecules adsorbed to the TiO_2. The experiment was performed both for ID1157 and ID1152 and it was found that double the amount of ID1157 molecules adsorbed compared to the amount of ID1152 molecules. The experiments were carried out by L. Pöttinger.

Other important factors that have to be considered when judging the signal intensity are the previously mentioned electronic resonance enhancement condition and the Raman cross sections of the two dyes. It was discussed that the dye ID1157 is more strongly enhanced than the dye ID1152 so that this fact could be a further reason for the higher signal intensity of ID1157 spectra. However, the Raman cross sections are the same for both dyes as can be seen from Raman spectra taken of the free dyes under the same experimental conditions (Fig. 4.40). Both spectra exhibit the same intensity. Moreover, the corresponding IR spectra are also shown. Their intensity is also very similar. Therefore, the VSFG signal from the two dyes, being the result of an IR and Raman process, is expected to be of the same strength as well. The Raman cross section can thus be ruled out as a reason for the VSFG signal difference of the two dyes. This thus leaves the electronic resonance enhancement condition as the only additional explanation for the signal difference apart from differences in surface density and dye layer ordering. The former most certainly influences the VSFG signal to some degree but the latter two are most probably stronger contributors to the dissimilar signal strength.

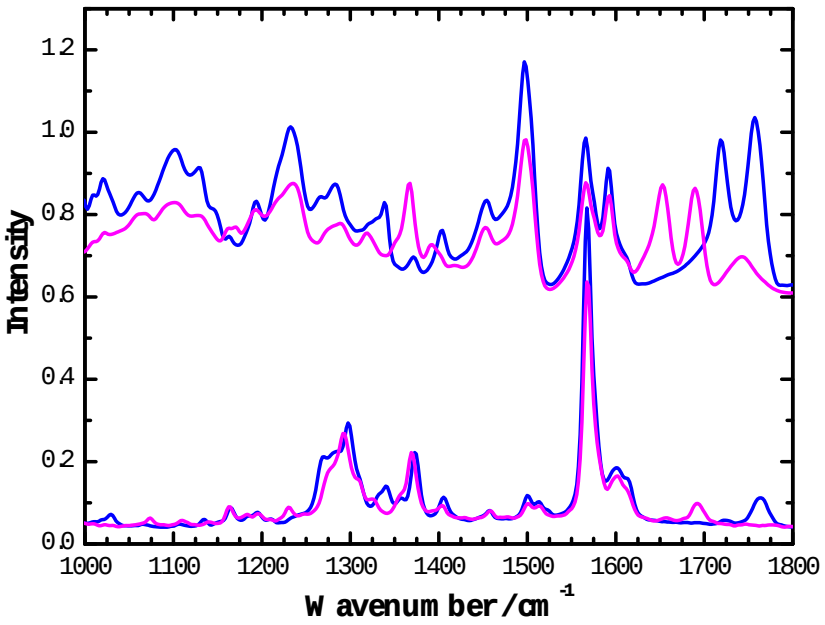

Fig. 4.40: Unnormalized IR and Raman spectra of dyes ID1157 (*magenta*) and ID1152 (*blue*). The IR and Raman spectra are given by the pairs of upper and lower curves, respectively.

4.2.5.8 Structure-function relationship between photocurrent and type of dye binding

As shown in the preceding sections, further insights have been gained into the binding modes of the different dyes on TiO_2. For example, it was found that the carboxylic acid group binds completely all dye molecules present at the TiO_2 surface presumably under a certain tilt angle via a bidentate coordination. In contrast, for the anhydride group it was found that not all molecules bind via bidentate coordination of both of the formed carboxylate groups but that some additional molecules also present at the TiO_2 surface bind only via physisorption of the closed anhydride group. Furthermore, it was found that the surface density of the adsorbed dyes was dependent on the anchoring group. The carboxylic acid group enables double the amount of dye to bind compared to the anhydride anchor. At the same time, the higher flexibility of the acid group as part of the glycine anchor allows for an increased order in the densely packed dye layer. Now, it remains to be determined how these different binding modes can be correlated to the dyes' photocurrent (see Section 4.2.2).

The electron injection from the dye to the TiO_2 depends on the electronic coupling between the LUMO of the dye and the CB of TiO_2 [27]. Among others the electronic coupling is influenced by the anchor group of the dye and its binding strength. In the situation where the anhydride group opens and binds both the carboxylic acid and the carboxylate formed, electron injection is superior through this group to electron injection through the carboxylic acid group [58]. However, when the anhydride group binds in its closed form, electron injection is much faster through the carboxylic acid anchor [63]. In addition, the photocurrent is dependent on the amount of dye adsorbed since more dyes can absorb more light and consequently generate more electrons. In this regard, an ordered dye layer is advantageous because it accommodates more dye molecules. Knowing the conditions for a high photocurrent it becomes quite understandable why ID1157 exhibits a much stronger one than ID1152: the dye layer of ID1157 is much denser and, in addition, all of its molecules are strongly bound. Moreover, the tilted geometry of ID1157 might allow for fast through-space electron tunneling from the perylene core to the TiO_2 surface [72].

4.3 Methanol-TiO_2 interaction studied by VSFG spectroscopy

Since the main idea of the S2F project is to use the dye-functionalized TiO_2 nanoparticles to convert CO_2 to methanol (MeOH) it was attempted in a first experiment to detect methanol on a pure TiO_2 film with VSFG. Only if pure methanol or a mixture of methanol and water can be probed, VSFG can be employed as a technique for the *in situ* detection of methanol as a potential product during the CO_2 reduction reaction. The focus of the investigations is put on the CH vibrations of methanol since most spectral information is expected there. Fig. 4.41 A shows a set of time delay-shifted VSFG spectra of a TiO_2 film in contact with methanol at a center frequency of 2890 cm^{-1}.

The spectrum at zero time delay exhibits two bands with the high-frequency one being asymmetric. These bands, found at 2835 and 2938 cm^{-1}, can be considered as real because they keep their position and disappear at longer delay times. The asymmetry of the latter band is most probably the result of an underlying band at 2900 cm^{-1}. All these bands can be attributed to molecularly adsorbed methanol. They are assigned to the symmet-

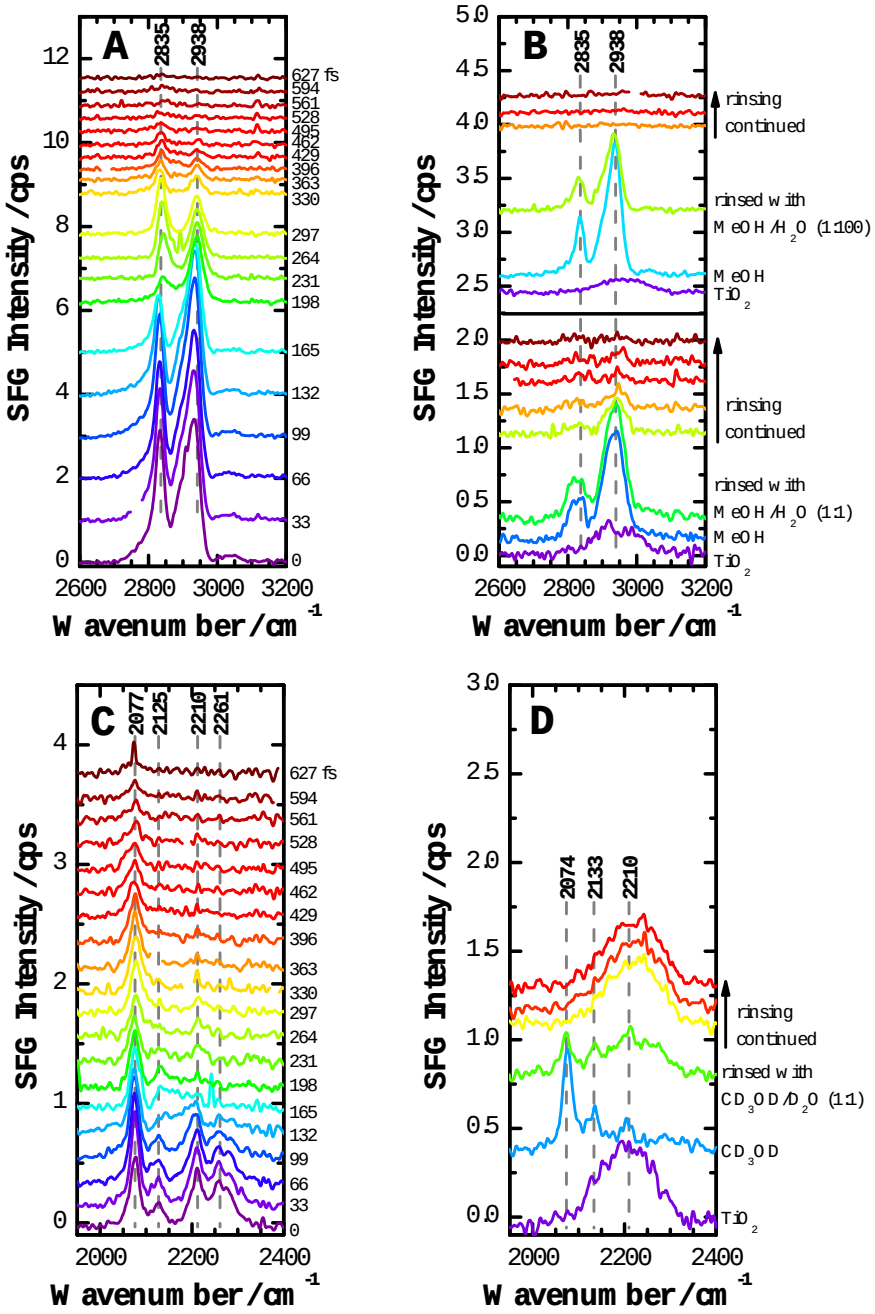

Fig. 4.41: (A) Set of time delay-shifted spectra of MeOH in contact with a TiO_2 film spin-coated on a CaF_2 prism. (B) Rinsing of a MeOH on TiO_2 sample with a 1:1 mixture of MeOH:H_2O (bottom) and a 1:100 mixture of MeOH:H_2O (top). (C) Set of time delay-shifted spectra of CD_3OD in contact with a TiO_2 film spin-coated on a CaF_2 prism. (D) Rinsing of a CD_3OD on TiO_2 sample with a 1:1 mixture of CD_3OD:D_2O.

ric stretching vibration of the CH_3 group and Fermi resonances of the symmetric stretch with overtones of the CH_3 bending vibration in the order of increasing frequency. The asymmetric stretching vibration of the CH_3 group to be found at $\sim$2970 cm^{-1} could not be detected [135, 207, 208]. Methanol is only molecularly bound in this sample because dissociative, i.e. chemisorptive, binding only occurs on the less abundant (100) crystalline

face of anatase and not on the predominant (101) face mostly exposed by the relatively large nanoparticles in this sample [101, 209]. Moreover, it was found that contaminations of the TiO_2 surface due to adsorbed hydrocarbons suppress dissociative adsorption of methanol [97, 101]. As seen in Fig. 4.12 H and I, the investigated samples are always slightly contaminated.

In a next step it is examined whether methanol is still detectable at the TiO_2 surface when water is present as well. To do so, a sample in contact with pure methanol was rinsed *in situ* with 1:1 and 1:100 mixtures of methanol and water (Fig. 4.41 B). It can be seen that the methanol bands disappear upon rinsing with both concentrations. This indicates that the water molecules displace the methanol molecules from the interface. Since the same result is obtained for both concentrations it can be excluded that the methanol molecules in the more concentrated solution form a double layer in which the methyl groups face each other at the TiO_2 surface in order to avoid mixing with water. Such a double layer would not be detectable with VSFG spectroscopy [208]. However, at the low concentration, it is assumed that only monolayer formation is possible. A monolayer should be detectable.

The measurements with methanol are repeated with deuterated methanol (CD_3OD) in order to exclude that bands originating from contaminations of adsorbed hydrocarbons interfere with detected methanol bands. The set of time delay-shifted spectra of a TiO_2 film immersed in pure CD_3OD at a center frequency of 2180 cm^{-1} is depicted in Fig. 4.41 C. The spectrum at zero time delay shows four bands which are associated with CD stretching vibrations. The band at 2077 cm^{-1} is assigned to the symmetric stretch of the CD_3 group, the bands at 2125 and 2210 cm^{-1} to the Fermi resonances and the band at 2261 cm^{-1} to the asymmetric stretch of the CD_3 group [207, 210, 211]. Upon rinsing of the sample with a 1:1 mixture of CD_3OD:D_2O, the CD_3OD signal disappears as observed for normal methanol (Fig. 4.41 D).

The results obtained on methanol and deuterated methanol show that pure methanol in contact with TiO_2 can be observed with VSFG spectroscopy. However, in the presence of water the methanol signal is immediately lost. The same phenomenon was already studied by Wang *et al.* who investigated the competitive adsorption of water and methanol on TiO_2 in the gas phase also using VSFG spectroscopy. They found that high amounts of water readily displace methanol [100]. Similarly, Zhang *et al.* found that VSFG spectra of methanol/water mixtures at fused silica surfaces are hardly detectable at all concentrations [212]. Consequently, using solely VSFG spectroscopy, it could prove difficult to detect low amounts of evolving methanol during the CO_2 reduction reaction in aqueous media.

4.4 CO_2 binding studied by VSFG spectroscopy

Beside the methanol adsorption, attempts were made to study the CO_2 adsorption from aqueous solution onto TiO_2 films on CaF_2 prisms with VSFG spectroscopy. CO_2 adsorbs as carboxylate or carbonate species on the TiO_2 surface which lead to characteristic bands between 1700 and 1300 cm^{-1} in the IR spectrum [213–215]. Thus, the center frequency was put to 1600 cm^{-1} in order to detect the strongest of them. In case it is possible to obtain a spectrum of adsorbed CO_2, the photocatalytic degradation or conversion of CO_2 under irradiation could be studied. Unfortunately, it was observed that the film being relatively stable in contact with pure water, detaches from the substrate quite rapidly

when the water was saturated with CO_2. This finding is assumed to be related to the progressive decrease in pH (pH $\approx$ 4) upon addition of CO_2:

$$CO_2 + H_2O \rightleftharpoons CO_3^{2-} + 2\,H^+. \tag{4.1}$$

Good adhesion of the TiO_2 film under acidic conditions was however found on fused silica slides. A transition from the CaF_2 to a SiO_2 substrate could not be carried out because silica is opaque throughout the IR region lower than 2000 cm^{-1}. To circumvent these limitations, the IR transmittance properties of the CaF_2 prism were combined with the adhesion properties of the fused silica slides by sputtering a 30 nm-thick layer of SiO_2 on the base plane of the CaF_2 prism. The IR transmittance of a SiO_2-coated CaF_2 plate was tested by IR spectroscopy and compared to the transmittance of a pure CaF_2 plate. The respective spectra are shown in Fig. 4.42 A.

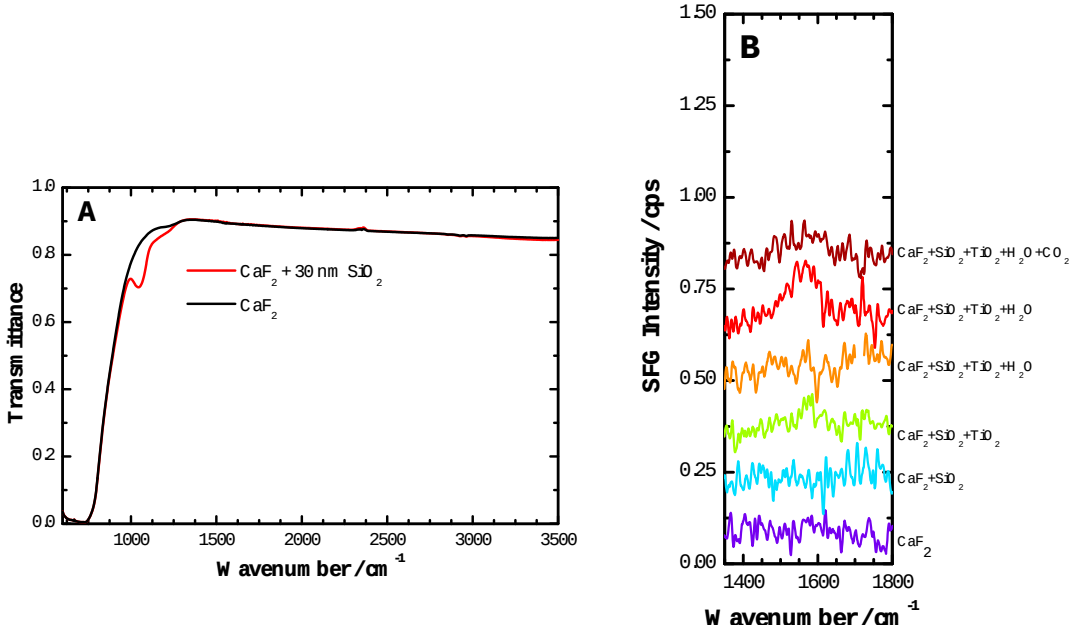

Fig. 4.42: (A) Comparison of IR transmission spectra of a CaF_2 plate (*black*) and a CaF_2 plate coated with 30 nm SiO_2 (*red*) and (B) Influence on the VSFG spectrum of a pure CaF_2 prism upon consecutive coating with layers of SiO_2, TiO_2, H_2O and $H_2O + CO_2$.

It is seen that the thin SiO_2 layer reduces the IR transmittance of the CaF_2 substrate ($\sim$70 %) only at wavenumbers lower than 1300 cm^{-1}. In addition, the adhesion of the TiO_2 film on the SiO_2-coated CaF_2 plate and prism was found to be as good as on the fused silica slides. As a result, a suitable substrate for the investigation of carbonate species is found. Very recently, Padermshoke *et al.* published data about the suitability of a novel SiO_2-deposited CaF_2 substrate for VSFG spectroscopy [216]. The VSFG spectra centered at 1600 cm^{-1} of the bare, SiO_2-coated, and TiO_2/SiO_2-coated CaF_2 prisms, are shown in Fig. 4.42 B. The first two spectra are both flat lines and it is thus demonstrated that the SiO_2 does not influence the VSFG signal from the CaF_2 substrate. Upon addition of a layer of TiO_2 a small NR background signal is observed. This stays at first very similar when the film is brought in contact with water. However, after around 30 min the NR background signal increases, presumably due to a change in the TiO_2 film. Upon exchanging the pure water with CO_2 saturated water, the NR signal remains the same and no new band is observed, even after 30 min immersion time. The CO_2 adsorption

most probably takes place but the adsorbed species do not perform SFG-active vibrations. Thus, it seems not possible to study the CO_2 adsorption in the spectral range where strong IR bands of adsorbed CO_2 species show up and in a second step its conversion with VSFG spectroscopy. Nevertheless, this technique can still be employed, as shown in the preceding sections, to study the dye behavior during the CO_2 reduction reaction.

Chapter 5

Conclusions and Outlook

A photocatalyst for solar light-driven CO_2 reduction based on dye-functionalized TiO_2 nanoparticles was investigated by UV/Vis, IR, Raman and VSFG spectroscopy. The dyes employed in this work were perylene-based with either carboxylic acid or anhydride groups as molecular anchor to the TiO_2 surface. Particular focus was put on elucidating the binding mode and molecular arrangement of the dyes ID1157 and ID1152, the two being structurally identical apart from their anchor group. Whereas ID1157 bears a carboxylic acid, ID1152 contains an anhydride group anchor. For further comparison and confirmation of the results obtained with the previous dyes, structurally similar perylene-based dyes, SF18 and ID28, bearing the same anchor groups, i.e. a carboxylic acid anchor in the case of SF18 and an anhydride group in the case of ID28, have been studied as well. Moreover, the model substance NA and its salt counterpart K2NA with cleaved anhydride group were chosen to facilitate the band assignment of the spectra taken from dyes with anhydride group. The dye binding geometry is particularly important because it influences the electron injection efficiency from the excited dye to the CB of TiO_2 and hence also the photocurrent output of any given dye/TiO_2 system. For the ID1157/TiO_2 and ID1152/TiO_2 systems, respectively, significantly different photocurrent amplitudes were observed; in the case of ID1157 it was 14 times higher than for ID1152. Subsequent spectroscopic analysis was then used to determine whether the dissimilar anchor groups of the dyes and their binding modes were the cause for the observed photocurrents.

With the help of UV/Vis absorption spectroscopy changes in the electronic structure upon binding of the dyes to TiO_2 were studied. For all dyes one main absorption band was observed which was attributed to an HOMO to LUMO transition with a strong CT character from the diphenylamine donor group to the perylene acceptor core. While this band did not shift upon binding of the carboxylic acid group, it blue-shifted upon coordination of the anhydride group. The latter observation was explained by the opening of the anhydride group. This could be concluded since the UV/Vis absorption spectra of the disodium salts of the chemically-cleaved dyes showed the same absorption maximum.

By employing IR and Raman spectroscopy to the powder samples of the free and bound dyes a detailed binding mode analysis of the carboxylic acid and anhydride anchor groups could be performed. In order to apply the empirical rule of Deacon and Phillips the spectra of the free and bound dyes were compared and spectral changes could be ascribed to a certain binding mode. In the case of ID1157 the binding mode of the carboxylic acid group was determined as bidentate bridging, while for ID1152 it was found

that the anhydride group opened to form a bidentate bridging coordination with two carboxylate groups. The IR and Raman spectra of bound NA and K2NA were of great use for unraveling the anhydride group binding mode since they showed distinct bands that could be assigned to $\nu_{as}(CO_2^-)$ and $\nu_s(CO_2^-)$ stretches. However, it remained unclear why a residual anhydride group signal was still observed in the spectra of the bound dyes.

In situ VSFG spectroscopy was applied to thin dye-functionalized TiO_2 films spin-coated on CaF_2 substrates using a photocatalytic flow cell in order to examine the surface-specific binding mode of the dyes and their molecular arrangement on the TiO_2 surface both in air and in water. In addition, since very few VSFG spectroscopic studies have dealt with complex nanoparticulate surfaces, it was therefore desirable to gain further VSFG-specific information on these samples. This was achieved by switching to a reflective Au substrate which changed the sampling geometry from TIR to normal reflection. Thus, it was possible to determine whether the free or buried dye/TiO_2 interface was probed. Finally, methanol and CO_2 adsorption on TiO_2 films was also investigated.

The VSFG spectra of the bound dyes could be obtained with good sensitivity, despite the presence of a strong NR background. These findings could be explained by the DR enhancement condition under which the spectra were recorded. The high sensitivity and NR background were attributed to simultaneous IR-Vis DR-SFG and Vis-IR DR-SFG processes. Usually the latter process is neglected because the electronic relaxation times are generally much shorter than the vibrational ones. However, in the case of perylene dyes the vibrational relaxation time of the excited state was found to be on the same timescale as the electronic one. As a consequence, both processes could interfere to give VSFG dye spectra with resonant and NR contributions. In order to remove the NR background the experimental suppression technique developed by Lagutchev *et al.* [146, 147] was applied and NR background-free survey spectra could be acquired. These spectra were taken for the surface-specific binding mode and dye arrangement analysis. Hence, the binding mode of the dye ID1157 determined with IR and Raman spectroscopy could be confirmed with VSFG spectroscopy. Moreover, based on the fact that the bound dyes gave rise to detectable VSFG signals in air, it was concluded that they had to be adsorbed in an orderly fashion, thus creating a defined dye/TiO_2 interface. The results found for ID1157 could be reproduced with the dye SF18. In addition, the VSFG signal strength of the spectra of bound SF18 allowed for polarization-dependent measurements using *ppp* and *ssp* polarization combinations. With the help of these, it was suggested that dye molecules adsorbed at the TiO_2 surface adopted on average a tilted geometry. When the ID1157 dye-coated TiO_2 film was brought in contact with water the binding mode remained unchanged but the order of the adsorbed dye layer decreased slightly. By switching substrates it could be shown that the free dye/TiO_2 interface was the one actually probed by VSFG spectroscopy.

For the dye ID1152 with anhydride group anchor the VSFG spectroscopic results were largely comparable to the ones found on ID1157. The binding mode analysis performed with IR and Raman spectroscopy was corroborated by VSFG spectroscopy. Moreover, the origin of the residual anhydride group signal could be explained. It was shown that dye molecules with closed anhydride group incorporated into the ordered layer of bound dye molecules. This was confirmed by measurements on the dye ID28 and more so on the model substance NA. In the VSFG spectrum of bound NA, a band assigned to the $\nu_s(CO_2^-)$ stretching vibration was observed, indicating the opening of the anhydride group of at

least some molecules; another band assigned to the ν_s(C=O) stretching vibration related instead to the coordination of closed anhydride groups. Similar to ID1157 the binding mode of ID1152 was not altered upon addition of water and the order of the bound dye layer was also slightly diminished. In the case of ID1152 the substrate change did not provide a clear answer as to whether the free or buried interface was probed but considering that the same film preparation and the same experimental conditions were used, it could be argued that the same interface as for ID1157 was probed. The direct comparison of the VSFG spectra of bound ID1157 and ID1152 revealed that ID1157 dye molecules adsorbed with a higher surface density and ordering.

In view of the results obtained on the binding geometry of the dyes ID1157 and ID1152 it was possible to give an interpretation of the dissimilar photocurrent signals from the two dye/TiO_2 systems. It is believed that the photocurrent output of ID1157 was much higher because dye molecules present at the TiO_2 surface adsorbed numerously via chemisorption, whereas in the case of ID1152 the surface density of bound molecules was lower and the binding occurred partly also via physisorption.

Finally, the methanol and CO_2 adsorption on TiO_2 films was studied with VSFG spectroscopy. In the case of 100 % methanol, the VSFG spectrum showed bands of molecularly adsorbed molecules. These bands disappeared upon addition of either water or methanol/water mixtures. Therefore, it was concluded that methanol evolving from a CO_2 reduction reaction in an aqueous phase would be easily displaced and, in turn, would be hardly detectable by VSFG spectroscopy. As for CO_2 adsorption, the CaF_2 substrate had to be modified with a thin SiO_2 layer in order to improve TiO_2 adhesion in acidic aqueous media. Nevertheless, no carbonate bands could be observed even after long contact times between the TiO_2 film and a CO_2-saturated aqueous solution.

Additional experiments on the dye/TiO_2 systems are needed to provide further insights on the dye arrangement at the TiO_2 surface and to assure the present results. Concerning the binding mode of the carboxylic acid and anhydride groups IR, Raman and VSFG spectroscopy studies of the sodium or potassium salts of the dyes should be carried out in order to obtain $\Delta\nu_{salt}$ values that can be compared to the $\Delta\nu_{ads}$ values of the adsorbed dyes. Moreover, the IR measurements should be performed under dry atmosphere so that the spectra do not have to be corrected for water vapor absorption after the experiment. Thus, the detection and assignment of the band of the $\nu_{as}(CO_2^-)$ stretching vibration should be facilitated. Speaking of the band assignment, simulations of the free/salt and bound dye spectra should be conducted to assist spectral interpretation and binding mode identification (compare Ref. [165]). Further VSFG spectroscopic experiments should not only study the influence of pure water on the bound dye layer but also the influence of pH. For instance, under basic conditions it could be verified that some ID1152 dye molecules bind with closed anhydride group and do not expose a protonated acid group. This should be possible because a free carboxylic acid group should become deprotonated and hence a spectral change should be observable. By contrast, an anhydride group should remain unaltered. Moreover, it seems worth to follow subsequent washing (with water) and reimmersing (in dye solution) steps of the dye-bound samples by VSFG spectroscopy in order to elucidate how dye reorganization on the TiO_2 surface influences the photocatalyst's performance (compare Ref. [202]). Furthermore, it would be interesting to study the dye adsorption on single-crystalline anatase(101) surfaces with polarization-dependent VSFG spectroscopy in combination with other techniques, e.g.

XPS and NEXAFS (compare Ref. [78]), to determine the tilt angle of the bound dyes on a surface with predefined orientation. Thus, it could be found out whether the tilted geometry suggested by the VSFG spectra in this thesis was actually a result of the binding geometry of the dye or the averaged orientation of the different crystal faces on the TiO_2 nanoparticles in the film. In addition, VSFG spectroscopic studies with a tunable Vis and IR laser beams could be applied to prove that the NR background in the VSFG spectra of the bound dyes was actually due to the DR condition. By changing the Vis wavelength off-resonance with the electronic CT transition of the dyes, the NR background should vanish.

So far CO_2 conversion applying the dye-functionalized TiO_2 nanoparticles as photocatalyst has not been successful. Future experiments applying a different dye-functionalized semiconductor, e.g. Cu-deposited ZnO, as catalyst to address this problem are on the way. However, the results obtained regarding the dye binding are equally useful and relevant for DSSC research.

Bibliography

[1] M. I. Hoffert, K. Caldeira, A. K. Jain, E. F. Haites, L. D. D. Harvey, S. D. Potter, M. E. Schlesinger, S. H. Schneider, R. G. Watts, T. M. L. Wigley, and D. J. Wuebbles. "Energy implications of future stabilization of atmospheric CO_2 content". *Nature*, 395(6705):881–884, 1998.

[2] N. S. Lewis and D. G. Nocera. "Powering the planet: Chemical challenges in solar energy utilization". *Proc. Natl. Acad. Sci. U. S. A.*, 103(43):15729–15735, 2006.

[3] S. Shafiee and E. Topal. "When will fossil fuel reserves be diminished?". *Energ. Policy*, 37(1):181–189, 2009.

[4] H. Balat and C. Oz. "Technical and economic aspects of carbon capture and storage - A review". *Energ. Explor. Exploit.*, 25(5):357–392, 2007.

[5] M. A. Mimikou and E. A. Baltas. "Climate change impacts on the reliability of hydroelectric energy production". *Hydrolog. Sci. J.*, 42(5):661–678, 1997.

[6] J. Barber. "Photosynthetic energy conversion: natural and artificial". *Chem. Soc. Rev.*, 38(1):185–196, 2009.

[7] E. Fujita. "Photochemical carbon dioxide reduction with metal complexes". *Coord. Chem. Rev.*, 185-6:373–384, 1999.

[8] T. Yui, Y. Tamaki, K. Sekizawa, and O. Ishitani. Photocatalytic Reduction of CO_2: From Molecules to Semiconductors. In *Photocatalysis*, volume 303 of *Topics in Current Chemistry*, pages 151–184. Springer-Verlag, Berlin, 2011.

[9] M. Mikkelsen, M. Jørgensen, and F. C. Krebs. "The teraton challenge. A review of fixation and transformation of carbon dioxide". *Energy Environ. Sci.*, 3(1):43–81, 2010.

[10] P. D. Tran, L. H. Wong, J. Barber, and J. S. C. Loo. "Recent advances in hybrid photocatalysts for solar fuel production". *Energy Environ. Sci.*, 5(3):5902–5918, 2012.

[11] C.-C. Yang, Y.-H. Yu, B. van der Linden, J. C. S. Wu, and G. Mul. "Artificial photosynthesis over crystalline TiO_2-based catalysts: Fact or fiction?". *J. Am. Chem. Soc.*, 132(24):8398–8406, 2010.

[12] H. W. N. Slamet, E. Purnama, S. Kosela, and J. Gunlazuardi. "Photocatalytic reduction of CO_2 on copper-doped Titania catalysts prepared by improved-impregnation method". *Catal. Commun.*, 6(5):313–319, 2005.

[13] O. Ishitani, C. Inoue, Y. Suzuki, and T. Ibusuki. "Photocatalytic reduction of carbon-dioxide to methane and acetic-acid by an aqueous suspension of metal-deposited TiO_2". *J. Photochem. Photobiol., A*, 72(3):269–271, 1993.

[14] C. Wang, R. L. Thompson, J. Baltrus, and C. Matranga. "Visible light photoreduction of CO_2 using CdSe/Pt/TiO_2 heterostructured catalysts". *J. Phys. Chem. Lett.*, 1(1):48–53, 2010.

[15] O. Ozcan, F. Yukruk, E. U. Akkaya, and D. Uner. "Dye sensitized CO_2 reduction over pure and platinized CO_2". *Top. Catal.*, 44(4):523–528, 2007.

[16] T.-V. Nguyen, J. C. S. Wu, and C.-H. Chiou. "Photoreduction of CO_2 over Ruthenium dye-sensitized TiO_2-based catalysts under concentrated natural sunlight". *Catal. Commun.*, 9(10):2073–2076, 2008.

[17] T. W. Woolerton, S. Sheard, E. Reisner, E. Pierce, S. W. Ragsdale, and F. A. Armstrong. "Efficient and clean photoreduction of CO_2 to CO by enzyme-modified TiO_2 nanoparticles using visible light". *J. Am. Chem. Soc.*, 132(7):2132–2133, 2010.

[18] T. W. Woolerton, S. Sheard, E. Pierce, S. W. Ragsdale, and F. A. Armstrong. "CO_2 photoreduction at enzyme-modified metal oxide nanoparticles". *Energy Environ. Sci.*, 4(7):2393–2399, 2011.

[19] B. Oregan and M. Grätzel. "A low-cost, high-efficiency solar-cell based on dye-sensitized colloidal TiO_2 films". *Nature*, 353(6346):737–740, 1991.

[20] A. Hagfeldt, G. Boschloo, L. Sun, L. Kloo, and H. Pettersson. "Dye-sensitized solar cells". *Chem. Rev.*, 110(11):6595–6663, 2010.

[21] K. Kalyanasundaram (Ed.). *"Dye-Sensitized Solar Cells"*. Fundamental sciences: chemistry. EPFL Press, Lausanne, 2010.

[22] A. L. Linsebigler, G. Lu, and J. T. Yates. "Photocatalysis on TiO_2 surfaces - principles, mechanisms, and selected results". *Chem. Rev.*, 95(3):735–758, 1995.

[23] M. K. Nazeeruddin, F. De Angelis, S. Fantacci, A. Selloni, G. Viscardi, P. Liska, S. Ito, T. Bessho, and M. Grätzel. "Combined experimental and DFT-TDDFT computational study of photoelectrochemical cell ruthenium sensitizers". *J. Am. Chem. Soc.*, 127(48):16835–16847, 2005.

[24] M. A. Green, K. Emery, Y. Hishikawa, and W. Warta. "Solar cell efficiency tables (version 37)". *Prog. Photovoltaics*, 19(1):84–92, 2011.

[25] J. M. Rehm, G. L. McLendon, Y. Nagasawa, K. Yoshihara, J. Moser, and M. Grätzel. "Femtosecond electron-transfer dynamics at a sensitizing dye-semiconductor (TiO_2) interface". *J. Phys. Chem.*, 100(23):9577–9578, 1996.

[26] A. F. Bartelt, R. Schuetz, A. Neubauer, T. Hannappel, and R. Eichberger. Influence of TiO_2/perylene interface modifications on electron injection and recombination dynamics. *J. Phys. Chem. C*, 113(50):21233–21241, 2009.

[27] A. Listorti, B. O'Regan, and J. R. Durrant. "Electron transfer dynamics in dye-sensitized solar cells". *Chem. Mater.*, 23(15):3381–3399, 2011.

[28] K. S. Finnie, J. R. Bartlett, and J. L. Woolfrey. "Vibrational spectroscopic study of the coordination of (2,2'-bipyridyl-4,4'-dicarboxylic acid)ruthenium(II) complexes to the surface of nanocrystalline titania". *Langmuir*, 14(10):2744–2749, 1998.

[29] C. P. Leon, L. Kador, B. Peng, and M. Thelakkat. "Characterization of the adsorption of Ru-bpy dyes on mesoporous TiO_2 films with UV-Vis, Raman, and FTIR spectroscopies". *J. Phys. Chem. B*, 110(17):8723–8730, 2006.

[30] K. E. Lee, M. A. Gomez, S. Elouatik, and G. P. Demopoulos. "Further understanding of the adsorption mechanism of N719 sensitizer on anatase TiO_2 films for DSSC applications using vibrational spectroscopy and confocal Raman imaging". *Langmuir*, 26(12):9575–9583, 2010.

[31] K. Suto, A. K., Y. Kawata, S. Tasaka, and A. Sugita. "Adsorption dynamics of the N719 dye on nanoporous titanium oxides studied by resonance Raman scattering and fourier transform infrared spectroscopy". *Chem. Phys. Lett.*, 536:45 – 49, 2012.

[32] A. Hagfeldt and M. Grätzel. "Light-induced redox reactions in nanocrystalline systems". *Chem. Rev.*, 95(1):49–68, 1995.

[33] J. Winkler. *"Titandioxid"*. Die Technologie des Beschichtens. Vincentz, Hannover, 2003.

[34] S. Gupta and M. Tripathi. "A review of TiO_2 nanoparticles". *Chin. Sci. Bull.*, 56:1639–1657, 2011.

[35] U. Diebold. "The surface science of titanium dioxide". *Surf. Sci. Rep.*, 48(5-8):53–229, 2003.

[36] C. Chen, W. Ma, and J. Zhao. "Semiconductor-mediated photodegradation of pollutants under visible-light irradiation". *Chem. Soc. Rev.*, 39(11):4206–4219, 2010.

[37] D. Hanaor and C. Sorrell. "Review of the anatase to rutile phase transformation". *J. Mater. Sci.*, 46:855–874, 2011.

[38] T. Dentani, K. Funabiki, J.-Y. Jin, T. Yoshida, H. Minoura, and M. Matsui. Application of 9-substituted 3,4-perylenedicarboxylic anhydrides as sensitizers for zinc oxide solar cell. *Dyes and Pigments*, 72(3):303–307, 2007.

[39] V. Shklover, Y. E. Ovchinnikov, L.S. Braginsky, S. M. Zakeeruddin, and M. Grätzel. "Structure of organic/inorganic interface in assembled materials comprising molecular components. Crystal structure of the sensitizer bis[(4,4 '-carboxy-2,2 '-bipyridine)(thiocyanato)]ruthenium(II)". *Chem. Mater.*, 10(9):2533–2541, 1998.

[40] M. Primet, P. Pichat, and M. V. Mathieu. "Infrared study of the surface of titanium dioxides. I. Hydroxyl groups". *J. Phys. Chem.*, 75(9):1216–1220, 1971.

[41] K. S. Finnie, D. J. Cassidy, J. R. Bartlett, and J. L. Woolfrey. "IR spectroscopy of surface water and hydroxyl species on nanocrystalline TiO_2 films". *Langmuir*, 17(3):816–820, 2001.

[42] X. Chen and S. S. Mao. "Titanium dioxide nanomaterials: Synthesis, properties, modifications, and applications". *Chem. Rev.*, 107(7):2891–2959, 2007.

[43] W. M. Campbell, A. K. Burrell, D. L. Officer, and K. W. Jolley. "Porphyrins as light harvesters in the dye-sensitised TiO_2 solar cell". *Coord. Chem. Rev.*, 248(13-14):1363–1379, 2004.

[44] A. Mishra, M. K. R. Fischer, and P. Baeuerle. "Metal-free organic dyes for dye-sensitized solar cells: From structure: property relationships to design rules". *Angew. Chem. Int. Ed.*, 48(14):2474–2499, 2009.

[45] J. N. Clifford, E. Martinez-Ferrero, A. Viterisi, and E. Palomares. "Sensitizer molecular structure-device efficiency relationship in dye sensitized solar cells". *Chem. Soc. Rev.*, 40(3):1635–1646, 2011.

[46] M. Miyashita, K. Sunahara, T. Nishikawa, Y. Uemura, N. Koumura, K. Hara, A. Mori, T. Abe, E. Suzuki, and S. Mori. "Interfacial electron-transfer kinetics in metal-free organic dye-sensitized solar cells: Combined effects of molecular structure of dyes and electrolytes". *J. Am. Chem. Soc.*, 130(52):17874–17881, 2008.

[47] Y. Zhang and E. Galoppini. "Organic polyaromatic hydrocarbons as sensitizing model dyes for semiconductor nanoparticles". *ChemSusChem*, 3(4):410–428, 2010.

[48] S. Wang, Y. L. Li, C. M. Du, Z. Q. Shi, S. X. Xiao, D. B. Zhu, E. Q. Gao, and S. M. Cai. "Dye sensitization of nanocrystalline TiO_2 by perylene derivatives". *Synth. Met.*, 128(3):299–304, 2002.

[49] E. Mete, D. Uner, M. Çakmak, O. Gulseren, and Ş. Ellialtoğlu. "Effect of molecular and electronic structure on the light-harvesting properties of dye sensitizers". *J.*

Phys. Chem. C, 111(20):7539–7547, 2007.

[50] C. Li and H. Wonneberger. "Perylene imides for organic photovoltaics: Yesterday, today, and tomorrow". *Adv. Mater.*, 24(5):613–636, 2012.

[51] E. Engel, K. Schmidt, D. Beljonne, J.-L. Bredas, J. Assa, H. Froeb, K. Leo, and M. Hoffmann. "Transient absorption spectroscopy and quantum-chemical studies of matrix-isolated perylene derivatives". *Phys. Rev. B*, 73(24):245216/1–245216/9, 2006.

[52] S. Ferrere, A. Zaban, and B. A. Gregg. "Dye sensitization of nanocrystalline tin oxide by perylene derivatives". *J. Phys. Chem. B*, 101(23):4490–4493, 1997.

[53] S. Ferrere and B. A. Gregg. "New perylenes for dye sensitization of TiO_2". *New J. Chem.*, 26(9):1155–1160, 2002.

[54] B. Burfeindt, T. Hannappel, W. Storck, and F. Willig. "Measurement of temperature-independent femtosecond interfacial electron transfer from an anchored molecular electron donor to a semiconductor as acceptor". *J. Phys. Chem.*, 100(41):16463–16465, 1996.

[55] Y. Shibano, T. Umeyama, Y. Matano, and H. Imahori. "Electron-donating perylene tetracarboxylic acids for dye-sensitized solar cells". *Org. Lett.*, 9(10):1971–1974, 2007.

[56] T. Edvinsson, C. Li, N. G. Pschirer, J. Schöneboom, F. Eickemeyer, R. Sens, G. Boschloo, A. Herrmann, K. Müllen, and A. Hagfeldt. "Intramolecular charge-transfer tuning of perylenes: Spectroscopic features and performance in dye-sensitized solar cells". *J. Phys. Chem. C*, 111(42):15137–15140, 2007.

[57] C. Li, J.-H. Yum, S.-J. Moon, A. Herrmann, F. Eickemeyer, Neil N. G. Pschirer, P. Erk, J. Schöneboom, K. Müllen, M. Grätzel, and M. K. Nazeeruddin. "An improved perylene sensitizer for solar cell applications". *ChemSusChem*, 1(7):615–618, 2008.

[58] J. Fortage, M. Severac, C. Houarner-Rassin, Y. Pellegrin, E. Blart, and F. Odobel. "Synthesis of new perylene imide dyes and their photovoltaic performances in nanocrystalline TiO_2 dye-sensitized solar cells". *J. Photochem. Photobiol., A*, 197(2-3):156–169, 2008.

[59] H. Imahori, T. Umeyama, and S. Ito. "Large pi-aromatic molecules as potential sensitizers for highly efficient dye-sensitized solar cells". *Acc. Chem. Res.*, 42(11):1809–1818, 2009.

[60] H.-P. Lu, C.-Y. Tsai, W.-N. Yen, C.-P. Hsieh, C.-W. Lee, C.-Y. Yeh, and E. W.-G. Diau. "Control of dye aggregation and electron injection for highly efficient porphyrin sensitizers adsorbed on semiconductor films with varying ratios of coadsorbate". *J. Phys. Chem. C*, 113(49):20990–20997, 2009.

[61] E. Galoppini. "Linkers for anchoring sensitizers to semiconductor nanoparticles". *Coordin. Chem. Rev.*, 248(13-14):1283–1297, 2004.

[62] S. Mathew and H. Imahori. "Tunable, strongly-donating perylene photosensitizers for dye-sensitized solar cells". *J. Mater. Chem.*, 21(20):7166–7174, 2011.

[63] F. Ambrosio, N. Martsinovich, and A. Troisi. "What is the best anchoring group for a dye in a dye-sensitized solar cell?". *J. Phys. Chem. Lett.*, 3(11):1531–1535, 2012.

[64] K. Murakoshi, G. Kano, Y. Wada, S. Yanagida, H. Miyazaki, M. Matsumoto, and S. Murasawa. Importance of binding states between photosensitizing molecules and the TiO_2 surface for efficiency in a dye-sensitized solar-cell. *J. Electroanal. Chem.*, 396(1-2):27–34, 1995.

[65] J. N. Clifford, E. Palomares, M. K. Nazeeruddin, M. Grätzel, J. Nelson, X. Li, N. J. Long, and J. R. Durrant. "Molecular control of recombination dynamics in dye-sensitized nanocrystalline TiO_2 films: Free energy vs distance dependence". *J. Am. Chem. Soc.*, 126(16):5225–5233, 2004.

[66] M. J. Griffith, M. James, G. Triani, P. Wagner, G. G. Wallace, and D. L. Officer. "Determining the orientation and molecular packing of organic dyes on a TiO_2 surface using X-ray reflectometry". *Langmuir*, 27(21):12944–12950, 2011.

[67] M. Grätzel. "Molecular photovoltaics that mimic photosynthesis". *Pure Appl. Chem.*, 73(3):459–467, 2001.

[68] H. Imahori, S. Kang, H. Hayashi, M. Haruta, H. Kurata, S. Isoda, S. E. Canton, Y. Infahsaeng, A. Kathiravan, T. Pascher, P. Chabera, A. P. Yartsev, and V. Sundstrom. "Photoinduced charge carrier dynamics of Zn-porphyrin-TiO_2 electrodes: The key role of charge recombination for solar cell performance". *J. Phys. Chem. A*, 115(16):3679–3690, 2011.

[69] H. Imahori, T. Umeyama, K. Kurotobi, and Y. Takano. "Self-assembling porphyrins and phthalocyanines for photoinduced charge separation and charge transport". *Chem. Commun.*, 48(34):4032–4045, 2012.

[70] R. Ernstorfer, L. Gundlach, S. Felber, W. Storck, R. Eichberger, and F. Willig. "Role of molecular anchor groups in molecule-to-semiconductor electron transfer". *J. Phys. Chem. B*, 110(50):25383–25391, 2006.

[71] L. Gundlach, J. Szarko, L. D. Socaciu-Siebert, A. Neubauer, R. Ernstorfer, and F. Willig. "Different orientations of large rigid organic chromophores at the rutile TiO_2 surface controlled by different binding geometries of specific anchor groups". *Phys. Rev. B*, 75(12):125320/1–125320/8, 2007.

[72] L. Gundlach, R. Ernstorfer, and F. Willig. "Pathway-dependent electron transfer for rod-shaped perylene-derived molecules adsorbed in nanometer-size TiO_2 cavities". *J. Phys. Chem. C*, 111(36):13586–13594, 2007.

[73] J. Lim, Y. S. Kwon, S.-H. Park, I. Y. Song, J. Choi, and T. Park. "Thermodynamic control over the competitive anchoring of N719 dye on nanocrystalline TiO_2 for improving photoinduced electron generation". *Langmuir*, 27(23):14647–14653, 2011.

[74] B. Völker, F. Wölzl, T. Bürgi, and D. Lingenfelser. "Dye bonding to TiO_2: In situ attenuated total reflection infrared spectroscopy study, simulations, and correlation with dye-sensitized solar cell characteristics". *Langmuir*, 28(31):11354–11363, 2012.

[75] H. Rensmo, K. Westermark, S. Södergren, O. Kohle, P. Persson, S. Lunell, and H. Siegbahn. "XPS studies of Ru-polypyridine complexes for solar cell applications". *J. Chem. Phys.*, 111(6):2744–2750, 1999.

[76] M. Hahlin, E. M. J. Johansson, S. Plogmaker, M. Odelius, D. P. Hagberg, L. Sun, H. Siegbahn, and H. Rensmo. "Electronic and molecular structures of organic dye/TiO_2 interfaces for solar cell applications: A core level photoelectron spectroscopy study". *Phys. Chem. Chem. Phys.*, 12(7):1507–1517, 2010.

[77] K. M. Karlsson, X. Jiang, S. K. Eriksson, E. Gabrielsson, H. Rensmo, A. Hagfeldt, and L. Sun. "Phenoxazine dyes for dye-sensitized solar cells: Relationship between molecular structure and electron lifetime". *Chem. Eur. J.*, 17(23):6415–6424, 2011.

[78] S. Yu, S. Ahmadi, M. Zuleta, H. Tian, K. Schulte, A. Pietzsch, F. Hennies, J. Weissenrieder, X. Yang, and M. Gothelid. "Adsorption geometry, molecular interaction, and charge transfer of triphenylamine-based dye on rutile TiO_2(110)". *J. Chem.*

Phys., 133(22):224704/1–224704/11, 2010.

[79] K. Hara, T. Sato, R. Katoh, A. Furube, Y. Ohga, A. Shinpo, S. Suga, K. Sayama, H. Sugihara, and H. Arakawa. "Molecular design of coumarin dyes for efficient dye-sensitized solar cells". *J. Phys. Chem. B*, 107(2):597–606, 2003.

[80] K. Hara, T. Sato, R. Katoh, A. Furube, T. Yoshihara, M. Murai, M. Kurashige, S. Ito, A. Shinpo, S. Suga, and H. Arakawa. "Novel conjugated organic dyes for efficient dye-sensitized solar cells". *Adv. Funct. Mater.*, 15(2):246–252, 2005.

[81] K. Srinivas, K. Yesudas, K. Bhanuprakash, V. J. Rao, and L. Giribabu. "A combined experimental and computational investigation of anthracene based sensitizers for DSSC: Comparison of cyanoacrylic and malonic acid electron withdrawing groups binding onto the TiO_2 anatase (101) surface". *J. Phys. Chem. C*, 113(46):20117–20126, 2009.

[82] G. B. Deacon and R. J. Phillips. "Relationships between the carbon-oxygen stretching frequencies of carboxylato complexes and the type of carboxylate coordination". *Coord. Chem. Rev.*, 33(3):227–250, 1980.

[83] K. Vinodgopal, X. Hua, R. L. Dahlgren, A. G. Lappin, L. K. Patterson, and P. V. Kamat. "Photochemistry of $Ru(bpy)_2(dcbpy)^{2+}$ on Al_2O_3 and TiO_2 surfaces. An insight into the mechanism of photosensitization". *J. Phys. Chem.*, 99(27):10883–10889, 1995.

[84] S. Umapathy, A. M. Cartner, A. W. Parker, and R. E. Hester. "Time-resolved resonance Raman spectroscopic studies of the photosensitization of colloidal titanium dioxide". *J. Phys. Chem.*, 94(26):8880–8885, 1990.

[85] T. J. Meyer, G. J. Meyer, B. W. Pfennig, J. R. Schoonover, C. J. Timpson, J. F. Wall, C. Kobusch, X. Chen, B. M. Peek, C. G. Wall, W. Ou, B. W. Erickson, and C. A. Bignozzi. "Molecular-level electron transfer and excited state assemblies on surfaces of metal oxides and glass". *Inorg. Chem.*, 33(18):3952–3964, 1994.

[86] N. W. Duffy, K. D. Dobson, K. C. Gordon, B. H. Robinson, and A. J. McQuillan. "In situ infrared spectroscopic analysis of the adsorption of ruthenium(II) bipyridyl dicarboxylic acid photosensitisers to TiO_2 in aqueous solutions". *Chem. Phys. Lett.*, 266(5-6):451–455, 1997.

[87] P. Falaras. "Synergetic effect of carboxylic acid functional groups and fractal surface characteristics for efficient dye sensitization of titanium oxide". *Sol. Energ. Mat. Sol. C*, 53(1-2):163–175, 1998.

[88] M. K. Nazeeruddin, R. Humphry-Baker, P. Liska, and M. Grätzel. "Investigation of sensitizer adsorption and the influence of protons on current and voltage of a dye-sensitized nanocrystalline TiO_2 solar cell". *J. Phys. Chem. B*, 107(34):8981–8987, 2003.

[89] F. Hirose, K. Kuribayashi, T. Suzuki, Y. Narita, Y. Kimura, and M. Niwano. "UV treatment effect on TiO_2 electrodes in dye-sensitized solar cells with N719 sensitizer investigated by infrared absorption spectroscopy". *Electrochem. Solid St.*, 11(7):A109–A111, 2008.

[90] F. Hirose, M. Shikaku, Y. Kimura, and M. Niwano. "IR study on N719 dye adsorption with high temperature dye solution for highly efficient dye-sensitized solar cells". *J. Electrochem. Soc.*, 157(11):B1578–B1581, 2010.

[91] K. Berrada, P. Dumas, Y. J. Chabal, and P. Dubot. "Adsorption states and orientation of n-alkyl anhydride molecules on oxidized aluminum surface". *J. Electron*

Spectrosc. Relat. Phenom., 54:1153–1162, 1990.

[92] S. Thery, D. Jacquet, and M. Mantel. "A study of chemical interactions at the stainless steel/polymer interface by infrared spectroscopy. Part 1: Interaction mechanisms between succinic anhydride and 304 stainless steel". *J. Adhes.*, 56(1-4):1–13, 1996.

[93] N. T. Do and M. Baerns. "Effect of support material on the adsorption structures of furan and maleic-anhydride on the surface of V_2O_5/P_2O_5 catalysts. 2. Results of insitu infrared spectroscopic studies". *Appl. Cat.*, 45(1):9–26, 1988.

[94] J. N. Wilson, D. J. Titheridge, L. Kieu, and H. Idriss. "Reactions of maleic anhydride over TiO_2 (001) single crystal surfaces". *J. Vac. Sci.Technol. A*, 18(4, Part 2):1887–1892, 2000.

[95] E. M. J. Johansson, S. Plogmaker, L. E. Walle, R. Scholin, A. Borg, A. Sandell, and H. Rensmo. "Comparing surface binding of the maleic anhydride anchor group on single crystalline anatase TiO_2 (101), (100), and (001) surfaces". *J. Phys. Chem. C*, 114(35):15015–15020, 2010.

[96] H. Ashima, W.-J. Chun, and K. Asakura. "Room-temperature-adsorption behavior of acetic anhydride on a TiO_2(110) surface". *Surf. Sci.*, 601(8):1822–1830, 2007.

[97] C. Y. Wang, H. Groenzin, and M. J. Shultz. "Molecular species on nanoparticulate anatase TiO_2 film detected by sum frequency generation: Trace hydrocarbons and hydroxyl groups". *Langmuir*, 19(18):7330–7334, 2003.

[98] C. Y. Wang, H. Groenzin, and M. J. Shultz. "Surface characterization of nanoscale TiO_2 film by sum frequency generation using methanol as a molecular probe". *J. Phys. Chem. B*, 108(1):265–272, 2004.

[99] C. Y. Wang, H. Groenzin, and M. J. Shultz. "Direct observation of competitive adsorption between methanol and water on TiO_2: An in situ sum-frequency generation study". *J. Am. Chem. Soc.*, 126(26):8094–8095, 2004.

[100] C. Y. Wang, H. Groenzin, and M. J. Shultz. "Comparative study of acetic acid, methanol, and water adsorbed on anatase TiO_2 probed by sum frequency generation spectroscopy". *J. Am. Chem. Soc.*, 127(27):9736–9744, 2005.

[101] N. Asong, F. Dukes, C. Wang, and M. J. Shultz. "The effect of iron doping on the adsorption of methanol on TiO_2 probed by sum frequency generation". *Chem. Phys.*, 339(1-3):86–93, 2007.

[102] C. Aliaga and S. Baldelli. "A sum frequency generation study of the room-temperature ionic liquid-titanium dioxide interface". *J. Phys. Chem. C*, 112(8):3064–3072, 2008.

[103] J. Chen, J. Kubota, A. Wada, J. N. Kondo, and K. Domen. "Sum frequency generation spectroscopic investigation of TiOx/Pt(111): Surface active sites and reaction paths probed by formate". *J. Phys. Chem. C*, 112(32):12477–12485, 2008.

[104] Z. Paszti and L. Guczi. "Amino acid adsorption on hydrophilic TiO_2: A sum frequency generation vibrational spectroscopy study". *Vib. Spectrosc.*, 50(1):48–56, 2009.

[105] T. A. Ishibashi, H. Uetsuka, and H. Onishi. "An ordered retinoate monolayer prepared on rutile TiO_2(110)". *J. Phys. Chem. B*, 108(44):17166–17170, 2004.

[106] C. L. Anfuso, R. C. Snoeberger, A. M. Ricks, W. Liu, D. Xiao, V. S. Batista, and T. Lian. "Covalent attachment of a rhenium bipyridyl CO_2 reduction catalyst to rutile TiO_2". *J. Am. Chem. Soc.*, 133(18):6922–6925, 2011.

[107] K. Uosaki, T. Yano, and S. Nihonyanagi. "Interfacial water structure at as-prepared and UV-induced hydrophilic TiO_2 surfaces studied by sum frequency generation spectroscopy and quartz crystal microbalance". *J. Phys. Chem. B*, 108(50):19086–19088, 2004.

[108] Y. Liu, J. I. Dadap, D. Zimdars, and K. B. Eisenthal. "Study of interfacial charge-transfer complex on TiO_2 particles in aqueous suspension by second-harmonic generation". *J. Phys. Chem. B*, 103(13):2480–2486, 1999.

[109] A. N. Shultz, W. Jang, W. M. Hetherington, D. R. Baer, L. Q. Wang, and M. H. Engelhard. "Comparative 2nd-harmonic generation and X-ray photoelectron-spectroscopy studies of the UV creation and O-2 healing of Ti^{3+} defects on (110)rutile TiO_2 surfaces". *Surf. Sci.*, 339(1-2):114–124, 1995.

[110] A. N. Shultz, W. M. Hetherington, D. R. Baer, L. Q. Wang, and M. H. Engelhard. "Comparative SHG and XPS studies of interactions between defects and N_2O on rutile TiO_2(110) surfaces". *Surf. Sci.*, 392(1-3):1–7, 1997.

[111] E. Kobayashi, K. Matsuda, G. Mizutani, and S. Ushioda. "SHG observation of rutile TiO_2(110)/H_2O interface under UV light illumination". *Surf. Sci.*, 427-28:294–297, 1999.

[112] E. Kobayashi, G. Mizutani, and S. Ushioda. "Surface optical second harmonic generation from rutile TiO_2(110) in air". *Jpn. J. Appl. Phys. 1*, 36(12A):7250–7256, 1997.

[113] S. Nakamura, K. Matsuda, T. Wakasugi, E. Kobayashi, G. Mizutani, S. Ushioda, T. Sekiya, and S. Kurita. "Optical second-harmonic generation from the anatase TiO_2 (101) face". *J. Lumin.*, 87-9:862–864, 2000.

[114] E. Kobayashi, T. Wakasugi, G. Mizutani, and S. Ushioda. "Optical second harmonic spectroscopy of rutile TiO_2(110) in air". *Surf. Sci.*, 402(1-3):537–541, 1998.

[115] B. Raecke and H. Schirp. "2,6-Naphthalenedicarboxylic acid". *Org. Synth.*, 40:71–74, 1960.

[116] C. Li, Z. Liu, J. Schöneboom, F. Eickemeyer, N. G. Pschirer, P. Erk, A. Herrmann, and K. Müllen. "Perylenes as sensitizers in hybrid solar cells: How molecular size influences performance". *J. Mater. Chem.*, 19(30):5405–5415, 2009.

[117] E. Meyer. "Atomic force microscopy". *Prog. Surf. Sci.*, 41(1):3–49, 1992.

[118] C. R. Brundle (Ed.). *"Encyclopedia of Materials Characterization: Surfaces, Interfaces, Thin Films"*. Materials characterization series. Butterworth-Heinemann, Boston, 1992.

[119] J. C. Vickerman (Ed.). *"Surface Analysis: The Principal Techniques"*. Wiley, Chichester, 2nd edition, 2009.

[120] L. Reimer (Ed.). *"Scanning Electron Microscopy: Physics of Image Formation and Microanalysis"*. Springer-Verlag, Berlin, 2nd edition, 1998.

[121] M. Reichenbächer and J. Popp. *"Strukturanalytik organischer und anorganischer Verbindungen"*. Teubner-Verlag, Wiesbaden, 2007.

[122] P. W. Atkins. *"Physikalische Chemie"*. Wiley-VCH-Verlag, Weinheim, 3rd edition, 2001.

[123] N. G. Pschirer, C. Kohl, F. Nolde, J. Qu, and K. Müllen. "Pentarylene- and hexarylenebis(dicarboximide)s: Near-infrared-absorbing polyaromatic dyes". *Angew. Chem. Int. Ed.*, 45(9):1401–1404, 2006.

[124] H.-H. Perkampus. *"UV-VIS Spectroscopy and its Applications"*. Springer-Verlag, Berlin, 1992.

[125] P. R. Griffiths and J.A. de Haseth. *"Fourier Transform Infrared Spectrometry"*. John Wiley & Sons, Hoboken, 2nd edition, 2007.

[126] E. Smith and G. Dent. *"Modern Raman Spectroscopy - A Practical Approach"*. John Wiley & Sons, Chichester, 2005.

[127] J. R. Ferraro, K. Nakamoto, and C. W. Brown. *"Introductory Raman Spectroscopy"*. Elsevier, Amsterdam, 2nd edition, 2003.

[128] T. H. Maiman. "Stimulated optical radiation in ruby". *Nature*, 187(4736):493–494, 1960.

[129] P. A. Franken, A. E. Hill, C. W. Peters, and G. Weinreich. "Generation of optical harmonics". *Phys. Rev. Lett.*, 7:118–119, 1961.

[130] J. A. Giordmaine. "Mixing of light beams in crystals". *Phys. Rev. Lett.*, 8:19–20, 1962.

[131] R. W. Terhune, P. D. Maker, and C. M. Savage. "Optical harmonic generation in calcite". *Phys. Rev. Lett.*, 8:404–406, 1962.

[132] J. A. Armstrong, N. Bloembergen, J. Ducuing, and P. S. Pershan. "Interactions between light waves in a nonlinear dielectric". *Phys. Rev.*, 127:1918–1939, 1962.

[133] N. Bloembergen and P. S. Pershan. "Light waves at the boundary of nonlinear media". *Phys. Rev.*, 128:606–622, 1962.

[134] P. Guyot-Sionnest, J. H. Hunt, and Y. R. Shen. "Sum-frequency vibrational spectroscopy of a Langmuir film - study of molecular-orientation of a two-dimensional system". *Phys. Rev. Lett.*, 59(14):1597–1600, 1987.

[135] J. H. Hunt, P. Guyot-Sionnest, and Y. R. Shen. "Observation of C-H stretch vibrations of monolayers of molecules optical sum-frequency generation". *Chem. Phys. Lett.*, 133(3):189–192, 1987.

[136] X. D. Zhu, H. Suhr, and Y. R. Shen. "Surface vibrational spectroscopy by infrared-visible sum frequency generation". *Phys. Rev. B*, 35(6):3047–3050, 1987.

[137] A. L. Harris, C. E. D. Chidsey, N. J. Levinos, and D. N. Loiacono. "Monolayer vibrational spectroscopy by infrared-visible sum generation at metal and semiconductor surfaces". *Chem. Phys. Lett.*, 141(4):350–356, 1987.

[138] A. G. Lambert, P. B. Davies, and D. J. Neivandt. "Implementing the theory of sum frequency generation vibrational spectroscopy: A tutorial review". *Appl. Spectrosc. Rev.*, 40(2):103–145, 2005.

[139] C. D. Bain. "Sum-frequency vibrational spectroscopy of the solid-liquid interface". *J. Chem. Soc., Faraday Trans.*, 91(9):1281–1296, 1995.

[140] R. W. Boyd. *"Nonlinear Optics"*. Elsevier, Academic Press, Amsterdam, 3rd edition, 2008.

[141] L. Dreesen, C. Humbert, M. Celebi, J. J. Lemaire, A. A. Mani, P. A. Thiry, and A. Peremans. "Influence of the metal electronic properties on the sum-frequency generation spectra of dodecanethiol self-assembled monolayers on Pt(111), Ag(111) Au(111) single crystals". *Appl. Phys. B*, 74(7-8):621–625, 2002.

[142] A. D. Curtis, S. B. Reynolds, A. R. Calchera, and J. E. Patterson. "Understanding the role of nonresonant sum-frequency generation from polystyrene thin films". *J. Phys. Chem. Lett.*, 1(16):2435–2439, 2010.

[143] F. Vidal and A. Tadjeddine. "Sum-frequency generation spectroscopy of interfaces". *Rep. Prog. Phys.*, 68(5):1095–1127, 2005.

[144] L. J. Richter, T. P. Petralli-Mallow, and J. C. Stephenson. "Vibrationally resolved

sum-frequency generation with broad-bandwidth infrared pulses". *Opt. Lett.*, 23(20):1594–1596, 1998.

[145] D. Verreault, V. Kurz, C. Howell, and P. Koelsch. "Sample cells for probing solid/liquid interfaces with broadband sum-frequency-generation spectroscopy". *Rev. Sci. Instrum.*, 81(6):063111/1–063111/10, 2010.

[146] A. Lagutchev, S. A. Hambir, and D. D. Dlott. "Nonresonant background suppression in broadband vibrational sum-frequency generation spectroscopy". *J. Phys. Chem. C*, 111(37):13645–13647, 2007.

[147] A. Lagutchev, A. Lozano, P. Mukherjee, S. A. Hambir, and D. D. Dlott. "Compact broadband vibrational sum-frequency generation spectrometer with nonresonant suppression". *Spectrochim. Acta, Part A*, 75(4):1289–1296, 2010.

[148] U. B. Cappel, M. H. Karlsson, N. G. Pschirer, F. Eickemeyer, J. Schoeneboom, P. Erk, G. Boschloo, and A. Hagfeldt. "A broadly absorbing perylene dye for solid-state dye-sensitized solar cells". *J. Phys. Chem. C*, 113(33):14595–14597, 2009.

[149] E. Johnson and R. Aroca. "Spectroscopic properties and packing of Langmuir-Blodgett monolayers of perylenetetracarboxylic anhydrides". *Langmuir*, 11(5):1693–1700, 1995.

[150] A. Lapinski, A. Graja, I. Olejniczak, A. Bogucki, M. Polomska, J. Baffreau, L. Perrin, S. Leroy-Lhez, and P. Hudhomme. "Vibrational and electronic properties of perylenediimide linked to fullerene and tetrathiafulvalene". *Mol. Cryst. Liq. Cryst.*, 447:405–421, 2006.

[151] J. Coates. *"Interpretation of Infrared Spectra, A Practical Approach"*. John Wiley & Sons, 2006.

[152] D. W. Mayo, F. A. Miller, and R. W. Hannah. *"Course Notes on the Interpretation of Infrared and Raman Spectra"*. Wiley-Interscience, Hoboken, 2004.

[153] M. Friedrich, G. Gavrila, C. Himcinschi, T.U. Kampen, A. Y. Kobitski, H. Mendez, G. Salvan, I. Cerrillo, J. Mendez, N. Nicoara, A. M. Baro, and D. R. T. Zahn. "Optical properties and molecular orientation in organic thin films". *J. Phys. Condens. Matter*, 15(38):S2699–S2718, 2003.

[154] K. Seto, P. John, and Y. Furukawa. "Infrared study on the molecular orientation in bulk-heterojunction films based on perylene and 3,4,9,10-perylenetetracarboxylic dianhydride". *Chem. Phys. Lett.*, 529:31–34, 2012.

[155] A. P. Kam, R. Aroca, and J. Duff. "Perylene tetracarboxylic-phthalocyanine mixed thin solid films. Surface-enhanced resonance Raman scattering imaging studies". *Chem. Mater.*, 13(12):4463–4468, 2001.

[156] U. Guhathakurtaghosh and R. Aroca. "Surface-enhanced Raman-scattering and surface-enhanced resonant Raman-scattering studies of perylenetetracarboxylic derivatives on Ag-coated Sn spheres and Ag and Au island films". *J. Phys. Chem.*, 93(16):6125–6128, 1989.

[157] S. Rodriguez-Llorente, R. Aroca, and J. Duff. "Vibrational spectra and thin solid films of a bi(propylperylenediimide)". *J. Mater. Chem.*, 8(10):2175–2179, 1998.

[158] B. Tolaieb, C. J. L. Constantino, and R. F. Aroca. "Surface-enhanced resonance Raman scattering as an analytical tool for single molecule detection". *Analyst*, 129(4):337–341, 2004.

[159] N. U. Zhanpeisov, S. Nishio, and H. Fukumura. "Density functional theory study of vibrational properties of the 3,4,9,10-perylene tetracarboxylic dianhy-

dride (PTCDA) molecule: IR, Raman, and UV-vis spectra". *Int. J. Quantum Chem.*, 105(4):368–375, 2005.

[160] P. Harder, M. Grunze, R. Dahint, G. M. Whitesides, and P. E. Laibinis. "Molecular conformation in oligo(ethylene glycol)-terminated self-assembled monolayers on gold and silver surfaces determines their ability to resist protein adsorption". *J. Phys. Chem. B*, 102(2):426–436, 1998.

[161] R. Scholz, A. Y. Kobitski, T. U. Kampen, M. Schreiber, D. R. T. Zahn, G. Jungnickel, M. Elstner, M. Sternberg, and T. Frauenheim. "Resonant Raman spectroscopy of 3,4,9,10-perylene-tetracarboxylic-dianhydride epitaxial films". *Phys. Rev. B*, 61(20):13659–13669, 2000.

[162] A. L. Goodman, E. T. Bernard, and V. H. Grassian. "Spectroscopic study of nitric acid and water adsorption on oxide particles: Enhanced nitric acid uptake kinetics in the presence of adsorbed water". *J. Phys. Chem. A*, 105(26):6443–6457, 2001.

[163] B. Völker. *Spektroskopische Charakterisierung von farbstoffsensibilisierten Solarzellen*. PhD thesis, University of Heidelberg, 2012.

[164] A. Vittadini, A. Selloni, F. P. Rotzinger, and M. Grätzel. "Formic acid adsorption on dry and hydrated TiO_2 anatase (101) surfaces by DFT calculations". *J. Phys. Chem. B*, 104(6):1300–1306, 2000.

[165] M. Pastore and F. De Angelis. "Computational modelling of TiO_2 surfaces sensitized by organic dyes with different anchoring groups: adsorption modes, electronic structure and implication for electron injection/recombination". *Phys. Chem. Chem. Phys.*, 14(2):920–928, 2012.

[166] M. L. A. Rigout and D. M. Lewis. "Use of Fourier transform infrared spectroscopy to follow the heterocumulene aided thermal dehydration of phthalic and naphthalic acids". *Appl. Spectrosc.*, 60(12):1405–1413, 2006.

[167] L. J. Fitzgerald, R. E. Gerkin, and G. D. Renkes. "Infrared-spectra of naphthalene-1,8-dicarboxylic acid and naphthalene-1,8-dicarboxylic anhydride". *Vib. Spectrosc.*, 2(4):269–271, 1991.

[168] E. Fuente, J. A. Menendez, M. A. Diez, D. Suarez, and M. A. Montes-Moran. "Infrared spectroscopy of carbon materials: A quantum chemical study of model compounds". *J. Phys. Chem. B*, 107(26):6350–6359, 2003.

[169] M.-O. Diesner, C. Howell, V. Kurz, D. Verreault, and P. Koelsch. "In vitro characterization of surface properties through living cells". *J. Phys. Chem. Lett.*, 1(15):2339–2342, 2010.

[170] I. V. Stiopkin, H. D. Jayathilake, C. Weeraman, and A. V. Benderskii. "Temporal effects on spectroscopic line shapes, resolution, and sensitivity of the broad-band sum frequency generation". *J. Chem. Phys.*, 132(23):234503/1–234503/9, 2010.

[171] T. Ishibashi and H. Onishi. "Vibrationally resonant sum-frequency generation spectral shape dependent on the interval between picosecond-visible and femtosecond-infrared laser pulses". *Chem. Phys. Lett.*, 346(5-6):413–418, 2001.

[172] A. D. Curtis, S. R. Burt, A. R. Calchera, and J. E. Patterson. "Limitations in the analysis of vibrational sum-frequency spectra arising from the nonresonant contribution". *J. Phys. Chem. C*, 115(23):11550–11559, 2011.

[173] A. D. Curtis, M. C. Asplund, and J. E. Patterson. "Use of variable time-delay sum-frequency generation for improved spectroscopic analysis". *J. Phys. Chem. C*, 115(39):19303–19310, 2011.

[174] A. D. Quast, A. D. Curtis, B. A. Horn, S. R. Goates, and J. E. Patterson. "Role of nonresonant sum-frequency generation in the investigation of model liquid chromatography systems". *Anal. Chem.*, 84(4):1862–1870, 2012.

[175] J. E. Laaser, W. Xiong, and M. T. Zanni. "Time-domain SFG spectroscopy using mid-Ir pulse shaping: practical and intrinsic advantages". *J. Phys. Chem. B*, 115(11):2536–2546, 2011.

[176] H. Yamamoto, N. Watanabe, A. Wada, K. Domen, and C. Hirose. "Adsorption and decomposition of formic acid on MgO(001) surface as investigated by temperature programmed desorption and sum-frequency generation spectroscopy: Recurrence induced defect sites". *J. Chem. Phys.*, 106(11):4734–4744, 1997.

[177] M. B. Raschke, M. Hayashi, S. H. Lin, and Y. R. Shen. "Doubly-resonant sum-frequency generation spectroscopy for surface studies". *Chem. Phys. Lett.*, 359(5-6):367–372, 2002.

[178] D. Wu, G.-H. Deng, Y. Guo, and H. Wang. "Observation of the interference between the intramolecular IR-visible and visible-IR processes in the doubly resonant sum frequency generation vibrational spectroscopy of rhodamine 6G adsorbed at the air/water interface". *J. Phys. Chem. A*, 113(21):6058–6063, 2009.

[179] J. Y. Huang and Y. R. Shen. "Theory of doubly resonant infrared-visible sum-frequency and difference-frequency-generation from adsorbed molecules". *Phys. Rev. A*, 49(5, Part b):3973–3981, 1994.

[180] M. Hayashi, S. H. Lin, M. B. Raschke, and Y. R. Shen. "A molecular theory for doubly resonant IR-UV-vis sum-frequency generation". *J. Phys. Chem. A*, 106(10):2271–2282, 2002.

[181] Y. Caudano, C. Silien, C. Humbert, L. Dreesen, A. A. Mani, A. Peremans, and P.A. Thiry. "Electron-phonon couplings at C-60 interfaces: a case study by two-color, infrared-visible sum-frequency generation spectroscopy". *J. Electron Spectrosc. Relat. Phenom.*, 129(2-3):139–147, 2003.

[182] L. Dreesen, C. Humbert, Y. Sartenaer, Y. Caudano, C. Volcke, A. A. Mani, A. Peremans, P. A. Thiry, S. Hanique, and J. M. Frere. "Electronic and molecular properties of an adsorbed protein monolayer probed by two-color sum-frequency generation spectroscopy". *Langmuir*, 20(17):7201–7207, 2004.

[183] C. Humbert, L. Dreesen, Y. Sartenaer, A. Peremans, P. A. Thiry, and C. Volcke. "On the protoporphyrin monolayers conformation". *ChemPhysChem*, 7(3):569–571, 2006.

[184] Q. Li, R. Hua, and Keng K. C. Chou. "Electronic and conformational properties of the conjugated polymer MEH-PPV at a buried film/solid interface investigated by two-dimensional IR-visible sum frequency generation". *J. Phys. Chem. B*, 112(8):2315–2318, 2008.

[185] B. Bozzini, L. D'Urzo, C. Mele, B. Busson, C. Humbert, and A. Tadjeddine. "Doubly resonant sum frequency generation spectroscopy of adsorbates at an electrochemical interface". *J. Phys. Chem. C*, 112(31):11791–11795, 2008.

[186] T. Maeda, T. Nagahara, M. Aida, and T. Ishibashi. "Identification of chemical species of fluorescein isothiocyanate isomer-I (FITC) monolayers on platinum by doubly resonant sum-frequency generation spectroscopy". *J. Raman Spectrosc.*, 39(11):1694–1702, 2008.

[187] T. Miyamae, K. Tsukagoshi, and W. Mizutani. "Two-color sum frequency generation study of poly(9,9-dioctylfluorene)/electrode interfaces". *Phys. Chem. Chem.*

Phys., 12(44):14666–14669, 2010.

[188] D. Ino, K. Watanabe, N. Takagi, and Y. Matsumoto. "Ultrafast excited state dynamics in 3,4,9,10-perylene tetracarboxylic dianhydride (PTCDA) thin films". *Chem. Phys. Lett.*, 383(3-4):261–265, 2004.

[189] D. B. O'Brien, T. C. Anglin, and A. M. Massari. "Surface chemistry and annealing-driven interfacial changes in organic semiconducting thin films on silica surfaces". *Langmuir*, 27(22):13940–13949, 2011.

[190] K. R. McCrea and G. A. Somorjai. "SFG-surface vibrational spectroscopy studies of structure sensitivity and insensitivity in catalytic reactions: cyclohexene dehydrogenation and ethylene hydrogenation on Pt(111) and Pt(100) crystal surfaces". *J. Mol. Catal. A-Chem.*, 163(1-2):43–53, 2000.

[191] W. Q. Fang, X.-Q. Gong, and H. G. Yang. "On the unusual properties of anatase TiO_2 exposed by highly reactive facets". *J. Phys. Chem. Lett.*, 2(7):725–734, 2011.

[192] D. C. Grinter, M. Nicotra, and G. Thornton. "Acetic acid adsorption on anatase TiO_2(101)". *J. Phys. Chem. C*, 116(21):11643–11651, 2012.

[193] C. A. Hunter and J. K. M. Sanders. "The nature of pi-pi interactions". *J. Am. Chem. Soc.*, 112(14):5525–5534, 1990.

[194] M. R. Hansen, T. Schnitzler, W. Pisula, R. Graf, K. Muellenand, and H. W. Spiess. "Cooperative molecular motion within a self-assembled liquid-crystalline molecular wire: The case of a TEG-substituted perylenediimide disc". *Angew. Chem. Int. Ed.*, 48(25):4621–4624, 2009.

[195] F. Zasada, W. Piskorz, S. Godlewski, J. S. Prauzner-Bechcicki, A. Tekiel, J. Budzioch, P. Cyganik, M. Szymonski, and Z. Sojka. "Chemical functionalization of the TiO_2(110)-(1 x 1) surface by deposition of terephthalic acid molecules. A density functional theory and scanning tunneling microscopy study". *J. Phys. Chem. C*, 115(10):4134–4144, 2011.

[196] D. C. Grinter, P. Nickes, T. Woolcot, S. N. Basahel, A. Y. Obaid, A. A. Al-Ghamdi, E. H. E-Mossalamy, A. O. Alyoubi, and G. Thornton. "Binding of a benzoate dye-molecule analogue to rutile titanium dioxide surfaces". *J. Phys. Chem. C*, 116(1):1020–1026, 2012.

[197] H.-F. Wang, W. Gan, R. Lu, Y. Rao, and B.H. Wu. "Quantitative spectral and orientational analysis in surface sum frequency generation vibrational spectroscopy (SFG-VS)". *Int. Rev. Phys. Chem.*, 24(2):191–256, 2005.

[198] F. Cecchet, D. Lis, J. Guthmuller, B. Champagne, Y. Caudano, C. Silien, A. A. Mani, P. A. Thiry, and A. Peremans. "Orientational analysis of dodecanethiol and p-nitrothiophenol SAMs on metals with polarisation-dependent SFG spectroscopy". *ChemPhysChem*, 11(3):607–615, 2010.

[199] T. C. Anglin, J. C. Speros, and A. M. Massari. "Interfacial ring orientation in polythiophene field-effect transistors on functionalized dielectrics". *J. Phys. Chem. C*, 115(32):16027–16036, 2011.

[200] R. Y. Wang, M. Himmelhaus, J. Fick, S. Herrwerth, W. Eck, and M. Grunze. "Interaction of self-assembled monolayers of oligo(ethylene glycol)-terminated alkanethiols with water studied by vibrational sum-frequency generation". *J. Chem. Phys.*, 122(16):164702/1–164702/6, 2005.

[201] P. T. Wilson, K. A. Briggman, W.E. Wallace, J. C. Stephenson, and L.J. Richter. "Selective study of polymer/dielectric interfaces with vibrationally resonant sum fre-

quency generation via thin-film interference". *Appl. Phys. Lett.*, 80(17):3084–3086, 2002.

[202] G. Bazzan, J. R. Deneault, T.-S. Kang, B. E. Taylor, and M. F. Durstock. "Nanoparticle/dye interface optimization in dye-sensitized solar cells". *Adv. Funct. Mater.*, 21(17):3268–3274, 2011.

[203] H.-H. Perkampus. *"UV-VIS Atlas of Organic compounds"*, volume 2: spectra D1/1 - M19, spectrum of *E. A. Johnson*. VCH, Weinheim, 2nd edition, 1992.

[204] J. Kattner and H. Hoffmann. *"External Reflection Spectroscopy of Thin Films on Dielectric Substrates"*, pages 1–19. John Wiley & Sons, Ltd, 2006.

[205] K. A. Briggman, J. C. Stephenson, W. E. Wallace, and L. J. Richter. "Absolute molecular orientational distribution of the polystyrene surface". *J. Phys. Chem. B*, 105(14):2785–2791, 2001.

[206] K.S. Gautam, A. D. Schwab A., Dhinojwala, D. Zhang, S. M. Dougal, and M. S. Yeganeh. "Molecular structure of polystyrene at air/polymer and solid/polymer interfaces". *Phys. Rev. Lett.*, 85(18):3854–3857, 2000.

[207] G. Ma and H. C. Allen. "Surface studies of aqueous methanol solutions by vibrational broad bandwidth sum frequency generation spectroscopy". *J. Phys. Chem. B*, 107(26):6343–6349, 2003.

[208] W. T. Liu, L. N. Zhang, and Y. R. Shen. "Interfacial layer structure at alcohol/silica interfaces probed by sum-frequency vibrational spectroscopy". *Chem. Phys. Lett.*, 412(1-3):206–209, 2005.

[209] A. Tilocca and A. Selloni. "Methanol adsorption and reactivity on clean and hydroxylated anatase(101) surfaces". *J. Phys. Chem. B*, 108(50):19314–19319, 2004.

[210] A. Serrallach, R. Meyer, and Hs.H. Günthard. "Methanol and deuterated species: Infrared data, valence force field, rotamers, and conformation". *J. Mol. Spectrosc.*, 52(1):94–129, 1974.

[211] J. Florian, J. Leszczynski, B. G. Johnson, and L. Goodman. "Coupled-cluster and density functional calculations of the molecular structure, infrared spectra, Raman spectra, and harmonic force constants for methanol". *Mol. Phys.*, 91(3):439–447, 1997.

[212] L. Zhang, W. Liu, Y. R. Shen, and D. G. Cahill. "Competitive molecular adsorption at liquid/solid interfaces: A study by sum-frequency vibrational spectroscopy". *J. Phys. Chem. C*, 111(5):2069–2076, 2007.

[213] D. J. C. Yates. "Infrared studies of the surface hydroxyl groups on titanium dioxide, and of the chemisorption of carbon monoxide and carbon dioxide". *J. Phys. Chem.*, 65(5):746–753, 1961.

[214] L. F. Liao, C. F. Lien, D. L. Shieh, M. T. Chen, and J. L. Lin. "FTIR study of adsorption and photoassisted oxygen isotopic exchange of carbon monoxide, carbon dioxide, carbonate, and formate on TiO_2". *J. Phys. Chem. B*, 106(43):11240–11245, 2002.

[215] W. Gu and C. P. Tripp. "Reaction of silanes in supercritical CO_2 with TiO_2 and Al_2O_3". *Langmuir*, 22(13):5748–5752, 2006.

[216] A. Padermshoke, S. Konishi, M. Ara, H. Tada, and T.-A. Ishibashi. "Novel SiO_2-deposited CaF_2 substrate for vibrational sum-frequency generation (SFG) measurements of chemisorbed mono layers in an aqueous environment". *Appl. Spectrosc.*, 66(6):711–718, 2012.

Acknowledgments

The experimental work of this thesis was carried out at the Institute of Toxicology and Genetics (ITG) at the Karlsruhe Institute of Technology (KIT) - Campus North in Eggenstein-Leopoldshafen. It was financed by third-party funding provided by BASF SE, EnBW AG and BMBF.

First, I would like to thank Prof. Dr. Michael Grunze for supervising and reviewing this work. The timely discussions with him always helped me and brought me forward in my project. I would also like to thank Prof. (apl.) Dr. Hans-Robert Volpp for kindly accepting to be my second reviewer.

I would like to give a special thanks to Prof. Dr. Patrick Koelsch who gave me the opportunity to conduct my thesis work in his research group. His catching optimism always motivated me to continue and to believe in my work. Also my thanks go to my former colleagues of the Koelsch group at KIT, Dr. Dominique Verreault, Dr. Christoph Barth, Dr. Mark-Oliver Diesner, Dr. Volker Kurz, Dr. Caitlin Howell and Markus Niermeyer, for their constant availability and willingness to give a hand. I would like to specially thank Dominique for spending motivation in fruitful discussions, for giving experimental assistance, and for accepting the task of correcting my thesis. Thank you!

I would like to take the opportunity to thank my collaboration partners in the S2F project, Prof. Dr. Thomas Bürgi (APC, Heidelberg), Prof. (apl.) Dr. Michael Zharnikov (APC), Dr. Florian Staier (APC), Dr. Jacek Stolarczyk (LMU, Munich), Dr. Yong Liu (BASF SE), Dr. Korinna Dormann (BASF SE) and Dr. Markus Dörr (BASF SE), for stimulating scientific discussions, experiments and workshops.

Leo Pöttinger and Thomas Kriesche, my colleagues from the APC are specially thanked for always welcoming me when my work brought me from time to time to Heidelberg. Special thanks go to Leo who collaborated with me in the S2F project, for getting me started in my work, for providing data and thoughts as well as for the AFM measurements.

Another big thank you also goes to the group of Dr. Michael Bruns and his group at the IAM-WPT (KIT), namely Vanessa Oberst, Udo Geckle, Vanessa Trouillet and Florian Stemme. Vanessa, thanks a lot for the preparation of my various substrates and Udo, thanks for your SEM measurements. I would like to thank Stefan Heissler at IFG (KIT) for the help with the IR and Raman measurements and his patience in explaining the instruments and techniques used. I'm grateful to Dorota Jakubczyk at IFG who let me work in her lab and helped me a lot with the chemical cleavage of NA. Thanks for all the time you spent to assist me.

Also, I would like to say thank you to Reinhold Jehle, Klaus Schmitt and his coworkers from the APC machine shop for their technical support in design and fabrication. I thank Artur Schneider, my former *Forschungspraktikant*, for experimental support as well as constructive scientific discussions at the very beginning of the project.

My appreciation also to Dr. Alex Welle (IBG, KIT) and Prof. Dr. Katja Schmitz (TU, Darmstadt) for accepting a seat on my TAC.

Finally, I would like to thank my family and friends for their constant support and motivation, especially in the hard times. I am glad that you are part of my life.

Eidesstattliche Erklärung

Ich erkläre hiermit, dass ich die vorgelegte Dissertation selbst verfasst und mich keiner anderen als der von mir ausdrücklich bezeichneten Quellen und Hilfen bedient habe. Außerdem habe ich an keiner anderen Stelle ein Prüfungsverfahren beantragt bzw. die Dissertation in dieser oder anderer Form bereits anderweitig als Prüfungsarbeit verwendet oder einer anderen Fakultät als Dissertation vorgelegt.

Anna Keese

Karlsruhe, 5. Oktober 2012